

# **Mode dynamics in coupled disk optical microresonators**

**Dissertation**  
**zur Erlangung des akademischen Grades**  
**doctor rerum naturalium (Dr. rer. nat.)**

**vorgelegt dem Rat der Physikalisch-Astronomischen Fakultät  
der Friedrich-Schiller-Universität Jena**

**von Diplom-Physiker Carsten Schmidt**  
**geboren am 08.09.1981 in Erfurt**

**Gutacher / Referees**

1. Prof. Dr. Thomas Pertsch, Friedrich-Schiller-Universität Jena
2. Prof. Dr. Karsten Buse, Albert-Ludwigs-Universität Freiburg
3. Prof. Dr. Hui Cao, Yale University, USA

**Tag der Disputation / Day of defense: 23.04.2013**

# Contents

<b>1</b>	<b>Introduction</b>	<b>3</b>
<b>2</b>	<b>Fundamental theoretical concepts</b>	<b>9</b>
2.1	Eigenmodes of single microdisks . . . . .	9
2.1.1	Analytic approximation of single microdisk resonances . . . . .	10
2.1.2	Finite-Element simulation of eigenmodes in a single microdisk . . . . .	17
2.2	Resonant modes of coupled microdisks . . . . .	23
2.2.1	Semi-analytical model for arbitrarily coupled circular disks . . . . .	24
2.2.2	General spectral analysis using resonant mode approximation . . . . .	26
2.2.3	Accurate field calculations using multiple mode orders . . . . .	33
2.3	Coupled mode theory for an arbitrary number of disks . . . . .	36
2.3.1	Single mode traveling wave resonator . . . . .	38
2.3.2	Modal coupling due to Rayleigh scattering . . . . .	39
2.3.3	Modes in coupled resonator structures . . . . .	41
<b>3</b>	<b>Experimental realization and basic characterization</b>	<b>44</b>
3.1	Fabrication of coupled microdisks . . . . .	44
3.2	Tapered fiber coupling . . . . .	46
3.3	Experimental setup . . . . .	52
3.4	General sample characterization . . . . .	54
3.4.1	Resonance spectrum characteristics . . . . .	54
3.4.2	Q-factor, optical losses and finesse . . . . .	57
<b>4</b>	<b>Mapping of eigenstates in coupled microdisks</b>	<b>64</b>
4.1	Mode mapping method . . . . .	65
4.2	Coupled mode theory including the scattering SNOM tip . . . . .	67
4.3	Experimental verification for a single microdisk . . . . .	69
4.4	Two coupled microdisks . . . . .	73
4.5	Three coupled microdisks - linear arrangement . . . . .	74
4.6	Three coupled microdisks - triangular arrangement . . . . .	76

<b>5</b>	<b>Optically induced thermal nonlinearity in coupled microdisks</b>	<b>79</b>
5.1	Coupled mode theory including thermal nonlinearity . . . . .	80
5.2	Optical bistability observable in tapered fiber coupled microdisks . . . . .	84
5.3	Direct measurement of the thermal relaxation time . . . . .	87
5.4	Nonlinear mode dynamics in coupled microdisks . . . . .	88
5.4.1	Two coupled disks . . . . .	90
5.4.2	Three coupled disks in linear arrangement . . . . .	91
5.5	Compensation of thermal nonlinearity . . . . .	93
<b>6</b>	<b>Summary and perspective</b>	<b>97</b>
<b>A</b>	<b>Bibliography</b>	<b>i</b>
<b>B</b>	<b>Useful mathematics and calculations</b>	<b>xv</b>
B.1	Vector algebra and integral theorems . . . . .	xv
B.2	Functional formulation for the FEM . . . . .	xvi
B.2.1	The standard vector wave equation . . . . .	xvi
B.2.2	Weak terms for axisymmetric resonators . . . . .	xviii
B.2.3	Convergence tests . . . . .	xx
B.3	Characteristic equation of a slab waveguide . . . . .	xxi
<b>C</b>	<b>Symbols, constants and parameters</b>	<b>xxiv</b>
<b>D</b>	<b>Abbreviations</b>	<b>xxxii</b>
<b>E</b>	<b>Zusammenfassung</b>	<b>xxxii</b>
<b>F</b>	<b>Publications</b>	<b>xxxiv</b>
<b>G</b>	<b>Acknowledgements</b>	<b>xxxviii</b>
<b>H</b>	<b>Short Curriculum Vitae</b>	<b>xl</b>

# 1 Introduction

In 1910 Lord Rayleigh described the phenomenon of the so called whispering-gallery observable in St. Paul’s cathedral in London [Ray10, Ray14]. Hence, conversations held on one side of the wall below the dome can be heard clearly at the other side. Rayleigh showed that the physical dimensions make the gallery below the dome a resonator for sound waves traveling along the wall by continuous reflections. This phenomenon can be transferred into optics where it happens on a much smaller micrometer scale when considering optical wavelengths in the visible and near infrared and hence leading to the new class of optical resonators: whispering-gallery-mode (WGM) microresonators [Vah03]. In such structures the light traveling in the high index material undergoes repetitive total internal reflections at the interface to the low index surrounding medium. After one roundtrip light interferes constructively for wavelengths that are multiples of the effective circumference resulting in distinct resonances. Contrary to, e.g., Fabry-Perot resonators, ideal single directional pumped WGM resonators are traveling wave resonators not showing standing wave patterns. Due to the imperfect total internal reflection at a curved interface a small fraction of the light can escape the resonator by tunneling [Sny75, Cul76]. Hence, even in the case of an ideal lossless material and a flat interface the light in the resonator will decay, resulting in a finite Q-factor or resonance bandwidth. Nevertheless, as the effect of light tunneling is very weak, the Q-factor can be extremely large, resulting in a long photon storage time inside the resonator. Another important property is the small size of the resonators down to several microns. In combination with the structure of the WGMs the light is strongly confined inside the resonator with only an evanescent tail in the surrounding medium which is characterized by the mode volume ( $V_{\text{mode}}$ ). Furthermore, the potentially small size of the cavity results in a large free spectral range (FSR) which in combination with the small resonance bandwidth leads to an exceptional high finesse. The long temporal and strong spatial confinement as well as the spectral isolation of the WGMs gives rise to strong enhancement of light matter interaction at significantly reduced thresholds in such systems and make WGM microresonators a versatile platform for fundamental physical studies in linear and nonlinear optics as well as for potential new applications.

The subject of this thesis “Mode dynamics in coupled disk optical microresonators” deals with the interaction of optical WGMs in mutually coupled microresonators. However, in order to understand the emerging effects and to point out the potential of coupled WGM microresonators a comprehensive knowledge of realizations and characteristics of the single microresonator is of importance.

## Current state of knowledge

The first experimental study on optical WGM microresonators was made with microspheres [Gar61] and microdroplets under free space illumination, demonstrating WGM lasing [Tze84, Lin86, Qia86], stimulated Brillouin and Raman scattering [Zha89, Lin94] as well as stimulated emission enhancement [Cam91]. Later on, lasing in on-chip semiconductor microdisks [McC92] and the photoluminescence into WGMs of micropillars [Gér96] was realized under free space illumination. Due to the spatial distribution of the WGMs along the circumference of the resonator, the efficiency of direct coupling to WGMs by free space illumination is very poor. One possibility to overcome this problem is an active medium inside the cavity that directly emits into the WGM when pumped from the outside. Another possibility is the coupling to the evanescent fields of the WGMs which allows for their direct excitation and passive investigation. This was first demonstrated by prism coupling to microspheres revealing efficient excitation of WGMs with Q-factors on the order of  $10^8$  [Bra89, Gor94]. In the following several groups tried to push the Q-factor toward the fundamental limit on the order of  $10^{10}$  in silica microspheres at optical wavelengths [Gor96] and identified the thermal nonlinearity as the lowest threshold nonlinearity in such systems under room temperature conditions leading to thermal bistability [Bra89, Col93, Gor94]. Under more exotic conditions in a 2 K superfluid helium environment thermal effects could be suppressed and bistability caused by Kerr nonlinearity was observed evidencing the extremely low pump power thresholds on the microwatt level [Tre98]. Furthermore, the coupling of counterpropagating WGMs caused by scattering at material imperfections of the resonator was shown [Wei95]. Experiments on cavity quantum electrodynamics (CQED) were performed revealing the strong interaction of atoms and photons in high-Q WGMs [Kim06, Ver98a]. Likewise, the direct coupling to the WGMs allows for the realization of WGM lasing with threshold pump powers of a few hundred nanowatt [San96]. Although prism coupling has limited efficiency and restrictions in terms of integration, the robustness and variety of accessible materials makes this method the method of choice for investigations of WGMs in high index crystalline microresonators. Utilizing materials like calcium fluoride [Sav04, Gru06] and lithium niobate [Ilc03] exceeds the Q-factor to the order of  $10^{11}$  [Sav07] and allows for low threshold and efficient parametric frequency conversion [Ilc04, Für10, Bec11].

Another ingredient pushing forward the development of the WGM microresonators was the introduction of tapered optical fibers for external coupling to WGMs [Kni97]. Tapered fibers allow single mode phase matched excitation of WGMs with a coupling efficiency of almost unity [Spi03] and provide direct access to the WGMs of on-chip microresonators like disks [Kip03] and toroids [Arm03]. Due to the effectively reduced dimensionality of the microdisks and microtoroids, their mode spectrum becomes much cleaner and the mode volume is reduced as compared to microspheres. This enhances the possibility of direct spectral mode identification, improves CQED experiments [Spi05] and results in on-chip single mode lasers with lowest thresholds [Yan03]. Furthermore, it enables the route to new and versatile sensing applications

for physical quantities or nanoparticles, e.g., viruses and biomolecules [Boy01, Vol02, Gaa06, Arm07, Zhu09, Li10, Dom11]. Likewise, the efficient tapered fiber coupling allows for the observation of nonlinear effects like optical parametric oscillations [Kip04b] as well as on-chip frequency comb generation [Del07] in microtoroids. The extension of the concept for integrated waveguide coupling makes WGMs accessible in a variety of materials in a fully integrated manner, e.g., semiconductor materials and in particular silicon that is of importance due to its compatibility to existing optoelectronic applications. The integration of coupling waveguide and resonator was first demonstrated for semiconductor microrings and -disks [Raf97] and later was realized for high-Q silicon WGM microdisks [Sol07b].

Based on the sophisticated fabrication of on-chip microresonators new effects, arising from the interaction of optical and mechanical degrees of freedom in these structures, were described in the scope of optomechanics [Kip07, Kip08, Jia09, Ros09]. From the variety of possible effects of optomechanics discussed in Ref. [Kip07] the radiation pressure induced quantum ground state cooling of a macroscopic mechanical oscillator might be the most stunning from a fundamental point of view [Sch09b, Riv11].

Beside the widely used sphere, disk, and toroid microresonators the development of advanced taper fiber fabrication techniques [War06] allows the experimental realization of another cavity type: WGM bottle microresonators [Sum04, Lou05] providing enhanced tunability while preserving Q-factors and mode volumes known from microspheres [Mur09, Pöl09].

One may also notice a development to smaller wavelength-scale microresonators [Sha09, Sol10], the exploration of new materials [Gri08], and further investigations of semiconductor microresonators [Sri06, Mic07] in order to improve their Q and  $V_{\text{mode}}$  characteristics. Variations in the resonator shape are investigated as an additional degree of freedom, particularly applied to semiconductor microdisks in order to realize a directional laser output [Lev93, Wie06, Bor06e, Det08, Dub08]. A promising approach realizing directional emission uses a smoothly deformed circumference of the cavity resulting in a so called asymmetric resonant cavity [Nöc97] where the high Q-factors are maintained [Son10, Son11]. Moreover, microresonators operating in fluidic environment were realized suitable for unlabeled biosensing applications [Arn03, Arm05, Vos07, Ost09]. Furthermore, surface-plasmon-polariton-WGMs were observed in an hybrid metal-dielectric microdisk [Min09] allowing for the realization of a plasmonic laser.

To conclude this brief review<sup>1</sup> of different fields of investigations of WGM microresonators, the particular influence of the main parameters Q and  $V_{\text{mode}}$  on the crucial characteristics should be summarized. Depending on the device geometry and the used materials, the Q-factor typically ranges from  $10^4$  to  $10^6$  in semiconductor microdisks and up to  $10^9$  to  $10^{11}$  for fused silica spheres and crystalline microresonators. The modal volume  $V_{\text{mode}}$  ranges from hundreds of  $\lambda^3$  in microspheres down to a few  $\lambda^3$  in semiconductor microdisks. A high Q-factor is mostly preferable, especially since the corresponding narrow resonance bandwidth

<sup>1</sup>The author raises no claim to completeness of this information. A comprehensive summary of WGM resonator characteristics and possible applications can be found in Refs. [Mat06, Ilc06].

determines the limits of WGM resonators as optical filter elements as well as that of narrow bandwidth photon sources and lasers as the threshold pump power scales with  $Q^{-1}$ . The Q-factor is also the dominating parameter for observation of nonlinear optical effects, e.g., optical parametric oscillations, second harmonic generation, or frequency comb generation in optical microresonators since the threshold pump powers scale according to  $V_{\text{mode}}Q^{-2}$ . The mode volume related to the size and hence the FSR of the resonator becomes important for effects depending mainly on the finesse like sensing applications as well as QED effects in the weak coupling regime, e.g., Purcell enhanced spontaneous emission that scales with  $QV_{\text{mode}}^{-1}$ . The  $QV_{\text{mode}}^{-1}$  dependence is also important for the observation of opto-mechanical coupling effects and typically is accompanied by a reduced form factor of the structure to allow high-Q mechanical modes and enables a regime of dominant optical forces [Ros09, Kip07].

## Coupled microresonators

The particular structure of WGMs allows for the mutual optical coupling of microresonators that are placed next to each other. The effects observable in coupled microresonators first were considered theoretically in the framework of electromagnetic plane wave scattering by aggregates of spherical particles described by rigorous modal expansion [Ful91, Mis02]. Experimentally the modes of such photonic molecules (in analogy to the electron states in molecules) were investigated in semiconductor micropillars [Bay98], polymer microspheres [Muk99] and semiconductor microdisks [Nak05, Ish06]. The collective excitations of longer chains of coupled polymer microspheres were investigated in the framework of coupled resonator optical waveguides (CROW) [Yar99] revealing a photonic bandstructure [Hee04, Har05, M l06] and hence typical effects like slow light can be expected. Experimentally this was demonstrated in coupled microring structures<sup>2</sup> [Poo06, Mor07]. Other effects studied in one-dimensional (1D) chains of coupled microrings are cavity enhanced four wave mixing [Mor11] and the realization of flat top add-drop filters [Pop06]. Furthermore, CROW-based optically tunable routers and switchers were investigated theoretically [Bor07]. The extension of the coupling of WGM to two-dimensional (2D) structures allows for even more complex photonic molecules and gives rise to Q-factor enhancement (at least for low-Q resonators) and increased sensitivity to changes of the environmental dielectric constant [Bor06a] which is important for sensing applications. The versatile structure of photonic molecules also allows for engineering highly directional far field emission patterns or quasi single mode operation of coupled microdisk lasers predicted by a rigorous theoretical analysis [Bor06c].

The experimental realization of coupled microresonator structures always struggles with

---

<sup>2</sup>One should mention that microrings usually are designed as curved single mode waveguides and the modes are not at all WGMs, especially when considering the inner boundary which is absent in real WGM resonators. Nevertheless, the observable effects are comparable to WGM resonators since no dramatic change of the mode characteristics is expected when shifting the inner boundary of the ring towards its center resulting in a microdisk, except for possible guiding of higher order radial modes and slightly increased Q-factors.



the uniformity of their single elements. Especially the fabrication of very high-Q reflow structures like spheres and toroids is less reproducible resulting in significant resonance mismatch of the individual resonators although strategies for the assembly of preselected resonators were developed [HZ07]. Hence, first experiments coupled different WGMs of distinct microtoroids [Gru09]. To this reason, identical coupled microresonators were realized so far from polymer microspheres assembled on a flat or patterned substrate [Ast04, Rak04, Har05, M l07] or coupled microrings [Poo06, Mor07] showing moderate Q-factors ( $10^3$  to  $10^5$ ). Since in particular the sorting out of size matching polymer microspheres is cumbersome the lithographic fabrication used for microrings seems to be the preferable method for the fabrication of identical microresonators matching the tolerances determined by the finite Q-factor or resonance bandwidth. Despite this problem, the coupling of size mismatched microresonators is of interest for studies of photon transport and light localization in random media [Wie97, Ast04, Ast07] as well as for directional output coupling of possible coupled microresonator lasers [Bor06c, Nos07].

## Aim and structure of this thesis

When the work on this thesis started in 2007 only a few experiments on coupled WGM microresonators were reported. As mentioned above, their main realizations were based on polymer microspheres or silicon microring resonators. On the one hand these coupled rings are only single mode structures not supporting higher order radial WGMs and on the other hand the WGMs in such coupled polymer spheres were excited unspecifically by means of stimulated emission of active dopants. This complicates a general and comprehensive experimental study of WGM characteristics in coupled microresonators.

The goal of this thesis was to establish an experimental platform allowing for fabrication of arbitrarily arranged two-dimensionally coupled microresonators and a detailed experimental investigation of the WGM characteristics in such structures. As material system a functional fused silica layer on top of a silicon substrate was chosen. The advantages of this approach are manifold: Firstly, the fabrication results in a symmetric refractive index distribution since the fused silica disks are free standing above the silicon substrate with a large spatial separation (tens of  $\lambda$ ). Secondly, the free standing microdisks are accessible by tapered optical fiber coupling. Thirdly, in fused silica the thermal nonlinearity has the lowest pump power threshold and can be investigated separately from other nonlinear effects, e.g., additional free carrier dispersion in silicon microdisks [Joh06, Bor06d].

The investigations are focused on the linear spectral characteristics of coupled microdisks. Of particular interest are the reproducibility of the fabrication and the question if the high Q-factors of single microdisks can be maintained for coupled structures. Additionally, a comprehensive analysis of the spectral and spatial distribution of the collective WGM excitations or eigenmodes of coupled microresonators is done. Furthermore, exploring the nonlinear opti-

cal power regime, the nonlinear dynamics of the WGMs in coupled microresonators are studied and the potentials for possible applications are discussed. The experimental data are used to support the development of theoretical models for the description of optical characteristics in coupled microresonators. Since there were presented versatile theoretical approaches considering different aspects of microresonator research in literature another objective of this thesis is to summarize and extend existing models for a comprehensive theoretical study of coupled WGM microresonators. Therefore, both analytical as well as numerical methods are used. Due to the general character of the investigations it is expected that both theoretical and experimental methods as well as the obtained results are applicable to other WGM microresonator geometries and materials, at least qualitatively.

This thesis is structured as follows: In chapter 2 the theoretical foundations for the description of coupled WGM microresonators are summarized. It starts with recapitulating the analytical 2D approximation of WGMs in single microdisks followed by a numerical analysis using a finite-element-method (FEM) to complement the calculation of basic characteristics of single microdisks. The analytical 2D approximation results in the formulation of a modal expansion scattering problem that is extended to allow for the calculation of resonances in arbitrarily coupled microdisks. Additionally, a coupled mode theory (CMT) is described, taking into account a tapered fiber excitation, thermal nonlinear effects as well as intra- and inter-disk coupling of WGMs. In chapter 3 the fabrication of coupled microdisks and of tapered optical fibers for the excitation of WGMs is described. Furthermore, the experimental setup and methods are introduced and the linear spectral characterisation of coupled microdisks is presented. In chapter 4 a method for the measurement of the spatial intensity distribution of the eigenmodes in coupled microdisks is described. It is based on scattering scanning near-field optical microscopy (SNOM) techniques and is accompanied by a detailed theoretical analysis using an adapted CMT. In chapter 5 the WGM dynamics in coupled fused silica microdisks are investigated under the influence of the thermal nonlinearity. With the results from chapter 4 new effects like differential all-optical resonance tuning in coupled microdisks are predicted by calculations and verified experimentally. Furthermore, the compensation of thermal nonlinear effects in coupled microdisks is discussed and realized. Finally, in chapter 6 the main results of this thesis are summarized and an outlook on further research activities is given.

The realization of this thesis benefits from the contributions of different people. The most important was the fabrication of the coupled microdisk samples, which was done by Dipl.-Ing. Thomas Käsebier from the Microstructure Technology group at the Institute of Applied Physics (IAP) at the Friedrich-Schiller-Universität Jena (FSU). The theoretical part was supported by Prof. Lev Deych from the Physics Department at the Queens College, New York, who developed the basic parts of the analytical modal expansion of WGMs in coupled microdisks. Furthermore, rigorous numerical finite difference time domain (FDTD) simulations were performed by Dr. Christoph Etrich from the Institute of Condensed Matter Theory and Solid State Optics (IFTO) at the FSU in order to test the validity of the applied approximative models.

## 2 Fundamental theoretical concepts

This chapter provides the theoretical foundation for the description of the optical properties of coupled WGM microdisks. The optical modes of single microdisks and their characteristics are calculated by analytical as well as numerical methods. For the description of coupled microdisks the analytical approach is extended to characterize the collective optical excitations in dependence of their geometrical arrangement and physical properties. The dynamics of the modes in coupled microdisks as well as their excitation are analyzed within the scope of a coupled mode theory.

### 2.1 Eigenmodes of single microdisks

The electromagnetic fields in optical microresonators can be described by Maxwell's equations, which for dielectric media (no free charges and currents) can be written in frequency space as [Jac99]

$$\nabla \times \mathbf{E}(\mathbf{r}, \omega) = i\omega \mathbf{B}(\mathbf{r}, \omega), \quad (2.1)$$

$$\nabla \times \mathbf{H}(\mathbf{r}, \omega) = -i\omega \mathbf{D}(\mathbf{r}, \omega), \quad (2.2)$$

$$\nabla \cdot \mathbf{D}(\mathbf{r}, \omega) = 0, \quad (2.3)$$

$$\nabla \cdot \mathbf{B}(\mathbf{r}, \omega) = 0, \quad (2.4)$$

with the space coordinate vector  $\mathbf{r}$ , the frequency of the optical field  $\omega$ , the macroscopic observable electric field  $\mathbf{E}$  and magnetic induction  $\mathbf{B}$  as well as the dielectric displacement  $\mathbf{D}$  and magnetic field  $\mathbf{H}$ . The vector fields  $\mathbf{F} \in \{\mathbf{E}, \mathbf{D}, \mathbf{B}, \mathbf{H}\}$  in frequency space are related to the corresponding field vectors in the time domain by the Fourier transform, defined as

$$\mathbf{F}(\mathbf{r}, t) = \int_{-\infty}^{\infty} \mathbf{F}(\mathbf{r}, \omega) e^{-i\omega t} d\omega \quad \text{and} \quad \mathbf{F}(\mathbf{r}, \omega) = \frac{1}{2\pi} \int_{-\infty}^{\infty} \mathbf{F}(\mathbf{r}, t) e^{i\omega t} dt. \quad (2.5)$$

Assuming a nonmagnetic medium and denoting the vacuum permittivity  $\epsilon_0$  and permeability  $\mu_0$  the constitutive relations can be written as

$$\mathbf{D}(\mathbf{r}, \omega) = \epsilon_0 \mathbf{E}(\mathbf{r}, \omega) + \mathbf{P}(\mathbf{r}, \omega), \quad (2.6)$$

$$\mathbf{B}(\mathbf{r}, \omega) = \mu_0 \mathbf{H}(\mathbf{r}, \omega). \quad (2.7)$$

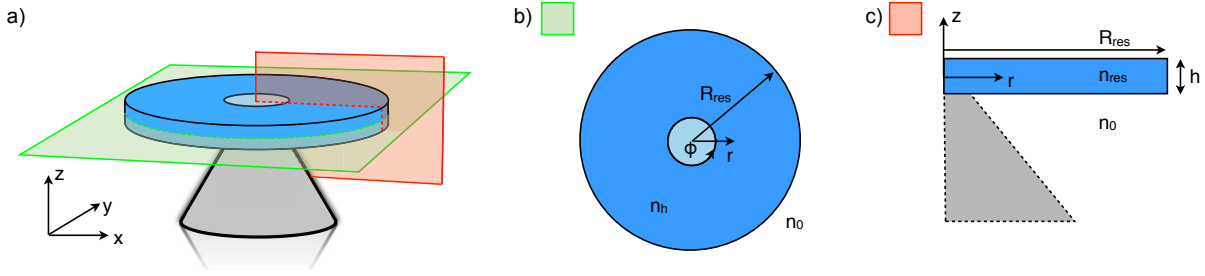


Fig. 2.1: (a) Schematic of a disk microresonator illustrating the approximations to reduce the complexity of the 3D problem to a 2D one for (b) the analytical approximation and (c) the finite element simulation.

For a linear and isotropic medium the polarization  $\mathbf{P}$  can be expressed as  $\mathbf{P}(\mathbf{r}, \omega) = \epsilon_0[\epsilon(\mathbf{r}, \omega) - 1]\mathbf{E}(\mathbf{r}, \omega)$  with the dielectric function  $\epsilon(\mathbf{r}, \omega)$ . The wave equation for the electric field can be derived by taking the curl of Eq. (2.1) and eliminating the magnetic field with the help of Eqs. (2.7) and (2.2). Using also Eq. (2.6) one obtains

$$\nabla \times \nabla \times \mathbf{E}(\mathbf{r}, \omega) - k_0^2 \epsilon(\mathbf{r}, \omega) \mathbf{E}(\mathbf{r}, \omega) = 0, \quad (2.8)$$

with  $k_0 = \omega/c$  and  $c = 1/\sqrt{\mu_0 \epsilon_0}$  the speed of light in vacuum. Further resolving the curl of the curl and taking the result of substituting Eq. (2.6) into Eq. (2.3) one can write<sup>1</sup>

$$\nabla^2 \mathbf{E}(\mathbf{r}, \omega) + \nabla \left[ \frac{1}{\epsilon(\mathbf{r}, \omega)} \mathbf{E}(\mathbf{r}, \omega) \cdot \nabla \epsilon(\mathbf{r}, \omega) \right] + k_0^2 \epsilon(\mathbf{r}, \omega) \mathbf{E}(\mathbf{r}, \omega) = 0. \quad (2.9)$$

For solving the general wave equation (2.9) one usually makes the approximation of piecewise homogeneous media, which reduces the equation to the vector wave equation. A full three-dimensional (3D) analytical solution is possible only for certain geometries, e.g., spherical microresonators or infinite extended cylinders [Boh83]. One can see from Eq. (2.9) that for the case of a translational invariance in at least one direction of the system it can be separated, allowing for the solution of just the transverse electric or the transverse magnetic fields.

In the following, two different approaches for the calculation of the optical modes of a single microdisk resonator are described: an analytical, effective index approximation (EIM) and the finite element method (FEM). The approximations, which are done to the structure are illustrated in Fig. 2.1.

### 2.1.1 Analytic approximation of single microdisk resonances

As mentioned above, for a piecewise homogeneous medium, Eq. (2.9) can be reduced to the vector wave equation for the fields  $\mathbf{F} \in \{\mathbf{E}, \mathbf{H}\}$

$$\nabla^2 \mathbf{F}(\mathbf{r}, \omega) + k_0^2 \epsilon(\mathbf{r}, \omega) \mathbf{F}(\mathbf{r}, \omega) = 0, \quad (2.10)$$

<sup>1</sup>A similar equation can be derived for the magnetic field.

which can be solved separately for the homogeneous parts of the system and the final solution is determined by the boundary conditions for the fields between these parts. For the investigated microdisks with a finite extend in z-direction no analytical solution can be found, even if one takes into account the invariance of the dielectric function along the  $\phi$ -direction in a cylindrical coordinate system resulting in  $\epsilon(\mathbf{r}) = \epsilon(r, \phi, z) = \epsilon(r, z)$ . An analytical solution can be approximated by reducing the system to two dimensions (2D), which becomes possible for disks with a height much smaller than their radius ( $h \ll R_{\text{res}}$ ). In this case the vertical confinement is similar to that of a slab waveguide of thickness  $h$  and one can use an effective index of the slab mode as an approximation for the refractive index of the disk in the 2D  $(r, \phi)$ -plane. A consequence of this approximation is the separation of the optical fields into two main polarization states, which is explained by the polarization dependent nature of plane-wave reflection at the interfaces of the slab [Sny83]. One can find TE modes with the electric field in the disk plane and TM modes with the electric field perpendicular to the disk plane, which allows to solve Eq. (2.10) independently for the transverse fields  $F_z \in \{E_z(TM), H_z(TE)\}$ , reducing the problem to a scalar equation. Representing the Laplacian operator in cylindrical coordinates ( $\nabla^2 = \partial^2/\partial r^2 + r^{-1}\partial/\partial r + r^{-2}\partial^2/\partial\phi^2 + \partial^2/\partial z^2$ ), using the refractive index  $n^2(r, z) = \epsilon(r, z)$  and the separation of variables  $F_z(r, \phi, z) = F_{z,\parallel} \cdot F_{z,\perp} = X(r, \phi)Y(z)$ , Eq. (2.10) can be written as (the frequency dependence of the fields is dropped to enhance readability)

$$\frac{1}{X(r, \phi)} \left( \frac{\partial^2 X(r, \phi)}{\partial r^2} + \frac{1}{r} \frac{\partial X(r, \phi)}{\partial r} + \frac{1}{r^2} \frac{\partial^2 X(r, \phi)}{\partial \phi^2} \right) + \frac{1}{Y(z)} \frac{\partial^2 Y(z)}{\partial z^2} + k_0^2 n^2(r, z) = 0. \quad (2.11)$$

This can be separated into two equations by introducing an effective slab mode index  $n_{\text{eff},z}$  for  $r \leq R_{\text{res}}$ :<sup>2</sup>

$$\frac{\partial^2 X(r, \phi)}{\partial r^2} + \frac{1}{r} \frac{\partial X(r, \phi)}{\partial r} + \frac{1}{r^2} \frac{\partial^2 X(r, \phi)}{\partial \phi^2} + k_0^2 n_{\text{eff},z}^2(r) X(r, \phi) = 0, \quad (2.12)$$

$$\frac{\partial^2 Y(z)}{\partial z^2} + k_0^2 (n^2(z) - n_{\text{eff},z}^2) Y(z) = 0. \quad (2.13)$$

Equation (2.13) is the standard eigenvalue problem of a slab waveguide with the solution found in many textbooks (e.g., see Ref. [Oka06] or Appendix B.3). The resulting  $n_{\text{eff},z}$  is used as the effective disk index in two dimensions ( $n_{\text{eff},z} \equiv n_h$  for  $r \leq R_{\text{res}}$  and  $n_{\text{eff},z} \equiv n_0$  for  $r > R_{\text{res}}$ ) in Eq. (2.12), which can be separated further using  $X(r, \phi) = X_r(r)X_\phi(\phi)$ :

$$\frac{\partial^2 X_r}{\partial r^2} + \frac{1}{r} \frac{\partial X_r}{\partial r} + \left( k_0^2 n_{\text{eff},z}^2(r) - \frac{m^2}{r^2} \right) X_r = 0, \quad (2.14)$$

$$\frac{\partial^2 X_\phi}{\partial \phi^2} + m^2 X_\phi = 0. \quad (2.15)$$

<sup>2</sup>Eq. (2.12) is valid also for  $r > R_{\text{res}}$  with  $n_{\text{eff},z} = n_0$  with  $n_0$  as the refractive index of the surrounding medium, whereas Eq. (2.13) makes no sense because no slab waveguide is present for  $r > R_{\text{res}}$ .

The solution of Eq. (2.15) gives a harmonic dependence of the field in the azimuthal direction  $X_\phi = e^{im\phi}$  with the mode number  $m \in \mathbb{Z}$  and  $|m|$  accounting for the number of field maxima (and minima) along the  $\phi$ -direction. The opposite sign of  $m$  distinguishes the modes traveling clockwise (cw,  $-m$ ) and counterclockwise (ccw,  $+m$ ), which are degenerated in frequency.<sup>3</sup> Equation (2.14) is a Bessel type differential equation. With the restriction that the solution should be finite at the origin as well as zero at infinity one finds a Bessel function  $J_m(kr)$  for  $r \leq R_{\text{res}}$  and a Hankel function of the first kind  $H_m^{(1)}(kr)$  for  $r > R_{\text{res}}$ . The solution of the field in two dimensions can be written as

$$F_{z,\parallel} = X(r, \phi) = X_r X_\phi = \begin{cases} J_m(n_h k_0 r) e^{im\phi} & r \leq R_{\text{res}}, \quad m \in \mathbb{Z} \\ H_m^{(1)}(n_0 k_0 r) e^{im\phi} & r > R_{\text{res}}, \quad m \in \mathbb{Z}. \end{cases} \quad (2.16)$$

The field profile  $F_{z,\perp}$  along the  $z$ -direction obtained from Eq. (2.13) is described by a cosine inside and a decaying exponential above and below the disk, considering only the lowest mode in this direction. In general, it is not useful to calculate the 3D field distribution  $F_z = F_{z,\parallel} F_{z,\perp}$  in this way due to the large inaccuracy, especially at the corner regions of the disk. However, the 2D solution of Eq. (2.16) can be used to approximate the resonance frequencies with a sufficient accuracy. To this end, one can either solve the eigenvalue problem by matching the internal and external tangential field components as described in Ref. [Bor06d], or seek for the resonances of the scattering problem by introducing an incident field [Boh83]. The latter has the advantage to solve for complex resonance frequencies, allowing to estimate the radiation  $Q$ -factor, but on the cost of a more complicated root-finding algorithm. The relative difference in the real parts of the resonance frequencies of both methods and the numerical finite element method (FEM) is much less than one percent (see Sect. 2.1.2). As it is also the foundation for the coupled microdisk model (see Sect. 2.2) the resonance approach is described here.

We introduce an incident, a scattered and an internal field ( $F_{z,\parallel} = F_{\text{inc,sc,int}}$ ) and expand them into the obtained eigen functions [Eq. (2.16)]

$$F_{\text{inc}}(r, \phi, \omega) = \sum_m a_m(\omega) e^{im\phi} J_m(n_0 k_0 r), \quad (2.17)$$

$$F_{\text{sc}}(r, \phi, \omega) = \sum_m b_m(\omega) e^{im\phi} H_m^{(1)}(n_0 k_0 r), \quad (2.18)$$

$$F_{\text{int}}(r, \phi, \omega) = \sum_m d_m(\omega) e^{im\phi} J_m(n_h k_0 r), \quad (2.19)$$

with the mode amplitudes  $a_m(\omega)$ ,  $b_m(\omega)$  and  $d_m(\omega)$ , respectively. The resonances can be found by matching the tangential components of external and internal fields ( $H_z$  and  $E_\phi$  for TE polarization,  $E_z$  and  $H_\phi$  for TM polarization) applying boundary conditions. The  $\phi$ -components can be easily obtained by analyzing Eqs. (2.1) and (2.2) in cylindrical coordinates.

<sup>3</sup>The relation between  $\pm m$  and (cw,ccw) depends on the definition of the azimuthal angle. Usually, in a theoretical context  $\pm m$  is used, whereas experimentally related work uses the cw,ccw-notation.

In general, one has

$$F_{\text{inc}}(R_{\text{res}}) + F_{\text{sc}}(R_{\text{res}}) = F_{\text{int}}(R_{\text{res}}), \quad (2.20)$$

$$\left. \frac{\partial}{\partial r} F_{\text{inc}}(r) \right|_{r=R_{\text{res}}} + \left. \frac{\partial}{\partial r} F_{\text{sc}}(r) \right|_{r=R_{\text{res}}} = \bar{n}^2 \left. \frac{\partial}{\partial r} F_{\text{int}}(r) \right|_{r=R_{\text{res}}}, \quad (2.21)$$

where  $\bar{n}^2 = n_0^2/n_h^2$  for TE polarization and  $\bar{n}^2 = 1$  for TM polarization. Substitution of Eqs. (2.17)-(2.19) into Eqs. (2.20) and (2.21) leads to the modal scattering coefficient as the ratio between scattered and incident mode amplitude

$$\alpha_m(x) = \frac{b_m(x)}{a_m(x)} = \frac{\bar{n}^2 \frac{n_h}{n_0} [J_m(n_h x)]' J_m(n_0 x) - J_m(n_h x) [J_m(n_0 x)]'}{J_m(n_h x) [H_m^{(1)}(n_0 x)]' - \bar{n}^2 \frac{n_h}{n_0} H_m^{(1)}(n_0 x) [J_m(n_h x)]'}. \quad (2.22)$$

Here, the normalized frequency  $x = k_0 R_{\text{res}} = \omega R_{\text{res}}/c$  was introduced and the prime denotes the derivative of the function with respect to the full argument. Similarly, the expansion coefficients of the internal fields can be related to the ones of the scattered fields by

$$\beta_m(x) = \frac{d_m(x)}{b_m(x)} = \frac{J_m(n_0 x) [H_m^{(1)}(n_0 x)]' - H_m^{(1)}(n_0 x) [J_m(n_0 x)]'}{\bar{n}^2 \frac{n_h}{n_0} [J_m(n_h x)]' J_m(n_0 x) - J_m(n_h x) [J_m(n_0 x)]'}. \quad (2.23)$$

The resonances of the microdisk are determined by the zeros of the denominator of Eq. (2.22) and the characteristic equation reads as

$$G_m(x) = J_m(n_h x) [H_m^{(1)}(n_0 x)]' - \bar{n}^2 \frac{n_h}{n_0} H_m^{(1)}(n_0 x) [J_m(n_h x)]' = 0. \quad (2.24)$$

The complex roots of  $G_m$  can be calculated by use of the Davidenko's method [Hej93], which was successfully applied to the dispersion relation of lossy waveguide structures [Tal85] and also to solve for the resonances of microspheres [Agh06]. The advantages over the Newton-Raphson and Müller's method [Pre92] are in terms of convergence and sensitivity to the initial guess of the complex root, but can only be used if an analytical expression for the derivative of the complex function exists [here  $G_x(x) = \partial G_m(x)/\partial x$ ]. In detail it transforms the algebraic Eq. (2.24) by use of the Jacobian matrix into two first order ordinary differential equations (ODE) in terms of the real and imaginary parts of the complex variable  $x = x_1 + ix_2$ <sup>4</sup>

$$\frac{dx_1}{dt} = -\frac{1}{|G_x(x)|^2} \{ \Re[G(x)] \Re[G_x(x)] + \Im[G(x)] \Im[G_x(x)] \}, \quad (2.25)$$

$$\frac{dx_2}{dt} = \frac{1}{|G_x(x)|^2} \{ \Re[G(x)] \Im[G_x(x)] - \Im[G(x)] \Re[G_x(x)] \}. \quad (2.26)$$

The solution of this system is decaying exponentially in  $t$ , and hence  $x_1$  and  $x_2$  converge to

<sup>4</sup>The main advantage of the method takes effect in the case of an  $n$ -dimensional system of nonlinear equations with  $n \geq 2$ .

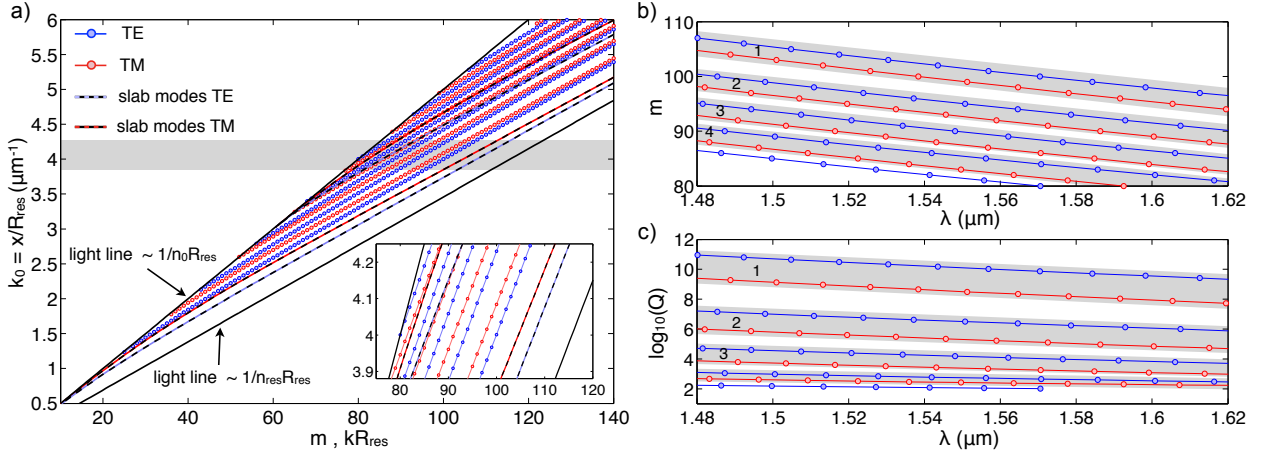


Fig. 2.2: (a) Dispersion diagram for the resonances in a microdisk with  $R_{\text{res}} = 20 \mu\text{m}$ ,  $h = 1 \mu\text{m}$ ,  $n_{\text{res}} = 1.445$  surrounded by air ( $n_0 = 1$ ). The discrete guided TE (blue dots) and TM (red dots) modes are bound between the light lines of the surrounding and bulk resonator material (black straight lines). Additionally, the propagation constants of the slab modes, according to Eq. (2.13), are plotted [blue(red)-black dashed line for TE(TM)]. The inset shows the experimentally observable range marked by the shaded area. The microdisk modes are plotted in a more convenient way for direct comparison with measured spectra in terms of mode number (b) and radiation  $Q$ -factor (c). The radial orders are distinguished from each other by the shaded areas starting with the first radial order having the largest azimuthal mode number  $m$  and largest  $Q$ , respectively.

the real and imaginary part of the complex root for  $t \rightarrow \infty$ .

For the implementation of Davidenko's method on the Eq. (2.24) a certain range of normalized frequencies  $x$  for a fixed mode number  $m$  was considered, looking for intervals with sign changes of  $G_m(x)$ . It turned out to be beneficial seeking first for the roots of  $\Im(G_m(x))$  in the selected intervals using a standard root search and taking them as initial values for the ODE solver. This significantly reduces the calculation time in comparison to solving the ODE system directly with an arbitrary value from the selected intervals. In Fig. 2.2(a) the calculated modes for a typical microdisk ( $R_{\text{res}} = 20 \mu\text{m}$ ,  $h = 1 \mu\text{m}$ ,  $n_{\text{res}} = 1.445$ ) are plotted in a general dispersion diagram [Sak01, Bor06d] allowing for a global view on the characteristics. The discrete guided modes are bound between the light lines of the surrounding air  $n_0 = 1$  and of the bulk resonator material  $n_{\text{res}}$ . As expected, the first order radial modes are closest to the bulk light line, whereas with increasing radial order the modes are located closer to the light line of the surrounding. According to the model the propagation constants of the slab modes are plotted as well, which as expected are upper bounds for the propagation constants of the disk modes. For the experimentally observable region [shaded region and magnified in the inset of Fig. 2.2(a)] second order slab modes are possible but play no significant role because they are close to cut-off. In general, for the same radial order the TE modes are stronger confined than TM modes resulting in larger azimuthal mode numbers  $m$ , connected to an effective microdisk mode index  $n_{\text{eff}} = m/(k_0 R_{\text{res}})$ . For the sake of comparison with experimental data it is preferable to plot the calculated modes in a more convenient way as mode number versus wavelength shown in Fig. 2.2(b), which directly can be used to identify



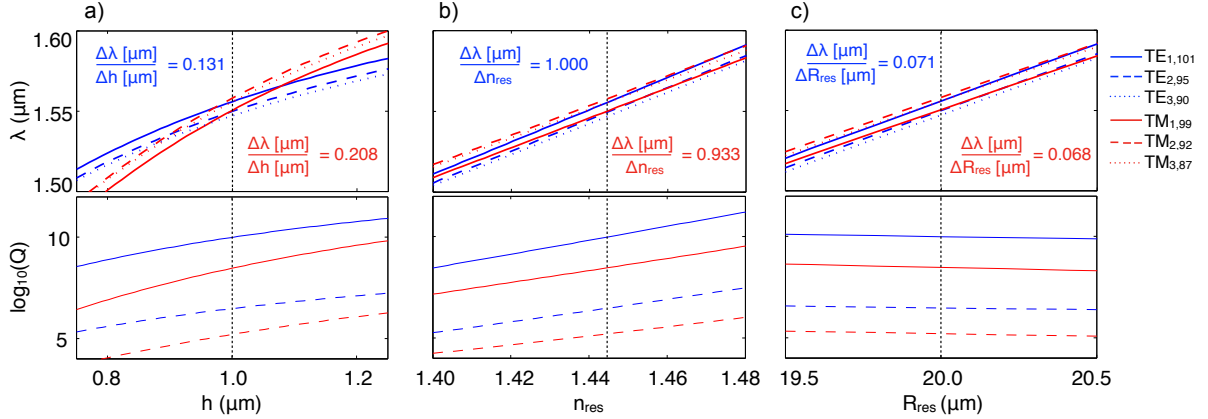


Fig. 2.3: Dependence of the resonance wavelength (upper graphs) and the radiation  $Q$ -factor (lower graphs) of TE and TM polarized modes of different radial order on the variation of (a) the microdisk thickness  $h$ , (b) the material refractive index  $n_{\text{res}}$  and (c) the radius  $R_{\text{res}}$ . The vertical line in each of the graphs marks the corresponding value of the parameter used as a constant in the other graphs. These constant values are the same as in Fig. 2.2. The given numbers are the slopes of the curves obtained from linearization around the initial parameter values.

the resonances in the measured spectra. The theoretical radiation  $Q$ -factors obtained from the model by  $Q = x_1/(2x_2)$  are plotted in Fig. 2.2(c). A fabricated disk will show significantly smaller  $Q$ -factors because of imperfect boundaries and nonzero material absorption, so the calculated values here can be seen as fundamental limits. The identification of the resonances can be done with the help of certain features in the spectrum, which are caused by different dispersion for different radial order or polarization. An example is the comparison of the first order radial TM modes ( $\text{TM}_{1,m}$ ) with the second order radial TE modes ( $\text{TE}_{2,m}$ ) in Fig. 2.2(b). For lower wavelengths the  $\text{TM}_{1,m}$  modes have larger resonance wavelengths than the  $\text{TE}_{2,m}$  modes, whereas for longer wavelengths it is opposite and at  $\lambda \approx 1.565 \mu\text{m}$  they almost coincide. These characteristics can be observed in the experiments as well and depend strongly on the microdisk parameters. Hence, the microdisk parameters can be obtained with very high accuracy (see Sect. 3.4.1).

The dependence of the resonance locations on the variations of  $R_{\text{res}}$ ,  $h$  and  $n_{\text{res}}$  are shown in Fig. 2.3. For each of the graphs one of the parameters was varied around its respective value used in Fig. 2.2, whereas the other two parameters were kept constant at these values. Increasing the disk thickness  $h$  in Fig. 2.3(a) leads to a red shift of the resonances for both TE and TM polarization. This is caused by the increasing effective slab mode index, which is used as the effective refractive index of the disk  $n_h$  in the 2D calculations and results in a smaller wavelength of the light in the material ( $\sim \lambda/n_h$ ). For constant  $R_{\text{res}}$  and  $n_{\text{res}}$  as well as for a constant mode number  $m$  this can be compensated only by a larger free space resonance wavelength. The polarization dependent slab mode dispersion leads to a significant difference of the slope for TE and TM polarization. Linearized around the initial disk parameters the slope is  $\Delta\lambda/\Delta h = 0.131(0.208)$  for TE(TM) polarization. For an estimation of

the relative impact on the resonance position a realistic uncertainty of the disk thickness of about 10 nm is assumed, which leads to a wavelength uncertainty of the resonance position of  $\Delta\lambda = 1.31 \text{ nm}(2.08 \text{ nm})$  for TE(TM), respectively. The variation of the material refractive index  $n_{\text{res}}$  in Fig. 2.3(b) gives qualitatively the same dependence because it also influences the effective refractive index of the 2D disk in the model. In contrast to the variation in  $h$ , the slope is stronger for the TE polarization:  $\Delta\lambda/\Delta n_{\text{res}} = 1.000 \text{ }\mu\text{m}(0.933 \text{ }\mu\text{m})$  for TE(TM). An uncertainty of  $\Delta n_{\text{res}} = 0.001$  leads to  $\Delta\lambda = 1.00 \text{ nm}(0.93 \text{ nm})$  for TE(TM), respectively. This uncertainty also covers the refractive index change due to material dispersion of the fused silica for the investigated wavelength range. According to literature values [Mal65],  $\Delta n_{\text{mat}} = \pm 6 \times 10^{-4}$  for the central wavelength of  $\lambda = 1.55 \text{ }\mu\text{m}$ . The material dispersion is neglected in the calculations but since it is normal ( $dn/d\lambda < 0$ ) it would slightly increase the wavelengths of the low wavelength resonances, whereas it decreases the wavelengths of the long wavelength resonances. Increasing the radius  $R_{\text{res}}$  in Fig. 2.3(c) leads to a red shift of the resonances as well. This can be understood by the fact that the resonance wavelength in the resonator material must increase for a mode of a certain azimuthal mode number  $m$ , provided its radial order is kept.<sup>5</sup> Due to the constant refractive index, also the free space resonance wavelength increases. This can be also seen from the relation of  $R_{\text{res}}$  and  $k_0 = 2\pi/\lambda_0$  in the normalized frequency  $x = k_0 R_{\text{res}}$ . The resonance condition [Eq. (2.24)] remains unchanged for constant  $x$ , which means increasing  $R_{\text{res}}$  must be compensated by increasing  $\lambda_0$ . Also in this case, the slope is stronger for the TE polarization:  $\Delta\lambda/\Delta R_{\text{res}} = 0.071(0.068)$  for TE(TM). Again assuming a realistic uncertainty of  $\Delta R_{\text{res}} = 10 \text{ nm}$  leads to  $\Delta\lambda = 0.71 \text{ nm}(0.68 \text{ nm})$  for TE(TM), respectively. A comparison shows that changing all three parameters in a realistic range of values leads to the same order of magnitude of the resonance shift, where the change of  $h$  and  $n_{\text{res}}$  has a slightly stronger impact than changing  $R_{\text{res}}$ .

In the lower row of the graphs in Fig. 2.3 the change of the Q-factors for the first two radial orders is shown depending on the corresponding parameter variation. For increasing  $h$  and  $n_{\text{res}}$  the Q-factors increase due to the stronger confinement of the modes. For increasing  $R_{\text{res}}$  the Q-factors decrease, which is not obvious from Eq. (2.24). The explanation must take into account the calculation of the effective slab mode index (2D disk index  $n_h$ ) in Eq. (2.13), which depends on the wavelength of the light. An increased  $\lambda_0$  due to a larger  $R_{\text{res}}$  leads to a smaller  $n_h$  and hence a more weakly confined resonator mode, which results in a smaller radiation Q-factor.

The advantage of the analytical 2D approximation [in the following referred to as effective index method (EIM)] is in the fast calculation of resonance wavelengths, which allows for automatization of the mode identification in measured spectra in dependence of the geometrical parameters  $R_{\text{res}}$ ,  $h$  and  $n_{\text{res}}$ . This can be used for the evaluation of the fabrication process, as well as for design of certain functionality of microdisks, e.g., in terms of the relative distance

<sup>5</sup>One may imagine a spoke wheel as a pictorial analogue, where the distance between the spokes increases along the radius of the wheel.

of certain resonances or adjustable absolute resonance wavelengths. Nevertheless, there is a lack of information on important characteristics, e.g., the full vectorial field distribution of different modes, mode volumes, etc., which can be obtained only numerically.

### 2.1.2 Finite-Element simulation of eigenmodes in a single microdisk

To overcome the limitations of the analytical EIM described above, a Finite-Element-Method (FEM) was used to calculate numerically the eigenmodes of single microdisks. The basic principles of the FEM<sup>6</sup> are [Jin02]:

- Reformulation of the boundary-value problem of a governing differential equation [e.g., Eq. (2.8)] in a variational form using either the Rayleigh-Ritz or the Galerkin method with the help of a trial function.
- Segmentation of the calculation domain into a finite number of elements at which the trial function is expanded usually in polynomials.<sup>7</sup> The elements are usually line segments in 1D, triangles or quadrilaterals in 2D, and tetrahedra or hexahedra in 3D.
- Substitution of the trial function expansion into the variational form together with the initial-, boundary-, and element-matching conditions leads to an algebraic system of equations which can be solved for the unknown expansion coefficients. The number of unknowns (or degrees of freedom) depends on the number of finite elements, the order of the expansion, the dimensionality of the calculation domain and the form of the solution, e.g. scalar or vectorial, and can be in the range of a few hundreds for scalar 1D problems to hundreds of millions for vectorial 3D problems.
- The found solution for the trial function represents an approximation to the solution of the differential equation.

To address especially the last three points the FEM software COMSOL<sup>8</sup> was used with the scripting interface to MATLAB<sup>9</sup>, which allows for flexible control, e.g., geometry parameter and mode number scans. The governing equation, which has to be solved, is the vector wave equation (2.8). If we assume only nonmagnetic materials for numerical reasons it is advantageous to solve the vector wave equation for the magnetic field  $\mathbf{H}$ , since it is continuous across all interfaces. Using the same procedure as described in Sect. 2.1 for Eq. (2.2), one obtains

$$\nabla \times [\hat{\epsilon}^{-1} \nabla \times \mathbf{H}(\mathbf{r}, \omega)] - k_0^2 \mathbf{H}(\mathbf{r}, \omega) = 0, \quad (2.27)$$

where in general  $\hat{\epsilon}^{-1} = \hat{\epsilon}^{-1}(\mathbf{r}, \omega)$  is the inverse relative permittivity tensor. The boundary conditions (assuming a calculation domain terminated by perfect conducting electric walls)

<sup>6</sup>Here the variational formulation and solution of the boundary value problem in the weak sense are considered.

<sup>7</sup>Other ansatz functions are possible, too.

<sup>8</sup><http://www.comsol.com/>

<sup>9</sup><http://www.mathworks.com/>

are

$$\hat{\mathbf{n}} \times [\hat{\epsilon}^{-1} \nabla \times \mathbf{H}(\mathbf{r}, \omega)] = 0, \quad \mathbf{H}(\mathbf{r}, \omega) \cdot \hat{\mathbf{n}} = 0 \quad \text{on } \partial V, \quad (2.28)$$

Here  $V$  is the Volume of the calculation domain,  $\partial V$  denotes the surface enclosing  $V$ , and  $\hat{\mathbf{n}}$  is the outward pointing surface normal. The solutions of Eq. (2.27) using the FEM procedure described here<sup>10</sup> will be contaminated by a lot of spurious solutions [Kon77, Dav82], which do not fulfill the divergence relation  $\nabla \cdot \mathbf{H} = 0$ . As discussed in Ref. [Jin02] they occur due to the nature of the variational formulation of the vector wave equation. The trial function used to formulate the variational functional must be twice differentiable. The expansion functions used in the FEM to approximate the trial function are forced to be continuous, but their derivatives do not have to be continuous (weak solution). To overcome this problem, the functional can be modified by explicitly imposing the condition of a divergence free solution [Kos84] using a penalty method [Lei68, Hop81]. As a result, Eq. (2.27) needs to be modified by a penalty term (see Appendix B.2.1)

$$\nabla \times [\hat{\epsilon}^{-1} \nabla \times \mathbf{H}(\mathbf{r}, \omega)] - \alpha \nabla [\nabla \cdot \mathbf{H}(\mathbf{r}, \omega)] - k_0^2 \mathbf{H}(\mathbf{r}, \omega) = 0 \quad \text{in } V. \quad (2.29)$$

As discussed in Ref. [Jin02], the penalty term may not eliminate the divergence of the solution completely, but reduces it substantially. Also the influence on the accuracy of the solution can be neglected for nonmagnetic materials. The parameter  $\alpha$  sets the strength of the divergence condition and, in general, can be used to find a good balance between suppression of spurious solutions and accuracy of the solution.

The variational functional form of Eq. (2.29) can be obtained by taking the inner product

$$\langle \mathbf{a}, \mathbf{b} \rangle = \int_V (\mathbf{b}^* \cdot \mathbf{a}) dV, \quad (2.30)$$

of both sides with the test function (or test magnetic field)  $\tilde{\mathbf{H}}$  [the dependence on  $(\mathbf{r}, \omega)$  is omitted] and leads to (see Appendix B.2.1)

$$F(\mathbf{H}) = \int_V \left[ (\nabla \times \tilde{\mathbf{H}}^*) \cdot (\hat{\epsilon}^{-1} \nabla \times \mathbf{H}) + \alpha (\nabla \cdot \tilde{\mathbf{H}}^*) (\nabla \cdot \mathbf{H}) - k_0^2 \tilde{\mathbf{H}}^* \cdot \mathbf{H} \right] dV. \quad (2.31)$$

It should be noted here, that the solution of Eq. (2.29) corresponds to the minimum of the functional (2.31) [ $\partial F(\mathbf{H}) = 0$  and  $\partial(\partial F(\mathbf{H})) > 0$ ] only for real  $\epsilon$  (lossless media) and homogeneous boundary conditions. A general formulation of the variational principle applicable to lossy and/or anisotropic media is based on an adjusted definition of the inner product

<sup>10</sup>Only scalar basis functions (node-based elements) for the expansion were used, although COMSOL allows for the use of vector basis functions (edge-based element), which are better suited for representation of electric and magnetic fields and inherently avoid the mentioned spurious solutions [Jin02]. Nevertheless, the results using the described approach are satisfactory.

[Eq. (2.30)] and can be found in Ref. [Jin02]. However, the obtained system will be identical to Eq. (2.31). The terms in the integrand of Eq. (2.31) are the three weak terms required for definition of the corresponding FEM model in COMSOL (or any other partial differential equation solver allowing a weak form representation) [Oxb07].

In considering only axisymmetric resonators (this involves the most common microresonator shapes like disks, spheres, toroids), the weak terms can be given explicitly. The system is reduced to a 2D problem in the  $(r, z)$ -plane [see Fig. 2.1], where the relative permittivity tensor reduces to the diagonal entries  $\hat{\epsilon} = \text{diag}(\epsilon_r, \epsilon_\phi, \epsilon_z)$ .<sup>11</sup> The magnetic field can be expressed as

$$\mathbf{H}(\mathbf{r}) = (H_r(r, z), iH_\phi(r, z), H_z(r, z))e^{im\phi}. \quad (2.32)$$

The imaginary unit has been introduced to the azimuthal component to allow all following expressions to be real valued containing the real amplitudes  $(H_r, H_\phi, H_z)$ , which have a common phase dependence of  $e^{im\phi}$ . A detailed derivation can be found in Ref. [Oxb07] or see Appendix B.2.2.

The particular geometry of WGM microresonators always leads to electromagnetic waves radiated from the microresonator and hence a finite radiation Q-factor. The perfect conducting walls used to truncate the calculation domain therefore will always cause reflections that influence the accuracy of the solution, especially if one is interested in the calculation of the radiation Q-factor. To solve this shortcoming, one can insert a perfectly matched layer (PML) [Ber94] between the outer layer and the boundary of the calculation domain. The PMLs allow for absorption of an incident plane wave without reflection for all frequencies, polarizations and angles of incidence due to the introduction of additional degrees of freedom to Maxwell's equations. In a simple picture its function can be described by an impedance matched inner boundary to avoid reflection of an incident wave and an increasing absorption towards the outer boundary of the calculation domain to decrease the amplitude of the wave significantly before hitting the perfect conducting outer boundary. An interpretation of the PML is a coordinate stretching in the frequency domain [Che94] with independent stretch factors in each coordinate direction as the additional degrees of freedom. From a different point of view the PML can be also interpreted as anisotropic absorber [Sac95] as a kind of special material with modified permittivity and permeability tensors. Following this approach, in cylindrical coordinates one can write for the axisymmetric restriction [Gre99] (the corresponding expression for the permeability can be obtained by replacing  $\hat{\epsilon}$  with  $\hat{\mu}$ )

$$\hat{\epsilon} = \hat{\epsilon}\hat{\Lambda} = \begin{pmatrix} \epsilon_r \frac{\tilde{r}}{r} \frac{s_z}{s_r} & 0 & 0 \\ 0 & \epsilon_\phi \frac{r}{\tilde{r}} s_z s_r & 0 \\ 0 & 0 & \epsilon_z \frac{\tilde{r}}{r} \frac{s_r}{s_z} \end{pmatrix}, \quad (2.33)$$

<sup>11</sup>Due to the axial symmetry  $\epsilon_r = \epsilon_\phi$  must apply, but with respect to the formulation of perfectly matched layers (PMLs) below, the different notations are preserved.

with the modified radius

$$\tilde{r} = \begin{cases} r & 0 \leq r \leq r_1, \\ r - i\delta_{\text{PML}} \frac{(r-r_1)^3}{3h_{\text{PML}}^2} & r > r_1, \end{cases} \quad (2.34)$$

and the additional stretching parameters

$$s_r = \begin{cases} 1 & 0 \leq r \leq r_1, \\ 1 - i\delta_{\text{PML}} \left( \frac{r-r_1}{h_{\text{PML}}} \right)^2 & r > r_1, \end{cases} \quad (2.35)$$

$$s_z = \begin{cases} 1 - i\delta_{\text{PML}} \left( \frac{z_1-z}{h_{\text{PML}}} \right)^2 & z < z_1, \\ 1 & z_1 \leq z \leq z_2, \\ 1 - i\delta_{\text{PML}} \left( \frac{z-z_2}{h_{\text{PML}}} \right)^2 & z > z_2. \end{cases} \quad (2.36)$$

Here  $r_1$ ,  $z_1$  and  $z_2$  denote the locations of the air to PML interfaces and  $h_{\text{PML}}$  is the thickness of the PML layer<sup>12</sup> [see Fig. 2.4(a)]. The real parameter  $\delta_{\text{PML}}$  is the growth factor of the attenuation towards the outer boundary. In continuous space the interface to the PML is reflectionless, whereas the discretization of the spatial domain leads to spurious reflections depending on  $\delta_{\text{PML}}$ . Therefore, this parameter has to be optimized for low reflection (small  $\delta_{\text{PML}}$ ) but strong enough attenuation (large  $\delta_{\text{PML}}$ ) in the PML, depending on the discretization and PML thickness. Although, only nonmagnetic materials are considered, the implementation of the PML requires modifications of the penalty term  $\alpha[\nabla \cdot (\hat{\mu} \tilde{\mathbf{H}}^*)][\nabla \cdot (\hat{\mu} \mathbf{H})]$  and the temporal weak term  $k_0^2 \hat{\mu} \tilde{\mathbf{H}}^* \mathbf{H}$  in Eq. (2.31) to take into account the variation of  $\hat{\mu}$ .

In Fig. 2.4(a) the geometry with definition of all subdomains and the refractive index distribution is shown for the disk parameters from Sect. 2.1.1. The upper half of the plot shows the real part of the refractive index profile, whereas the lower part shows the imaginary part of the refractive index.<sup>13</sup> One can see a continuous increase of the imaginary part in the PML region, which is responsible for the absorption of the traveling waves towards the outer boundary. In Fig. 2.4(b) two typical mesh cases (low resolution in the upper half; high resolution in the lower half) are shown. To allow a proper resolution of the disk geometry a mesh refinement area was defined, covering the main part of the disk as well as the air in close vicinity. The mesh element size for the coarse (fine) mesh is usually  $0.6\lambda$  ( $\lambda/6$ ) in the PML region and  $\lambda/10$  ( $\lambda/30$ ) in the refined disk region. Figs. 2.4(c,d) show the intensity distribution of a fundamental TE and TM mode. Again, the pictures are split showing the distribution on a normal scale in the upper half and on a log-scale [ $\log(I/I_{\text{max}})$ ] in the lower half. One

<sup>12</sup>In general, the thickness  $h_{\text{PML}}$  in each of the Eqs. (2.34) to (2.36) can be different, where in the considered case only a single value was used.

<sup>13</sup>For the case of disks with vertical sidewalls the problem shows a mirror symmetry along  $z = 0$  that can be used to truncate the calculation domain and reduce the computational effort. Here the redundancy was used to present additional information in a more compact form.

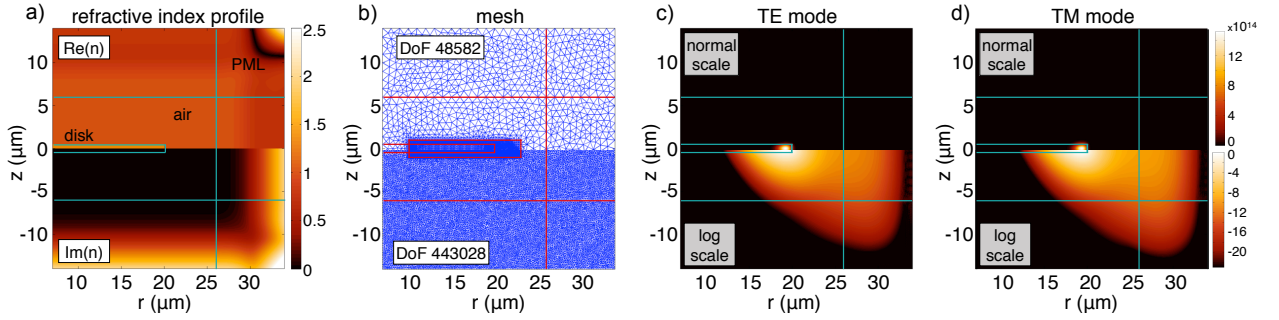


Fig. 2.4: (a) FEM geometry for an axisymmetric microdisk ( $R_{\text{res}} = 20 \mu\text{m}$ ,  $h_{\text{res}} = 1 \mu\text{m}$ ,  $n_{\text{res}} = 1.445$ ) showing the refractive index distribution of the real part (upper half) and imaginary part (lower half). (b) Two mesh cases used for FEM calculations. The coarse mesh (upper half) has an element size of  $0.6\lambda$  ( $\lambda/10$ ) in the PML region (refined disk region). The fine mesh (lower half) has an element size of  $\lambda/6$  ( $\lambda/30$ ) in the PML region (refined disk region) and is not resolved in the picture. In (c) and (d) the intensity profile of a TE and a TM mode is shown on a normal scale (upper half) and on a log-scale (lower half). When hitting the outer boundary the intensity is dropped by more than 22 orders of magnitude, which avoids reflections back to the calculation domain.

can see that the intensity decreases more than 22 orders of magnitude before hitting the outer boundary, which efficiently reduces reflections back to the calculation domain.

The convergence of the solution was investigated in terms of resonance wavelength and Q-factor by optimization of the thickness of the PML layer  $h_{\text{PML}}$ , the PML growth factor  $\delta_{\text{PML}}$ , the penalty term strength  $\alpha$ , the mesh resolution as well as the extension of the air domain between disk and PML (determined by  $h_{\text{air}}$  and  $R_{\text{air}}$ ). The optimal values for the given disk parameters can be summarized to  $h_{\text{air}} = 12 \mu\text{m}$ ,  $R_{\text{air}} = 26 \mu\text{m}$ ,  $\delta_{\text{PML}} = 2.5$ ,  $h_{\text{PML}} = 5 \mu\text{m}$ ,  $\alpha = 5$  and a not too coarse mesh ( $\geq 10^5$  elements). A detailed discussion of the influences of each of the parameters can be found in the Appendix B.2.3.

In Fig. 2.5 the resonances calculated with the FEM are compared to the results of the analytical EIM for the first three radial mode orders. The resonances from the analytical EIM calculation are always at slightly larger wavelengths, which is caused by the overestimation of the effective refractive index of the slab mode in comparison to the real mode profile.<sup>14</sup> This discrepancy gets stronger for higher order radial modes as the mode profile deviates significantly from a fundamental slab mode (see Fig. 2.6). By reducing  $n_{\text{res}}$  in the EIM the calculated resonances can be shifted towards the resonances obtained by the FEM. The maximum deviation of about  $\Delta\lambda = 3.8 \text{ nm}$  can be compensated by  $\Delta n_{\text{res}} = 0.0047$  which corresponds to 0.3% for both parameters. The radiation Q-factor obtained from the FEM calculations is five times larger than the value from the EIM for all resonances. Nevertheless, the analytical EIM provides a fast method to get an estimate of the correct order of magnitude for the Q-factor and the resonance wavelengths of the microdisks.

<sup>14</sup>As mentioned in Sect. 2.1.1, the found resonance frequencies from the analytical real eigenvalue problem (not shown here) coincide almost perfectly with the FEM results but no information about the radiation Q-factor can be obtained.

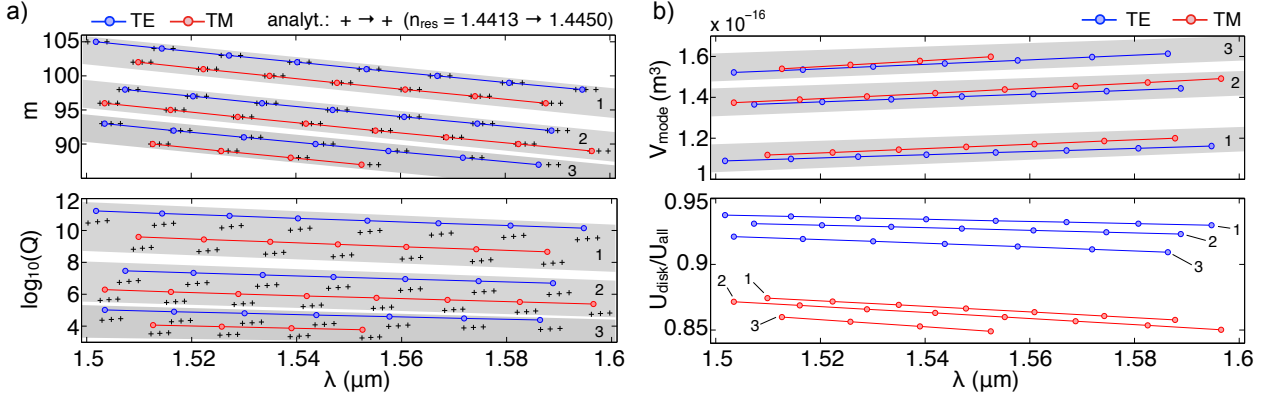


Fig. 2.5: Characteristics of microdisk resonances calculated by FEM with the disk parameters  $R_{\text{res}} = 20 \mu\text{m}$ ,  $h_{\text{res}} = 1 \mu\text{m}$ , and  $n_{\text{res}} = 1.445$ . In (a) the resonance wavelengths and Q-factors are compared to analytical EIM calculations. The deviation in the resonance wavelengths increases with increasing radial order according to the approximations of the EIM. By reducing  $n_{\text{res}}$  in the EIM this deviation can be compensated (the plus signs from left to right in each group correspond to  $n_{\text{res}} = 1.4413, 1.4431, 1.445$ ). From the FEM one can calculate (b) the mode volume  $V_{\text{mode}}$  and the confinement of the electromagnetic energy  $U_{\text{disk}}/U_{\text{all}}$  for the microdisk resonances.

From the calculated field distributions further information on the microdisk modes can be obtained, which are the mode volume (according to [Sri06])

$$V_{\text{mode}} = \frac{\int_V \hat{\epsilon}(\mathbf{r}) |\mathbf{E}(\mathbf{r})|^2 dV}{\max(\hat{\epsilon}(\mathbf{r}) |\mathbf{E}(\mathbf{r})|^2)}, \quad (2.37)$$

with the integration over the modes bright spot (corresponding to the refined mesh region in Fig. 2.4) and the electromagnetic energy

$$U = \frac{1}{2} \int_V (\epsilon_0 |\mathbf{E}(\mathbf{r})|^2 + \frac{1}{\mu_0} |\mathbf{B}(\mathbf{r})|^2) dV, \quad (2.38)$$

stored in the resonator. In Fig. 2.5(b)  $V_{\text{mode}}$  and the energy confinement ratio  $U_{\text{res}}/U_{\text{all}}$  ( $U_{\text{res}}$  is the energy in the disk,  $U_{\text{all}}$  is the energy in the disk and the air layer) is plotted. The mode volume is smallest for the fundamental radial mode orders and increase with the resonance wavelength (for fixed disk parameters). The TE modes show a slightly smaller mode volume than the TM modes for the same radial order. Normalization to the cubic wavelength inside the material results in  $V_{\text{mode}} = 85$  to  $100 (\lambda/n)^3$  for the first radial order. A significant difference between TE and TM modes can be seen in the stored energy inside the disk indicating a stronger confinement of the TE modes.

A comparison of the field and intensity distribution for the first two radial orders of TE and TM modes is shown in Fig. 2.6. For the TE modes the intensity shows a discontinuity across the disk sidewall corresponding to the main field component in radial direction. For the TM modes the discontinuity is across the top and bottom surfaces according to the main field component in axial ( $z$ ) direction. In contrast to the assumptions in the analytical EIM the



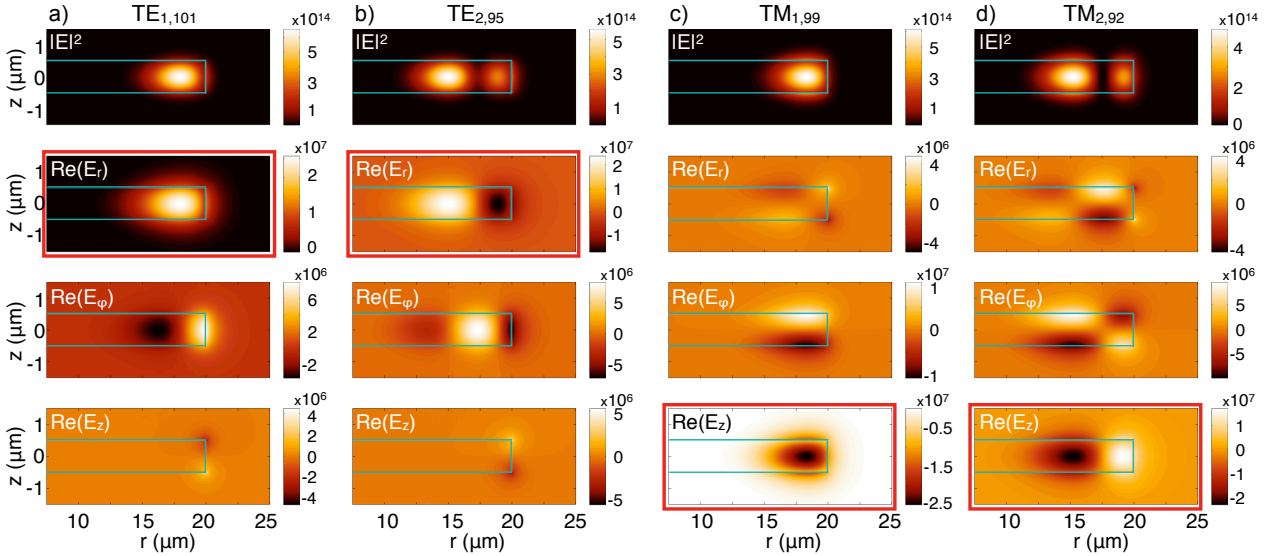


Fig. 2.6: Intensity and field distributions of the microdisk modes (a)  $TE_{1,101}$ , (b)  $TE_{2,95}$ , (c)  $TM_{1,99}$  and (d)  $TM_{2,92}$  obtained from FEM calculation. The disk parameters are  $R_{\text{res}} = 20 \mu\text{m}$ ,  $h_{\text{res}} = 1 \mu\text{m}$ , and  $n_{\text{res}} = 1.445$ . The main field component of each of the modes is highlighted by the red frame. The other field components are approximately one order of magnitude smaller but, in contrast to the assumptions of the analytical EIM in Sec. 2.1.1, not zero. Whereas, the TE modes have a strong radial field component making them sensitive to imperfections of the sidewall of the disk, the TM modes have a strong axial component giving rise to enhanced sensitivity to roughness along the top and bottom surface of the disk.

field components  $E_\phi$  and  $E_z$  for TE and  $E_r$  and  $E_\phi$  for TM are nonzero but approximately one order of magnitude smaller than the main component. For arbitrarily shaped cross sections the strength of these field components might be even larger, therefore the general classification of different mode polarizations is determined by the main field component according to  $E_r > E_z$  for TE and  $E_z > E_r$  for TM. One can also see that for TM modes all but the strongest field component shows odd symmetry along the  $z$ -direction, whereas for the TE mode only the  $E_z$  component has odd symmetry. The comparison of first and second order radial modes shows a decrease of the maximum intensity for the higher order due to the weaker confinement of the mode. As pointed out in Ref. [Bor06d] the strong field at the sidewall of the disk for the TE modes makes them more sensitive to sidewall roughness than the TM modes, whereas the TM modes with a strong field at the top and bottom interface are sensitive to imperfections along these interfaces.

## 2.2 Resonant modes of coupled microdisks

The rigorous theoretical description of the electromagnetic fields and spectral response of coupled microdisks has been studied by a variety of methods based on the numerical solution of integral equations [Bor06a, Bor04, Nos07] that allow for an arbitrary shape of the microdisks' boundary. All the approaches make use of the reduction of the problem to a 2D one with the help of the effective refractive index method as described in Sect. 2.1.1 for single disks. Caused

by the almost ideal circular shape and relatively large radius of the microdisks used in this thesis a simpler approach based on modal expansion can be used. As mentioned in Ref. [CS5], this approach is similar to multisphere Mie scattering analysis [Mis02] and its application to the case of high-Q WGMs in coupled spherical microresonators [Miy00, Dey06, CS6, CS7]. In the limit of high-Q WGMs a single mode approximation further simplifies the problem giving reliable results for the spectral positions of the resonances, whereas for the fields to appear correctly the contribution of non-resonant modes needs to be taken into account.

A general formulation of the model and the discussion of both the spectrum and the aspects of field calculation will be given in the following.

### 2.2.1 Semi-analytical model for arbitrarily coupled circular disks

The scattering problem of an ensemble of microdisks with adjacent disks close enough to exchange optical energy due to the overlap of their evanescent fields can be solved in extension to the single disk case described in Sect. 2.1.1. Introducing an incident, scattered and internal field in analogy to Eqs. (2.17) - (2.19) one can write for the  $p$ th disk of the ensemble

$$F_{\text{inc}}^{(p)}(\mathbf{r}, \mathbf{r}_p, \omega) = \sum_m a_m^{(p)}(\omega) e^{im\phi_p} J_m(n_0 k_0 |\mathbf{r} - \mathbf{r}_p|) + \sum_{q \neq p} \sum_m b_m^{(q)}(\omega) e^{im\phi_q} H_m^{(1)}(n_0 k_0 |\mathbf{r} - \mathbf{r}_q|), \quad (2.39)$$

$$F_{\text{sc}}^{(p)}(\mathbf{r}, \mathbf{r}_p, \omega) = \sum_m b_m^{(p)}(\omega) e^{im\phi_p} H_m^{(1)}(n_0 k_0 |\mathbf{r} - \mathbf{r}_p|), \quad (2.40)$$

$$F_{\text{int}}^{(p)}(\mathbf{r}, \mathbf{r}_p, \omega) = \sum_m d_m^{(p)}(\omega) e^{im\phi_p} J_m(n_h k_0 |\mathbf{r} - \mathbf{r}_p|). \quad (2.41)$$

Again,  $F$  denotes the  $z$ -component of either the electric (TM) or the magnetic (TE) field and  $a_m^{(p)}(\omega)$ ,  $b_m^{(p)}(\omega)$  and  $d_m^{(p)}(\omega)$  are the corresponding field expansion coefficients or modal amplitudes. The coordinates  $\mathbf{r}$  and  $\mathbf{r}_p$  are the point of observation and the center of the  $p$ th disk in the global coordinate system, respectively. The angular coordinate  $\phi_p$  is measured in the individual coordinate system of the  $p$ th disk centered at  $\mathbf{r}_p$  and has the same orientation for all disks in the structure (see Fig. 2.7). The main difference to the single disk problem is the additional term in the expansion of the incident field, which accounts for the scattered fields of all but the  $p$ th disk as contributions to the incident field on the  $p$ th disk. In order to apply the boundary conditions [Eqs. (2.20), (2.21)] at the rim of the  $p$ th disk, it is necessary to rewrite the scattered field in its local coordinate system  $(x_p, y_p)$ . To achieve this, the translational properties of Hankel functions can be used [Bor06a, Abr72]

$$e^{im\phi_q} H_m^{(1)}(n_0 k_0 |\mathbf{r} - \mathbf{r}_p|) = \sum_{n=-\infty}^{+\infty} H_{n-m}^{(1)}(n_0 k_0 R_{q,p}) e^{i(m-n)\theta_{q,p}} J_n(n_0 k_0 |\mathbf{r} - \mathbf{r}_p|) e^{in\phi_q}, \quad (2.42)$$

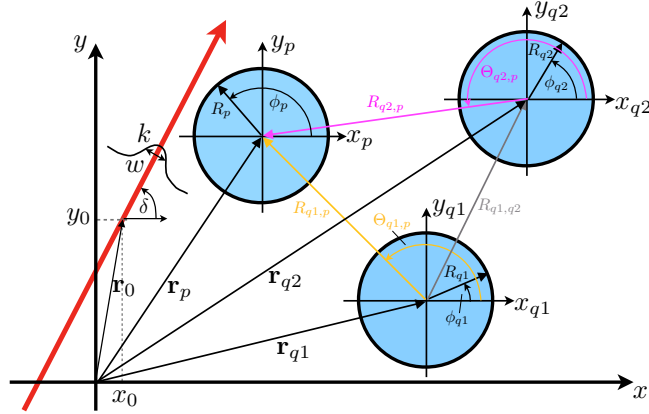


Fig. 2.7: Sketch of an arbitrary coupled disk configuration showing the relevant model parameters. The parameters  $R_{q,p}$  and  $\theta_{q,p}$  used in Eq. (2.42) are shown for two different disks in magenta and orange. The red arrow marks the gaussian distribution of the exciting field as an approximation of the tapered fiber with the center  $\mathbf{r}_0$  and the width  $w$ , which is used for the field calculations in the full model.

where  $R_{q,p}$  and  $\theta_{q,p}$  are the radial and azimuthal coordinates of the  $p$ th disk in the local coordinate system of the  $q$ th disk. Substituting Eq. (2.42) in Eq. (2.39) the incident field on the  $p$ th disk can be expressed as

$$F_{\text{inc}}^{(p)}(\mathbf{r}, \mathbf{r}_p, \omega) = \sum_m \left\{ \left[ a_m^{(p)}(\omega) + \sum_{q \neq p} \sum_n b_n^{(q)}(\omega) H_{m-n}^{(1)}(n_0 k_0 R_{q,p}) e^{i(n-m)\theta_{q,p}} \right] \times e^{im\phi_p} J_m(n_0 k_0 |\mathbf{r} - \mathbf{r}_p|) \right\}. \quad (2.43)$$

Matching the fields of Eqs. (2.40), (2.41), and (2.43) according to Eqs. (2.20) and (2.21), the relation between the expansion coefficients of the scattered and incident fields can be obtained

$$b_m^{(p)}(\omega) = \alpha_m^{(p)}(\omega) \left[ a_m^{(p)}(\omega) + \sum_{q \neq p} \sum_n b_n^{(q)}(\omega) H_{m-n}^{(1)}(n_0 k_0 R_{q,p}) e^{i(n-m)\theta_{q,p}} \right], \quad (2.44)$$

where  $\alpha_m^{(p)}(\omega)$  is the single disk scattering amplitude already introduced in Eq. (2.22). Equation (2.43) describes a system of linear coupled equations with the unknown mode amplitudes of the scattered fields  $b_m^{(p)}$  of  $p = 1, \dots, N$  coupled disks, which has to be solved for certain structural parameters ( $R_p$ ,  $n_{h,p}$ ,  $n_0$ ,  $R_{q,p}$ , and  $\theta_{q,p}$ ) and excitation amplitudes  $a_m^{(p)}$ .

From the characteristics of the Hankel function one can estimate the contribution of different modes of adjacent disks to the scattering amplitude. The asymptotic form [Abr72] of  $H_m^{(1)}(x) \sim \sqrt{2/\pi x} e^{i(x - m\pi/2 - \pi/4)}$  for fixed order  $m$  and large arguments  $|x| \rightarrow \infty$  reveals a decreasing absolute value  $|H_m^{(1)}(n_0 k_0 R_{q,p})| \sim \sqrt{1/R_{q,p}}$  with increasing distance of the coupled disks for a fixed wavelength. To the first approximation this allows to take into account nearest neighbor coupling only. The asymptotic form for a fixed argument but large order  $m \rightarrow \infty$  reads as [Abr72]  $H_m^{(1)}(x) \sim -i\sqrt{2/\pi m} (ex/(2m))^{-m}$ , which results in a heavily growing absolute value

$|H_m^{(1)}(n_0 k_0 R_{q,p})| \sim (m/e)^m$  for increasing mode orders. This gives the second approximation of resonant mode coupling, since the order of the Hankel function in Eq. (2.44) is maximized for the coupling of mode  $m$  in one disk to the counterpropagating mode of the same order  $n = -m$  in the other disk. The coupling to nearby mode orders that also give large orders of the coupling Hankel function can be usually neglected because they do not spectrally overlap with the resonance at the investigated wavelength [see Fig. 2.2(b)].

Further approximations can be made with the restriction to one-dimensional linear chains of identical, equidistant coupled microdisks, which fixes  $R_{q,p} = 2R + d_{\text{gap}} = D$  and  $\theta_{q,p} = \pi$  or  $\theta_{q,p} = 0$  depending on whether the coupling is to the right or left neighbor in the chain. An analytical solution can be found by applying a discrete sine Fourier transform, as shown in Ref. [CS5], resulting in a dispersion relation of<sup>15</sup>

$$G_m^l(\omega) = [\alpha_m(\omega)]^{-1} \pm 2H_{2m}^{(1)}(n_0 k_0 D) \cos\left(\frac{\pi l}{N+1}\right) = 0. \quad (2.45)$$

Here, the index  $l = 1, \dots, N$  indicates the splitting of the single disk resonance into different super-modes of the structure according to the number of disks  $N$  in the chain. From Eq. (2.45) one can see that the coupling does not remove the double degeneracy of cw and ccw modes existing in a single microdisk.

### 2.2.2 General spectral analysis using resonant mode approximation

For a more general analysis of the spectral behavior of arbitrary coupled disks Eq. (2.44) was used in the limit of single disk excitation, which means that  $a_m^{(p)} = 1$  for the excited disk and  $a_m^{(q \neq p)} = 0$  for all others. Furthermore, the resonant mode approximation fixes  $m$  to the mode number of the resonance under consideration. The coupling of all disks in the ensemble to each other was taken into account. In Fig. 2.8 the calculated spectra for an increasing number of disks and different arrangements is shown. The disks are assumed to be identical with the parameters as in Fig. 2.2 ( $R_p = R = 20 \mu\text{m}$ ,  $n_{\text{res},p} = n_{\text{res}} = 1.445$ ,  $h_p = h = 1 \mu\text{m}$ ) and a gap size  $d_{\text{gap}} = 300 \text{ nm}$ . The calculations are done for the  $\text{TE}_{1,101}$  mode with the single disk resonance at  $\lambda = 1.5559 \mu\text{m}$ . The shown spectral lines correspond to the total scattering intensities of each disk  $I_m^{(p)} = (|b_m^{(p)}|^2 + |b_{-m}^{(p)}|^2)/|a_m|^2$  with  $a_m = a_m^{(p)} = 1$ , which for all graphs in Fig 2.2 are plotted in the same units to allow for comparison among each other. Next to each of the resonance peaks the corresponding intensity distribution along the coupled disk structure is plotted on a gray scale (white to black means low to high intensity).

For the line arrangement always the leftmost disk was excited ( $p = 1$ ) and for an increasing number of disks in the line an increasing number of peaks appears according to the number of disks. Only for an odd number of disks (excited at an odd numbered disk) a resonance

<sup>15</sup>The resulting dispersion relation is similar to the one obtained from a Bloch-mode approach for linear chains of microresonators [Ste98, Yar99, M0l07].

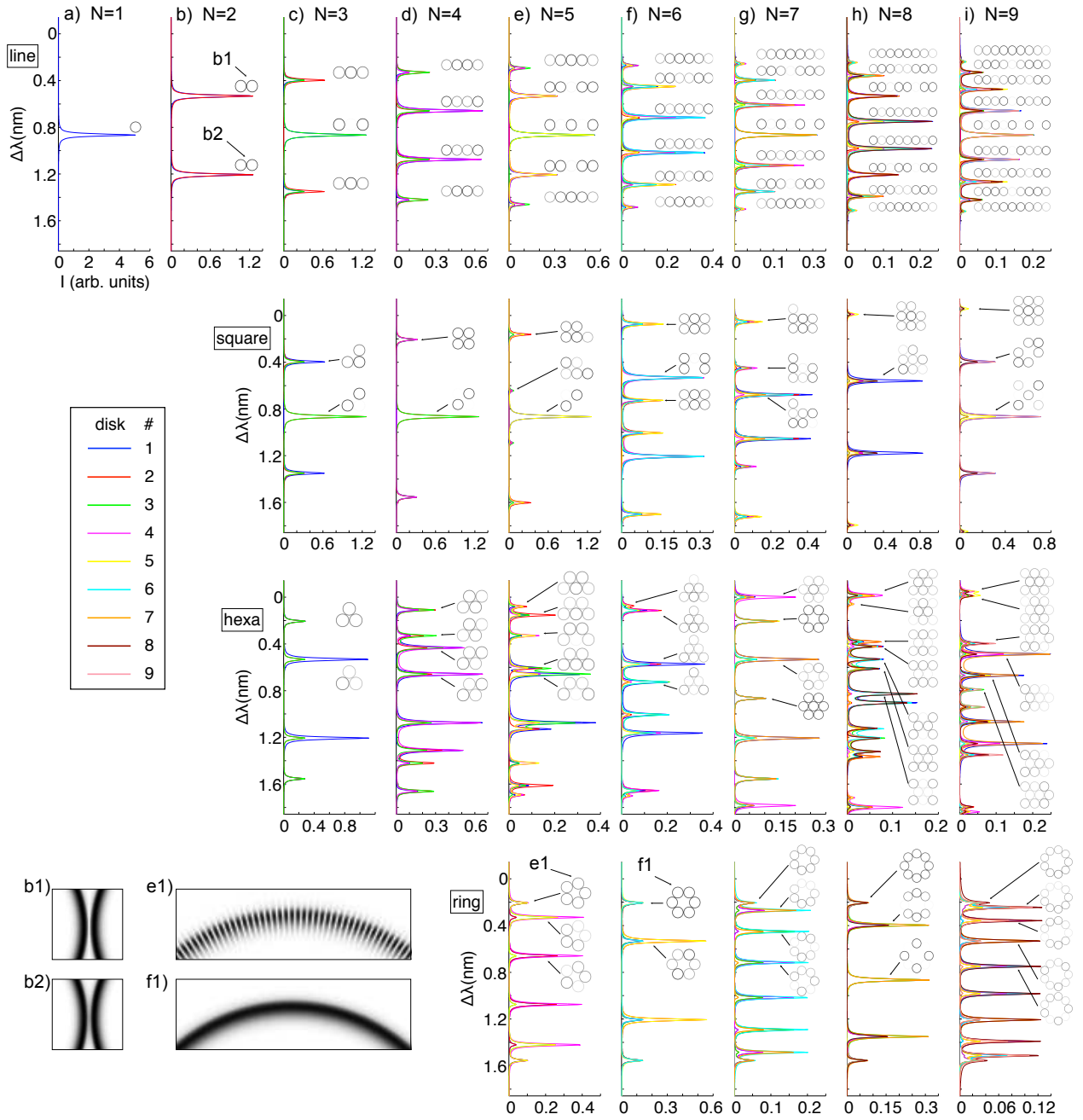


Fig. 2.8: Calculated spectral splitting and intensity distributions of the  $TE_{1,101}$  mode for the coupling of an increasing number of disks [(a)  $N = 1$  to (i)  $N = 9$ ] in different configurations (1. row: line arrangement, 2. row: square lattice, 3. row: hexagonal lattice, 4. row: ring arrangement) with a gap size of 300 nm. The spectral lines correspond to the total intensity in a certain disk according to the legend. The intensity scale (horizontal axis) is in arbitrary units but the same for all plots, so the graphs can be compared relative to each other. The wavelength (vertical axis) is plotted relative to an arbitrary chosen value, the peak for the single disk [1. row in (a)] corresponds to the resonance wavelength of the  $TE_{1,101}$  mode at  $\lambda = 1.5559 \mu\text{m}$ . Close to each of the resonance peaks the corresponding intensity distribution along the coupled disk structure is plotted on a gray scale (white to black means low to high intensity). In general, the intensity distributions for the corresponding resonance peaks below and above the single disk resonance are equal [see line arrangement (b)-(i)], except that the lower wavelengths are the antisymmetric and the larger wavelengths are the symmetric super-modes. The difference can be recognized from presence or absence of the intensity in the gaps between the disks [see magnification (b1) and (b2)]. Therefore, the intensity distributions for the square, hexagonal and ring arrangement are only plotted for half of the peaks. Depending on the symmetry of the structure standing (e1) or traveling (f1) wave mode patterns appear. In all calculations the  $TE_{1,+101}$  mode in the lowest leftmost disk was excited (except for the ring arrangement of  $N=5$  disks, where the leftmost lowest disk was excited).

peak at the single disk resonance can be observed.<sup>16</sup> The intensity distribution of corresponding resonance peaks below and above the single disk resonance are quite similar and differ only in the intensity in the gaps between the disks. The shorter wavelengths are the anti-symmetric combinations of the single disk modes showing destructive interference in the gap [Fig. 2.2(b1)], whereas the longer wavelengths are the symmetric combinations resulting in constructive interference in the gap [Fig. 2.2(b1)].<sup>17</sup> The total splitting of the resonance peaks (distance between peaks with lowest and longest wavelength) also increases with increasing number of disks but converges to the finite value for an infinitely long chain. The explicit value  $\Delta\lambda_b = \lambda_{\max} - \lambda_{\min}$  can be found from Eq. (2.45) with  $N \rightarrow \infty$  from the two solutions of  $[\alpha_m(\lambda_{\max,\min})]^{-1} = \pm 2H_{2m}^{(1)}(n_0k_0D)$ . For the used resonance and disk parameters this gives  $\Delta\lambda_b = 1.3$  nm which corresponds to a frequency bandwidth of  $\Delta\nu_b = 161.1$  GHz. One can see that this value is already reached for the line arrangement of 9 disks [Fig. 2.8(i)] and a further increase of the number of disks would only increase the number of resonance peaks within this bandwidth and reduces their mutual distance. If the distance becomes smaller than the single peak resonance bandwidth the band appears as a continuous one, which rigorously speaking is true only for  $N \rightarrow \infty$ .

An extension of the coupling to two dimensions increases the complexity of the spectra depending on the symmetry of the structure as well as on the excited disk of this structure. For the three disk case [Fig. 2.8(c)] in the square arrangement there is no difference to the spectra of the line structure indicating a negligible diagonal coupling of the disks due to the large distance.<sup>18</sup> In comparison to the 4 coupled disks [Fig. 2.8(d)], the additional one in the 5 disk arrangement [Fig. 2.8(e)] shows only a weak influence for the given excitation condition. Both structures have three main resonance peaks showing almost the same intensity distribution. For the 5 disks another very small peak appears with a significant intensity located in the additional disk. This small peak would, of course be much stronger, if the additional disk would be excited. Another example of the influence of the combination of excitation and symmetry of the structure on the observable resonances are the 7 and 8 disks cases [Fig. 2.8(g,h)]. The nonsymmetric excitation of the nonsymmetric structure (N=7) shows more resonance peaks than the symmetric excitation of the more symmetric structure (N=8). As in the case of the line arrangement the increasing number of disk leads to a stronger splitting. The total bandwidth is expected to be twice the bandwidth of the line structure

<sup>16</sup>This effect limits somehow the combinations of spectra for different excitation scenarios that can be shown within the limited extent of this thesis. Especially, for larger structures the possible number of combinations, and hence different spectra, increases significantly.

<sup>17</sup>In Fig. 2.2 the gaps are not resolved well. See Chap. 4 for more details on the difference of symmetric and antisymmetric super-modes.

<sup>18</sup>The continuous change of the position of the third disk along the rim of the second disk from the line to the square arrangement shows a periodic phase change of the scattering field coefficient of the third disk. Nevertheless, no alteration of the resonance wavelength can be observed. For the coupling of very small disks a more rigorous model indeed shows an influence of the resonance wavelength and also the Q-factor on the angle of a kink in a line arrangement [Pis07].

due to the two orthogonal coupling directions.<sup>19</sup>

For the coupling of disks on a hexagonal lattice the number of adjacent coupled disks increases, which drastically increases the number of resonances appearing in the spectra. This can be seen, e.g., for the cases of 4 disks [Fig. 2.8(d)] and 9 disks [Fig. 2.8(i)] when comparing to the square arrangement. But also here the symmetry of the structure and of the excitation has strong influence on the degeneracy of resonances and hence the number of peaks in the spectra [see symmetric configurations in Fig. 2.8(f) and (g)]. In general, the number of modes appearing in the spectra of the coupled disks in a square or hexagonal arrangement can be predicted and classified according to the symmetry of the structure and the excitation with the methods of group theory applied to photonic crystals [Sak01].

Another interesting configuration for coupled disks is the ring arrangement shown in the last row of Fig. 2.8. It corresponds to an infinitely long chain of coupled disks with even or odd periodicity depending on the number of disks. For  $N = 3$  the ring arrangement is identical with the hexagonal arrangement and for  $N = 4$  this is the case for the square arrangement. Due to the periodic boundary conditions all the peaks except the ones at the band edge show the same intensity (expansion coefficient for the excited disk) and the bandwidth already reaches the  $N \rightarrow \infty$  limit. The number of visible resonance peaks follows the rules  $N/2 + 1$  for even  $N$  and  $N + 1$  for odd  $N$ , in agreement with the results in Ref. [Chr07] studying ring arrangements of disks in detail. The total number of modes which the structures support, will, in general, be larger due to degeneracy as discussed in Refs. [Chr07, Yan07, Bor06b]. Related to this, ring arrangements show different characteristics of the mode distributions depending on whether the number of disks is even or odd. For even  $N$  the modes are traveling waves resulting in a constant intensity along the azimuthal direction in a single disk [see Fig. 2.2(f1)]. Starting with a cw traveling wave in the excited disk it will be coupled to the ccw mode in the adjacent disk and due to the even number of disks after one round trip along the whole ring it will be coupled again in the cw direction of the excited disk. In contrast, for odd  $N$  the initial cw mode will be coupled to the ccw mode of the same disk after one round trip along the ring resulting in a standing wave pattern due to interference of counter propagating modes [see Fig. 2.2(e1)]. With the same argumentation a constant intensity can be found in the disks of the line and square arrangements, whereas standing wave patterns can be found for the hexagonal arrangement [except for certain modes of highly symmetric structures, e.g.,  $N = 7$  in Fig. 2.8(g)]. The standing wave and traveling wave mode patterns can be distinguished in Fig. 2.8 by the contrast of the intensity rings to the white background. The high intensity values of the traveling waves appear much darker than high intensity values of the standing waves.

Figure 2.8 gives an overview of a variety of possible configurations and their expected spectral characteristics as well as mode distributions. They are calculated for identical disks

---

<sup>19</sup>This was tested by calculating the spectra for a large number of disks in different structures of up to  $9 \times 9$  arrays.

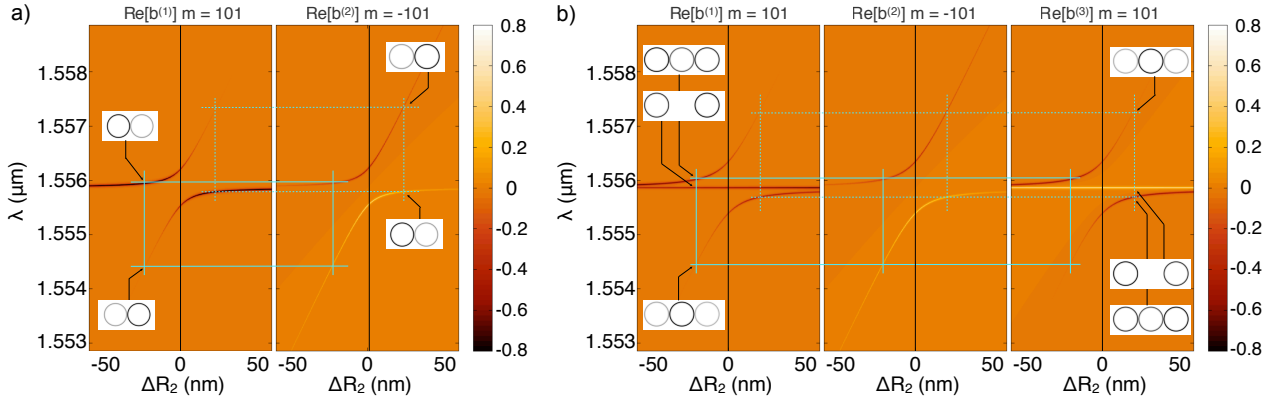


Fig. 2.9: Dependence of the resonance splitting on the variation of the radius of the second disk ( $\Delta R_2$ ) for (a) two coupled disks and (b) three coupled disks (here  $R_2$  is the radius of the middle disk). The other disk parameters are the same as in Fig. 2.8. For each disk the normalized real part of the dominant expansion coefficient  $b_m^{(p)}$  is plotted from which the mode symmetry at a certain wavelength can be identified by comparing their sign, respectively. For a radius mismatch  $\Delta R_2 = -20$  nm (solid cyan line) and  $\Delta R_2 = 20$  nm (dashed cyan line) the intensity distributions of the appearing resonances are plotted. It shows that the characteristics of the intensity distribution are exchanged between symmetric and antisymmetric modes upon an increasing  $\Delta R_2$ .

which might not be the case in the experiment. The model based on Eq. (2.44) can be used to predict effects of a distorted geometry on the spectrum and mode characteristics since it depends directly on the geometrical parameters.

According to the results of the parameter tuning in a single disk (Sect. 2.1.1), the variations of  $h$ ,  $n_{\text{res}}$  and  $R_{\text{res}}$  show the same effect on the resonance wavelengths, whereas the disk radius is expected to show the strongest variation along a coupled disk structure due to the fabrication process (see Sect. 3.1). Therefore, the influence of a varying radius of one of the disks in a two and three disks structure on the coupling between them was investigated and shown in Fig. 2.9. Plotting the real part of the dominant expansion coefficient  $b_m^{(p)}$  in each disk, one can infer the symmetry of the super-modes of the structure. For the two disk case [Fig. 2.9(a)] the  $\Re(b^{(1)})$  and  $\Re(b^{(2)})$  of the low wavelength resonance have opposite sign, indicating a phase difference of  $\pi$  and hence a anti-symmetric mode, whereas for the long wavelength resonance  $\Re(b^{(1)})$  and  $\Re(b^{(2)})$  have equal sign (no phase difference) indicating a symmetric mode. One can also see that for nonzero radius mismatch the splitting of the resonances is nonsymmetric around the single disk resonance wavelength. For a mismatch of  $\Delta R_2 = -20$  nm and  $\Delta R_2 = 20$  nm the intensity distribution for the corresponding resonances is shown. Comparing them, one can see an exchange of the characteristics of the intensity distribution (high or low intensity in a certain disk) between the symmetric and antisymmetric resonance, whereas the spectral lines show an anti-crossing. This effect is typical for coupled resonant systems.<sup>20</sup>

For the case of three coupled disks [Fig. 2.9(b)] similar effects can be observed. Again, the radius of the second disk was varied, which corresponds to the disk in the center of

<sup>20</sup>Besides the intensity distribution also other characteristics, e.g., resonance bandwidth exchange between the two resonance peaks.



the structure. Comparing the sign of the plotted coefficients  $\Re(b^{(1)})$ ,  $\Re(b^{(2)})$  and  $\Re(b^{(3)})$  the symmetry of the appearing modes can be identified also in this case. For the low wavelength resonance they show altering sign between adjacent disks, corresponding to a phase difference of  $\pi$  for the antisymmetric mode. For the central resonance the phase difference is  $\pi/2$  between adjacent disks, leading to a vanishing field expansion coefficient  $\Re(b^{(2)})$  for the second disk at this wavelength. At the long wavelength resonance all coefficients have the same sign, indicating a symmetric mode. As for the two disks, the splitting between the resonances is not equidistant except for identical disks. In the three disk case the central resonance is expected to be at the same wavelength as the single disk resonance. Additionally, the different spectral distance of symmetric and antisymmetric mode to the central resonance can be used to identify a radius mismatch (or more generally a resonance mismatch) independent of the gap size, which is not possible for the two coupled disks.

As seen from the plotted intensity distributions for  $\Delta R_2 = -20 \text{ nm}$  and  $\Delta R_2 = 20 \text{ nm}$  the distribution characteristics are exchanged between symmetric and antisymmetric mode by changing  $\Delta R_2$ , whereas the distribution of the central resonance remains unchanged.

Besides the resonance mismatch of the individual disks in a coupled structure, the distance between them is the other important parameter influencing the observable coupling. Due to the exchange of optical energy via the evanescent fields of the WGMs it is expected that the coupling will be stronger for a smaller gap distance  $d_{\text{gap}}$  between the disks. In Fig. 2.10 the resonance splitting for two coupled disk (parameters as above) as a function of  $d_{\text{gap}}$  is shown separately for the normalized intensity of the first (excited) disk [Fig. 2.10(a)] and the second disk [Fig. 2.10(b)]. For  $d_{\text{gap}} \geq 2 \mu\text{m}$  the coupling is negligible and almost all optical energy is located inside the first disk as can be seen in the additional plot (cyan line and right y-axis) in Fig. 2.10(a). Decreasing the gap to  $d_{\text{gap}} = 1.3 \mu\text{m}$  increases the energy in disk two slightly, but due to the finite line width of the resonances no splitting can be observed, as seen from the additional line width plot in Fig. 2.10(b).<sup>21</sup> Decreasing  $d_{\text{gap}}$  further leads to a resonance splitting observable in the intensities of both disks and a homogeneous distribution of the energy (in both disks half of the energy is located). The resonance splitting measured from the total intensity of both disks [cyan line in Fig. 2.10(b)] increases exponentially to  $\Delta\lambda = 1.63 \text{ nm}$  for  $d_{\text{gap}} = 0$ . This corresponds to a maximum splitting of the  $\text{TE}_{1,101}$  mode of about  $\Delta\nu = 202 \text{ GHz}$ .

In Fig. 2.10(c) the wavelength dependence of the coupling of two coupled disks is shown for the single disk modes investigated so far in Fig. 2.2 and Fig. 2.5. The gap size was fixed to  $d_{\text{gap}} = 300 \text{ nm}$ . Generally, the splitting increases with increasing wavelength according to the asymptotic behavior of the coupling Hankel term discussed above. Counterintuitively, the slow decrease of the Hankel function for increasing argument relative to the rapid increase for increasing mode order (the mode number  $m$  increases for modes with shorter wavelength) is

<sup>21</sup>For comparison of the calculations to the experimental results, the imaginary part of the refractive index of the disks was adjusted to mimic the observable Q-factor or resonance line width.

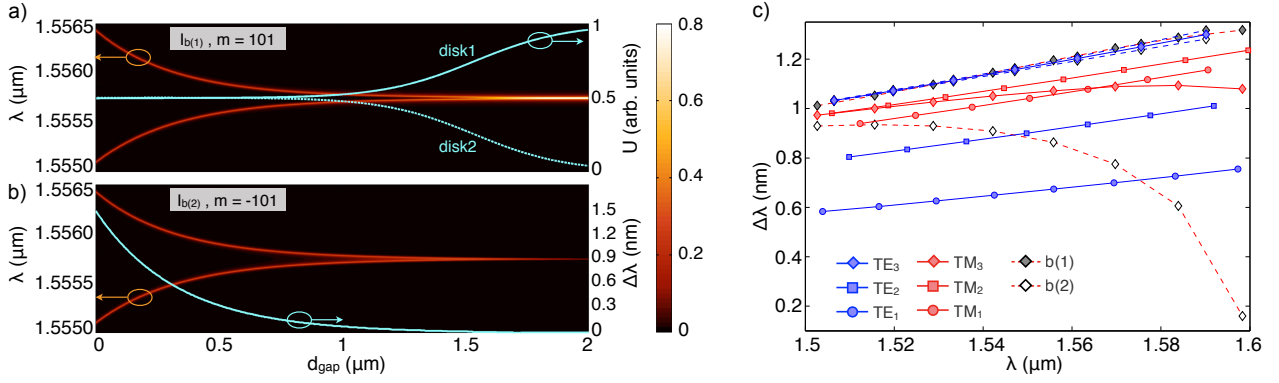


Fig. 2.10: Splitting of the  $TE_{1,101}$  mode for two coupled disks observable in the intensity of the (a) first, excited and (b) second disk. When the gap size decreases the splitting in the intensity spectrum of each disk increases and the normalized amount of energy in each of the disks equalizes [as seen from the additional plot with the right y-axis in (a)]. In (b) the additional plot shows the splitting in the spectrum measured from the combined intensity of both disks. The dependence of the splitting on the wavelength and mode polarization is shown in (c) for the first three radial mode orders. The gap was fixed to  $d_{\text{gap}} = 300$  nm and the other parameters are the same as used above ( $R_{\text{res}} = 20$   $\mu\text{m}$ ,  $h_{\text{res}} = 1$   $\mu\text{m}$ ,  $n_{\text{res}} = 1.445$ ). The splitting was measured from the spectrum of the total intensity of both disks. For the third radial order the splitting obtained from the individual disk spectra is plotted, too, showing the differences when the splitting and the resonance bandwidth are comparable.

dominating. To understand this, the asymptotic behavior of the modal scattering coefficient  $\alpha_m$  [Eq. (2.22)] has to be considered, especially the nominator, since it is multiplied with the Hankel term in Eq. (2.45) to solve for the roots of  $G_m^l$ . Whereas the dependence of  $|J_m(x)|$  for  $|x| \rightarrow \infty$  and fixed  $m$  is the same as for the  $|H_m^{(1)}(x)|$ , their behavior is opposite for fixed argument  $x$  but increasing order  $m \rightarrow \infty$ , which therefore cancel upon multiplication. Physically, one may argue that the decreasing confinement for an increasing resonance wavelength of the modes inside the disk [see Fig. 2.5(b)] increases the overlapping amount of energy and therefore the splitting of the resonances. The same argumentation holds for the different behavior of TE and TM polarized modes. For the first and second radial mode order the TM modes show stronger splitting than the TE modes, since they are weaker confined. For higher radial orders the decreasing Q-factor comes into play, resulting in a saturation or even decrease of the splitting, in particular for the TM modes [see line for the  $TM_3$  mode in Fig. 2.10(c)]. In this case we are in a regime, where the resonance line width reaches the splitting value, which compared to Fig. 2.10(a, b) is the region of  $d_{\text{gap}} \approx 1.2$   $\mu\text{m}$ . Here it is of importance how the splitting is measured, since the intensity in the first disk already shows splitting in two resonances [Fig. 2.10(a)], whereas for the intensity in the second disk the splitting can not be resolved [Fig. 2.10(b)]. This difference can also be seen in Fig. 2.10(c) where the separately measured splitting for the intensities in each disk for the third order radial modes is shown. Deviations to the measured splitting from the total intensity of both disks are significant only for the third order modes and very strong for the TM polarization.

Another difference between the TE and TM modes is the amount of increase of the splitting when increasing the radial mode order. For the TM modes the change of the splitting is very

small or even zero whereas for the TE modes the splitting increases significantly for higher radial mode order. This can be explained by the different orientations of the main field component. The strongest field component for the TE modes is in radial direction (Fig. 2.6), resulting in a strong dependence of the splitting on the radial mode order due to the decreasing confinement in the direction of the gap. The decreasing confinement of the main  $z$ -component of the TM modes for increasing radial order does not feel the gap that strongly.

The splitting in the investigated wavelength range for the first radial order is in the range of  $\Delta\lambda \approx 0.6$  nm to 0.75 nm ( $\Delta\nu \approx 80$  GHz to 90 GHz) for TE modes and  $\Delta\lambda \approx 0.9$  nm to 1.15 nm ( $\Delta\nu \approx 125$  GHz to 135 GHz) for TM modes (for a fixed gap of  $d_{\text{gap}} = 300$  nm).

### 2.2.3 Accurate field calculations using multiple mode orders<sup>22</sup>

The above used resonant mode approximation, taking into account only one WGM with a single mode number  $m$  at a certain resonance wavelength and neglecting the coupling to other (higher or lower order) modes is well-suited for the description of the spectral response of coupled microdisks [CS5]. However, in this approximation the calculated fields show discontinuities at the disk boundaries also for physically continuous fields (e.g.,  $B_z$  for TE modes). This leads to an incorrect representation of the fields in the gap region. For the exact field calculation it is necessary to take into account all mode numbers  $m = -m_{\text{max}}, \dots, m_{\text{max}}$ , with  $m_{\text{max}}$ , chosen such that convergence of the fields is guaranteed, which usually depends on the symmetry of the incident field. The incident field has to be reconsidered when dealing with the coupling of all mode numbers  $m$ , because the singular excitation of one WGM ( $a^{(p)} = 1$  and  $a^{(q \neq p)} = 0$ ) as used in the resonant mode approximation will fail. In order to match the experimental conditions of a tapered fiber waveguide excitation (see Sect. 3.2) in a simplest approximation, a one-dimensional Gaussian distribution with a plane phase perpendicular to the propagation direction was used. With the center of the Gaussian distribution  $\mathbf{r}_0 = (x_0, y_0)$  and the width  $w$  (corresponding to the width of the mode of the tapered fiber with the effective mode index  $n_{\text{eff}}$ ), the global exciting field can be written as

$$F_{\text{inc}}^{\text{glob}} = A e^{i n_{\text{eff}} k [(x-x_0)\cos\delta - (y-y_0)\sin\delta]} e^{-[(x-x_0)\sin\delta + (y-y_0)\cos\delta]^2 / w^2}. \quad (2.46)$$

Here  $A$  is the amplitude (without loss of generality  $A = 1$  is set) and  $\delta$  is the angle between the tapered fiber axis and the  $x$  axis of the global coordinate system (for geometrical relations see Fig. 2.7). The nonzero expansion coefficients of the incident field  $a_m^{(p)}$  used in Eq. (2.44) can be obtained from the expansion of the global incident field in terms of the local incident field at the boundary  $\Omega^{(p)}$  of the  $p$ th disk

$$F_{\text{inc}}^{\text{glob}}|_{\Omega^{(p)}} = \sum_m a_m^{(p)} e^{im\phi} J_m(n_0 k_0 R_p) = F_{\text{inc}}^{(p)}|_{\Omega^{(p)}}. \quad (2.47)$$

<sup>22</sup>The main results of this section can be found in Ref. [CS2].

By multiplication of Eq. (2.47) with the complex conjugate  $e^{-im\phi_p} J_m^*(n_0 k_0 R_p)$  and integration along the  $\phi$ -coordinate, the  $a_m^{(p)}$  can be calculated to

$$a_m^{(p)} = \frac{1}{2\pi |J_m(n_0 k R_p)|^2} \int_0^{2\pi} F_{\text{inc}}^{\text{glob}} J_m^*(n_0 k R_p) e^{-im\phi} d\phi. \quad (2.48)$$

For the particular case of the Gaussian distribution [Eq. (2.46)] Eq. (2.48) gives

$$a_m^{(p)} = \frac{J_m^*(n_0 k R_p)}{2\pi |J_m(n_0 k R_p)|^2} \int_0^{2\pi} \left[ e^{-im\phi} e^{in_{\text{eff}}k[(x_{\text{gl}}^{(p)} - x_0)\cos\delta - (y_{\text{gl}}^{(p)} - y_0)\sin\delta]} \right. \\ \left. \times e^{-[(x_{\text{gl}}^{(p)} - x_0)\sin\delta + (y_{\text{gl}}^{(p)} - y_0)\cos\delta]^2/w^2} \right] d\phi, \quad (2.49)$$

with the points of the boundary of the  $p$ th disk in the global coordinate system (depending on the integration variable  $\phi$ )

$$(x_{\text{gl}}^{(p)}, y_{\text{gl}}^{(p)}) = (x_p + R_p \cos \phi, y_p + R_p \sin \phi). \quad (2.50)$$

The integral is solved numerically and the accuracy was checked by the convergence of the local incident field calculated from the obtained  $a_m^{(p)}$  coefficients to the global incident field. Depending on the orientation of the Gaussian distribution it is preferable to take into account the directly excited disk(s) only, since the distance to the other disks is usually so large that the approximation  $a_m^{(p)} \approx 0$  holds. The total field distribution of the coupled disk structure can then be calculated with the obtained expansion coefficients by solving Eq. (2.44) and their substitution into the field expansions [Eqs. (2.39) - (2.41)].

To test the approach the spectrum and intensity distribution of the  $\text{TE}_{1,35}$  mode for a triangular arrangement of three coupled disks [compare to hexagonal arrangement in Fig. 2.8(c)] with  $R = 7.5 \mu\text{m}$ ,  $n_{\text{res}} = 1.445$ ,  $h = 1 \mu\text{m}$  and  $d_{\text{gap}} = 400 \text{ nm}$  was calculated.<sup>23</sup> For comparison, a full 3D finite difference time domain (FDTD) calculation of the same structure was performed, but including a tapered fiber as exciting waveguide.<sup>24</sup> In the FDTD the spectral response was obtained by a short pulse excitation of the structure spectrally covering the wavelength range of interest. The temporal evolution of the electromagnetic field at a point close to the boundary inside a disk was recorded until almost all energy was lost due to the finite radiation Q-factor. A Fourier transformation then gives the spectral response of the structure. For the field calculations a continuous wave excitation through the tapered fiber was performed at a resonant wavelength found from the spectra. Due to the dimensions of the calculation domain for this particular structure of  $35 \mu\text{m} \times 35 \mu\text{m} \times 2 \mu\text{m}$  and a high resolution of about 30 nm to resolve the narrow gaps, the FDTD simulations are very time consum-

<sup>23</sup>The small radius was chosen to allow for the investigation of the resulting structure by rigorous numerical methods.

<sup>24</sup>The FDTD calculations were done by Dr. Christoph Etrich from the *Institute of Condensed Matter Theory and Solid State Optics* at the Friedrich-Schiller-Universität Jena.

ing, which allows to compare only a few cases. As in the FEM calculations (Sect. 2.1.2) the calculation domain was enclosed by PMLs to avoid back reflections of outgoing waves.

In Fig. 2.11(a) the spectra calculated with the analytical model in the resonant approximation, the full model and from the FDTD are compared. In the resonant approximation four peaks are observed, which are symmetric to the single disk resonance (as discussed above). Since the  $b_{35}$  coefficient of the first disk is excited, it differs from the ones in the second and third disk. In this configuration the excitation is symmetric with respect to the positions of disk 2 and disk 3, so their coefficients coincide. Using the full model<sup>25</sup> and the excitation through the Gaussian distribution the symmetry is broken, hence the spectra of the  $b_{35}$  coefficients for all disks can be distinguished. In comparison the resonances are slightly redshifted and no longer symmetric with respect to the single disk resonance. Nevertheless, also four resonance peaks can be identified. The spectrum obtained from the FDTD is shifted slightly to lower wavelengths and shows less splitting. Since field monitors were placed in disk 1 and disk 2 only, two spectral lines are plotted. Also here four peaks can be identified. For the first resonance (marked by the two black arrows) the intensity distribution was plotted in Fig. 2.11(b) for the modal expansion and in Fig. 2.11(c) for the FDTD (snapshot of a continuous wave excitation), which shows good agreement. To point out the importance of using the full modal expansion model for the correct calculation of the fields, the normalized magnetic field across the boundaries between the first and second disk [marked by the dashed line in Fig. 2.11(b)] was plotted in Fig. 2.11(d) for the resonant approximation and the full model. The resonant approximation results in unphysical discontinuities across the boundaries of the disks, whereas the field calculated with the full model shows a smooth transition. Here, one has to note that the calculated fields from the modal expansion sometimes show spurious distributions of very high order radial modes. This happens because the model does not take into account additional losses present in the real system, which mainly affect these higher order modes (e.g., stronger influence of surface inhomogeneities due to less confinement). Usually, this is not a problem, since the effect occurs only if the higher order mode spectrally overlaps with the mode under investigation.

One also should point out that the described model of modal expansion is a good compromise between reasonable field distributions of also large coupled disk ensembles and relatively fast and flexible calculations, compared to rigorous FDTD or also FEM calculations. Although, the incident field distribution is well described by the artificial approximation of the excitation with a Gaussian distribution, it does not take into account any influences of the real exciting tapered fiber. Therefore, it is not possible to extract any transmission and reflection signals comparable to the experimental situation (see Chap. 3). A consideration of the tapered fiber as a waveguide (with boundaries) in the calculation domain would solve this issue, but would lead to additional expansion of the waveguide field and boundary conditions

---

<sup>25</sup> $m_{\max} = 45$  was used; the relative error of the incident field expansion at the boundary of disk 1 is  $10^{-7}$ .

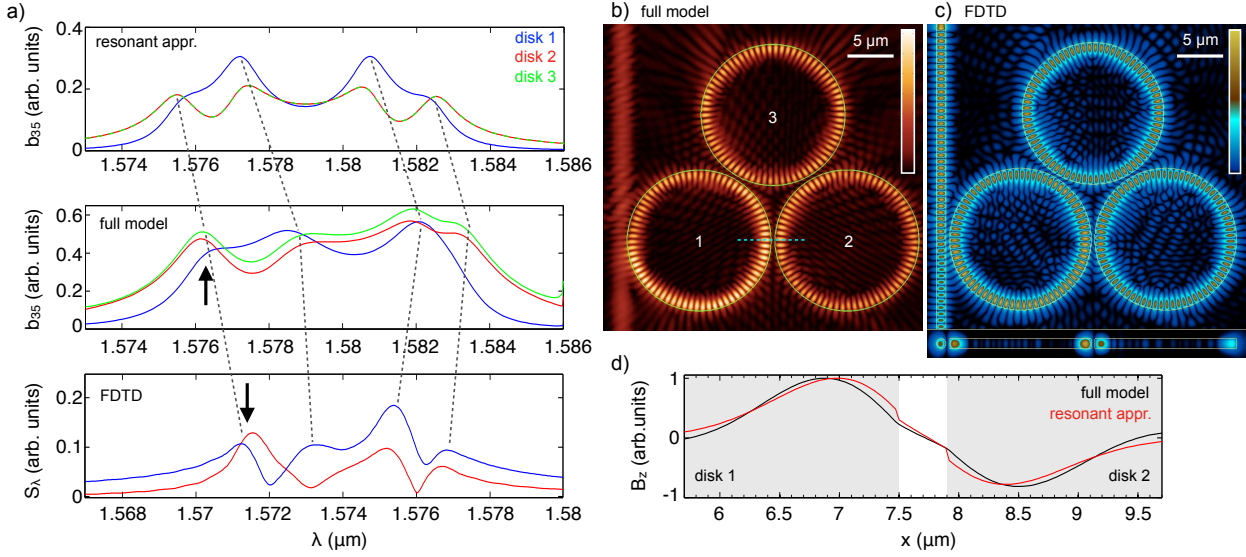


Fig. 2.11: Comparison of the spectral and field characteristics of the  $\text{TE}_{1,35}$  mode of three coupled disks in a triangular arrangement obtained from different methods. The single disk parameters are  $R = 7.5 \mu\text{m}$ ,  $n_{\text{res}} = 1.445$ ,  $h = 1 \mu\text{m}$  and the gap between the disks is  $d_{\text{gap}} = 400 \text{ nm}$ . In (a) from top to bottom the spectra are shown for the modal expansion in resonant approximation, using the full model with  $m_{\text{max}} = 45$ , and from a rigorous 3D FDTD simulation. Although the spectra differ, the expected four peaks are observed in each graph. For the first resonance peak [black arrows in (a)] the intensity distribution is plotted for (b) the full modal expansion and (c) the FDTD, which show good agreement. In (d) the field  $B_z$  across the gap between disk 1 and disk 2 [dashed line in (b)] is plotted. The unphysical discontinuities from the resonant approximation are avoided in the full model.

(overlap integrals). This would make the calculation much more complex. For comparison, a more rigorous model for smaller ring resonators including waveguide excitation is presented in Ref. [Ham10].

## 2.3 Coupled mode theory for an arbitrary number of disks

Taking into account the experimental situation of pumping and collecting of light through a waveguide coupled to one of the microdisks of a whole ensemble, a coupled mode theory (CMT) approach [Hau84] can be used. The approach uses a modal expansion of the electric field to obtain the temporal dynamics of the mode amplitudes and is widely used for the description of the characteristics of optical microresonators.<sup>26</sup> A derivation for particular cases, e.g., nonlinear effects in single resonators or Rayleigh scattering can be found in Refs. [Gor00, Joh06, Joh09], whereas the basic concept is more general and can be adapted from other discrete coupled systems, like optical waveguide arrays [Per03].

The key point is to take into account additional polarization terms

$$\mathbf{P}(\mathbf{r}, \omega) = \epsilon_0[\epsilon(\mathbf{r}, \omega) - 1]\mathbf{E}(\mathbf{r}, \omega) + \Delta\mathbf{P}(\mathbf{r}, \omega), \quad (2.51)$$

<sup>26</sup>See references given in the introduction (Chap. 1).

which results in a modified wave equation (2.9) (with the assumption of a piecewise homogeneous medium)

$$\nabla^2 \mathbf{E}(\mathbf{r}, \omega) + \frac{\omega^2}{c^2} \epsilon(\mathbf{r}, \omega) \mathbf{E}(\mathbf{r}, \omega) = -\mu_0 \omega^2 \Delta \mathbf{P}(\mathbf{r}, \omega). \quad (2.52)$$

Assuming that  $\Delta \mathbf{P}(\mathbf{r}, \omega)$  is small compared to the linear polarization, the problem can be solved using perturbation theory. Therefore, the electric field can be expanded into the eigenmodes of the unperturbed system

$$\mathbf{E}(\mathbf{r}, \omega) = \sum_m d_m(\omega) \mathbf{E}_m(\mathbf{r}, \omega_m), \quad (2.53)$$

with the modal amplitudes  $d_m(\omega)$ .<sup>27</sup> Substitution of Eq. (2.53) into Eq. (2.52) gives

$$\sum_m d_m(\omega) \left[ \frac{\omega_m^2}{c^2} \epsilon(\mathbf{r}, \omega_m) \right] - \frac{\omega^2}{c^2} \epsilon(\mathbf{r}, \omega) \sum_m d_m(\omega) \mathbf{E}_m(\mathbf{r}, \omega_m) = -\mu_0 \omega^2 \Delta \mathbf{P}(\mathbf{r}, \omega), \quad (2.54)$$

where we used that the eigenfunctions  $\mathbf{E}_m(\mathbf{r}, \omega_m)$  are solutions of the homogeneous wave equation. Using the orthogonality of eigenmodes [Joa95] one can find an expression for the mode amplitude  $d_m(\omega)$  by multiplying Eq. (2.54) with the complex conjugate  $\mathbf{E}_m^*(\mathbf{r}, \omega_m)$  and integration over the entire volume

$$-(\omega_m^2 + \omega^2) d_m(\omega) = -\mu_0 \omega^2 c^2 \frac{\int [\mathbf{E}_m^*(\mathbf{r}, \omega_m) \Delta \mathbf{P}(\mathbf{r}, \omega)] d\mathbf{r}}{\int [\epsilon(\mathbf{r}, \omega_m) |\mathbf{E}_m(\mathbf{r}, \omega_m)|^2] d\mathbf{r}}. \quad (2.55)$$

Here we also assumed a spectrally narrow excitation<sup>28</sup>  $\omega = \omega_0 + \Delta\omega$  with  $\omega_0 \gg \Delta\omega$  and a weakly dispersive material, so that  $\epsilon(\mathbf{r}, \omega) \approx \epsilon(\mathbf{r}, \omega_m)$  for the second term in Eq. (2.54). Upon back transformation to the time domain [according to Eq. (2.5)] one obtains

$$\frac{d^2}{dt^2} [d_m(t)] + \omega_m^2 d_m(t) = -\frac{\frac{d^2}{dt^2} \int [\mathbf{E}_m^*(\mathbf{r}, \omega_m) \Delta \mathbf{P}(\mathbf{r}, t)] d\mathbf{r}}{\epsilon_0 \int [\epsilon(\mathbf{r}, \omega_m) |\mathbf{E}_m(\mathbf{r}, \omega_m)|^2] d\mathbf{r}}. \quad (2.56)$$

Using the slowly varying amplitude approximation by separating the fast phase term of the carrier frequency  $\omega_0$  according to  $d_m(t) = \bar{d}_m(t) e^{-i\omega_0 t}$  [and analog for  $\Delta P(\mathbf{r}, t)$ ], one can evaluate the second order time derivative and keeping only first order terms to obtain

$$\frac{d}{dt} [\bar{d}_m(t)] = \frac{i}{2\omega_0} \left[ (\omega_0^2 - \omega_m^2) \bar{d}_m(t) + \frac{\omega_0^2 \int [\mathbf{E}_m^*(\mathbf{r}, \omega_m) \Delta \bar{\mathbf{P}}(\mathbf{r}, t)] d\mathbf{r}}{\epsilon_0 \int [\epsilon(\mathbf{r}, \omega_m) |\mathbf{E}_m(\mathbf{r}, \omega_m)|^2] d\mathbf{r}} \right]. \quad (2.57)$$

Since  $\omega_0 \approx \omega_m$  according to the assumption of a spectrally narrow excitation, Eq. (2.57) can

<sup>27</sup>The naming of the mode amplitude is chosen to underline the parallels to the above described 2D model for the calculation of the resonances of the structure (Sect. 2.1.1). In a 2D approximation the eigenmodes may have the form as in Eq. (2.19).

<sup>28</sup>In the experiment only continuous wave laser radiation was used, so this assumption is valid.

be simplified further using  $\omega_0^2 - \omega_m^2 \approx 2\omega_0(\omega_0 - \omega_m)$ , resulting in the final equation

$$\frac{d}{dt} [\bar{d}_m(t)] = i(\omega_0 - \omega_m)\bar{d}_m(t) + \frac{i\omega_0 \int [\mathbf{E}_m^*(\mathbf{r}, \omega_m)\Delta\bar{\mathbf{P}}(\mathbf{r}, t)] d\mathbf{r}}{2\epsilon_0 \int [\epsilon(\mathbf{r}, \omega_m)|\mathbf{E}_m(\mathbf{r}, \omega_m)|^2] d\mathbf{r}}. \quad (2.58)$$

In the following several effects are taken into account by specification of the perturbative polarization term. One can distinguish between local perturbations describing effects of a single microresonator (e.g., intrinsic losses  $\Delta\bar{\mathbf{P}}_{\text{loss}}$  and scattering induced modal coupling  $\Delta\bar{\mathbf{P}}_{\text{mc}}$ ) and remote influences (e.g., due to external coupling for excitation  $\Delta\bar{\mathbf{P}}_{\text{ext}}$  or coupling of several microresonators  $\Delta\bar{\mathbf{P}}_m^{(p)}$ ).

### 2.3.1 Single mode traveling wave resonator

To obtain the coupled mode equation for a single microresonator considering only a single mode and the excitation from an external waveguide we introduce two polarization terms, one of which is

$$\Delta\bar{\mathbf{P}}_{\text{loss}}(\mathbf{r}, t) = \epsilon_0[i\Delta\epsilon''(\omega_m)]\bar{d}_m(t)\mathbf{E}_m(\mathbf{r}, \omega_m), \quad (2.59)$$

to take into account the intrinsic losses with  $\Delta\epsilon''(\omega_m)$  being the nonzero imaginary part of a refractive index perturbation  $\Delta\epsilon(\mathbf{r}, \omega_m) = \Delta\epsilon'(\mathbf{r}, \omega_m) + i\Delta\epsilon''(\omega_m)$ , usually not depending on the spatial coordinate. The other polarization term for the external coupling reads as

$$\Delta\bar{\mathbf{P}}_{\text{ext}}(\mathbf{r}, t) = \epsilon_0[\hat{\epsilon}(\mathbf{r}, \omega_0) - \Delta\hat{\epsilon}_m(\mathbf{r}, \omega_0)]\bar{a}_{\text{in}}(t)\mathbf{E}_{\text{in}}(\mathbf{r}, \omega_0). \quad (2.60)$$

Here  $\hat{\epsilon}(\mathbf{r}, \omega_0)$  is the dielectric function of the whole structure (microresonator + excitation waveguide) and  $\Delta\hat{\epsilon}(\mathbf{r}, \omega_0)$  is the change the microresonator introduces to the dielectric constant compared to its absence. Here we also assume that the exciting field can be expanded into eigenmodes  $\mathbf{E}_{\text{in}}(\mathbf{r}, \omega_0)$  and is described by a single, slowly varying mode amplitude  $\bar{a}_{\text{in}}(t)$ . This can be done by considering a basis for the expansion of the electric field including resonator and waveguide modes as discussed in Ref. [Joh09]. An example for the particular case of a tapered optical fiber coupled to a spherical microresonator can be found in Ref. [Lit99]. Substitution of Eqs. (2.59) and (2.60) into Eq. (2.58) leads to

$$\frac{d}{dt} [\bar{d}_m(t)] = [i(\omega_0 - \omega_m) - \frac{\gamma_0}{2}]\bar{d}_m(t) + i\kappa\bar{a}_{\text{in}}(t), \quad (2.61)$$

with

$$\gamma_0 = \omega_0 \frac{\int [\Delta\epsilon''(\omega_m)|\mathbf{E}_m(\mathbf{r}, \omega_m)|^2] d\mathbf{r}}{\int [\epsilon(\mathbf{r}, \omega_m)|\mathbf{E}_m(\mathbf{r}, \omega_m)|^2] d\mathbf{r}}, \quad (2.62)$$

$$\kappa = \frac{\omega_0 \int \{[\hat{\epsilon}(\mathbf{r}, \omega_0) - \Delta\hat{\epsilon}_m(\mathbf{r}, \omega_0)]\mathbf{E}_m^*(\mathbf{r}, \omega_m)\mathbf{E}_{\text{in}}(\mathbf{r}, \omega_0)\} d\mathbf{r}}{2 \int [\epsilon(\mathbf{r}, \omega_m)|\mathbf{E}_m(\mathbf{r}, \omega_m)|^2] d\mathbf{r}}. \quad (2.63)$$



Since the exciting waveguide offers an additional loss channel for the field in the resonator, one has to introduce an energy loss rate  $\gamma_{\text{ext}}$  in analogy to the intrinsic loss. From energy conservation and time reversal symmetry one can find the relation  $\kappa = \sqrt{\gamma_{\text{ext}}}$  [Hau84]. If we substitute  $\Gamma_0 = \gamma_0/2$ ,  $\Gamma_{\text{ext}} = \gamma_{\text{ext}}/2$  and  $\Delta\omega_m = \omega_0 - \omega_m$  in Eq. (2.61) we get

$$\frac{d}{dt} [\bar{d}_m(t)] = [i\Delta\omega_m - (\Gamma_0 + \Gamma_{\text{ext}})]\bar{d}_m(t) + i\sqrt{2\Gamma_{\text{ext}}}\bar{a}_{\text{in}}(t). \quad (2.64)$$

This is the standard single resonator mode equation widely used in literature [Hau84, Bor05, Kip02, Lin08, Gor99]. The field normalization is usually chosen such that  $|\bar{d}_m|^2$  describes the energy stored in the  $m$ th mode of the resonator, whereas  $|\bar{a}_{\text{in}}|^2$  is the input power carried by the exciting waveguide. Due to the continuous wave excitation, we are mainly interested in the steady state response of the microresonator obtained by setting the time derivative to zero

$$\bar{d}_m = \frac{-i\sqrt{2\Gamma_{\text{ext}}}\bar{a}_{\text{in}}}{i\Delta\omega_m - (\Gamma_0 + \Gamma_{\text{ext}})}. \quad (2.65)$$

The transmitted amplitude through the coupling waveguide can be written as  $\bar{a}_{\text{trans}}(t) = \bar{a}_{\text{in}}(t) + i\sqrt{2\Gamma_{\text{ext}}}\bar{d}_m(t)$ , which for steady state gives the transmissivity

$$\mathcal{T}(\Delta\omega_m) = \left| \frac{\bar{a}_{\text{trans}}}{\bar{a}_{\text{in}}} \right|^2 = \left| 1 + \frac{i\sqrt{2\Gamma_{\text{ext}}}\bar{d}_m}{\bar{a}_{\text{in}}} \right|^2 = \frac{(\Delta\omega_m)^2 + (\Gamma_{\text{ext}} - \Gamma_0)^2}{(\Delta\omega_m)^2 + (\Gamma_{\text{ext}} + \Gamma_0)^2}, \quad (2.66)$$

which describes a Lorentzian dip at  $\Delta\omega_m = 0$  with the full-width at half-maximum (FWHM) of  $2(\Gamma_0 + \Gamma_{\text{ext}})$ .

### 2.3.2 Modal coupling due to Rayleigh scattering

As already mentioned above, due to the rotational symmetry of an ideal WGR there exist two counterpropagating modes, degenerated in frequency. The direction of light propagation in the coupling waveguide determines which mode gets excited. Since the early days of microresonator studies [Wei95] a splitting of the resonances was observed due to coupling of the counterpropagating modes, which can be attributed to Rayleigh scattering induced by bulk and surface inhomogeneities of the resonator material. According to Refs. [Gor00, Joh09], this effect can be taken into account in the CMT by an additional polarization term

$$\Delta\bar{\mathbf{P}}_{\text{mc}}(\mathbf{r}, t) = \epsilon_0\delta\epsilon(\mathbf{r}, \omega_m) [\bar{d}_{+m}(t)\mathbf{E}_m(\mathbf{r}, \omega_m) + \bar{d}_{-m}(t)\mathbf{E}_{-m}(\mathbf{r}, \omega_m)], \quad (2.67)$$

where the two counterpropagating modes  $\bar{d}_{\pm m}$  are considered. To underline the meaning of the opposite sign they are also denoted as  $\bar{d}_{\text{cw}, \text{ccw}}$  for clockwise (cw) and counterclockwise (ccw) propagation. The inhomogeneities are described by variations of the dielectric function  $\delta\epsilon(\mathbf{r}, \omega_m)$ . Substituting Eq. (2.67) into Eq. (2.58) (two equations for the  $+m$  and  $-m$  mode)

one obtains two possible contributions of the form

$$\gamma_{\pm m, \pm m} = \omega_0 \frac{\int [\delta\epsilon(\omega_m) |\mathbf{E}_{\pm m}(\mathbf{r}, \omega_m)|^2] d\mathbf{r}}{\int [\epsilon(\mathbf{r}, \omega_m) |\mathbf{E}_m(\mathbf{r}, \omega_m)|^2] d\mathbf{r}} \quad (2.68)$$

$$\gamma_{\pm m, \mp m} = \omega_0 \frac{\int [\delta\epsilon(\omega_m) \mathbf{E}_{\pm m}^*(\mathbf{r}, \omega_m) \mathbf{E}_{\mp m}(\mathbf{r}, \omega_m)] d\mathbf{r}}{\int [\epsilon(\mathbf{r}, \omega_m) |\mathbf{E}_m(\mathbf{r}, \omega_m)|^2] d\mathbf{r}}, \quad (2.69)$$

related to the four coupling combinations  $\pm m \rightarrow \pm m$  or  $\pm m \rightarrow \mp m$ . In most cases the main contribution to  $\delta\epsilon$  comes in the form of surface roughness, which to the first approximation is zero on average along the surface. Therefore, the coefficients  $\gamma_{\pm m, \pm m}$  in Eq. (2.68) vanish on average with the physical meaning that the coherent forward scattering does not influence the mode amplitudes, e.g., induces no additional shift of the resonances. With the assumption that the induced modal coupling in both directions is equal and by substitution of  $\Gamma_{\text{mc}} = \gamma_{\pm m, \mp m}/2$  the mode dynamics reads as

$$\frac{d}{dt} [\bar{d}_{+m}(t)] = [i\Delta\omega_m - (\Gamma_0 + \Gamma_{\text{ext}})] \bar{d}_{+m}(t) + i\Gamma_{\text{mc}} \bar{d}_{-m}(t) + i\sqrt{2\Gamma_{\text{ext}}} \bar{a}_{\text{in}}(t), \quad (2.70)$$

$$\frac{d}{dt} [\bar{d}_{-m}(t)] = [i\Delta\omega_m - (\Gamma_0 + \Gamma_{\text{ext}})] \bar{d}_{-m}(t) + i\Gamma_{\text{mc}} \bar{d}_{+m}(t). \quad (2.71)$$

Here we also assume that only the  $+m$  mode is excited. The steady state solutions can be found in the form of

$$\bar{d}_{+m} = \frac{-i\sqrt{2\Gamma_{\text{ext}}} \bar{a}_{\text{in}} [i\Delta\omega_m - (\Gamma_0 + \Gamma_{\text{ext}})]}{[i\Delta\omega_m - (\Gamma_0 + \Gamma_{\text{ext}})]^2 + \Gamma_{\text{mc}}^2}, \quad (2.72)$$

$$\bar{d}_{-m} = \frac{-\Gamma_{\text{mc}} \sqrt{2\Gamma_{\text{ext}}} \bar{a}_{\text{in}}}{[i\Delta\omega_m - (\Gamma_0 + \Gamma_{\text{ext}})]^2 + \Gamma_{\text{mc}}^2}. \quad (2.73)$$

The transmissivity and reflectivity can be found to be

$$\mathcal{T}(\Delta\omega_m) = \left| \frac{(i\Delta\omega_m - \Gamma_0)^2 - \Gamma_{\text{ext}}^2 + \Gamma_{\text{mc}}^2}{[i(\Delta\omega_m + \Gamma_{\text{mc}}) - (\Gamma_0 + \Gamma_{\text{ext}})] [i(\Delta\omega_m - \Gamma_{\text{mc}}) - (\Gamma_0 + \Gamma_{\text{ext}})]} \right|^2, \quad (2.74)$$

$$\mathcal{R}(\Delta\omega_m) = \left| \frac{-i2\Gamma_{\text{ext}}\Gamma_{\text{mc}}}{[i(\Delta\omega_m + \Gamma_{\text{mc}}) - (\Gamma_0 + \Gamma_{\text{ext}})] [i(\Delta\omega_m - \Gamma_{\text{mc}}) - (\Gamma_0 + \Gamma_{\text{ext}})]} \right|^2, \quad (2.75)$$

which obviously is a resonance doublet with dips at  $\Delta\omega_m = \pm\Gamma_{\text{mc}}$ . The reflectivity is defined in analogy as the ratio between the out-coupled amplitude from the resonator in backward direction and the incoming amplitude

$$\mathcal{R}(\Delta\omega_m) = \left| \frac{\bar{a}_{\text{refl}}}{\bar{a}_{\text{in}}} \right|^2 = \left| \frac{i\sqrt{2\Gamma_{\text{ext}}} \bar{d}_{-m}}{\bar{a}_{\text{in}}} \right|^2. \quad (2.76)$$

The resonance splitting is only observable if the splitting  $\Gamma_{\text{mc}}$  is larger than the single resonance bandwidth determined again by  $2(\Gamma_0 + \Gamma_{\text{ext}})$ .

### 2.3.3 Modes in coupled resonator structures

The coupling of modes of different microresonators can be introduced into the CMT in analogy to the coupling to an external waveguide for excitation. The perturbative polarization term induced in the  $p$ th microresonator for an ensemble of  $N$  coupled cavities reads as

$$\Delta\bar{\mathbf{P}}_m^{(p)}(\mathbf{r}, t) = \epsilon_0 \sum_{q=1, p \neq q}^N [\hat{\epsilon}(\mathbf{r}, \omega_m) - \Delta\hat{\epsilon}^{(p)}(\mathbf{r}, \omega_m)] \bar{d}_{-m}^{(q)}(t) \mathbf{E}_{-m}^{(q)}(\mathbf{r}, \omega_m). \quad (2.77)$$

where  $\hat{\epsilon}(\mathbf{r}, \omega_m)$  is the dielectric function of the whole coupled resonator structure and  $\Delta\hat{\epsilon}^{(p)}(\mathbf{r}, \omega_m)$  is the change the  $p$ th cavity introduces to the dielectric constant compared to its absence. If we again assume that the coupling is uni-directional, which is justified if the coupling regions do not introduce additional scattering, we obtain for the cw and ccw mode in each resonator

$$\frac{d}{dt} \left[ \bar{d}_{+m}^{(p)}(t) \right] = \Delta\Omega^{(p)} \bar{d}_{+m}^{(p)}(t) + i\Gamma_{\text{mc}} \bar{d}_{-m}^{(p)}(t) + i \sum_{q=1, p \neq q}^N \Gamma_{qp} \bar{d}_{-m}^{(q)}(t) + i\sqrt{2\Gamma_{\text{ext}}^{(p)}} \bar{a}_{\text{in}}(t), \quad (2.78)$$

$$\frac{d}{dt} \left[ \bar{d}_{-m}^{(p)}(t) \right] = \Delta\Omega^{(p)} \bar{d}_{-m}^{(p)}(t) + i\Gamma_{\text{mc}} \bar{d}_{+m}^{(p)}(t) + i \sum_{q=1, p \neq q}^N \Gamma_{qp} \bar{d}_{+m}^{(q)}(t), \quad (2.79)$$

with the abbreviation  $\Delta\Omega^{(p)} = i\Delta\omega_m^{(p)} - (\Gamma_0 + \Gamma_{\text{ext}}^{(p)})$  and the inter-resonator coupling coefficient (equal for cw  $\rightarrow$  ccw and vice versa)

$$\Gamma_{qp} = \frac{\gamma_{qp}}{2} = \frac{\omega_0}{2} \frac{\int \{ [\hat{\epsilon}(\mathbf{r}, \omega_m) - \Delta\hat{\epsilon}^{(p)}(\mathbf{r}, \omega_m)] \mathbf{E}_m^{*(p)}(\mathbf{r}, \omega_m) \mathbf{E}_{-m}^{(q)}(\mathbf{r}, \omega_m) \} d\mathbf{r}}{\int [\epsilon(\mathbf{r}, \omega_m) |\mathbf{E}_m^{(p)}(\mathbf{r}, \omega_m)|^2] d\mathbf{r}}. \quad (2.80)$$

Here we allow that each of the coupled microresonator modes has its unique resonance frequency and hence a slightly different mismatch  $\Delta\omega_m^{(p)}$ . Also the external coupling rate may be different for each resonator, since usually only one of them is excited. The intrinsic loss rate  $\Gamma_0$  and the intra-resonator coupling  $\Gamma_{\text{mc}}$  are assumed to be equal for the investigated samples, since material properties as well as fabrication induced inhomogeneities should not differ much between the resonators of one sample.

The steady state transmissivity and reflectivity through the exciting waveguide can be calculated in analogy to the relations in the two last sections by solving the linear system of equations (2.78) and (2.79) for the mode amplitudes  $\bar{d}_{\pm m}^{(p)}$  of the excited resonator. To point out the influence of the inter-resonator coupling the system was solved for two coupled identical resonators with one of them externally excited. The transmissivity can be found to

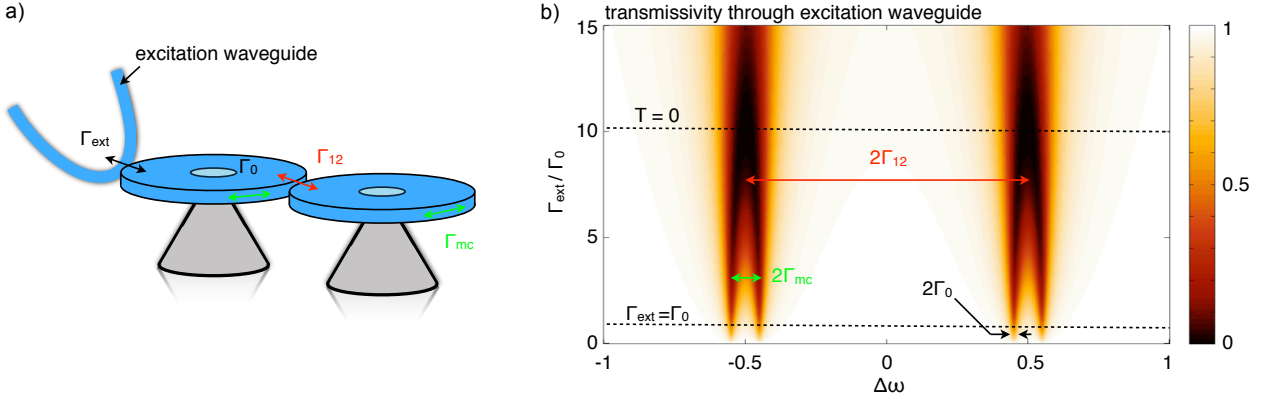


Fig. 2.12: Illustration of the influence of the different coupling and loss rates on the resonance spectrum. (a) Schematic of the coupled disk sample with excitation waveguide. (b) Transmissivity according to Eq. (2.81) for variable  $\Gamma_{\text{ext}}$  as a function of detuning  $\Delta\omega_m$ . The other parameters are  $\Gamma_0 = 0.01$ ,  $\Gamma_{\text{mc}} = 0.05$ , and  $\Gamma_{12} = 0.5$ .

be

$$\mathcal{T} = \left| 1 + \frac{2\Gamma_{\text{ext}} \left\{ (i\Delta\omega_m - \Gamma_0) [(i\Delta\omega_m - \Gamma_0)^2 + \Gamma_{\text{mc}}^2 + \Gamma_{12}^2] - \Gamma_{\text{ext}} [(i\Delta\omega_m - \Gamma_0)^2 + \Gamma_{\text{mc}}^2] \right\}}{\left\{ [i(\Delta\omega_m \pm \Gamma_{\text{mc}}) - \Gamma_0] [i(\Delta\omega_m \pm \Gamma_{\text{mc}}) - (\Gamma_0 + \Gamma_{\text{ext}})] - \Gamma_{12}^2 \right\}} \right|^2, \quad (2.81)$$

where the denominator has to be understood as product of the term in braces with + sign and with – sign replacing the  $\pm$  sign, respectively. As expected from the previous sections a splitting in four resonance peaks can be observed with the resonance frequencies

$$\omega_{\pm, \pm} = \frac{1}{2} \left[ -i(2\Gamma_0 + \Gamma_{\text{ext}}) \pm 2\Gamma_{\text{mc}} \pm \sqrt{4\Gamma_{12}^2 - \Gamma_{\text{ext}}^2} \right], \quad (2.82)$$

where each of the four combinations ++, +–, –+ and –– gives a different resonance. Usually,  $\Gamma_{12} > \Gamma_{\text{mc}}$  and for weak excitation  $\Gamma_{\text{ext}} \ll \Gamma_{12}, \Gamma_{\text{mc}}$  the resonances can be found at  $\Re(\omega_{\pm, \pm}) \approx \pm\Gamma_{12} \pm \Gamma_{\text{mc}}$ . In Fig. 2.12, Eq. (2.81) was solved for normalized parameters  $\Gamma_0 = 0.01$ ,  $\Gamma_{\text{mc}} = 0.05$ ,  $\Gamma_{12} = 0.5$  and variable  $\Gamma_{\text{ext}}$  as a function of the detuning  $\Delta\omega_m$  to illustrate the influence of the different coupling and loss rates.

## Chapter summary

In this chapter different theoretical models for the calculation of optical characteristics of disk microresonators were presented. For single microdisks a 2D analytical modal expansion model [or effective index method (EIM)] can be used to obtain the resonance frequencies as well as the radiation Q-factor. The approach uses the  $(r, \phi)$ -plane parallel to the disk's top and bottom surface with an effective refractive index approximation, since the radius is much larger than the thickness. In this plane the model is able to predict also the electromagnetic field distribution. The extension to a 2D scattering problem of an arbitrary number of coupled circular microdisks is straight forward. The advantages of the model are the flexibility and

relatively fast calculation, which allows for parameter scans as well as fitting against experimental data to estimate geometrical parameters of the investigated samples. The results were briefly compared to 3D FDTD calculations which shows good agreement.

To gain more insight into the modal characteristics a finite-element-method (FEM) was used. For a circular symmetric structure the FEM also can be reduced to a 2D calculation, but now in the  $(r, z)$ -plane perpendicular to the disk, and therefore allows the consideration of single disks only. Nevertheless, it is capable of calculating the 'exact' field distribution<sup>29</sup> of a mode in this plane, which can be easily extruded to the full 3D distribution. The main advantage of the FEM is the possibility to handle axisymmetric resonators with arbitrary profiles as well as multilayered structures with high accuracy. The important parameters obtained from a FEM are the mode volume, energy or intensity ratios of light guided inside and outside of the disk material as well as more accurate resonance frequencies and radiation Q-factors.

In order to get a better description of the experimental situation, where the sample is excited by an external waveguide, a more general and comprehensive coupled mode theory can be used. As an advantage, various effects can be taken into account as long as they can be treated perturbatively, e.g., intrinsic losses, modal coupling due to Rayleigh scattering and inter-disk coupling. Also nonlinear interactions can be described as shown in Refs. [Spi04, Lin08, Joh09]. Here we will take into account an optically induced thermal nonlinear response described in Chap. 5. Since for microdisks the modal field distribution cannot be calculated analytically all the coupling term integrals have to be solved numerically, which is a drawback of the rigorous approach. This is also an issue for a 2D approximation of such systems but there additional assumptions for the coupling coefficients can be made, which reduces the numerical effort significantly [Hir05, Ham10]. In the experiments it is useful to extract the coefficients, whenever possible, from corresponding independent experimental data as shown below.

To summarize the limits of applicability, the above described models are justified for thin disks<sup>30</sup> and weak material dispersion. The CMT, in particular, is valid only for weak perturbations of the linear polarization (so that the unperturbed eigenfunctions properly describe the fields also in the perturbed case) as well as for excitations consistent with the slowly varying amplitude approximation. Throughout this thesis all requirements are fulfilled. In its entirety the described models allow a comprehensive understanding of experimentally observable effects and will provide a valuable tool for designing coupled microdisk structures with particular characteristics.

---

<sup>29</sup>In a sense of an arbitrarily good approximation to the exact solution.

<sup>30</sup>Compared to the disk radius.

## 3 Experimental realization and basic characterization

The theoretical analysis of Chap. 2 defines the requirements for the experimental realization of optically coupled microdisks. The key aspect is the resonance mismatch between the individual microdisks in the coupled structures, which is mainly determined by their radius difference. This requires a highly reproducible and controllable fabrication of single resonators with an accuracy of the radius of at least 20 nm (see Fig. 2.9). Another point is that the various possible arrangements should be investigated under the same conditions for quantitative statements. This calls for a flexible, standardized sample platform and also defines the conditions for the experimental setup as well as the excitation of the samples. To account for all the requirements we used an electron beam lithography (EBL) with subsequent physical and chemical etching to fabricate on-chip microdisk samples, which are excited by tapered optical fiber coupling in an automated measurement setup. The following sections describe the capabilities and limitations of the used experimental methods and techniques as well as basic characterizations of the fabricated single and coupled microdisks, in order to determine key parameters (e.g., Q-factors, mode numbers, coupling rates, etc.), which are of importance for further studies. In particular this involves thermal nonlinear effects investigated in Chap. 5.

### 3.1 Fabrication of coupled microdisks

The fabrication of the coupled fused silica disk microresonators investigated throughout this thesis is shown schematically in Fig. 3.1. It starts with a silicon wafer covered with a thermally oxidized fused silica layer of approximately 1  $\mu\text{m}$  thickness. A chromium layer and electron beam resist (FEP) are deposited on top. The sample layout pattern is then transferred into the resist by direct electron beam writing. After the development process the remaining resist is used as an etching mask for the chromium layer. The chromium layer of 80 nm thickness is structured by inductively coupled plasma etching (ICP) and acts as a resistant etch mask for all following processes. Using only the resist without the chromium layer as mask would not allow for deep structures and at the same time high lateral resolution. The fused silica layer is then anisotropically etched by ICP using fluorofrom ( $\text{CHF}_3$ ). To functionalize the silica layer as a waveguiding structure it has to be released from the high refractive index

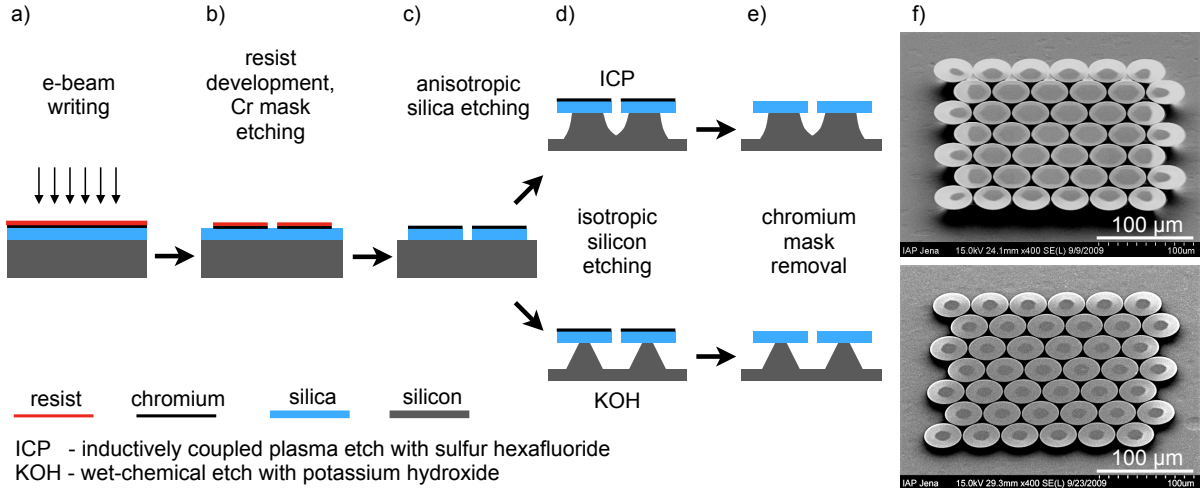


Fig. 3.1: Schematic view of the fabrication process: (a) electron beam writing of the disk pattern into the resist; (b) resist development and chromium mask etching; (c) anisotropic etching of the fused silica layer; (d) isotropic etching of the silicon substrate either by inductively coupled plasma (ICP) etching (top) or by wet-chemical etching (KOH) (bottom); (e) chromium mask removal. The difference between both etching methods is shown for a large array of coupled disks (f). For the ICP etch the inner region of the array is not sufficiently under-etched, whereas for the KOH etch a homogeneous under-etching throughout the whole array is obtained.

substrate, which is done by isotropic etching of the silicon, resulting in free standing fused silica disks supported by silicon pedestals at the center of each disk. For the isotropic silicon etching two approaches can be used, either an ICP etching with sulfur hexafluoride ( $\text{SF}_6$ ) or a wet-chemical etching with potassium hydroxide (KOH). The difference between both processes becomes important for the fabrication of large 2D arrays of coupled microdisks. In this case ICP etching is strongly selective with respect to the inner and outer region of the array. The inner disks are insufficiently under-etched, which can be explained by a shielding of the reactive plasma due to the disks. In contrast, a very homogeneous under-etching is obtained from the wet-chemical etch process. In Fig. 3.1(f) scanning electron microscope (SEM) images illustrate this effect for an array of 48 hexagonally coupled microdisks. Finally, after the silicon etching the chromium mask is removed.

Typical samples investigated in this thesis (see Fig. 3.2) have a single disk diameter of  $D = 30 \mu\text{m}$  to  $40 \mu\text{m}$ , a thickness of about  $h = 0.9 \mu\text{m}$  to  $1.2 \mu\text{m}$  and a material refractive index of  $n_{\text{res}} = 1.445^1$ . The gap between two coupled disks ranges from  $d_{\text{gap}} = 200 \text{ nm}$  to  $500 \text{ nm}$ .

Depending on the process parameters in the mask and silica etching steps the sidewall angle of the disks can be tuned from vertical to wedge shape [two examples are shown in Fig. 3.2(d, e)]. Although it was shown that a wedge shaped sidewall can increase the Q-factor of the resonator due to a reduction of the mode overlap with the rough sidewall [Kip03], for the coupling of disks it is preferable to have vertical sidewalls or only small angles. Due to

<sup>1</sup>The exact values of  $h$  and  $n_{\text{res}}$  are obtained by fitting of broad range resonance spectra. Estimation of  $h$  from SEM images fixes the correct combination of  $h$  and  $n_{\text{res}}$ . For details see Sect. 3.4.

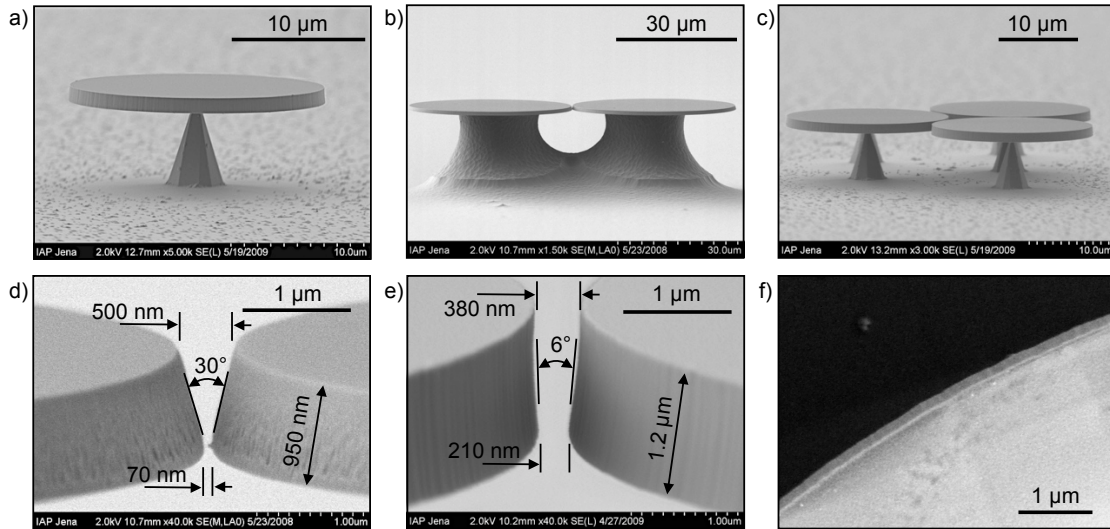


Fig. 3.2: Scanning electron microscope (SEM) images of typical samples investigated in this thesis - (a) single disk, (b) two coupled disks and (c) three coupled disks in a triangular arrangement. Depending on the process parameters the sidewall angle can be tuned from (d) large to (e) small values, where for optical coupling a small angle is preferred. (f) A magnified section of the disk rim which is used for sidewall roughness analysis.

the wedge, the effective distance between the disks increases, which leads to a reduction of the optical coupling strength. From the SEM images one can also see that there is a certain roughness present on the sidewalls. It results from a finite electron beam position accuracy and the graininess of the resist and chromium layers, which transfers into the fused silica. Using a method of resist reflow [Bor05] for reducing the sidewall roughness cannot be applied here, because it will inhibit the formation of the very narrow gaps between the disks, which are essential for the optical coupling. Two main effects related to the surface roughness can be expected: first, the limitations of the Q-factor<sup>2</sup> due to induced surface scattering losses and second, the coupling to counterpropagating waves inside the resonator (see Sects. 2.3 and 3.4).

## 3.2 Tapered fiber coupling

Tapered optical fiber coupling [Kni97] is a highly efficient method to couple light in and out of an optical microresonator. The idea is to adiabatically thin down a standard telecom optical fiber with a cladding diameter of 125 μm to a diameter of about 1 μm. As illustrated in Fig. 3.3 the initial single core guided mode is transferred to a cladding guided mode with a significant amount of optical power in the air surrounding the fiber taper. This can be used to couple to the evanescent field of the microresonator. Beside the mode overlap, simultaneous matching of the resonator and fiber mode in time and space is essential for effective coupling. The first is simply provided by tuning the frequency of an exciting laser to a resonance frequency of the

<sup>2</sup>A discussion of different contributions to the total loss is given in Sect. 3.4.2.



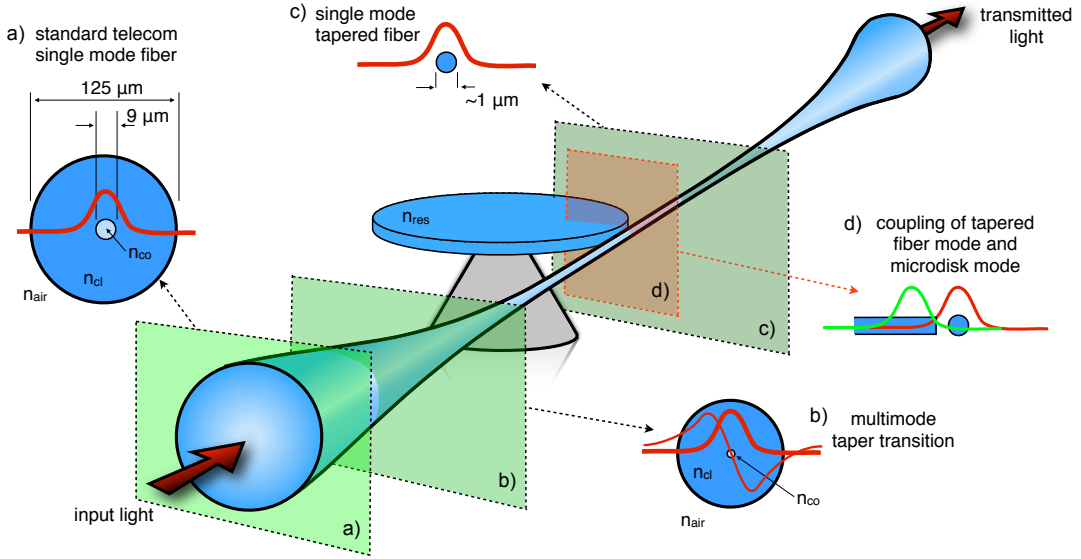


Fig. 3.3: Schematic of a tapered optical fiber and its coupling to a microdisk resonator. (a) Initial single mode standard telecom fiber profile with a core guided mode. (b) Transition region of reduced cladding and core diameter. The initial mode becomes cladding guided. Higher order cladding guided modes are not excited for an adiabatically transition but might have to be considered in the experiments. (c) Tapered optical fiber with a final diameter of about  $1 \mu\text{m}$  and a single cladding guided mode. The initial core region disappears. (d) Illustration of the coupling of the tapered fiber mode to the WGM by overlapping of the evanescent fields. The illustrations are merely included as a visualization aid and are not true to scale.

resonator. The second depends on the propagation constants of the tapered fiber mode and the resonator mode and is referred to as phase matching.

For the calculation of the taper modes and their respective propagation constants one can use the fact that the thinnest taper section is very long compared to the wavelength and can be assumed as constant in diameter. Therefore, the taper modes are that of a step-index fiber, but due to the large refractive index contrast between cladding material and air a full vectorial description of the fiber modes has to be used, based on the solution of the Helmholtz equation in cylindrical coordinates [Sny83, Yar97]. The required diameter of the tapered fiber  $d_{\text{tf}}$  to obtain phase matching between a taper mode and a mode of a microresonator can be calculated from the characteristic equation for the propagation constant  $\beta_{\text{tf}}$  of the taper modes

$$\left( \frac{J'_l(U)}{U J_l(U)} + \frac{K'_l(W)}{W K_l(W)} \right) \left( \frac{J'_l(U)}{U J_l(U)} + \frac{n_{\text{air}}^2 K'_l(W)}{n_{\text{cl}}^2 W K_l(W)} \right) = \left( \frac{l \beta_{\text{tf}}}{k_0 n_{\text{cl}}} \right)^2 \left( \frac{V}{UW} \right)^4, \quad (3.1)$$

with the Bessel function of the first kind  $J_l$ , the modified Bessel function of the second kind  $K_l$ , the mode order  $l$ , the vacuum wave number  $k_0$  and the numerical refractive index of the mode guiding cladding  $n_{\text{cl}}$  and the surrounding air  $n_{\text{air}}$ , respectively. The parameters  $U$ ,  $W$ , and  $V$  are defined as

$$U = \frac{d_{\text{tf}}}{2} \sqrt{k_0^2 n_{\text{cl}}^2 - \beta_{\text{tf}}^2}, \quad (3.2)$$

$$W = \frac{d_{\text{tf}}}{2} \sqrt{\beta_{\text{tf}}^2 - k_0^2 n_{\text{air}}^2}, \quad (3.3)$$

$$V = \sqrt{U^2 + W^2}. \quad (3.4)$$

The coupling between a tapered fiber mode and a fundamental mode of a microdisk resonator can be approximated by the coupling of a straight and a curved waveguide using coupled mode theory<sup>3</sup> [Mat75, Row93]. By projecting the curved waveguide onto the propagation direction of the straight waveguide the coupled mode equations can formally be written as for two straight waveguides with effective propagation constants. For the case of two parallel waveguides the coupling efficiency varies proportional to  $\text{sinc}(\Delta\beta)$  [Sal91], where  $\Delta\beta = \beta_1 - \beta_2$  is the difference between the propagation constants of the two waveguides. For phase matching ( $\Delta\beta = 0$ ) the maximum coupling efficiency is obtained. In general, the coupling coefficient can be calculated by [Sny83]<sup>4</sup>

$$\kappa_{ij} = \frac{k_0}{4} \left( \frac{\epsilon_0}{\mu_0} \right)^{\frac{1}{2}} \int_A (n^2(\mathbf{r}) - n_i^2) \hat{\mathbf{E}}_i^\perp \hat{\mathbf{E}}_j^\perp dA. \quad (3.5)$$

The  $\hat{\mathbf{E}}_{i,j}^\perp$  represent the unperturbed normalized electric fields of the taper and resonator mode perpendicular to the propagation direction,  $n_i$  is the refractive index of waveguide  $i$ , and  $n(\mathbf{r})$  describes the refractive index profile of the structure [ $n(\mathbf{r}) = n_i$  in waveguide  $i$ ,  $n(\mathbf{r}) = n_j$  in waveguide  $j$ , and  $n(\mathbf{r}) = n_{\text{air}}$  in air]. The same relation can be used to calculate the coupling coefficient for the coupled straight and bend waveguides for the point of minimum separation, with  $(i, j)$  being replaced by the domain of the resonator (res) or the tapered fiber (tf), respectively.

An analytical solution to Eq. (3.5) can be given only for analytically available mode profiles, e.g., for the coupling of a tapered fiber to a microsphere [Lit99]. Since the contribution of the transverse field overlap to the coupling strength is mainly determined by the distance between taper and resonator, the optimal coupling can be found experimentally by recording the taper transmission for varying taper-resonator gap. According to the transmissivity of a tapered fiber coupled to a single mode microresonator [Eq. (2.67)] and recalling the relation  $\kappa = \sqrt{2\Gamma_{\text{ext}}}$ , three regimes of coupling can be distinguished, comparing external ( $\Gamma_{\text{ext}}$ ) and intrinsic loss rates ( $\Gamma_0$ ). These are the under-coupled regime with the optical energy decay determined by the intrinsic losses ( $\Gamma_{\text{ext}} < \Gamma_0$ ), the over-coupled regime with the coupling losses dominating ( $\Gamma_{\text{ext}} > \Gamma_0$ ) and the critical coupling ( $\Gamma_{\text{ext}} = \Gamma_0$ ), for which the transmissivity<sup>5</sup> reaches a minimum (or zero for  $\Delta\omega_m = 0$ ). The critical coupling condition depends on the loss channels of the microresonator, hence taking into account intra-disk modal coupling  $\Gamma_{\text{mc}}$  and inter-disk coupling  $\Gamma_{qp}$  (according to Sect. 2.3) will shift the point of zero transmissivity. For two coupled

<sup>3</sup>Under the assumption of weak coupling between tapered fiber and microresonator.

<sup>4</sup>In analogy to Eq. (2.64).

<sup>5</sup>The transmissivity is defined as the transmitted optical power through the taper normalized to the input power. See also Sect. 2.3.

microdisks the critical coupling condition on resonance [ $\mathcal{T}(\Delta\omega_m = \Gamma_{12}) = 0$  from Eq. (2.81)] reads as

$$\Gamma_{\text{ext}} = \Re \left\{ \sqrt{\frac{[(2\Gamma_{12} + i\Gamma_0)^2 - \Gamma_{\text{mc}}^2][\Gamma_0^2 + \Gamma_{\text{mc}}^2]}{(\Gamma_{12} + i\Gamma_0)^2 - \Gamma_{\text{mc}}^2}} \right\}. \quad (3.6)$$

To spectrally observe additional effects, the coefficients  $\Gamma_{12}$  and  $\Gamma_{\text{mc}}$  have to be larger than  $\Gamma_0$  and hence the critical coupling shifts towards the over-coupled regime (as compared to a single mode resonator; see also Fig. 2.12). For  $\Gamma_{12} = 0$  Eq. (3.6) reduces to the well known relation for the critical coupling of a single disk with modal coupling [Kip02].

The phase matching is determined by the oscillatory components of the fields parallel to the propagation direction ( $y$ -direction)

$$\mathbf{E}_{\text{tf}}(\mathbf{r}) = \mathbf{E}_{\text{tf}}^\perp e^{i\beta_{\text{tf}}y}, \quad (3.7)$$

$$\mathbf{E}_{\text{res}}(\mathbf{r}) = \mathbf{E}_{\text{res}}^\perp e^{im\phi} = \mathbf{E}_{\text{res}}^\perp e^{i\frac{m}{R_{\text{res}}}R_{\text{res}}\phi} \approx \mathbf{E}_{\text{res}}^\perp e^{i\beta_{\text{res}}y}. \quad (3.8)$$

The projection of the azimuthal propagation of the resonator mode onto the propagation direction of the tapered fiber mode in Eq. (3.8) leads to the simple phase matching condition

$$\Delta\beta = \beta_{\text{tf}} - \beta_{\text{res}} = 0 \Rightarrow \beta_{\text{tf}} = \beta_{\text{res}} = m/R_{\text{res}}. \quad (3.9)$$

The last relation gives an approximation of the required diameter of the tapered fiber, but overestimates it due to the finite diameter of the taper and the fact that the maximum of the resonator mode is located inside the resonator ( $r_{\text{max}} < R_{\text{res}}$ ). A better approximation of the matched propagation constant can be written as  $\beta_{\text{res}}^{\text{eff}} = \beta_{\text{res}}(1 - d_{\text{sep}}/2R_{\text{res}}) = 0$ , taking into account the separation  $d_{\text{sep}} = d_{\text{tf}}/2 + d_{\text{ext}} + \Delta R_{\text{res}}$  of the mode maxima in the tapered fiber and the resonator [Row93]. Nevertheless, the distance of the mode maximum from the rim of the resonator  $\Delta R_{\text{res}}$  requires the knowledge of the field distribution which can be calculated only numerically (see Sect. 2.1.2). Assuming typical values, the deviation between Eq. (3.9) and the more exact relation is approximately 3%. Figure 3.4(a) shows the calculated effective mode index  $n_{\text{eff}} = \beta/k_0$  of the tapered fiber modes [Eq. (3.1)] and of typical TE and TM modes of a microdisk resonator used in this thesis [Eq. (2.24)]. According to Eq. (3.9), phase matching can be assumed for an effective taper mode index of 1.25 (1.22) for the first order disk modes of TE (TM) polarization. In Fig. 3.4(b) the optimal taper radius  $r_{\text{tf}}$  for the excitation of certain disk modes is calculated for a wavelength range of  $\lambda = 1.5 \mu\text{m}$  to  $\lambda = 1.6 \mu\text{m}$  and a disk radius of  $R_{\text{res}} = 15 \mu\text{m}$  to  $R_{\text{res}} = 25 \mu\text{m}$ . Matching of a first order radial disk mode (TE) requires a radius  $r_{\text{tf}} = 0.6 \mu\text{m}$  ( $d_{\text{tf}} = 1.2 \mu\text{m}$ )<sup>6</sup>. This radius will not be the optimum for excitation of a first order TM mode or a higher order radial mode. Usually, one taper is used for testing of different modes and samples which results in non-optimal phase matching. Nevertheless, also

<sup>6</sup>The value deviates by  $\pm 7\%$  for the range of tested samples according to the shaded region for the first order TE mode in Fig. 3.4(b)

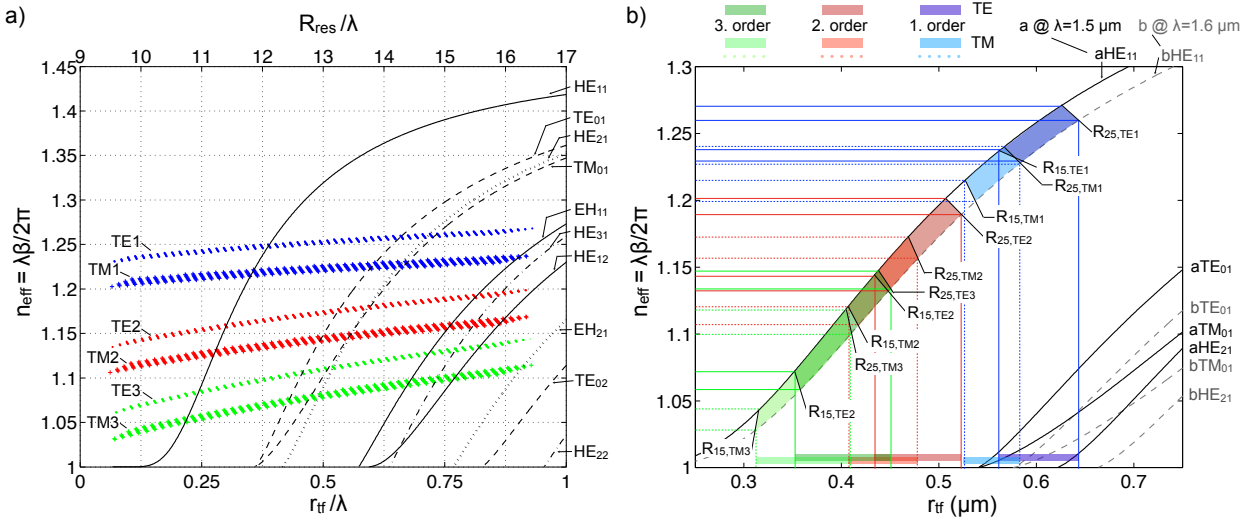


Fig. 3.4: (a) The effective refractive mode indices for a disk resonator with typical dimensions used in this thesis and of a step-index fiber using Eq. (3.1) indicate phase matching around  $n_{\text{eff}} = 1.25$  (1.22) for a first order TE (TM) resonator mode. (b) The phase matching taper radius  $r_{\text{tf}}$  for the first three radial orders of disk modes. The  $n_{\text{eff}}$  for the fiber taper modes are shown as black solid lines (e.g., aHE<sub>11</sub> with 'a' indicating  $\lambda = 1.5 \mu\text{m}$ ) and gray dashed lines (e.g., bHE<sub>11</sub> with 'b' indicating  $\lambda = 1.6 \mu\text{m}$ ). The disk modes are calculated close to this wavelengths for  $R_{\text{res}} = 15 \mu\text{m}$  (e.g.,  $R_{15, \text{TE1}}$  for the first order radial mode of TE polarization) and  $R_{\text{res}} = 25 \mu\text{m}$  resulting in four intersections with the taper mode lines 'a' and 'b', which define the color shaded areas (blue - first radial order TE modes; light blue - first radial order TM modes, etc.). Since one taper is used for excitation of different samples the optimal taper radius range is determined by the projection of the shaded areas on the x-axis, e.g., matching of the first order radial disk TE modes requires a radius  $r_{\text{tf}} = 0.6 \mu\text{m}$  ( $d_{\text{tf}} = 1.2 \mu\text{m}$ ). The thickness of the disks was  $h = 1 \mu\text{m}$  for all calculations (see Sect. 2.1 for influences on the disk modes).

a deviation of a few percent in the effective mode index allows significant coupling, even when the power transfer at critical coupling is not maximized.

For the obtained  $r_{\text{tf}}$  the tapered fiber is not single mode [as seen in Fig. 3.4(b)]. The energy coupled from the resonator to the taper can also couple to the higher order modes of the taper and will be lost due to the adiabatic transition to the standard single mode optical fiber. The parameter describing this parasitic loss mechanism at the taper-resonator-junction is called ideality and is discussed in detail in [Spi03]. If the taper is thin enough, close to cut-off of the higher order taper modes, the ideality is almost unity. If the taper becomes thicker the coupling to higher order modes is significant, especially in the over-coupled regime. For the used tapered fibers and microdisk resonators the coupling to higher order modes can be neglected because the phase mismatch is relatively large also for higher order resonator modes and the distance is usually set to be close to the critical or under-coupled regime.

## Fabrication of tapered optical fibers

For the fabrication of tapered optical fibers a flame-brushing technique was used as shown in Fig. 3.5. With the help of a hydrogen microflame torch (Model 120, Bryzel Inc.) temperatures

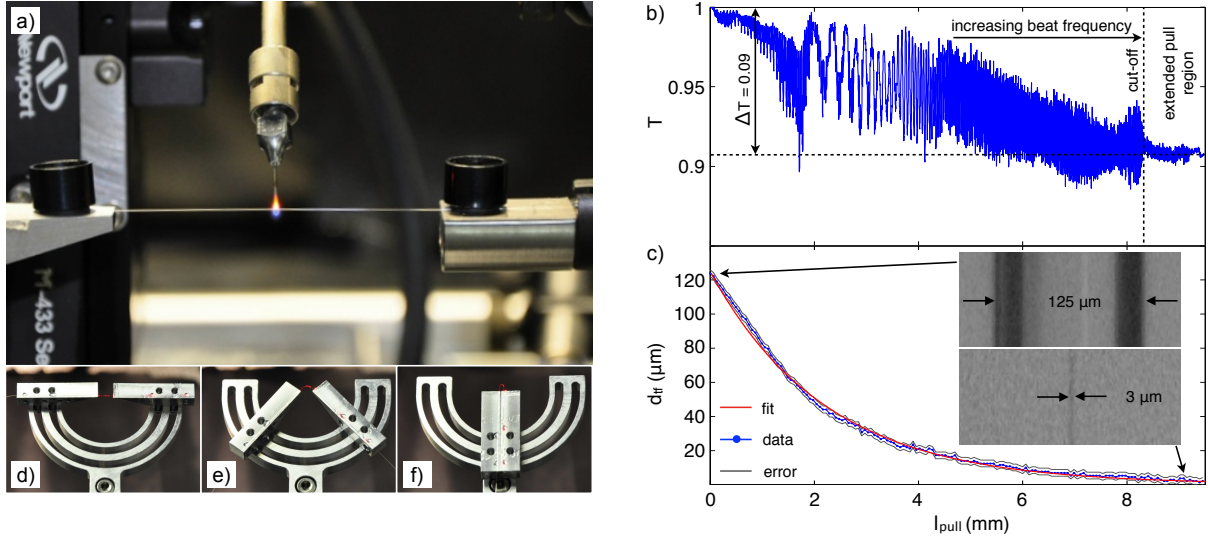


Fig. 3.5: (a) Taper fabrication setup with ignited hydrogen torch and optical fiber before pulling. After fabrication the taper was bend on a special holder (d-f, taper is visible due to scattering of launched red laser light). The transmission through the fiber during the pulling (b) shows interference of cladding modes, which disappear close to the correct taper radius. (c) The measured taper diameter  $d_{\text{tf}}$  for one of the taper transitions. The total length is twice the displayed pull length  $l_{\text{pull}}$  of one motorized stage. Fitting with Eq. (3.10) gives a heat zone length  $L_0 = (2.1 \pm 0.1)$  mm in agreement with the set value for the flame oscillation.

of up to  $1200^\circ\text{C}$  are provided<sup>7</sup> to locally heat the silica fiber above its melting temperature. The fiber is fixed on two motorized stages, which pull it in opposite directions. This leads to a diameter reduction in the heated zone. The torch is also mounted on a translation stage to allow an extension of the region of constant taper diameter by moving the torch along the fiber during the pulling. A variation of the length of the heating zone during the tapering process allows arbitrary longitudinal diameter profiles of the taper [Bir92]. Using a constant length of the heating zone  $L_0$ , as well as a constant velocity of the pulling stages, leads to an exponential shape described by

$$d_{\text{tf}}(z) = d_0 e^{-z/L_0}, \quad (3.10)$$

with the initial fiber diameter  $d_0$  and the pulling in  $z$ -direction. If the velocity is chosen slow enough, an almost adiabatic energy transfer from the initial fiber mode to the taper mode can be achieved.<sup>8</sup> The shape of a typically fabricated taper is shown in Fig. 3.5(c) together with a fit using Eq. (3.10) and  $L_0$  as a fit parameter. The obtained value  $L_0 = (2.1 \pm 0.1)$  mm matches the experimentally set value of the flame oscillation range of 2 mm. The larger measured value can be explained by the finite size of the flame. Figure 3.5(b) shows the measured taper transmission during the tapering process. At a pull distance of 2 mm oscillations start, indicating interference of the initial fiber mode with higher orders of the cladding guided taper modes. The oscillation period decreases with increasing taper

<sup>7</sup>Generation of hydrogen on demand and using acetone as buffer gas.

<sup>8</sup>The optimal profile for adiabatic transition of the single fiber mode to the fundamental taper mode requires a nontrivial flame movement [Bir92].

length and at a pull distance of 8.5 mm the oscillations disappear. This suggests a single mode operation of the taper but experimental observation shows that the taper diameter at this point is still too large for single mode operation as well as for phase matching to the WGMs. In [Din10b] a detailed analysis of the transmission oscillation was presented, using a short-time Fourier transform (or Gabor transform) emphasizing the non-single mode operation also for a flat transmission signal. An additional pull distance of about 1 mm was applied to obtain the required taper diameter around  $1.2\ \mu\text{m}$ . The transmission drop of about 9% is attributed to the relatively short taper length needed for comfortable handling after fabrication and is not critical for the experiments in this thesis.

After finishing the pulling process the taper can be placed on different types of holders to keep it straight or to form an u-turn shaped bend taper [see Fig. 3.5(d)-(f)], required for excitation of samples on the fabricated dense packed chips.<sup>9</sup>

### 3.3 Experimental setup

For characterization the microdisk samples are placed on a two axis translation stage for positioning in the horizontal plane and a rotation stage in order to change their orientation relative to the position of the tapered optical fiber used for excitation. To control and stabilize the temperature of the samples a Peltier element and a temperature controller (TED 4015, Thorlabs) are used. At the left and right side of the sample stage tapered fibers can be placed on two three-axis positioning stages (Nanomax 301, Thorlabs) with stepper motors for coarse alignment and closed loop piezo actuators for high precision adjustment of the coupling between microdisk and taper. The two tapers make the setup highly flexible for investigation of different configurations, which are, e.g., add-drop filters, pump and probe experiments, excitation of different disks in one sample at the same time, etc. In addition, these stages can be used to carry micromanipulators or detectors, offering a set of possibilities for investigation of coupled microdisk (or even other micro-fabricated) samples. Behind the sample stage a SNOM head (MV4000, Nanonics Imaging) can be installed,<sup>10</sup> which is used for manipulation of the samples on the nano scale as well as for the mode mapping of WGMs in coupled microdisks (see Chap. 4). The sample and the coupling to the tapered fibers are visualized by a microscope setup (x100 NIR, Mitotoyo) with a CCD camera for the visible spectrum range (Pike F145, Allied Vision Technologies) and another one for the infrared (SU128, Sensors Unlimited), which is used to collect the out-of-plane scattered light of excited WGMs. The whole setup is placed on an active vibration isolation (Vario 60, Accurion) and the load of all

---

<sup>9</sup>Also a fiber-rotation holder on one of the pulling stages was implemented for twisting the fabricated taper to create fiber taper loops providing a smaller radius of curvature than the u-turn shaped tapers, e.g., for a point-like excitation of photonic crystal resonators and waveguides as well as microresonators of different (high-index) material.

<sup>10</sup>Also this access to the sample is not restricted to the SNOM head and can be used for different purpose.

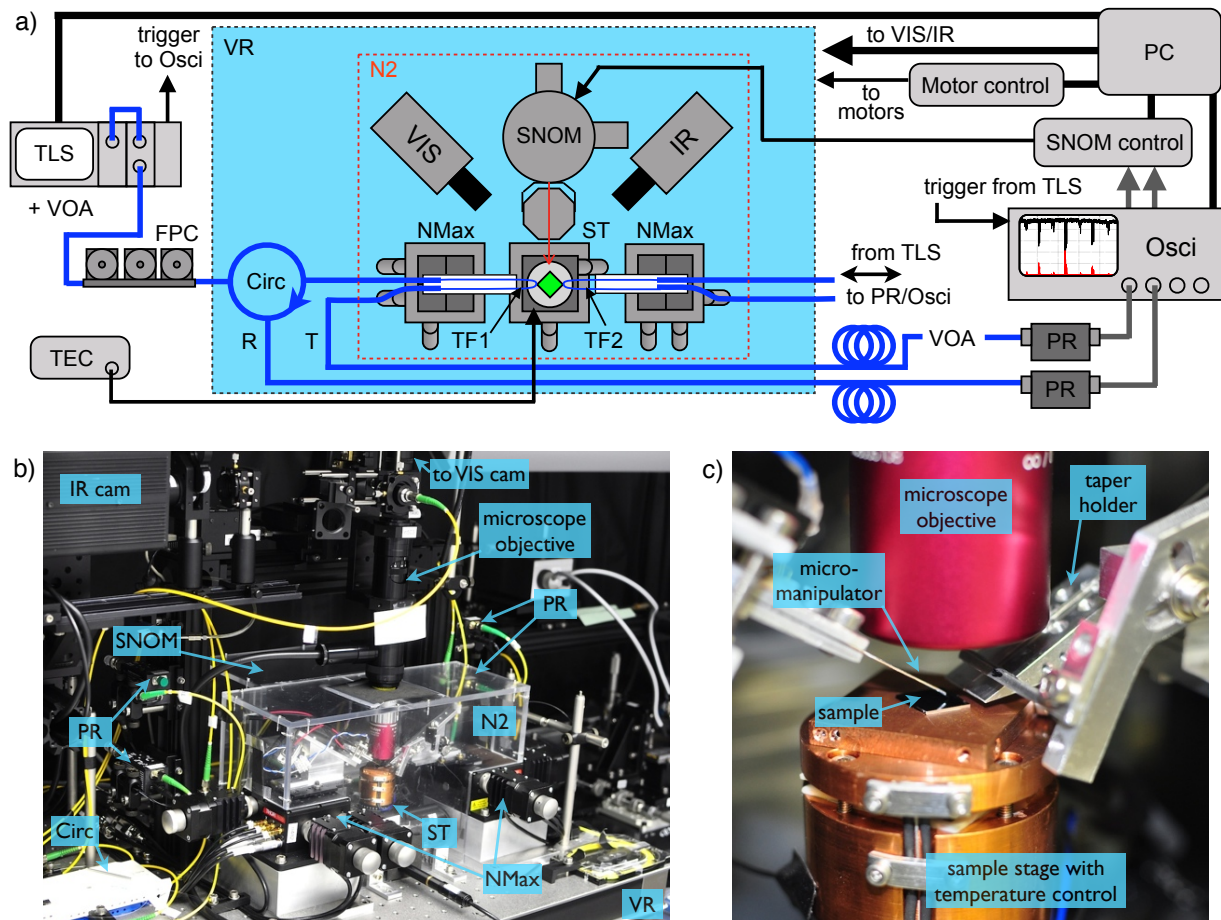


Fig. 3.6: (a) Schematic of the setup (f.l.t.r): TLS - tunable laser source, VOA - variable optical attenuator for pump power control, FPC - fiber polarization controller, TEC - temperature controller for Peltier element under the sample, VR - active vibration isolation, Circ - fiber optic circulator to capture the reflection signal (R), T - transmission signal fiber, N2 - nitrogen purged enclosure, VIS - CCD camera for visible light (observation of alignment), SNOM - scanning near-field optical microscope (red arrow represents SNOM-tip), IR - infrared camera, NMax - 3-axis translation stages with motorized actuators and piezos, ST - sample stage (2 linear translation stages, 1 rotation stage, Peltier element, sample chip in green), TF1/2 - left and right tapered fiber for excitation, VOA - variable optical attenuator to fix working point of photo receiver (PR) for high pump power operation, Osci - Oscilloscope (triggered by TLS), SNOM-control - SNOM controller, Motor control - driver for all motorized actuators, PC - computer for setup control and data capturing. (b) Picture from the lab showing the main parts of the setup. (c) Picture of the sample stage with sample chip, microscope and holder of tapered fiber and micromanipulator.

stages, as well as the SNOM head, are housed in a nitrogen purged box to prevent them from external vibration, air flow and water contamination. The tapered fiber coupling described above allows for an all fiber based setup being beneficial in terms of stability and alignment complexity. For optical excitation of the samples two different fiber coupled tunable laser sources (TLS) are used (81640A and 81980A, Agilent) for high wavelength accuracy and also high power operation of up to 10 mW.<sup>11</sup> The used wavelengths range from 1510 nm to 1580 nm. In combination with two variable optical attenuators (VOA, 81577A Agilent, mVOA-A2 JDSU) power scans as well as fixed working point operation of the detectors are possible. The polarization of the input light is set by fiber polarization controllers. Using a

<sup>11</sup>A few hundreds of  $\mu\text{W}$  are enough to observe thermal nonlinear effects for the investigated samples.

circulator in front of the tapered fiber enables to collect back-reflected light from the resonator. The transmission and reflection signals are detected by InGaAs photoreceivers (TIA-525I, Terahertz Technology) and displayed on an oscilloscope (DSO6104A, Agilent). The whole setup is computer controlled, using the LABVIEW environment (National Instruments<sup>12</sup>) to allow automatic measurements on parameter scans with minimal external perturbation.

Three channels of optical information have been used to characterize the system of coupled microresonators, which are optical spectrum analysis, far-field scattered light and optical near-field characterization. The near-field characterization method is described in detail in Chap. 4 as a main part of this thesis. The far-field scattered light is collected by the IR camera, which was used to obtain information about the intensity distribution across the coupled microdisk sample. The most general information about the sample's optical characteristics are obtained from optical spectrum measurement. For this, the TLS is scanned continuously over a certain wavelength range and triggers the oscilloscope displaying the measured transmission and reflection signal when starting the scan. If the wavelength of the excitation is off-resonant the transmission signal is high (light is not coupled to the resonator). If the excitation is on-resonant light is coupled to a disk mode. The light from the disk, which is  $\pi$  phase-shifted, couples back to the taper and interferes destructively with the light transmitted in the taper. This leads to a transmission signal drop on the oscilloscope. Due to the continuous scan of the excitation wavelength, the mode spectrum can be observed as a time dependent signal on the oscilloscope and with the trigger from the TLS the time axis can be transformed to a wavelength axis, giving the resonance wavelengths of the resonator modes.

## 3.4 General sample characterization

### 3.4.1 Resonance spectrum characteristics

Figure 3.7(a) shows a typical transmission spectrum recorded for both TE and TM polarization for a single microdisk with a diameter  $D_{\text{res}} = 40 \mu\text{m}$ . Due to the different dispersion, the relative distance between the modes for both polarizations changes (as discussed in Sect. 2.1.1). In this particular case the TE mode has a lower (at  $\lambda = 1522 \text{ nm}$ ), almost the same (at  $\lambda = 1535 \text{ nm}$ ) or a larger (at  $\lambda > 1545 \text{ nm}$ ) resonance wavelength than the TM mode. This can be used to unambiguously identify the resonances from the fitting with the analytical EIM or FEM (see Chap. 2) if the thickness is approximately known from SEM images. Keeping the disk radius fixed (design value), the free parameters for the fitting are the disk thickness  $h$  and the material refractive index of the disk  $n_{\text{res}}$ . For the fit in Fig. 3.7(a) the obtained values from the EIM (FEM) are  $h = 911 \text{ nm}$  (915 nm) and  $n_{\text{res}} = 1.451$  (1.453). The obtained thickness is close to the measured value of  $h_{\text{SEM}} = (920 \pm 40) \text{ nm}$  and the refractive index is in

<sup>12</sup><http://www.ni.com/labview/>



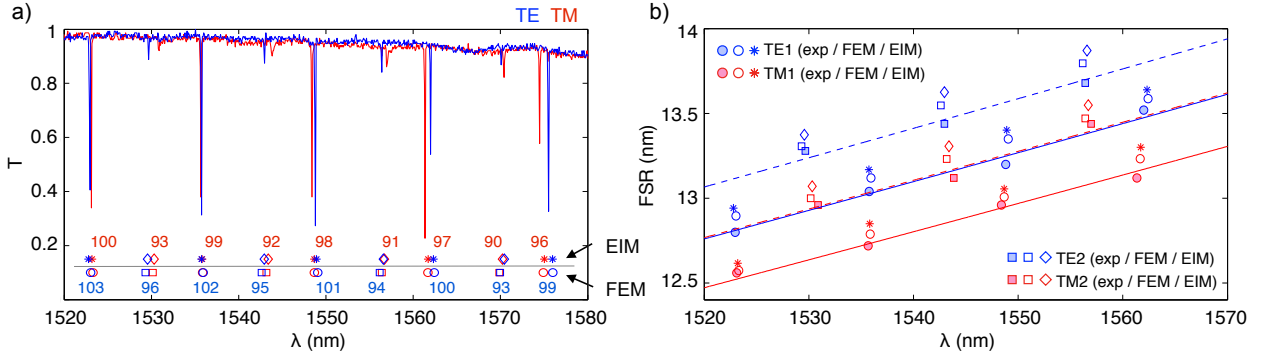


Fig. 3.7: (a) Measured transmission signal shows the resonance spectrum for a single disk with a diameter  $D_{\text{res}} = 40 \mu\text{m}$ . The fitting of the resonance positions using the EIM (FEM) gives the thickness  $h = 911 \text{ nm}$  ( $915 \text{ nm}$ ) and the refractive index  $n_{\text{res}} = 1.451$  ( $1.453$ ). The obtained thickness is in agreement with measurements from SEM images  $h_{\text{SEM}} = (920 \pm 40) \text{ nm}$ . (b) Extracting the FSR from measurements and simulation for first (TE1/TM1) and second radial (TE2/TM2) order modes and using Eq. (3.13) for fitting (shown for experimental data only, solid/dashed line - first/second radial order) gives the group index  $n_g = 1.44 \pm 0.01$  ( $1.47 \pm 0.01$ ) for TE1 (TM1) and  $n_g = 1.41 \pm 0.01$  ( $1.44 \pm 0.01$ ) for TE2 (TM2).

agreement with reported values for fused silica in the investigated spectral range [Mal65]. The correct identification of the measured resonances requires additional knowledge of the sample, e.g., the disk thickness measured from SEM images. If one would use another set of “wrong” parameters with significantly larger thickness than measured by SEM ( $h = 1067 \text{ nm}$ ,  $n_{\text{res}} = 1.443$ ) one could obtain comparable agreement of the measured resonance wavelengths with all azimuthal mode numbers  $m$  increased by one.

The measured dispersion is shown in Fig. 3.7(b) in terms of variation in the FSR ( $\delta\lambda_{\text{FSR}}$ ) for subsequent resonances. According to Ref. [Bor06d],  $\delta\lambda_{\text{FSR}}$  can be related to the group velocity  $v_g$  of a light pulse inside the resonator by

$$v_g = \frac{\partial \omega}{\partial \beta} = -\frac{2\pi c}{\lambda^2} \frac{\partial \lambda}{\partial \beta} = -\frac{2\pi c}{\lambda^2} \frac{\delta \lambda_{\text{FSR}}}{\frac{m+1}{R_{\text{res}}} - \frac{m}{R_{\text{res}}}} = -\frac{2\pi c R_{\text{res}}}{\lambda^2} \delta \lambda_{\text{FSR}}. \quad (3.11)$$

Introducing a group index  $n_g = c/v_g$ , the absolute value of the FSR can be written as

$$\delta \lambda_{\text{FSR}} = \frac{\lambda^2}{2\pi n_g R_{\text{res}}}. \quad (3.12)$$

Equation (3.12) was used for fitting of  $\delta\lambda_{\text{FSR}}$  [Fig. 3.7(c)] obtained from the measured and calculated resonances [Fig. 3.7(a)], which results in group indices for different radial order and polarization of  $n_g = 1.441 \pm 0.007$  ( $n_g = 1.407 \pm 0.011$ ) for TE1 (TE2) and  $n_g = 1.474 \pm 0.006$  ( $n_g = 1.440 \pm 0.013$ ) for TM1 (TM2). To infer the effect of modal and waveguide dispersion, a comparison to the material dispersion of a bulk material can be made. The group index [Mal65] calculated from  $n_{g,\text{bulk}}(\lambda) = n(\lambda) - \lambda(dn/d\lambda)$  giving  $n_{g,\text{bulk}} \approx n_{\text{res}} + 0.02 = 1.47$  for the investigated spectral range. Generally, the TM modes show a smaller FSR and hence a larger  $n_g$  than the TE modes of the same radial order. Higher radial order modes have larger FSR

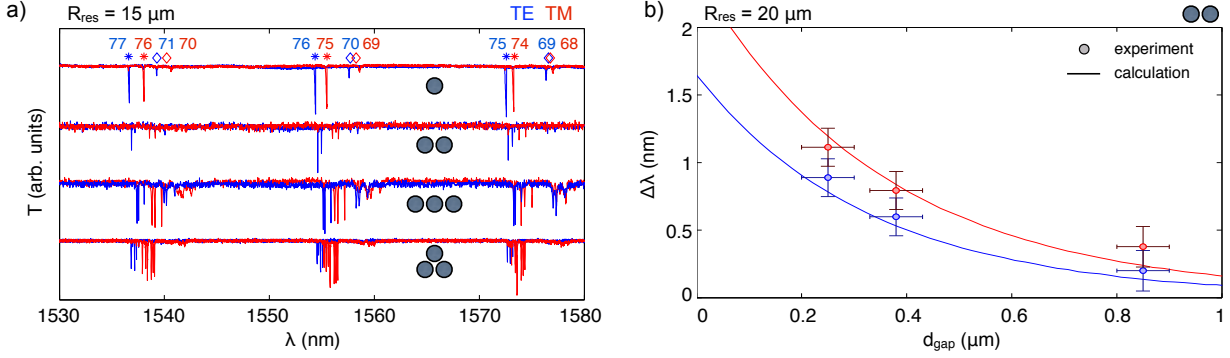


Fig. 3.8: (a) The measured transmission signal for an increasing number of coupled disks ( $R_{\text{res}} = 15 \mu\text{m}$ ) shows spectrally well separated mode families with an increasing number of resonance dips. (b) The measured resonance splitting for samples with a different gap size (dots) agrees with the calculated splitting within the uncertainty of the gap size measurement from SEM images and the radius mismatch of the disks induced by fabrication tolerances.

or smaller  $n_g$ . This also reflects the weaker confinement of the TM modes with the intensity maxima closer to the disk rim as well as the position of the intensity maxima of higher radial orders closer to the center of the disk, as can be seen from calculated mode profiles (Fig. 2.6). The found properties are of importance for the spectral response of microdisks under pulsed excitation spectrally covering multiple modes [Ger04, Dri07, CS1].

Increasing the number of coupled disks results in a splitting of the modes, forming closely spaced mode families as shown in Fig. 3.8(a). The number of modes as well as their relative position differs slightly from the calculations in Sect. 2.2.2, especially for the three disk case. This is due to a resonance mismatch of the single disks in the structure induced by fabrication tolerances. A detailed investigation of the different modes in one mode family can be found in Chap. 4. The dependence of the induced splitting on the gap size between the disks was measured for different samples of two coupled disks and shown in Fig. 3.8(b). Agreement was obtained within the uncertainty of the measured gap size from SEM images and the uncertainty of the disk radius induced by fabrication tolerances [see Fig. 2.9(a)]. An additional detuning of the two disks due to the stronger influence of the tapered fiber on the directly excited disk is significant only for very strong coupling and was avoided in these measurements.

From Fig. 2.9 we know that a mismatch of the coupled disks leads to an increased splitting and different excitation strengths of the resonances, whereas an increased coupling strength (e.g., Fig. 2.10) changes only the splitting as long as the coupling is strong enough. This fact can be used to distinguish both influences and determine the coupling rate  $\Gamma_{12}$  and the resonance mismatch  $\Delta\lambda_{12}$  needed for appropriate calculations with the CMT (see Sect. 2.3). Therefore, a measurement of the resonance spectrum for increasing excitation strength (decreasing taper-disk-gap  $d_{\text{ext}}$ ) was recorded for two coupled disks and compared to CMT calculations in Fig. 3.9. The low input power of the exciting laser (in the following referred to as pump power) was  $P_{\text{pump}} = 100 \mu\text{W}$  to avoid nonlinear effects. The optimal agreement of ex-

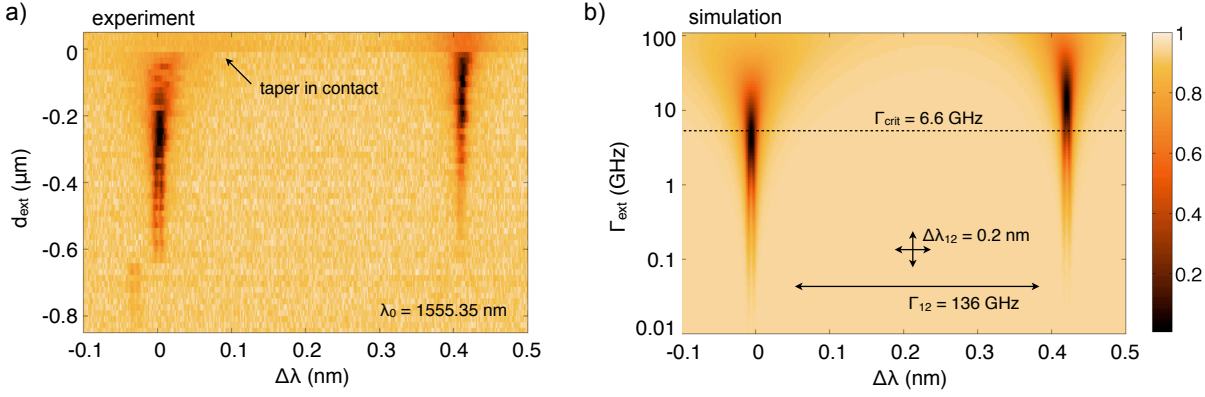


Fig. 3.9: Determination of the resonance mismatch of the two individual disks ( $R_{\text{res}} = 20 \mu\text{m}$ ) in a coupled structure and the coupling strength by (a) measuring the resonance spectrum (TE mode at  $\lambda_0 = 1555.3 \text{ nm}$ ) for decreasing taper-disk-gap  $d_{\text{ext}}$  (negative values indicate open taper-disk-gap) and comparing this to (b) CMT calculations for increasing external coupling rate  $\Gamma_{\text{ext}}$ . The  $\Gamma_{\text{ext}}$ -axis in (b) underlines the exponential dependence of the coupling rate on the distance between taper and disk. The optimal agreement of experiment and simulation gives  $\Delta\lambda_{12} = 0.2 \text{ nm}$  and  $\Gamma_{12} = 136 \text{ GHz}$ . The dashed line in (b) marks the critical coupling point predicted from Eq. (3.6).

periment and simulation gives  $\Delta\lambda_{12} = 0.2 \text{ nm}$  and  $\Gamma_{12} = 136 \text{ GHz}$ . The scale of the  $\Gamma_{\text{ext}}$ -axis in Fig. 3.9(b) underlines the exponential dependence of the coupling rate on the distance between taper and disk. Using the parameters  $\Gamma_0 = 1.6 \text{ GHz}$  and  $\Gamma_{\text{mc}} = 2.9 \text{ GHz}$ , which are obtained independently from Q-factor measurements described in Sect. 3.4.2, one can estimate the critical coupling condition using Eq. (3.6). The obtained value of  $\Gamma_{\text{ext,crit}} = 6.6 \text{ GHz}$  [dashed line in Fig. 3.9(b)] coincides with the zero transmissivity, at least for one of the resonances.

### 3.4.2 Q-factor, optical losses and finesse

The Q-factor of a resonator is generally defined as [Jac99]

$$Q \equiv \omega_0 \frac{U_{\text{stored}}}{P_{\text{loss}}} = 2\pi \frac{U_{\text{stored}}}{U_{\text{loss/cycle}}}, \quad (3.13)$$

with the angular frequency  $\omega_0$ , the stored energy inside the cavity  $U_{\text{stored}}$ , the lost power  $P_{\text{loss}}$  and the energy loss per cycle  $U_{\text{loss/cycle}}$ . Using energy conservation, Eq. (3.13) implies an exponential decay for the time dependence of the energy stored in the resonator

$$U_{\text{stored}}(t) = U_{0,\text{stored}} e^{-\omega_0 t/Q} = U_{0,\text{stored}} e^{-t/\tau_0}, \quad (3.14)$$

where in the last term the decay time  $\tau_0 \equiv Q/\omega_0$  is introduced as the time required for a decay to the  $1/e$ -value of the initial stored energy. Considering the electric field inside the cavity, the time dependence is given by

$$E(t) = E_0 e^{-\omega_0 t/2Q} e^{-i\omega_0 t}, \quad (3.15)$$

and with Fourier transformation the energy distribution in the frequency domain is

$$|E(\omega)|^2 \sim [(\omega - \omega_0)^2 + (\omega_0/2Q)^2]^{-1}, \quad (3.16)$$

with the full width at half maximum (FWHM) bandwidth  $\delta\omega_0 = \omega_0/Q$ . This can be transferred into the wavelength domain to  $\delta\lambda_0 = \lambda_0/Q$ . By definition the Q-factor can be related to the energy loss rate  $\gamma_0 = 2\Gamma_0 = \tau_0^{-1} = \omega_0/Q$ .

The energy dissipation in dielectric microresonators is caused by various processes leading to a total Q-factor

$$1/Q = 1/Q_{\text{int}} + 1/Q_{\text{ext}} = 1/Q_{\text{mat}} + 1/Q_{\text{surf}} + 1/Q_{\text{rad}} + 1/Q_{\text{ext}}, \quad (3.17)$$

which can be separated into intrinsic losses  $1/Q_{\text{int}}$  and external losses  $1/Q_{\text{ext}}$ , e.g., due to the coupling to the tapered fiber for excitation. The intrinsic losses can be divided into different components inversely proportional to the respective Q-factors.  $Q_{\text{rad}}$  takes into account the “quasi-mode” nature of the whispering-gallery resonances due to the incomplete total internal reflection at the curved resonator interface. This leads to energy leakage also for perfect materials and surfaces and depends only on the size of the resonator. The values on the order of  $Q_{\text{rad}} \approx 10^{11}$  calculated in Sect. 2.1.1 for the microdisks under investigation do not limit the observable Q-factors, as expected.  $Q_{\text{mat}}$ , representing the material loss due to absorption and Rayleigh scattering at bulk inhomogeneities, can be found to be on the order of  $Q_{\text{mat}} \approx 10^9$  to  $10^{10}$  [Col93, Ver98b] and hence also is not the limiting factor. Absorption and Rayleigh scattering at surface inhomogeneities, described by  $Q_{\text{surf}}$ , are caused by adsorption of water and contaminations from the etchants as well as roughness of the surface induced by the etching process. For the chemically inert silica the adsorption of water limits the Q-factor on the order of  $10^9$  [Kip04a], whereas the surface roughness will limit the observable Q-factors for the microresonators investigated in this thesis.

To quantify the surface scattering loss, the so-called volume current method [Kuz83] can be used. At the index perturbations  $\delta\epsilon$  on the surface the unperturbed field of the mode  $\mathbf{E}_0$  induces polarization currents  $\mathbf{J} = -i\omega\delta\epsilon\mathbf{E}_0$  acting as source term in the wave equation [e.g., Eq. (2.8)]. A solution to this radiation problem can be given by the vector potential

$$\mathbf{A}_{\text{rad}}(\mathbf{r}) = \frac{\mu_0}{4\pi} \left( \frac{e^{-ikr}}{r} \right) \int_V \mathbf{J}(\mathbf{r}') e^{-ik\hat{\mathbf{r}}\mathbf{r}'} d\mathbf{r}', \quad (3.18)$$

where  $k$  is the wave vector in the surrounding medium and  $\hat{\mathbf{r}}$  is the unit vector in radial direction. The solution of Eq. (3.18) for the case of low-loss microdisks is developed in detail in [Bor06d] using two assumptions briefly summarized here. First, a one-dimensional refractive

index perturbation is assumed

$$\delta\epsilon = \epsilon_0 \delta n^2 h \Delta R(\phi) \delta(r - R) \delta(z), \quad (3.19)$$

where  $\delta n^2 = n_{\text{res}}^2 - n_0^2$  and  $\Delta R(\phi)$  is the radius variation relative to the unperturbed disk radius  $R$  and  $r$ ,  $\phi$ , and  $z$  are polar coordinates centered at the disk. The disk thickness  $h$ , as well as the refractive indices of disk and surrounding medium  $n_{\text{res}}$  and  $n_0$ , are defined in Fig. 2.1. This assumption is valid because the vertically directed anisotropic silica etching results in a nearly invariant disk radius along the disk height compared to the azimuthal variation [see Fig. 3.2(e)]. Together with  $\mathbf{E}_0 = \mathbf{E}_m(r, z) \exp(im\phi)$  (see Sect. 2.1.1) this simplifies the volume integral in Eq. (3.18) to an integral along the azimuthal direction. Secondly, the surface roughness is assumed to be much smaller than the wavelength in the disk. Therefore, surface perturbations can be treated statistically independent if their distance is much larger than a characteristic correlation length  $L_c$ , which allows for a statistical solution of the remaining integral. The total radiated power can be obtained by

$$P_{\text{rad}} = \int (\mathbf{S} \cdot \hat{\mathbf{r}}) r^2 d\Omega, \quad (3.20)$$

with the averaged Poynting vector given by  $\langle \mathbf{S} \rangle = \hat{\mathbf{r}} \omega k_0 \langle |\hat{\mathbf{r}} \times \mathbf{A}_{\text{rad}}|^2 \rangle / (2\mu_0)$  using the ensemble average of Eq. (3.18). With the definition of the Q-factor (3.13) and the stored energy in the ideal resonator  $U_{\text{stored}} = 1/2 \int \epsilon(\mathbf{r}) |\mathbf{E}|^2 d\mathbf{r}$ , the surface scattering Q-factor can be written as

$$Q_{\text{surf}} = \frac{\lambda_0^3}{\pi^{7/2} n_0 (\delta n^2)^2 V_s^2 \sum_{\hat{\eta}} \bar{u}_{\text{surf}}(\hat{\eta}) G(\hat{\eta})}, \quad (3.21)$$

with the effective volume of a scatterer  $V_s = \sqrt{RL_c} h \sigma_R$  determined by the correlation length  $L_c$  and the standard deviation  $\sigma_R$  of the surface roughness. The summation in Eq. (3.21) is carried out over all polarization components of the normalized, spatially averaged electric field energy density at the disk edge  $\bar{u}_{\text{surf}}$ , weighted by a polarization dependent geometrical radiation factor  $G(\hat{\eta})$ . For TM polarization an analytical approximation of  $\bar{u}_{\text{surf}}$  can be given as [Bor06d]

$$\bar{u}_{\text{surf}}(\hat{\mathbf{z}}) \approx \frac{2n_{\text{eff}}^2}{V_d n_{\text{res}}^2 (n_{\text{eff}}^2 - n_0^2)}, \quad (3.22)$$

with the disk volume  $V_d$ . Therefore, Eq. (3.21) can be simplified to

$$Q_{\text{surf}} = \frac{3\lambda_0^3}{8\pi^{7/2}} \frac{n_{\text{res}}^2 (n_{\text{eff}}^2 - n_0^2) V_d}{n_0 n_{\text{eff}}^2 (\delta n^2)^2 V_s^2}. \quad (3.23)$$

$L_c$  and  $\sigma_R$  of the surface roughness can be estimated from SEM images of the microdisk edge like in Fig. 3.2(f). A typical radius variation along the rim of a disk is shown in Fig. 3.10(a). Calculation of the autocorrelation and fitting assuming a gaussian distribution

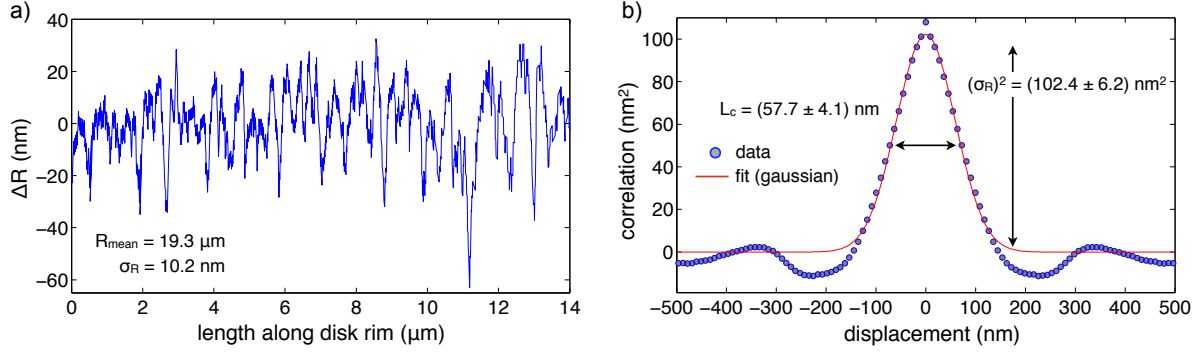


Fig. 3.10: (a) Variation of the disk radius  $\Delta R$  along the rim of the disk extracted from SEM images. (b) Calculation of the autocorrelation and fitting with a gaussian distribution gives the correlation length  $L_c$  and the standard deviation  $\sigma_R$  used for calculation of the effective volume  $V_s$  of a typical scatterer.

leads to  $L_c = (57.7 \pm 4.1)$  nm and  $\sigma_R = (10.1 \pm 0.4)$  nm [Fig. 3.10(b)]. Plugging these values into Eq. (3.23) results in a surface scattering limited Q-factor of  $Q_{\text{surf}} = (1.9 \pm 0.4) \times 10^5$ . Equation (3.23) also shows the potential of Q-factor enhancement by reducing the surface roughness due to the quadratic dependence in the effective volume of the scatterer, e.g., reducing  $\sigma_R$  by a factor of 10 to approximately 1 nm will increase  $Q_{\text{surf}}$  by two orders of magnitude.

In a similar manner the coupling Q-factor between cw and ccw modes due to surface roughness can be estimated to [Bor06d]

$$Q_{\text{mc}} = \frac{1}{\sqrt{2}\pi^{3/4}} \frac{n_{\text{res}}^2 (n_{\text{eff}}^2 - n_0^2) V_d}{n_{\text{eff}}^2 \delta n^2 V_s}, \quad (3.24)$$

resulting in  $Q_{\text{mc}} = (2.6 \pm 0.5) \times 10^4$ , which according to  $Q_{\text{mc}} = \lambda_0 / \Delta\lambda_{\text{mc}}$  leads to a splitting of the resonances of  $\Delta\lambda_{\text{mc}} = (60 \pm 11)$  pm.

Equations (3.14) and (3.16) indicate two possibilities of measuring the quality factor. In the time domain a “ring down”-measurement can be performed if the pump which loads the resonator can be switched off much faster than  $\tau_0$ . Using an electro-optic modulator, switching times of a few ns can be achieved, making this method suitable for microresonators with  $Q \geq 10^7$  [Arm03]. For the microdisks under investigation typical quality factors of  $10^5$  to  $10^6$  are expected, which give decay times below 1 ns. Therefore, a second method estimating the Q-factor from the spectral bandwidth of the measured resonances was used. For reliable measurements it is important to work in the under-coupled regime, where the resonator mode is only very weakly excited. A typical measurement is shown in Fig. 3.11(a). To extract the Q-factor, a simplified coupled mode model taking into account a single disk with coupling of cw ( $-m$ ) and ccw ( $+m$ ) modes [derived from Eqs. (2.70) and (2.71)] was used [Gor00, Bor05]

$$\dot{\bar{d}}_{+m}(\omega) = (i\Delta\omega - \Gamma_0 - \Gamma_{\text{ext}})\bar{d}_{+m} + i\Gamma_{\text{mc}}\bar{d}_{-m} + i\sqrt{2\Gamma_{\text{ext}}}\bar{a}_{\text{in}}, \quad (3.25)$$

$$\dot{\bar{d}}_{-m}(\omega) = (i\Delta\omega - \Gamma_0 - \Gamma_{\text{ext}})\bar{d}_{-m} + i\Gamma_{\text{mc}}\bar{d}_{+m}. \quad (3.26)$$

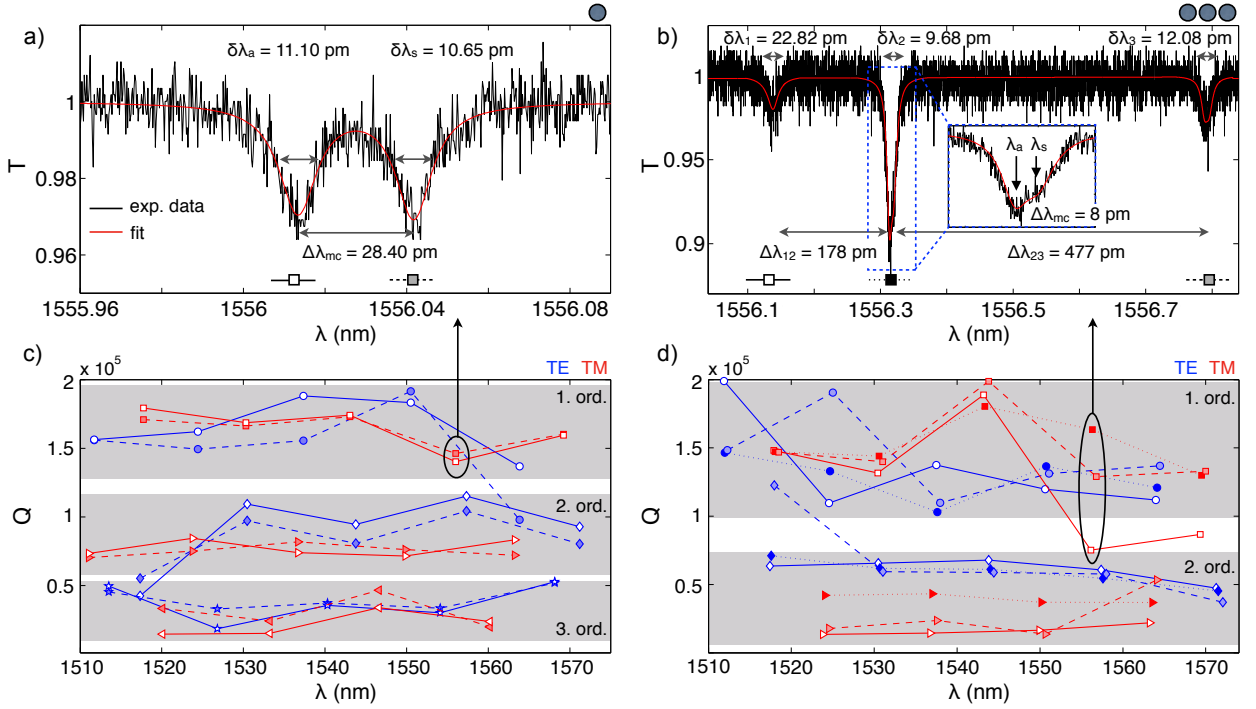


Fig. 3.11: (a) Q-factor characterization for a typical single disk resonance showing a doublet of symmetric ( $\lambda_s$  - light-colored symbols, dashed lines) and antisymmetric ( $\lambda_a$  - white-colored symbols, solid lines) combinations of cw and ccw propagating modes. The red line shows a fit of the resonance using a single disk coupled mode model. (c) The Q-factors for all resonances in the observed spectral range are shown for both polarizations (TE blue, TM red) with the different radial mode orders highlighted by the shaded areas. The notation of symmetric and antisymmetric modes is the same as in (a) with the color according to the polarization. Analogue data for three coupled disks in a line are shown in (b, d) with the splitting in three resonances due to the coupling of the disks ( $\lambda_1$  - white-colored symbols, solid lines;  $\lambda_2$  - dark-colored symbols, dotted lines;  $\lambda_3$  - light-colored symbols, dashed lines). Each of the dips was fitted individually with the same model as in (a) - see inset in (b) - but for the graph in (d) the mean of the Q-factors of  $\lambda_a$  and  $\lambda_s$  was used. Only minor decrease of the Q-factor is observed when coupling the disks to each other.

Changing the basis to symmetric (s) and antisymmetric (a) combinations of  $\bar{d}_{+m}$  and  $\bar{d}_{-m}$ , according to  $\bar{d}_{s,a} = (\bar{d}_{+m} \pm \bar{d}_{-m})/\sqrt{2}$ , decouples Eqs. (3.25) and (3.26) and leads to the solution

$$\bar{d}_{s,a}(\omega) = \frac{-i\sqrt{\Gamma_{\text{ext}}}\bar{a}_{\text{in}}}{i(\Delta\omega \pm \Gamma_{\text{mc}}) - (\Gamma_{0s,0a} + \Gamma_{\text{ext}})}, \quad (3.27)$$

which is generalized to allow different loss rates for the symmetric and antisymmetric modes due to their relative phase difference and hence different overlap with surface inhomogeneities. The transmissivity of the tapered fiber can then be written as

$$\mathcal{T}(\omega) = \left| 1 + \frac{-i\sqrt{\Gamma_{\text{ext}}}(\bar{d}_s(\omega) + \bar{d}_a(\omega))}{\bar{a}_{\text{in}}} \right|^2, \quad (3.28)$$

and was used to fit the measured resonances [red lines in Fig. 3.11(a,b)]. From this fit the FWHM bandwidth of the symmetric and antisymmetric mode can be obtained as well as the coupling ratio between them. Figure 3.11(c) shows the obtained Q-factors for all measured

resonances in the wavelength range of 1510 nm to 1570 nm for both polarizations (TE blue, TM red). The different radial orders show different Q-factors highlighted by the shaded areas. As expected the highest Q-factors around  $Q = 1.7 \times 10^5$  are observed for first radial order modes. For the second radial order  $Q = 0.9 \times 10^5$  and for the third radial order  $Q = 0.3 \times 10^5$  were found. The measured values for the first order modes agree very well with the limit of the surface scattering Q-factor estimated above [Eq. (3.23)]. Although it is expected that TM polarized modes (main field component  $E_z$ ) are less affected by the particular structure of the vertical sidewall imperfections than the TE modes, the investigated sample here shows no significant difference in the Q-factor for both polarizations. This might be due to non-perfectly smooth top and bottom disk surfaces affecting mainly the TM modes and reducing their Q-factor. Spot-checking another chip of samples (used in Chap. 5) shows indeed higher Q-factors for the TM polarized modes of up to  $Q = 4.5 \times 10^5$  in comparison to  $Q = 2.5 \times 10^5$  for TE modes. Looking at the difference between symmetric [white-colored symbols, solid lines in Fig. 3.11(c)] and antisymmetric modes [light-colored symbols, dashed lines in Fig. 3.11(c)] a slightly larger Q-factor for the antisymmetric mode can be observed for most of the measured resonances, especially for first and second radial order. This can be understood by the fact that the field of the antisymmetric mode is distributed to minimize the overlap with the refractive index perturbations along the surface. Consequently, the field of the symmetric mode maximizes the overlap [Bor06d, Zhu09]. A coupling induced splitting of the resonances of  $\Delta\lambda_{\text{mc}} \approx 30$  pm was measured, which is on the order of magnitude of the theoretical approximation using Eq. (3.24).

Coupling of three disks in a line arrangement leads to a splitting into three resonances shown in Fig. 3.11(b) with the coupling induced splitting ( $\Delta\lambda_{12} = 178$  pm,  $\Delta\lambda_{23} = 477$  pm) much larger than due to the backscattering into the counterpropagating mode ( $\Delta\lambda_{\text{mc}} = 8$  pm). Therefore, each of the resonances can be fitted individually using Eq. (3.28) [see inset in Fig. 3.11(b)]. As the difference of the symmetric and antisymmetric Q-factor of each resonance is small, the mean value was plotted in Fig. 3.11(d), where the white-colored symbols with solid lines denote the short wavelength resonance, the light-colored symbols with dashed lines belong to the long wavelength resonance and the dark-colored with dotted line symbols mark the central resonance. In comparison to the single disk case the Q-factors of the first order radial modes tend to be slightly decreased. A stronger variance can be observed, which is indicated by the extended shaded area in Fig. 3.11(d). It is possible to find resonances with equal or even slightly larger Q than for the single disk. For the second order radial modes the Q-factor significantly reduces by approximately a factor of two which is due to the weaker confinement of the fields and hence a stronger perturbation of the modes due to the coupling of the disks (see Sect. 2.1.2). Also a difference between TE and TM polarized modes can be observed in this case due to the generally weaker confinement for the TM modes.

The observed Q-factors and resonance splittings for single and coupled microdisks correspond to intrinsic loss rates of  $\Gamma_0 \approx 1.5$  GHz to 4.3 GHz and intra-disk modal coupling rates



of  $\Gamma_{\text{mc}} \approx 2.5 \text{ GHz}$  to  $10 \text{ GHz}$ .

With the Q-factor and the FSR at hand, the finesse of the resonant system can be calculated by [Sal91]

$$\mathcal{F} \equiv \frac{\delta\omega_{\text{FSR}}}{\delta\omega_0} \equiv \frac{\delta\lambda_{\text{FSR}}}{\delta\lambda_0} = \frac{Q}{m} = \frac{2\pi\tau_0}{\tau_{\text{rt}}}. \quad (3.29)$$

The first two relations are the definitions of the finesse as the ratio of FSR and resonance bandwidth. In the last relation  $\tau_{\text{rt}}$  is the round trip time of a photon in the resonator. As the Q-factor is a measure of how many times the field oscillates until it is decayed, the finesse can be seen as the number of round trips of a photon before it is lost. Using the obtained values from above, a finesse of about  $\mathcal{F} \approx 2 \times 10^3$  can be found for the investigated microdisks. With the results from Sect 2.3.1 the above relations can be used to estimate the circulating optical power inside the disk

$$P_{\text{circ}} = \frac{|\bar{d}_m|^2}{\tau_{\text{rt}}} = \frac{2}{\pi} \frac{\Gamma_{\text{ext}}(\Gamma_0 + \Gamma_{\text{ext}})}{(\Gamma_0 + \Gamma_{\text{ext}})^2 + \Delta\omega^2} \mathcal{F} P_{\text{pump}}. \quad (3.30)$$

On resonance and for critical coupling this relation reduces to  $P_{\text{circ}} = (\mathcal{F}/\pi)P_{\text{pump}}$  for a given coupled pump power  $P_{\text{pump}}$ . According to the used pump powers of  $0.1 \text{ mW}$  to  $4 \text{ mW}$  circulating powers of  $60 \text{ mW}$  to  $2.4 \text{ W}$  can be achieved. These values might be reduced by up to a factor of two, if the modal coupling between cw and ccw modes becomes significant [Kip02].

## Chapter summary

This chapter provided the framework needed for a detailed experimental investigation of coupled disk microresonators. Two possible fabrication processes were described that give similar high quality coupled microdisk samples. Nevertheless, for larger two-dimensional arrays it turned out that the wet-chemical KOH process is preferable. The fabrication of tapered optical fibers with the required diameter for efficient coupling and phase matching to the modes of the microresonators was realized according to a theoretical analysis. Furthermore, the utilized experimental setup was described and a general characterization of the coupled microdisk samples was presented. The obtained spectral characteristics are in agreement with theoretical predictions using the models described in Sects. 2.1 and 2.2. A theoretical analysis of the Q-factor taking into account the sidewall roughness of the fabricated samples shows good agreement with the measured Q-factors. As a main result, the advantageous properties of single microresonators do not change dramatically when they are coupled to each other. Additionally, the performed experiments can be used to obtain the characteristic loss and coupling rates of the investigated samples. These coefficients are necessary for the application of the CMT in the following chapters.

## 4 Mapping of eigenstates in coupled microdisks<sup>1</sup>

The spectrum analysis of microresonators described in Sect. 3.4 is a standard method to obtain information about their performance and characteristics. Bandwidths, coupling efficiencies, circulating powers, etc. can be obtained, and with the help of theoretical models the distribution of light in such systems can be calculated. Nevertheless, there is a lack of experimental evidence about the light distribution in coupled microresonators.<sup>2</sup> For coupled microdisks such information can be obtained in the far-field by collecting the out-of-plane scattered light [CS5]. These measurements show a difference of the light intensity distribution for different excited resonances but usually with a very low spatial resolution. This limited resolution and the incoherence of the scattering process neither provides insight into the difference of the intensity distribution of excited modes of different radial and azimuthal mode order, nor resolves the different mode symmetry. An increase of the spatial resolution can be achieved by using erbium doped microresonators [Car08], which allow to observe scattered signals in the visible<sup>3</sup> due to a three photon up-conversion process in the investigated spectral range. Nevertheless, no near-field information on different mode symmetries can be obtained. To address these issues a high resolution scanning near-field optical microscopy (SNOM) method [Hec00] was implemented. SNOM measurements of the WGM in single microdisks were already done by direct collection of the near-field through an aperture tip [Bal99] and by collecting the scattered light from the SNOM tip placed in the near-field of the WGM [Bla10]. The latter method succeeds in resolving the difference of the distribution of symmetric and antisymmetric modes formed due to scattering at surface imperfections (see Sect. 3.4.2).<sup>4</sup>

Here we follow a different approach that also makes use of a sharp scattering SNOM tip, but instead of measuring a very weak scattering signal from the tip, the change of the spectral response of the taper-disk-system in the presence of the SNOM tip was recorded [CS2]. Due to the significant amount of evanescent field outside of the resonator and the high Q-factor,

---

<sup>1</sup>The main results of this chapter can be found in Ref. [CS2].

<sup>2</sup>For coupled microspheres doped with semiconductor nanocrystals, far-field scattering measurements of the intensity distribution were described in Refs. [Möl06, Möl07].

<sup>3</sup>The advantages are the higher resolution due to the decreased wavelength, the suppression of speckles due to the incoherence of the up-conversion process as well as the possible use of standard high resolution CCD cameras for the visible instead of very expensive low resolution InGaAs-CCD cameras for the infrared.

<sup>4</sup>The scattering SNOM technique was also successfully used for WGM mappings in single microspheres [Göt01].

the spectral response depends strongly on changes of the surrounding. This results in a higher signal-to-noise ratio at the same spatial resolution as compared to the far-field scattering SNOM method [Bla10]. The measurement principle is adapted from waveguide mode mapping [Rob06] as well as from investigations of eigenmodes in photonic crystal cavities [Hop06].

In the following, the method is described in detail and is compared to a theoretical analysis based on the combination of CMT and analytical field calculations of microdisks (Sects. 2.3 and 2.2.3). The method was then used to measure the intensity distributions of modes in two and three coupled microdisks.

## 4.1 Mode mapping method

The mode mapping principle makes use of a gold coated fiber tip (SNOM tip) with a tip radius between 50 nm and 100 nm, which is scanned above the microdisk sample [Fig. 4.1(a)]. When the pump laser wavelength is fixed to one of the resonances a certain transmissivity and reflectivity at both tapered fiber ends is measured. Placed in the near field of the excited mode, the polarizability of the tip changes the effective refractive index of the environment, which has two effects on the system. First, this influences the resonance condition and leads to a shift of the resonance wavelength. Second, the tip acts as a scatterer coupling photons of the excited WGM to either radiative modes or to other WGMs that spectrally and spatially overlap with the excited WGM. The only WGM that matches the latter conditions for the microresonators under investigation is the mode counterpropagating to the excited WGM. This contributes to the splitting of the resonances due to coupling of cw and ccw modes induced by surface roughness (Sect. 3.4.2). The scattering of photons into radiative modes is an additional loss channel that leads to spectral broadening of the resonances. Therefore, both effects have influences on the measured transmission and reflection signals depending on the strength of the interaction of the WGM with the SNOM tip. The signal changes can be correlated to the position of the tip, resulting in an intensity map of the mode, because the interaction strength depends on the field intensity at the position of the tip.

An intensity map obtained for a scan of the SNOM tip across the gap of two coupled disks is shown in Fig. 4.1(b). From the overlay with the topography the two flat disk surfaces as well as the gap between them can be clearly identified. The strongest signals are recorded when the tip is placed in the vicinity of the rim of the disks, indicating the excitation of a first order radial mode. For more details the transmissivity (T) and reflectivity (R) mode maps are plotted separately in Fig. 4.1(b) to point out the characteristics and limitations of the method. Generally, the signal contrast in reflection is better than in transmission. Both signals remain unperturbed when the tip is positioned above the disk but outside of the near field of the mode or above the substrate. In contrast, a signal modulation can be observed when the tip is perturbing the near field of the mode. This modulation involves smaller and

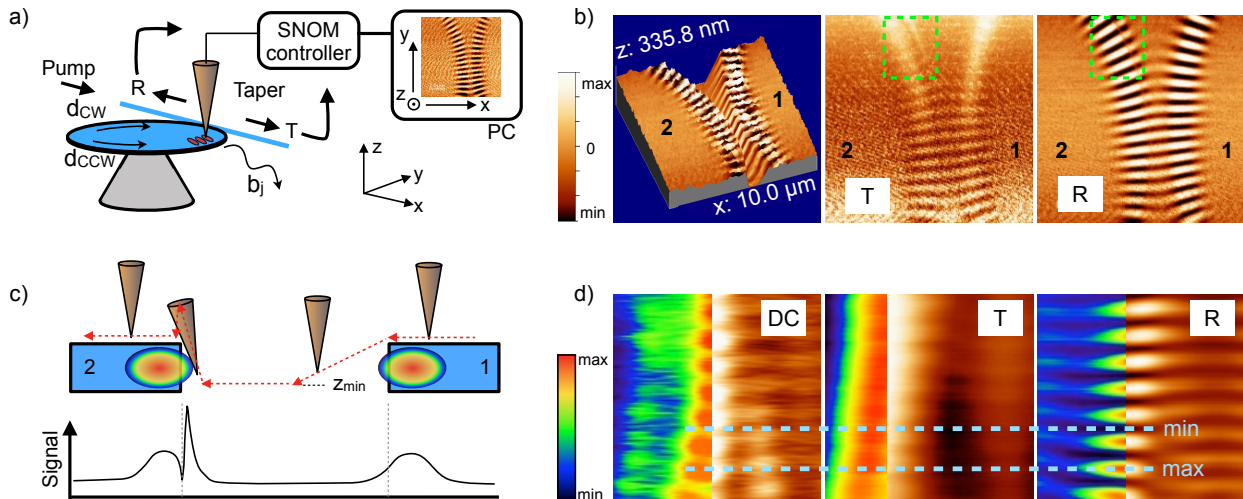


Fig. 4.1: (a) Microdisk mode mapping principle. The presence of the SNOM tip in the near-field of the WGM leads to additional coupling between cw and ccw modes as well as coupling to reservoir modes  $b_j$  resulting in additional losses. The mode maps are obtained as variations of the reflection and transmission signal through the tapered fiber depending on the position of the SNOM tip. (b) Typical mode map signals for two coupled disks (numbered as 1 and 2) showing topography information as well. The reflection signal (R) shows better contrast than the transmission signal (T). The green dashed rectangles highlight measurement artifacts explained by the characteristics of the SNOM tip movement in (c). Scanning from disk 1 the tip drops smoothly down to the lowest  $z$  position. When approaching disk 2 the tip first retracts not fast enough and touches the disk rim, and then overshoots which leads to the disturbed signals. (d) A comparison to the direct collection (DC) of the optical near-field with an aperture SNOM tip shows that the maximum signal measured in the reflection mode maps is related to a maximum in the near-field intensity, and hence an antinode of the standing wave pattern, whereas the minimum corresponds to a node.

larger signal levels compared to the background, which is surprising because the method is sensitive to the mode intensity only. When the tip is placed at an intensity node of the mode distribution, it should not have any influence on the measured transmission and reflection signals. To exclude systematic measurement errors, a comparison of the method to the direct collection of the near field of the mode was done with an aperture SNOM tip and the results are shown in Fig. 4.1(d). The diameter of the aperture SNOM tip is significantly larger than that of the scattering SNOM tip. Nevertheless, it can also be used to measure transmissivity and reflectivity mode maps in parallel, although with a lower resolution. As expected, the optical collection signal is always larger than the background even when the tip is in a node of the disk mode. Because of the larger tip size, the transmission signal gets blurred out and the mode structure in the azimuthal direction can hardly be resolved. The reflection signal is almost the same as for the scattering SNOM tip, underlining the high sensitivity of the method. In comparison to the direct collection, the reflection signal shows a stronger (weaker) signal than the background for the tip in an antinode (node) of the disk mode.

The free standing disk geometry in combination with the used tapping mode of the SNOM<sup>5</sup> leads to artifacts in the measured mode maps, which appear as a stripe of unperturbed signal

<sup>5</sup>The tip oscillates vertically above the sample to get feedback from the sample about the topography as the oscillation frequency shifts due to the interaction with the surface.

at the rim of disk 2 marked in Fig. 4.1(b). This is a result of the particular movement of the SNOM tip across the sample and is illustrated in Fig. 4.1(c). Usually, the starting point of a scan is chosen above a disk (here disk 1), and the fast scan axis is almost normal to the rim of the disk or gap between two disks. When the tip senses the rim of the disk, it starts to drop down smoothly toward the substrate. If the gap size is sufficiently large, the tip reaches its minimum vertical position a few hundred nm below the disk surface. When the tip recognizes the other disk, it retracts much faster (indicated by the steeper transition) and the tip touches the sidewall of the disk.<sup>6</sup> This leads to a very strong interaction and hence a strong signal. Due to the fast retraction, the tip overshoots when reaching the top surface level of the disk, leading to a weaker interaction and signal. The effect is more pronounced when the separation between the disks becomes larger because of the delayed response of the vertical movement of the tip when it rests at the minimum  $z$  level. No significant influence on the measured data is observed in the region where the disks are closest to each other.

The interaction of a SNOM tip with the WGMs of microdisk resonators as well as the signal collection through a tapered fiber have strong impact on the measured signals. However, we are only interested in the mode distribution of the coupled microdisks and not in the response of the whole system. A link from the measured signals to the intensity distribution of the modes in the coupled microdisks becomes possible when combining the calculations of the intensity distribution (Sect. 2.2.3) and the CMT (Sect. 2.3) by taking into account the scattering SNOM tip.

## 4.2 Coupled mode theory including the scattering SNOM tip

The CMT from Sect. 2.3.3 describes the experimental situation of an array of microdisks coupled to a tapered fiber for excitation. It includes scattering losses and coupling processes between modes accounted for by appropriate coefficients. In order to take into account the interaction with a SNOM tip, its two main effects on the system need to be analyzed, which are the additional coupling of modes and additional scattering losses. This can be done using dipole approximation [Jac99] by modeling the tip as a single subwavelength Rayleigh scatterer. The electric field of the resonator mode induces a dipole moment  $\mathbf{p} = \epsilon_0 \alpha \mathbf{E}_{\text{mode}}$  in the scatterer, which is approximated as a spherical particle of radius  $R_{\text{tip}}$  and effective relative permittivity  $\epsilon_{\text{tip}}$ . With the relative permittivity of the surrounding medium  $\epsilon_{\text{med}}$  the polarizability  $\alpha$  of the scatterer can be written as

$$\alpha = 4\pi R_{\text{tip}}^3 \frac{\epsilon_{\text{tip}} - \epsilon_{\text{med}}}{\epsilon_{\text{tip}} + 2\epsilon_{\text{med}}}. \quad (4.1)$$

<sup>6</sup>As illustrated in Fig. 4.1(c) at this position the sidewall of the tip recognizes the disk first, which leads to a strong feedback on the tip movement.

In Ref. [Maz07a] a semi-quantum optical description of the coherent coupling of cw and ccw propagating WGMs ( $d_{+m}$ ,  $d_{-m}$ ) and resonator losses due to such a dipole interaction is presented.<sup>7</sup> The description of the resonator losses is based on the interaction of cw and ccw WGMs with a reservoir of harmonic oscillators [Kli99, Dun01]. Under the assumptions of elastic scattering, negligible cross-polarization coupling and a point-like scatterer, the coupling of cw to ccw modes and vice versa due to the scatterer can be expressed by a single coupling coefficient [Maz07a]

$$g = -\frac{\alpha[f(\mathbf{r}_{\text{tip}})]^2\omega_0}{2V_{\text{mode}}}. \quad (4.2)$$

Here  $\omega_0$  denotes the resonance frequency,  $V_{\text{mode}}$  is the mode volume of the resonator mode and  $f(\mathbf{r}_{\text{tip}})$  describes the normalized field strength  $f$  of the microdisk mode at the position of the SNOM tip  $\mathbf{r}_{\text{tip}}$ . Equation (4.2) exhibits the connection between the CMT (Sect. 2.3) and the field calculations in Sect. 2.2.3. In the same way the coupling of cw and ccw WGMs to reservoir modes  $b_j$  can be described by a single coefficient [Maz07a]

$$g' = -\frac{\alpha[f(\mathbf{r}_{\text{tip}})]^2\omega_0}{2\sqrt{V_{\text{mode}}V_j}}(\hat{\mathbf{n}}_{\text{mode}} \cdot \hat{\mathbf{n}}_j), \quad (4.3)$$

with the quantization volume of the reservoir mode  $V_j$  and the respective field unit vectors  $\hat{\mathbf{n}}_{\text{mode},j}$ . While the scattering of a photon into a disk mode leads to an additional splitting of the observable resonances, the coupling to the reservoir modes act as an additional loss channel. Using a Weisskopf-Wigner approximation [Maz07b], the explicit coupling to the reservoir modes can be eliminated by the derivation of a damping rate

$$\gamma_{\text{rs}} = \frac{\alpha^2 f^2(\mathbf{r}_{\text{tip}})\omega_0^4}{6\pi c^3 V_{\text{mode}}}. \quad (4.4)$$

Here  $c$  is the speed of light in vacuum. With  $g$  from Eq. (4.2) and  $\Gamma_{\text{rs}} = \gamma_{\text{rs}}/2$ , the coupled equations for the slowly varying mode amplitudes [Eqs. (2.78) and (2.79)] can be modified to

$$\dot{\bar{d}}_{+m}^{(p)} = \left[ i(-\Delta\omega^{(p)} + g^{(p)}) - \Gamma^{(p)} \right] \bar{d}_{+m}^{(p)} + \left[ i(\Gamma_{\text{mc}} + g^{(p)}) - \Gamma_{\text{rs}}^{(p)} \right] \bar{d}_{-m}^{(p)} + \Gamma_{-m}^{(pq)} + A_{+m}^{(p)}, \quad (4.5)$$

$$\dot{\bar{d}}_{-m}^{(p)} = \left[ i(-\Delta\omega^{(p)} + g^{(p)}) - \Gamma^{(p)} \right] \bar{d}_{-m}^{(p)} + \left[ i(\Gamma_{\text{mc}} + g^{(p)}) - \Gamma_{\text{rs}}^{(p)} \right] \bar{d}_{+m}^{(p)} + \Gamma_{+m}^{(pq)} + A_{-m}^{(p)}, \quad (4.6)$$

with the total loss rate of the  $p$ th disk  $\Gamma^{(p)} = \Gamma_{\text{rs}}^{(p)} + \Gamma_0^{(p)} + \Gamma_{\text{ext}}^{(p)}$ , the frequency detuning  $\Delta\omega^{(p)} = \omega - \omega_0^{(p)}$ , the coupling to other disks  $\Gamma_{+m,-m}^{(pq)} = i \sum_{q=1, q \neq p}^N \Gamma_{pq} \bar{d}_{+m,-m}^{(q)}$ , and the external coupling term to each mode  $A_{+m,-m}^{(p)} = i\sqrt{2\Gamma_{\text{ext}}^{(p)}} \bar{a}_{+m,-m}^{\text{in}}$ . The CMT for coupled ensembles of microdisks deals with the mode amplitudes in each of the resonators. The interaction of the SNOM tip with the field also needs to be treated locally, depending on the location of the tip. This has to be taken into account in Eqs. (4.2) and (4.4) with the field distribution depending

<sup>7</sup>See Fig. 4.1(a) for a sketch of the system under consideration. A comparable analysis of the SNOM tip induced resonance shift of a photonic crystal cavity can be found in Refs. [Koe05, Lal07].

on the disk number  $f^{(p)}(\mathbf{r}_{\text{tip}})$ . For simplicity it is further assumed that the SNOM tip when located in the gap region couples only to the modes of one disk, whereas in reality it can couple to the modes of both disks forming the gap. The solution of Eqs. (4.5) and (4.6) follows the way described in Sect. 2.3, leading formally to the same transmissivity and reflectivity of the tapered fiber coupled to the  $p$ th disk

$$\mathcal{T} = \left| 1 + \frac{i\sqrt{2\Gamma_{\text{ext}}^{(p)}}\bar{d}_{+m}^{(p)}}{\bar{a}_{+m}^{\text{in}}} \right|^2, \quad (4.7)$$

$$\mathcal{R} = \left| \frac{i\sqrt{2\Gamma_{\text{ext}}^{(p)}}\bar{d}_{-m}^{(p)}}{\bar{a}_{+m}^{\text{in}}} \right|^2. \quad (4.8)$$

Using the model in Sect. 2.2.1 to calculate the two-dimensional intensity distribution of the excited mode, Eqs. (4.2) and (4.4) give corresponding distributions of the tip-induced scattering strength, which results in theoretical predictions of transmissivity and reflectivity mode maps [Eqs. (4.7) and (4.8)]. All unknown coefficients in Eqs. (4.5) and (4.6) can be obtained by independent measurements without SNOM tip perturbation.

### 4.3 Experimental verification for a single microdisk

To test the theoretical model and its ability to describe the experimental data, a single disk as the simplest case was considered. With this restriction, the steady state solutions of Eqs. (4.5) and (4.6) can be given explicitly by

$$\bar{d}_{+m} = \frac{-i\sqrt{2\Gamma_{\text{ext}}}\bar{a}_{+m}^{\text{in}} [i(-\Delta\omega + g) - (\Gamma_{\text{rs}} + \Gamma_0 + \Gamma_{\text{ext}})]}{[i(-\Delta\omega + g) - (\Gamma_{\text{rs}} + \Gamma_0 + \Gamma_{\text{ext}})]^2 - [i(\Gamma_{\text{mc}} + g) - \Gamma_{\text{rs}}]^2}, \quad (4.9)$$

$$\bar{d}_{-m} = \frac{i\sqrt{2\Gamma_{\text{ext}}}\bar{a}_{+m}^{\text{in}} [i(\Gamma_{\text{mc}} + g) - \Gamma_{\text{rs}}]}{[i(-\Delta\omega + g) - (\Gamma_{\text{rs}} + \Gamma_0 + \Gamma_{\text{ext}})]^2 - [i(\Gamma_{\text{mc}} + g) - \Gamma_{\text{rs}}]^2}. \quad (4.10)$$

This results in the transmissivity and reflectivity

$$\mathcal{T} = \left| 1 + \frac{2\Gamma_{\text{ext}} [i(-\Delta\omega + g) - (\Gamma_{\text{rs}} + \Gamma_0 + \Gamma_{\text{ext}})]}{[i(-\Delta\omega + g) - (\Gamma_{\text{rs}} + \Gamma_0 + \Gamma_{\text{ext}})]^2 - [i(\Gamma_{\text{mc}} + g) - \Gamma_{\text{rs}}]^2} \right|^2, \quad (4.11)$$

$$\mathcal{R} = \left| \frac{-2\Gamma_{\text{ext}} [i(\Gamma_{\text{mc}} + g) - \Gamma_{\text{rs}}]}{[i(-\Delta\omega + g) - (\Gamma_{\text{rs}} + \Gamma_0 + \Gamma_{\text{ext}})]^2 - [i(\Gamma_{\text{mc}} + g) - \Gamma_{\text{rs}}]^2} \right|^2. \quad (4.12)$$

The unknown parameters  $\Gamma_0$ ,  $\Gamma_{\text{mc}}$  and  $\omega_0$  were obtained from an independent spectrum measurement of the weakly excited disk when the tip was absent and by using the theoretical model without SNOM tip perturbation for fitting. For the measured microdisk a TM polarized first order radial mode was chosen, resulting in the values  $\Gamma_0 = 1.55$  GHz,  $\Gamma_{\text{mc}} =$

2.89 GHz and  $\lambda_0 = 2\pi c/\omega_0 = 1556.055$  nm. For the perturbed system, the unknown parameters  $g$ ,  $\Gamma_{rs}$  and  $\Gamma_{ext}$  can be approximated. The coupling coefficient  $g$  and the scattering rate  $\Gamma_{rs}$  depend on the polarizability of the SNOM tip and the mode volume. From FEM simulations (see Sect. 2.1.2) a mode volume of  $V_{mode} = 6.7 \times 10^{-17}$  m<sup>3</sup> and the normalization of the field strength at the tip position of about 10 nm above the disk of  $f_{norm}(x, y) = 0.52f(x, y, z)$  can be estimated. Although, the height of the tip above the disk might change or is not exactly known, this value was kept fixed. The polarizability  $\alpha$  depends on the radius of the tip (approximated as a sphere) and its effective relative permittivity. For the gold coated SNOM tip  $\epsilon_{tip} = -131.718 + i12.639$  [Pal91] was used. The radius was allowed to vary in the range of  $R_{tip} = 10$  nm to 150 nm due to possible degradation during the large number of measurements. The external coupling rate  $\Gamma_{ext}$  was chosen in the range of 1 GHz to 10 GHz. Although  $\Gamma_{ext}$  is set at the beginning of each mapping, fluctuations of the tapered fiber position during the measurement can change this value. Due to the stepwise wavelength scan and the accompanying adjustments of the whole setup, it was unlikely to obtain exactly the same coupling conditions for each of the mode mappings. Within the given parameter ranges, the calculations are compared to the measured data.

In Fig. 4.2(a) the transmission signal of the resonance under investigation is shown. The taper is slightly overcoupled and the splitting is hidden by the loaded bandwidth of the symmetric and antisymmetric mode. A mode map was recorded at each wavelength marked with the red lines. The mode maps were taken close to the rim to measure the first order radial mode, but with the tip not scanning across the rim to avoid vertical tip movements and the above mentioned artifacts. The scan window has a size of  $1.5 \times 1.5 \mu\text{m}^2$  and the 11 transmissivity and reflectivity mode maps are arranged successively in Figs. 4.2(c) and 4.2(e). The intensity distributions for the respective wavelengths are calculated for the same section of the disk and arranged in the same way in Fig. 4.2(b). The corresponding calculated transmissivity and reflectivity mode maps are shown in Figs. 4.2(d) and 4.2(f), respectively. Several characteristic features can be identified when comparing measurements and simulations:

- The first, most obvious characteristic is the expected phase shift, which the intensity distribution undergoes when scanning the excitation wavelength through the resonance. This shift can be seen in any of the picture series in Figs. 4.2(b)-(f) and is tracked by the dotted lines.
- Unlike the intensity, which shows only positive values, the calculated transmissivity and reflectivity maps show both positive and negative values, which is in agreement with the measured data. As also mentioned above, the transmission signal shows less contrast than the reflection signal.
- The calculated intensity maximum (corresponding to the minimum of the taper transmission spectrum) in frame 5, Fig. 4.2(b) does not coincide with the strongest signal either in the transmissivity or reflectivity mode maps. Also the absolute maximum sig-



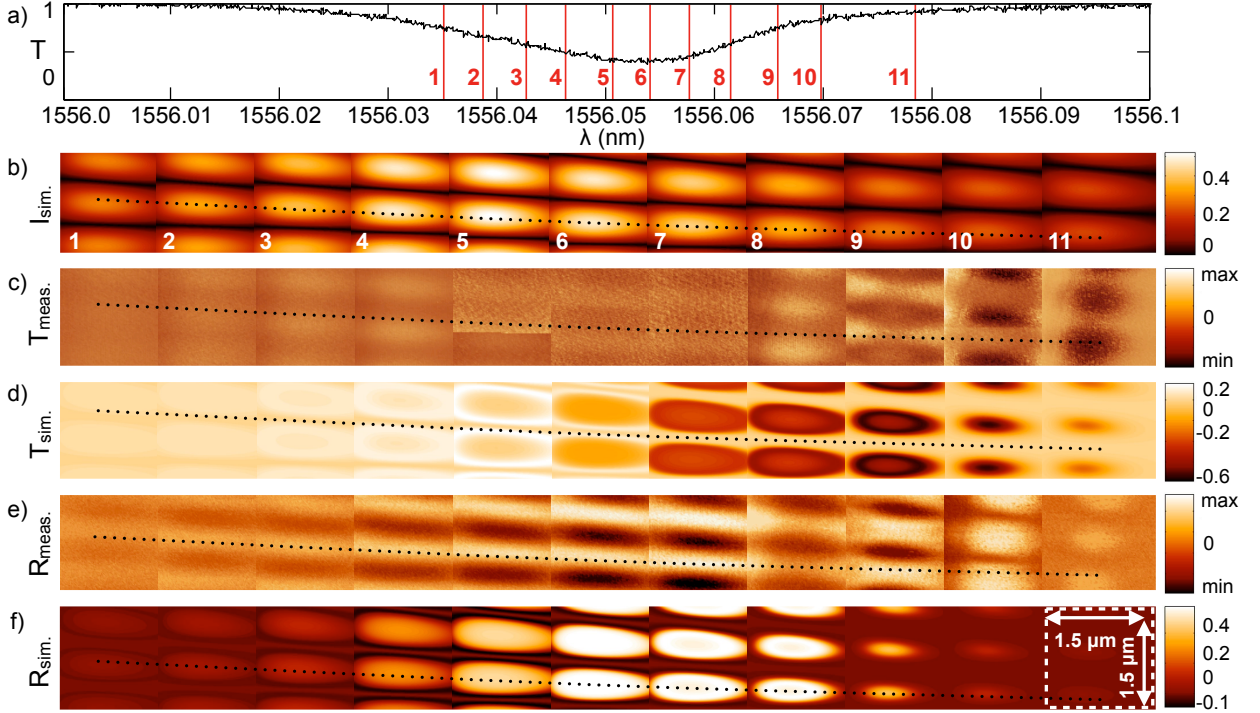


Fig. 4.2: Successive mode mappings for a stepped wavelength scan of the exciting laser through a resonance of a single disk using the perturbation of a scattering SNOM tip. For each of the 11 wavelengths marked in the transmission spectrum, (a) a scan window of  $1.5 \times 1.5 \mu\text{m}^2$  [highlighted in (f), frame 11] was mapped and arranged horizontally to a picture series (numbered 1 to 11) for (c) transmission and (e) reflection signals. For the same area of the disk (and arranged in the same way), the intensity distributions of the mode were calculated in (b), and from this the theoretical (d) transmission and (f) reflection signal maps were obtained. The dotted lines in (b) - (f) indicate the phase shift that the mode distribution shows when scanning through the resonance. A good agreement is obtained for the shift of the signal maximum in transmission [(e), (f), frames 6, 7] and reflection [(c), (d), frames 8, 9] compared to the expected intensity maximum of the mode [(b), frame 5]. In addition, complex patterned maps are obtained from the measured signal in agreement with the calculations [ring structure in (c), (d), frame 9].

nal in the transmissivity maps [frame 9 and 10, Fig. 4.2(c)] does not coincide with the absolute maximum in the reflectivity maps [6 and 7, Fig. 4.2(e)], which is well reproduced by the calculated maps.

- From the comparison with the optical collection measurement [Fig. 4.1(d)], it is expected that the intensity maxima and the maxima in the reflectivity maps coincide, which is also seen here in Figs. 4.2(b), (d), and (f). For the transmissivity maps a phase shift between frame 10 and frame 11 in Fig. 4.2(b) occurs that is not observable in the reflection mode maps and could be attributed to a stronger change in the excitation condition to a regime where transmissivity and reflectivity maps are inverted.<sup>8</sup>
- A ringlike structure is observable in the transmissivity mode maps in both experiment and calculation [frame 9, Figs. 4.2(c) and (d)].

<sup>8</sup>This regime was also observed for several mappings of two coupled disks where the reflectivity maps show only smaller values than the background and the transmissivity maps show larger values than the background at the same coordinates (not shown here).

The observed maps are a result of the complex interplay of excitation wavelength, external coupling rate and perturbation by the SNOM tip. The found characteristics indicate a redshift of the resonance due to the perturbation, identifiable from the shifted absolute transmission and reflection signal in comparison to the intensity maximum as well as the ring structure described above. Perturbing the mode while it is excited above the resonance leads to a decrease of the transmission signal and an increase of the reflection signal. For the ring structure the perturbation is strong enough to shift the resonance through the transmission minimum, which leads to the increase of the transmission signal at the center of the intensity maximum. Due to less spectral features in the reflection signal (e.g., see Sect. 5.4), the ring structure is not observable in the reflectivity mode maps.

On the one hand, the observations contradict the results in Refs. [Zhu11, Wan10] where a metallic perturbation leads to a blueshift of the resonances. Furthermore, the statement that the perturbation affects only the symmetric mode can not be verified here, which has at least two possible reasons. First, the mode splitting in the experiment was weak (due to the strong coupling to the tapered fiber) and the shift of the symmetric mode did not overcome the bandwidth at all. Second and more likely, there is no redistribution of the symmetric and antisymmetric mode for different positions of the tip (as described in Ref. [Zhu11]) since they are fixed due to the distribution of the surface roughness and the location of the taper excitation.<sup>9</sup> Therefore, both modes are influenced by the tip and get shifted. On the other hand, in the observed interaction regime the influence of the tip on the mode can not be neglected as in Ref. [Bla10] since no signal would be observed at all.

The simulation of the above mentioned details show that the described model is capable of explaining the measured results by the rather simple dipole approximation of the interaction of the SNOM tip with the disk resonator mode. From this one can conclude that the measured transmission and reflection signals are related to the actual intensity distributions of the WGMs in coupled microdisks. The measurements also reveal the standing wave nature due to the coupling of cw and ccw WGM. Although the surface perturbations are randomly distributed along the sidewall of the disk, the measured reflection signal indicates a fixed phase relation between the individual scatterers and a fixed standing wave pattern. This is also substantiated by the nature of the symmetric and antisymmetric combinations of cw and ccw modes, where the former tends to maximize its overlap with the high index regions and the latter one with the low index regions.

In the following sections of this chapter eigenmode mappings of two and three coupled microdisks in different arrangements are presented. Depending on the number of coupled disks and the symmetry of their arrangement, a splitting into a certain number of normal modes occurs (see Sect. 2.2.2). Only first order radial modes with a single intensity maximum ring

---

<sup>9</sup> Otherwise no standing wave pattern would be observable because, e.g., the maximum of the intensity of the symmetric mode would follow the tip position instantaneously. Also a much stronger splitting of the resonances in the presence of the SNOM tip should be observed, which was not the case in the experiments.

along the rim of the disks are investigated. The mapping of the mode distribution of the entire coupled disk structure is not necessary in this case, because from theoretical calculations it is expected that the differences of the intensity distributions emerge in the gap regions. Hence, the mappings were taken across the gaps of neighboring disks only. For each gap, a squared scan window of of  $5 \times 5 \mu\text{m}^2$  or  $10 \times 10 \mu\text{m}^2$  was chosen. This approach has the advantage of reduced scanning time and avoids measurement artifacts when scanning far from the gap regions. For the comparison with calculations, the intensity maps from the modal expansion method (Sect. 2.2.3) were used. On the one hand, this is motivated by the fact that for all measured modes and gaps, the coupling conditions during the scan could be different, which would result in a large number of simulations (parameter adjustments). On the other hand, the calculated intensity distribution from the rigorous modal expansion agrees quite good with the measured reflectivity mode maps for a relatively large range of detunings from the exact resonance wavelength, although the maxima of both do not coincide [Figs. 4.2(b) and (f)]. This leads to fast and reliable calculations for comparison with experimental data.

## 4.4 Two coupled microdisks

For two coupled microdisks, a splitting in two resonances can be observed in the spectra (see Chap. 3 or [CS5]). These are the symmetric and antisymmetric combinations of the eigenmodes of each of the single disks. The difference in the intensity can be observed when scanning across the gap between the two disks. In Figs. 4.3(a) and 4.3(b), the respective mode mappings and the calculated intensity distributions are shown. At the shorter wavelength antisymmetric mode, the fields in both disks have a phase difference of  $\pi$ , which leads to a destructive interference in the gap region. The recorded reflection mode map shows no notable signal change in the center of the gap between the disks, which is in excellent agreement with the simulations of the mode intensity [Fig. 4.3(a)]. The intensity profile along the blue dashed lines in the mode maps shows that the signal reaches the background level in the gap. For the symmetric mode at long wavelengths, the fields in both disks are in phase, which leads to constructive interference in the gap. This can be seen by the strong signal changes in the gap of the reflection mode map in agreement with the simulated intensity distribution [Fig. 4.3(b)]. Here the intensity profile shows much larger values than the background level.

From the measured standing wave pattern the effective wavelength and the effective mode index of the excited resonance can be extracted. To this end, the intensity profile along the green dashed line in Fig. 4.3(b) is plotted in Fig. 4.3(d), which shows a regularly oscillating curve. The distance between successive maxima corresponds to half of the wavelength in the disk. Calculating numerically the fast Fourier transform (FFT) gives the spectrum of this oscillation shown in Fig. 4.3(e). The main peak appears at an effective wave vector  $k_{\text{eff}} = 2\pi n_{\text{eff}}/\lambda = (5.08 \pm 0.33) \mu\text{m}^{-1}$ , resulting in an effective mode index of

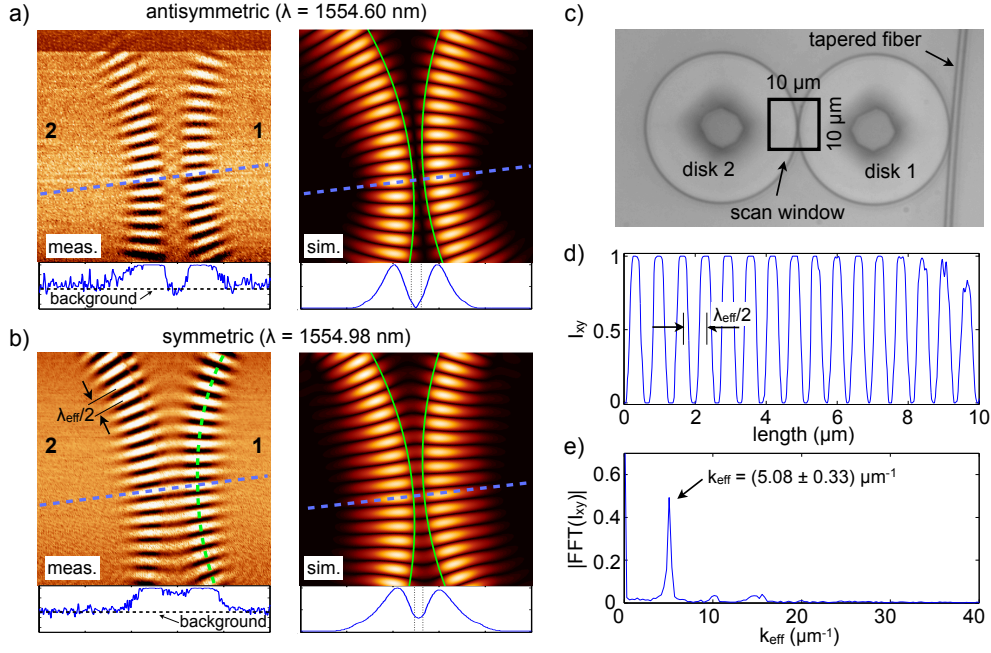


Fig. 4.3: Measured reflection mode maps and calculated intensity distributions across the gap of two coupled microdisks of the (a) antisymmetric and (b) symmetric mode. The profile in each picture is along the blue dashed line and shows the difference between the two modes. For the antisymmetric mode the signal in the gap between disk 1 and 2 drops down to the background level, whereas for the symmetric mode a significant signal in the gap can be measured in agreement with the calculated intensity. (d) The profile along the green dashed line in (b) is used to extract the effective mode index of the excited resonance. (e) The FFT from the signal in (d) results in a main spatial frequency of  $k_{\text{eff}} = (5.08 \pm 0.33) \mu\text{m}^{-1}$ , which gives  $n_{\text{eff}} = 1.258 \pm 0.082$  in agreement with calculations for first order radial modes (see Fig. 3.4).

$n_{\text{eff}} = 1.258 \pm 0.082$ . This value is in agreement with the calculations for the first order radial modes based on the analytical EIM model in Sect. 2.1.1 (see also Fig. 3.4 for comparison) and hence verifies the measurement of standing waves in the microdisks. In the spectrum in Fig. 4.3(e) peaks at higher orders of the main spatial frequency can be observed, which are due to a slight saturation of the detector at the maximum and minimum values for the mode mapping shown in Fig. 4.3(d).<sup>10</sup>

## 4.5 Three coupled microdisks - linear arrangement

For three coupled microdisks in a line arrangement the splitting into three resonances can be observed. In general they are not equally spaced in the wavelength spectrum (for comparison see Fig. 3.11 or the discussion in Sect. 2.2.1). In the same way as for the two coupled disks, the mode maps were recorded for each of the three eigenmodes across the two gaps. Figure 4.4 shows the measured mode maps with the disk numbered from right to left with 1, 2 and 3, where always the right disk (disk 1) was excited. In Fig 4.4(a) the measured and calculated intensity distribution for the antisymmetric mode at the shortest wavelength of the three

<sup>10</sup>The intensity profile was subtracted by the background level and normalized to the maximum value.

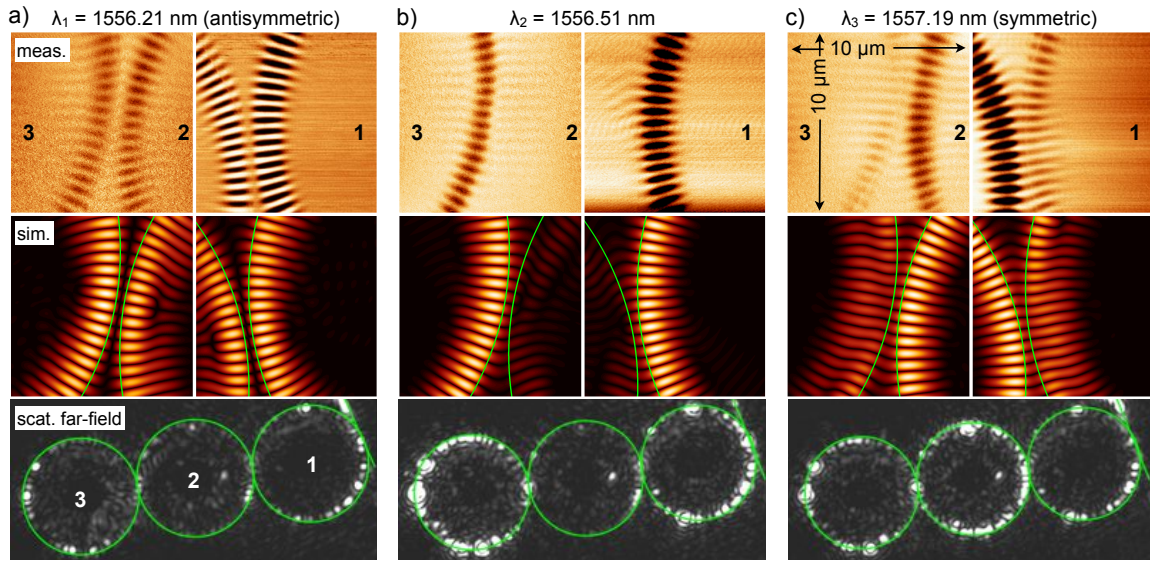


Fig. 4.4: Measured reflection mode maps and calculated intensity distributions across the two gaps of three coupled microdisks of the (a) antisymmetric, (b) intermediate and (c) symmetric mode. For the antisymmetric mode (a) no signal from the gaps but from all disks with almost equal strength is obtained. For the middle resonance (b) a signal is measured in disk 1 and 3 but not in disk 2. For the symmetric mode (c) a signal from all disks as well as from the gaps is measured, with the strongest signal from disk 2. All measurements are in good agreement with the calculated intensity distributions of the same sample sections ( $10 \times 10 \mu\text{m}^2$  window covering the gap region). Corresponding far-field scattering signals are shown in the lowest row of each subfigure, from which the intensity distribution can be obtained roughly.

resonances is shown. As in the case of two disks, the fields in adjacent disks have a phase difference of  $\pi$ , which leads to destructive interference in the gaps between the disks. The differences in the signal strength and characteristics of the measured maps of the two gaps are caused by the measurement procedure itself: for one gap, all modes were mapped first before the SNOM tip was moved to the other gap. This requires new alignment of the taper-disk gap as well as the resonance wavelength for each mode. It was shown in Sect. 4.3 that these parameters have a strong influence on the characteristics of the recorded mode maps and it is unlikely to match exactly the same conditions of the complex system at different measurement times. Nevertheless, there is an agreement between measurements and simulations. For the central resonance [Fig. 4.4(b)], the phase differences between the fields in adjacent disks is  $\pi/2$ , which leads to a cancellation of the field in the complete middle disk (disk 2), and therefore no signal changes can be measured in agreement with the simulation. The symmetric mode at longest wavelength [Fig. 4.4(c)] shows a signal from all three disks, while the signal from the central disk is strongest. The fields in adjacent disks are in phase, so their constructive interference leads to an intensity signal in the gap, which is clearly seen in the measurements and the simulated mode maps. An interesting detail is the agreement of the relative signal strength in the weaker excited disk (1 and 3) when comparing measurement and simulation. At the region where the gap is smallest, the intensity in these disks is lower than further away from the gap along the rim and the signal extends more toward the center of disk.

For each of the modes in Fig. 4.4 an image of the corresponding far-field scattering signal is shown in the last row of each subfigure. From these images the intensity distribution can be obtained roughly. Particularly, the dark middle disk (disk 2) can be identified at the central resonance [Fig. 4.4(b)] as well as the higher intensity from disk 2 of the symmetric mode [Fig. 4.4(c)]. Nevertheless, no details about the mode symmetry and distribution can be obtained due to the random distribution of the scatterers and the low resolution of the infrared camera.

## 4.6 Three coupled microdisks - triangular arrangement

For the coupling of three identical disks in a triangular arrangement, a splitting into four resonances is expected from the theory developed in Sect. 2.2.1. The measured spectrum in Fig. 4.5(a) shows six (numbered) resonances, which can be explained by a nanoscale size mismatch of the disks. This results in a lift of degeneracy of modes, which for identical coupled disks have the same resonance wavelength but different mode distributions. Comparison to the calculated spectrum indicates that all disks have a slightly different radius:  $R_1 = 15.1008 \mu\text{m}$ ,  $R_2 = 15.0958 \mu\text{m}$  and  $R_3 = 15.1012 \mu\text{m}$  with a maximum deviation of  $\Delta R = 5.4 \text{ nm}$ . The weaker, unnumbered resonances in the spectrum belong to a mode with different polarization, which spectrally overlap and are not suppressed completely. For the numbered resonances a mode map across each gap was recorded and is shown together with the corresponding simulation in Fig. 4.5(c)-(h). The disks are numbered according to the microscope image shown in Fig. 4.5(b) with disk 1, disk 2 and disk 3. The gaps are denoted as gap 1-2 for the gap between disk 1 and 2, gap 2-3 for the gap between disk 2 and 3 and gap 1-3 for the gap between disk 1 and 3. The first resonance [Fig. 4.5(c)] is justified as the antisymmetric mode with zero intensity in the gaps. For the measurement of gap 1-3 the mode was not excited exactly at the same wavelength as for the other gaps, which can be seen by the slight phase difference between the fields in disk 1 and 3 and a weak signal in the gap region. Both can be reproduced by the simulation when taking the shifted excitation wavelength into account. For the second mode [Fig. 4.5(d)] the fields in disk 1 and 2 have a phase difference of  $\pi$ , resulting in a destructive interference in the gap between them. The phase difference of both disks with respect to disk 3 is  $\pi/2$ , leading to the observed cancellation of the field in disk 3. The agreement between the measured map and the simulation for the gap 1-3 [third row of pictures in Fig. 4.5(d)] is remarkable, where the signal from disk 1 fills the gap and disappears at the surface of disk 3. For the third mode [Fig. 4.5(e)] the fields in disk 1 and 3 have a phase difference of  $\pi$ , hence no intensity from the gap 1-3 is observed, whereas the phase difference of both to disk 2 leads to a cancellation in disk 2 (almost no signal is measured from disk 2 at both gaps, 1-2 and 2-3). In the case of identical disks, the two cases [Figs. 4.5(d) and (e)] would be indistinguishable and the resonances in the spectrum would be degenerated, whereas

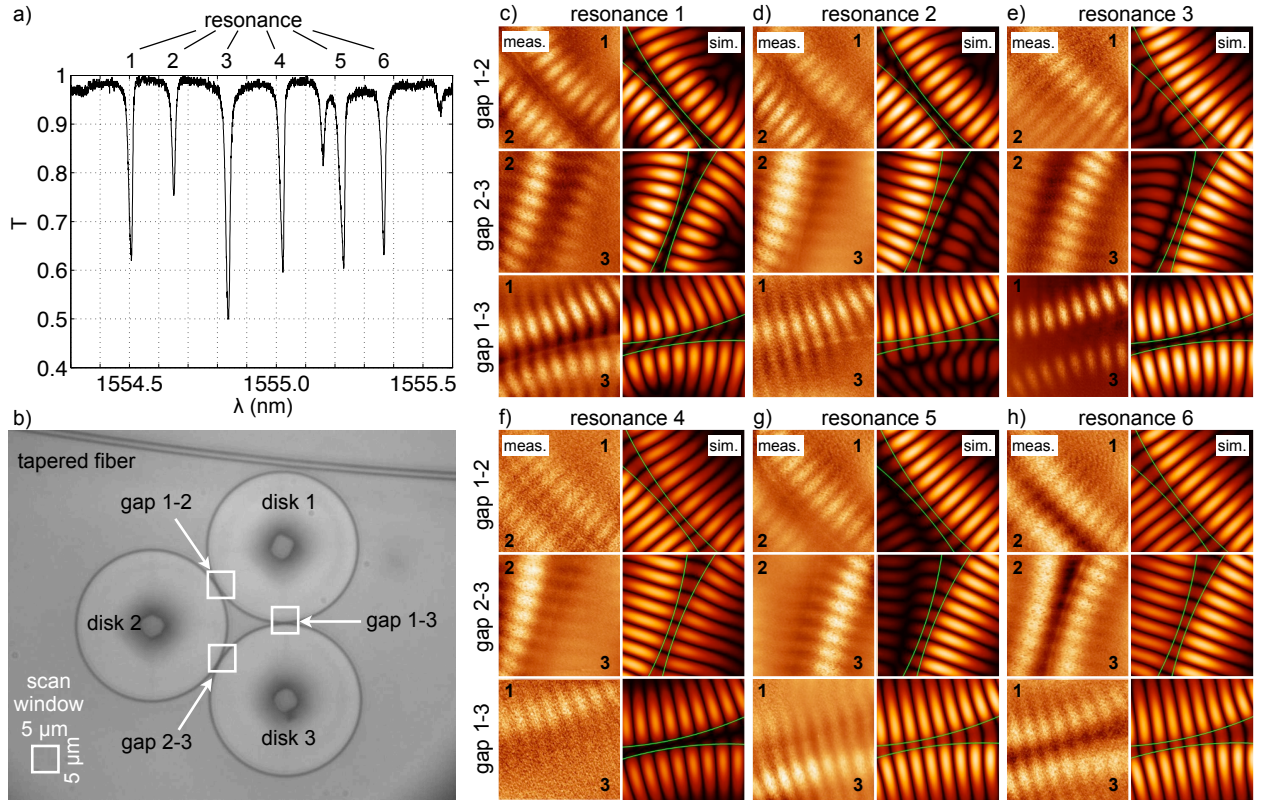


Fig. 4.5: (a) Measured transmission spectrum for three coupled microdisks in a triangular arrangement shows splitting in six eigenmodes. The unnumbered dips belong to the other polarization state, which was not suppressed completely. (b) A top view of the measured sample with the tapered fiber for excitation of disk 1. The white squares highlight the SNOM scan windows of  $5 \times 5 \mu\text{m}^2$ . The resulting intensity distribution for each of the gaps (1-2, 2-3, 1-3) is shown in (c)-(h) for the numbered resonances in (a). In each measurement (meas.) square the numbers highlight the particular disk, whereas in the corresponding simulation (sim.), the green lines mark the rim of the disks.

the small radius difference leads to different energy levels and hence distinguishable resonance wavelengths.

The mode maps for the long wavelength resonances 4, 5 and 6 [Fig. 4.5(f)-(h)] show the same characteristics but for the symmetric modes of the system. This means that in general an intensity signal from the gap between two disks can be observed when there is a signal in both of the disks. In detail, for resonance 4 [Fig. 4.5(f)] no intensity was measured in disk 3, whereas for the resonance 5 [Fig. 4.5(g)] no intensity was obtained from disk 2. The fields in the remaining disks for both modes are in phase and interfere constructively in the gap. The simulations are in good agreement for resonance 5 but deviate a little for resonance 4. Here the intensity in disk 3 is not well reproduced. This indicates the strong sensitivity of the system on the exact parameters. The fully symmetric resonance 6 shows an intensity signal from all three disks and gaps in the measurement as well as in the simulation. However, the measured maps show relatively weak contrast, which can be explained by the degradation of the used SNOM tip. After dozens of scans the tip loses sharpness, which results in reduced contrast of the intensity signal during the measurements. Nevertheless, all modes can be identified from

the associated maps in agreement with the simulations.

## Chapter summary

To summarize this chapter, the implementation of an experimental method for high resolution near-field mapping of WGM in coupled microdisk resonators was presented. The perturbation of the transmission and reflection signals in a coupled taper-disk system by the presence of a scattering SNOM tip can be used to extract the intensity distribution of the WGM in the disks. This approach outperforms the resolution of a direct near-field collection by an aperture SNOM tip [Bal99]. Additionally, the stronger interaction of the tip results in a better signal-to-noise-ratio than the far-field collection of the scattered light from the scattering SNOM tip [Bla10]. But the latter characteristic also points out the complexity of the method because the interaction with the SNOM tip can no longer be neglected when interpreting the results. Using a combination of a rigorous modal expansion method with a coupled mode model, the influence of the SNOM tip can be taken into account at reasonable computational effort<sup>11</sup> and allows to perform several important parameter variations. The model offers the ability to simulate the transmission and reflection signals measured at both tapered fiber ends used for excitation of the microdisk samples and to predict the characteristics observed in the measured scattering SNOM mode maps. Moreover, detailed near-field mode mappings of two and three coupled microdisks are presented, which show excellent agreement with theoretical calculations.

In spite of the demonstrated agreement between measurements and simulation, the accuracy of the model could be enhanced further by taking into account details of the shape of the SNOM tip and by describing its interaction with the disk mode beyond the dipole approximation. In order to improve the experimental setup an interferometric detection scheme could be added, which would allow to measure phase information of the mode distributions inside the disks.

The obtained data from spectrum measurements and the respective mode intensity distributions can be used, on the one hand, to identify size variations of the individual disks in the fabricated coupled disk samples and, on the other hand, to selectively excite or tune the resonances of such a coupled resonator system. In particular, the samples consisting of three coupled disks can be of interest for sensing applications because it is possible to spatially resolve perturbations of the system. For example, the position of adsorbed nanoparticles, which cause a resonance shift and broadening [Zhu09], can be identified because only certain modes of the system are influenced. Also it is possible to selectively tune the spectral distance of the modes, e.g., by changing the temperature of a certain disk in the coupled ensemble, which might be useful for optical filter applications.

---

<sup>11</sup>In comparison to computationally demanding FDTD or FEM simulations.



# 5 Optically induced thermal nonlinearity in coupled microdisks

The high Q-factor and small mode volume of the WGMs in microresonators lead to a strong enhancement of the circulating intensities given by (according to Sect. 3.4.2)

$$I_{\text{circ}} = \frac{\mathcal{F}P_{\text{pump}}}{\pi A_{\text{mode}}} = \frac{\lambda}{2\pi n_g} \frac{Q}{V_{\text{mode}}} P_{\text{pump}}, \quad (5.1)$$

with the excitation wavelength  $\lambda$ , the pump power  $P_{\text{pump}}$ , the finesse  $\mathcal{F}$ , the cross sectional mode area  $A_{\text{mode}}$ , the mode volume  $V_{\text{mode}}$ , the Q-factor  $Q$  and the group index  $n_g$  [Eq. (3.12)]. The typical parameters obtained for the investigated microdisks [ $\lambda = 1.55 \mu\text{m}$ ,  $n_g = 1.441$ ,  $Q = 2 \times 10^5$ , and  $V_{\text{mode}} = 85(\frac{\lambda}{n})^3$ ] and  $P_{\text{pump}} = 1 \text{ mW}$  result in  $I_{\text{circ}} \approx 32 \text{ MW/cm}^2$ . In comparison to other fused silica based microresonators like spheres and toroids, this value is up to two orders of magnitude lower [Vah03], which obviously is due to the lower Q-factor in the microdisks. This also inhibits the observation of Kerr nonlinearity based effects<sup>1</sup> [Bra89, Rok05], e.g., optical parametric oscillations [Spi04] or stimulated Raman scattering [Joh09] in the microdisks for pump powers of a few milliwatts. According to the pump power threshold observed for silica microtoroids and the  $V/Q^2$  dependence [Kip04a], one can estimate the parametric oscillation threshold to a few watts (if other requirements are fulfilled, e.g., resonance detuning).

Thermal nonlinearity (or temperature induced dispersion) [Bra89, Ilc92, Gor04, Fom05], on the other hand, relies on heating of the resonator material due to linear absorption of light in the material. The related temperature dependent quantities are the positive thermal refractivity  $n^{-1}dn/dT$  and expansion coefficient  $\alpha_{\text{th}}$  summarized in the experimentally observable thermal coefficient  $\beta_{\text{th}}$

$$\beta_{\text{th}} = \frac{1}{n} \frac{dn}{dT} + \alpha_{\text{th}}. \quad (5.2)$$

In fused silica microtoroids threshold powers of approximately 50 nW were estimated [Sch09a]. Translated to the Q-factor observed for the microdisks, thermal effects come into play for pump powers larger than  $P_{\text{pump}} = 50 \mu\text{W}$ . They are thus the lowest threshold nonlinear effect in fused silica microresonators. Although thermal effects are slow in comparison to the instantaneous Kerr effect, for sufficiently slow power modulation (e.g., slowly sweeping through a

---

<sup>1</sup>In amorphous fused silica the third order nonlinear term is the first contributing to the nonlinear polarization.

resonance) they can lead to effects similar to those which can be observed for Kerr nonlinearity like bistability and hysteresis. For this reason these effects are of interest for the realization of optical switching and all optical tuning of resonances in microresonators.

In this chapter the consequences of the thermal nonlinearity for the spectral response of coupled microdisks are investigated in detail. To this end, the CMT is extended to take into account the thermal nonlinear effects. The temperature dynamics inside the microdisks is described by means of a heat equation and different relaxation time scales are identified. Experimentally, the impact of thermal nonlinearity is observable as a pump power dependent resonance frequency shift. This can be measured either by fixed wavelength pump power tuning with focus on the transmission signal changes or by sweeping excitation at different pump power levels observing distortions in the spectral shape of the resonances. The applicability of both methods for the particular system of tapered coupled microdisks is discussed in detail. Furthermore, a pump and probe technique is implemented to measure the temperature relaxation time independently since it is the most important characteristic for proper description of the thermal nonlinearity by the extended CMT. With a reliable experimental measurement technique and the important parameters of the microdisks at hand, the nonlinear resonance spectra of two and three coupled microdisks are investigated comprehensively and new effects like differential all optical resonance tuning are discussed. Finally, a concept for compensation of the thermal refractivity of the resonator material is discussed and experimentally realized since thermal resonance shifts are detrimental for particular practical applications.

## 5.1 Coupled mode theory including thermal nonlinearity

The CMT (Sect. 2.3) can be expanded to take into account the thermal nonlinear effects by introducing the polarization term

$$\Delta \bar{\mathbf{P}}_{\text{th}}(\mathbf{r}, t) = \epsilon_0 \Delta \epsilon_{\text{th}}(\mathbf{r}, \omega_m) \bar{d}_m(t) \mathbf{E}_m(\mathbf{r}, \omega_m), \quad \text{and} \quad \Delta \epsilon_{\text{th}}(\mathbf{r}, \omega_m) = 2n(\omega_m) \frac{dn(\omega_m)}{dT} \delta T(\mathbf{r}, t). \quad (5.3)$$

Substitution into Eq. (2.58) leads to the mode dynamics (single disk with external coupling)

$$\frac{d}{dt} [\bar{d}_m(t)] = [i(\omega_0 - \omega_m) - (\Gamma_0 + \Gamma_{\text{ext}})] \bar{d}_m(t) + i\omega_0 \beta_{\text{th},n} \overline{\delta T}(t) \bar{d}_m + i\sqrt{2\Gamma_{\text{ext}}} \bar{a}_{\text{in}}(t), \quad (5.4)$$

with the mode distribution averaged temperature change  $\overline{\delta T}$  and the thermal refractivity  $\beta_{\text{th},n}$

$$\overline{\delta T}(t) = \frac{\int \epsilon(\mathbf{r}, \omega_m) \delta T(\mathbf{r}, t) |\mathbf{E}_m(\mathbf{r}, \omega_m)|^2 d\mathbf{r}}{\int \epsilon(\mathbf{r}, \omega_m) |\mathbf{E}_m(\mathbf{r}, \omega_m)|^2 d\mathbf{r}}, \quad \text{and} \quad \beta_{\text{th},n} = \frac{1}{n(\omega_0)} \frac{dn(\omega_0)}{dT}. \quad (5.5)$$

For the derivation of Eq. (5.4) only the thermal refractivity was used since for fused silica it is much larger than the thermal expansion. To be more accurate one can take into account

thermal expansion by replacing  $\beta_{\text{th},n}$  with  $\beta_{\text{th}}$  from Eq. (5.2).<sup>2</sup> The resonance frequency shift per Kelvin can be inferred from Eq. (5.5) to  $\Delta\nu_{\text{th}} = -(\omega/2\pi)\beta_{\text{th}}$ , which for a wavelength around 1550 nm calculates to  $\Delta\nu_{\text{th}} = -1.58 \text{ GHz K}^{-1}$  corresponding to  $\Delta\lambda_{\text{th}} = 12.7 \text{ pm K}^{-1}$  ( $\alpha_{\text{th}} = 5.5 \times 10^{-7} \text{ K}^{-1}$  [Web03],  $dn/dT = 1.1 \times 10^{-5} \text{ K}^{-1}$  [Mal65]).<sup>3</sup>

The temperature dynamics can generally be described by the heat equation for the deviation  $\delta T(\mathbf{r}, t)$  from a reservoir temperature

$$\frac{d}{dt}\delta T(\mathbf{r}, t) - \frac{k_{\text{th}}}{\rho C_p} \nabla^2 \delta T(\mathbf{r}, t) = \frac{\alpha_{\text{abs}}}{\rho C_p} I, \quad (5.6)$$

with the thermal conductivity  $k_{\text{th}}$ , the material density  $\rho$  and the specific heat capacity (at constant pressure)  $C_p$ . The temperature increase is driven by the linear material absorption  $\alpha_{\text{abs}}$  of the optical intensity  $I$  carried by the WGM. The right hand side of Eq. (5.6) can be written as<sup>4</sup>  $\alpha_{\text{abs}} I / (\rho C_p) = \alpha_{\text{abs}} c |d_m(t)|^2 / (\rho C_p n V_{\text{mode}})$ . Here the relation for the intensity  $I = \langle u \rangle c / n$  in terms of energy density  $\langle u \rangle$  and light velocity in the medium  $c/n$  was used as well as the energy stored in the resonator  $|d_m(t)|^2$ . The temperature relaxation can be due to different heat exchange mechanisms: heat conductivity of the bulk material, heat conductivity and convection of the surrounding gas or thermal radiation. Usually, microresonators are fixed to substrates (disks and toroids) or optical fibers (spheres) and hence heat conduction into the resonator material and the support are the main contributions. If the microresonator is placed in a non-evacuated environment also heat convection of the surrounding gas can have significant influence as mentioned in Ref. [Ilc92]. For a detailed analysis of the relaxation dynamics one has to distinguish between different regimes:

- First, one can consider the relaxation of the temperature in the mode volume to the remainder of the resonator, which is heated by the linear absorption of the WGM. Since the mode volume is generally very small compared to the volume of the resonator (especially for spheres), the relaxation is expected to be relatively fast. Assuming a constant (mean) temperature throughout the mode volume, the second spatial derivative in Eq. (5.6) can be approximated as  $\nabla^2 \overline{\delta T} = -2\overline{\delta T} / b^2$  [Ilc92] with the FWHM width of the mode profile  $b$ . This leads to a temperature relaxation rate of

$$\gamma_{\text{th},f} = \frac{2k_{\text{th}}}{\rho C_p b^2}, \quad (5.7)$$

which for the corresponding values (see appendix C) gives a fast relaxation time  $\tau_{\text{th},f} \approx 1 \mu\text{s}$ .

- Secondly, the relaxation of the temperature in the whole resonator to the environment

<sup>2</sup>Formally, one could add a term  $2\epsilon(\mathbf{r}, \omega_m)\alpha_{\text{th}}\delta T$  to  $\Delta\epsilon_{\text{th}}$  in Eq. (5.3) and interpret it as change of the dielectric function at the boundary of the microdisk inducing additional polarization. A comprehensive perturbation theory for moving boundaries of a dielectric can be found in [Joh02].

<sup>3</sup>Depending on the reference the value of  $dn/dT$  varies between  $1 \times 10^{-5} \text{ K}^{-1}$  and  $1.3 \times 10^{-5} \text{ K}^{-1}$ .

<sup>4</sup>This strictly holds only for plane waves and is used as the lowest order approximation. In general one has to use the Poynting vector to describe the intensity of an arbitrary field.

has to be considered. For the conducting case the contact to the substrate determines the relaxation rate. In contrast to the fast relaxation we assume an averaged temperature of the whole resonator and replace the spatial derivative by the resonator radius. Therefore, we set  $\gamma_{\text{th,s}} = k_{\text{th}}/(\rho C_{\text{p}} R_{\text{res}}^2)$ , which for  $R_{\text{res}} = 20 \mu\text{m}$  gives a relaxation time  $\tau_{\text{th,s}} \approx 420 \mu\text{s}$ . The above mentioned heat energy transfer due to convection of the surrounding gas can be important especially for a constant pump power or very slow pump power modulation. It leads to a relaxation rate  $\gamma_{\text{th,s,conv}} = \widetilde{Nu} k_{\text{th}}/(\rho C_{\text{p}} R_{\text{res}}^2)$ , where  $\widetilde{Nu}$  is the so called Nusselt number describing the ratio of convective and conductive heat transfer at a boundary (for air at room temperature  $\widetilde{Nu} \approx 0.3$ ) [Ilc92]. This would lead to a characteristic relaxation time of  $\tau_{\text{th,s,conv}} \approx 1.4 \text{ms}$ , approximately on the same order as the slow conductive relaxation time.

The general solution of the heat equation may be found with the help of spectral decomposition [Fom05] but usually is hard to calculate and the approximations described above [for the spatial derivative in Eq. (5.6)] are applied as well. Nevertheless, for the microdisk geometry the heat equation can be reduced to a 1D problem in the Fourier domain with the assumption that the temperature is constant across the height and azimuthal direction of the disk [Sch09a]. Further assuming that the heat source (absorption region) is located only at the edge of the disk at  $R_{\text{res}}$  and the temperature above the pillar supporting the disk (with radius  $R_{\text{pil}}$ ) is constant, leads to a standard inhomogeneous Bessel differential equation. Expansion of the solution in terms of Fourier thermal frequencies  $\Omega$  up to the first order results in a general cut-off frequency, i.e., a highest possible frequency of a propagating temperature wave [Sch09a]

$$\Omega_1 = -\frac{4 \ln(R_{\text{pil}}/R_{\text{res}})}{1 - (R_{\text{pil}}/R_{\text{res}})^2 + 2 \ln(R_{\text{pil}}/R_{\text{res}})[1 + \ln(R_{\text{pil}}/R_{\text{res}})]} \frac{k_{\text{th}}}{\rho C_{\text{p}} R_{\text{res}}^2}. \quad (5.8)$$

This maximum frequency can be interpreted as fastest possible thermal relaxation rate and the corresponding relaxation time can be found to  $\tau_{\text{th,s}} = 2\pi/\Omega_1 \approx 950 \mu\text{s}$  for typical radii  $R_{\text{pil}} = 5 \mu\text{m}$  and  $R_{\text{res}} = 20 \mu\text{m}$  and is at the same order as the slow relaxation time from the approximation above. Taking into account the second order of the spectral decomposition of the heat equation, a second cut-off for an extended heating source with the size of the mode can be found. This results in the same relation for the fast relaxation rate (5.7) as given above.

From the steady state solution of the combined Eqs. (5.4) and (5.6) one can estimate the pump power threshold for the thermal nonlinear effects to appear in the spectral response of the microdisks

$$\left[ i(\Delta\omega + \omega_0 \beta_{\text{th}} \overline{\delta T}) - (\Gamma_0 + \Gamma_{\text{ext}}) \right] \bar{d}_m = -i\sqrt{2\Gamma_{\text{ext}}} \bar{a}_{\text{in}}, \quad (5.9)$$

$$\overline{\delta T} = \frac{1}{\gamma_{\text{th}}} \frac{\alpha_{\text{abs}}}{\rho C_{\text{p}}} \frac{c}{nV_{\text{mode}}} |\bar{d}_m|^2 = \frac{B_{\text{th}}}{\gamma_{\text{th}}} |\bar{d}_m|^2, \quad (5.10)$$

with  $\Delta\omega = \omega_0 - \omega_m$ . Taking the absolute value of Eq. (5.9) and replacing  $\overline{\delta T}$ , one ends

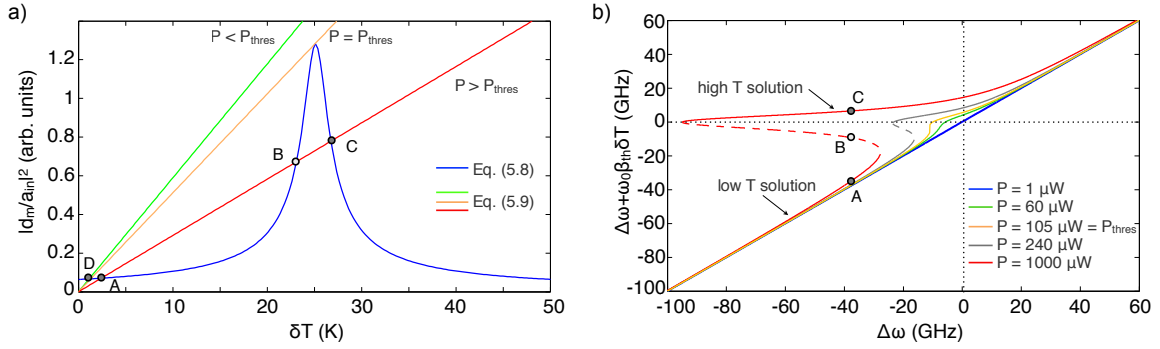


Fig. 5.1: Steady state analysis of the Eqs. (5.9) and (5.10). In (a) a graphical representation with possible solutions for the intersections of the curves showing one solution (D) below threshold and three solutions (two stable A and C and one unstable B) above threshold. In (b) the temperature induced total resonance shift as a function of the pump laser detuning from the unperturbed resonance is calculated numerically for different pump powers (for parameters see appendix C). For a red detuned excitation above threshold the two stable solutions are the non-shifted low temperature and the shifted high temperature solution. The latter one compensates for the pump detuning and shifts the system on resonance. The unstable branch is plotted as dashed line. For a weak red detuned excitation above threshold (red line for  $\Delta\omega > -25$  GHz, orange line for  $\Delta\omega > -15$  GHz) only the high temperature solution appears (no bistability). Below threshold only a weak redshift of the resonance occurs (green line).

up with a cubic equation in  $|d_m|^2$ . Using the pump power  $|a_{in}|^2$  as control parameter the system bifurcates into three real solutions if the discriminant of the polynomial vanishes, which happens at ( $\Delta\omega = 0$ )

$$P_{thres} = |a_{in}|_{thres}^2 = \frac{(\Gamma_0 + \Gamma_{ext})^3 \gamma_{th}}{3\sqrt{3}\Gamma_{ext}\omega_0\beta_{th}B_{th}} = \frac{2\gamma_{th}}{3\sqrt{3}\beta_{th}B'_{th}} \frac{V_{mode}}{Q^2}, \quad (5.11)$$

where for the last relation critical coupling ( $\Gamma_{ext} = \Gamma_0$ ) was assumed and the relations  $Q = \omega_0/2\Gamma$  and  $B'_{th} = B_{th}V_{mode}/\omega_0$  were used to show the  $V/Q^2$ -dependence of the threshold pump power. With the typical values for the investigated microdisks this gives  $P_{thres} \approx 80 \mu W$  in agreement with the estimates from the beginning of the chapter. In Fig. 5.1(a) the graphical representation of the solution of Eqs. (5.9) and (5.10) is shown for three different pump powers. The intersections of the resonance curve [Eq. (5.9)] with the straight lines from [Eq. (5.10)] are possible solutions of the system. Below the threshold power only a single solution exists but above threshold three intersections can be found, where the middle one is an unstable solution and the other two are stable. The existence of two stable solutions, or stable output states for a given input state, indicates optical bistability [Gib85]. In Fig. 5.1(b) this is shown from the numerical solution of Eqs. (5.9) and (5.10) by calculation of the temperature induced total resonance shift  $\Delta\omega + \omega_0\beta_{th}\delta T$  as a function of the pump laser detuning from the unperturbed resonance  $\Delta\omega$ . For a red detuned excitation ( $\Delta\omega < 0$ ) and pump powers above threshold  $P_{thres}$  the two stable solutions are the non-shifted low temperature solution (at the low power straight line) and the high temperature solution, where the induced shift compensates the detuning of the excitation to resonance (exactly only at the threshold power for a given detuning). If the

initial red detuning becomes less for a given pump power above threshold, the low temperature solution disappears as does the bistability. For further increase of the blue detuning the shift of the high temperature solution decreases with respect to the linear solution. Below threshold only a small redshift of the resonance occurs for excitations close to resonance.

## 5.2 Optical bistability observable in tapered fiber coupled microdisks

With the knowledge of the above mentioned characteristics the optical bistability usually is measured in terms of the system's output power as a function of the input power, in this case for a red detuned excitation, where typically a hysteresis can be observed [Gib85]. Translated to the measured transmission signal through the tapered fiber, which is coupled to the microresonator, the hysteresis is generated as follows [illustrated with the help of Fig. 5.1(b)]: The initially red detuned pump causes an off-resonant high transmission signal [e.g.,  $\Delta\omega \approx -25$  GHz at the low temperature branch in Fig. 5.1(b)]. When increasing the pump power above a certain threshold, the induced resonance shift compensates the detuning and the system switches on resonance resulting in a low transmission signal [ $P \approx 1000$   $\mu$ W, switching from low to high temperature solution]. A subsequent decrease of the pump power results in a low transmission on-resonant state, until a second, lower threshold is reached, below which the system is off-resonant again showing a high transmission signal [ $P \approx 240$   $\mu$ W, switching from high to low temperature solution]. A measured hysteresis can be found in [Alm04b] for an on-chip silicon ring resonator coupled to a ridge waveguide.

The measurements of the power dependent hysteresis for a tapered fiber coupled microdisk at fixed wavelengths is shown in Fig. 5.2(a). The observations for increasing and decreasing pump power contradict with the expectations of the simulations. A detailed analysis identifies optically induced mechanical oscillations of the coupling tapered fiber considerably influencing the measurements. First investigated in detail in Ref. [Eic07], the bend tapered fiber can be forced to mechanical displacement due to induced polarizations by the optical field stored in the cavity. The repelling force reaches its maximum in the overcoupled regime leading to a dynamical interaction of the power coupled to the cavity and the position of the tapered fiber. The tapered fiber can be seen as a mechanical oscillator and the dynamical interaction can drive its oscillations.

For this reason the transmission signal will permanently switch between the two stable solutions. However, the measurements of the transmission signal over time for different pump powers and different detuning [Fig. 5.2(b, c)] indeed shows differences depending on whether the pump power increases or decreases. Taking the time averaged transmission signal for each pump power and detuning, one obtains the hysteresis curves in Fig. 5.2(a). Although the branches for decreasing and increasing pump power are switched due to the influence of the

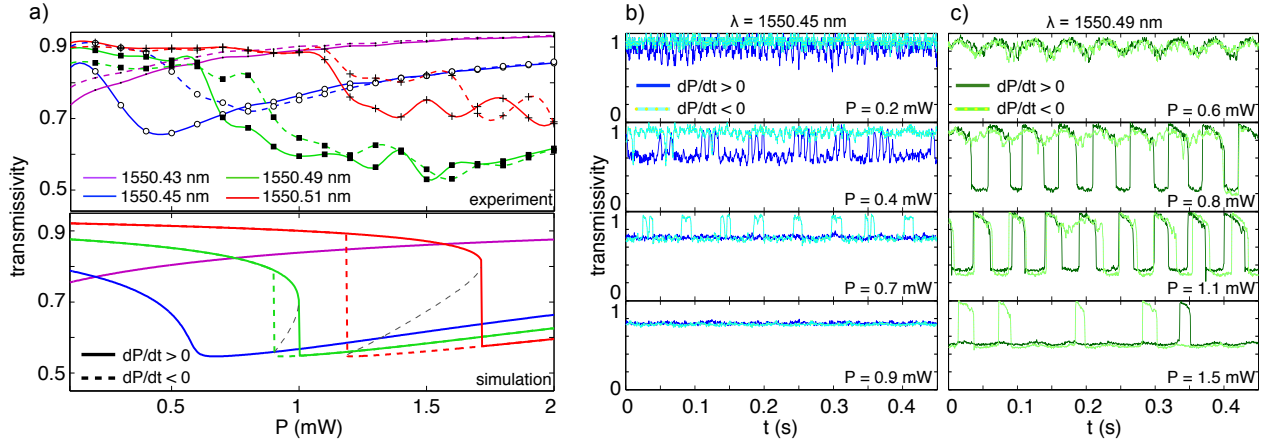


Fig. 5.2: Bistability measurements by pump power tuning for fixed wavelengths around a resonance at  $\lambda = 1550.445$  nm. (a) For a red detuned excitation bistability hystereses can be observed for the time averaged transmission signals in qualitative agreement with calculations. In the experiment the onset of the hysteresis occurs for less red detuning than expected from the simulations and also the different branches for up and down pump power tuning are interchanged as compared to theoretical expectations [see also Fig. 5.1(b)]. The differences are caused by optically induced mechanical oscillations of the tapered fiber leading to periodic alterations of the transmission signal over time shown in (b) and (c) with different strength depending on the detuning of the excitation. The period of the oscillations is independent of the detuning [e.g., compare  $P = 0.7$  mW in (b) and  $P = 1.1$  mW in (c)].

taper oscillation dynamics, the shape and size of the hysteresis agrees qualitatively with the simulations of the power and detuning dependent transmission [Fig. 5.2(a), calculated from Eqs. (5.9), (5.10) and (2.66)].

The oscillations of the bend tapered fiber were analyzed experimentally in further detail to identify the parameter ranges where they play a significant role. Measuring the time traces of the transmission signal for different pump powers and detuning from resonance one obtains the spectral components of the taper oscillation by Fourier transformation. The main oscillation is found at 130 Hz. The taper oscillation prevents the system to be held at a constant transmission signal level and hence is the limiting factor for performing reproducible experiments. Especially, for high pump powers the taper displacement amplitudes can become so large that the taper eventually gets stuck to the resonator.

To circumvent the drawbacks of the fixed wavelength excitation one can measure the bistability also in the case of a wavelength sweeping excitation used for the resonance spectrum measurements.<sup>5</sup> Sweeping the excitation from smaller to longer wavelengths (positive sweeping) across a resonance for high enough pump power, leads to a distorted asymmetric resonance line shape (smooth transition at the low wavelength side of the resonance, steep transition at the long wavelength side of the resonance). The pump laser traps the resonance, which gets thermally shifted, up to a maximum detuning corresponding to the actual pump power. As the excitation tunes above this wavelength the system switches from the on-resonant to the off-resonant state and the resonance relaxes to its initial (cold cavity) wavelength. When

<sup>5</sup>This method was used from the early days on to measure bistability hystereses [Ilc92].

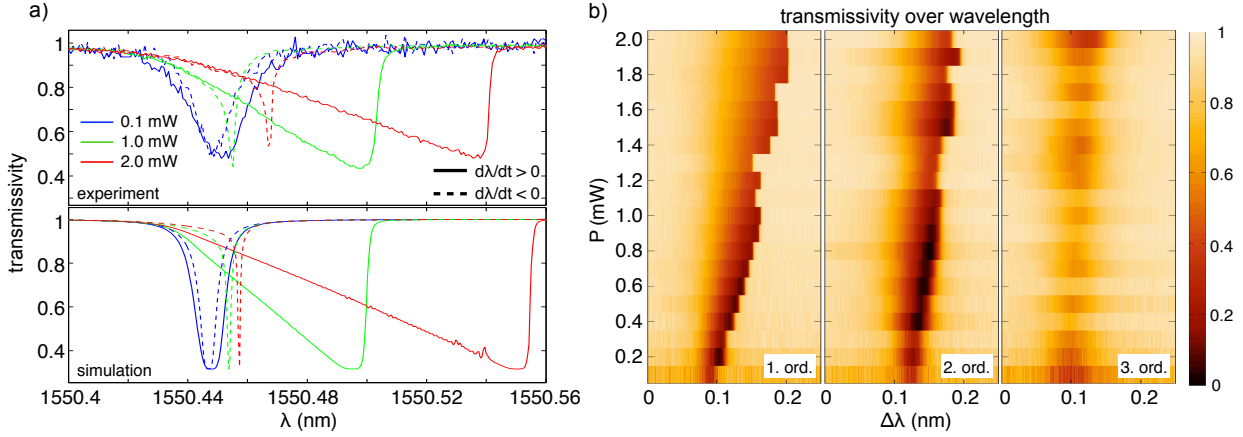


Fig. 5.3: Bistability measurements with sweeping excitation of a single microdisk (same microdisk as in Fig. 5.2). (a) For a positive wavelength sweeping ( $v_{\text{sweep}} = 40 \text{ nm s}^{-1}$ ) the resonance shape becomes asymmetric with an increasing redshift of the transmission signal minimum for increasing pump powers. A negative sweeping at the same power levels results in a narrow and weakly shifted resonance. In the lower graph corresponding simulations based on Eqs. (5.9), (5.12) and (5.13) show good agreement, although for high pump powers ( $P = 2 \text{ mW}$ ) again the onset of taper oscillations can shift the transition wavelength of the signal. (b) The bistability hysteresis is most pronounced for the first order radial modes and disappears for the third order modes caused by the reduced Q-factor.

tuning the excitation from longer to smaller wavelengths (negative sweeping) the transmission signal becomes low at the cold cavity resonance (or close to it for higher pump powers). Since the laser sweeping is opposite to the temperature induced resonance shift, the system gets off-resonant immediately. This behavior is illustrated in Fig. 5.1(b), where for the positive wavelength sweeping one has to start on the right upper corner of the graph following the high temperature branch, and for the negative sweeping one starts at the lower left corner following the low temperature branch. To observe the bistable hysteresis the sweeping time through the resonance must be on the order of or slower than the thermal relaxation [CS8]. However, it must be faster than the response of the taper oscillations to keep a constant coupling while scanning through the resonance. The maximum sweeping speed of the available tunable laser was  $40 \text{ nm s}^{-1}$ , which for a resonance with a Q-factor of about  $10^5$  results in a sweeping time through resonance of  $\tau_{\text{sweep}} \approx 250 \mu\text{s}$ . This indeed is on the order of the slow thermal relaxation time estimated above and confirms that the whole resonator is thermalized during this time due to the fast relaxation of the temperature in the pumped mode volume. As a result the excitation is much faster than the mechanical oscillation period, leading to a constant coupling strength uninfluenced by self-induced taper vibrations.

Typical measurement curves for a single disk resonance ( $\lambda = 1550.445 \text{ nm}$ , compare Fig. 5.2) in Fig. 5.3(a) show the increasing hysteresis for increasing pump powers as expected from the considerations above. For the simulation of the measured spectra Eq. (5.9) can still be used in the steady state approximation since the Q-factor corresponds to a mode relaxation time  $\tau_0 \approx 100 \text{ ps}$  much faster than  $\tau_{\text{sweep}}$ . The sweeping dynamics is introduced by an explicit time



dependence of the detuning as

$$\Delta\omega(t) = \omega_0(t) - \omega_m = \frac{2\pi c}{\lambda_0 + v_{\text{sweep}}t} - \omega_m. \quad (5.12)$$

The temperature relaxation must be calculated dynamically since  $\tau_{\text{sweep}} \approx \tau_{\text{th,s}}$  and reads as

$$\frac{d}{dt}\bar{\delta T} = -\gamma_{\text{th,s}}\bar{\delta T} + B_{\text{th}}|\bar{d}_m|^2. \quad (5.13)$$

The calculated transmission signal hystereses are plotted in the lower graph of Fig. 5.3(a) and show good agreement with the corresponding measured data. The difference in the position of the steep signal transition when comparing simulation and experiment, especially for high pump powers, is again caused by the onset of taper oscillations because the on-resonant time becomes comparable to the taper response time due to the resonance trapping effect. Nevertheless, the influence is much weaker than for the fixed wavelength pump power tunings, which allows reliable and reproducible measurement of the temperature induced nonlinearity. In Fig. 5.3(b) a comparison of the power dependent resonance shape is shown for different radial mode orders. As expected, the nonlinear resonance shift is strongest for the high-Q first order modes and decreases for increasing radial mode order. For the third order only a small shift of the resonance is observed but no distorted resonance shape or bistability hysteresis.

### 5.3 Direct measurement of the thermal relaxation time

The thermal relaxation rate in Eq. (5.13) so far was estimated from theoretical considerations and used as a fitting parameter in the calculations of thermal nonlinear effects (which is common practice in literature, e.g., see [Joh06, He09, CS3]). To reduce the uncertainties of this parameter and to possibly confirm the values from the dynamic models one has to measure the thermal relaxation time independently. Here we use a pump and probe experiment involving two separate first order resonances of a single microdisk. A sketch of the setup is shown in Fig. 5.4(a). A high power pump laser with a fixed wavelength at a microdisk resonance  $\lambda_{\text{pump}}$  is coupled through a first tapered fiber. The low power probe laser, coupled to the microdisk through a second tapered fiber, sweeps over another resonance  $\lambda_{\text{probe}}$  spectrally distinct from the pump mode. The sweep start of the probe laser triggers a pulse generator that allows to switch off the pump laser with a variable time delay  $\Delta t$  by use of an acousto-optical modulator (AOM). The switching time of the pump signal is about 200 ns, which is much faster than any thermal effects. The two tapered fibers are used to reduce the impact of taper oscillations due to the high power pump switching on the probe measurement and also allow for different coupling ratios of pump and probe signal. The probe should be coupled much less to avoid thermal or resonance broadening effects by the probe laser itself. After the microdisk the signals are filtered using wavelength-division-multiplexer (WDM) to measure only pump or

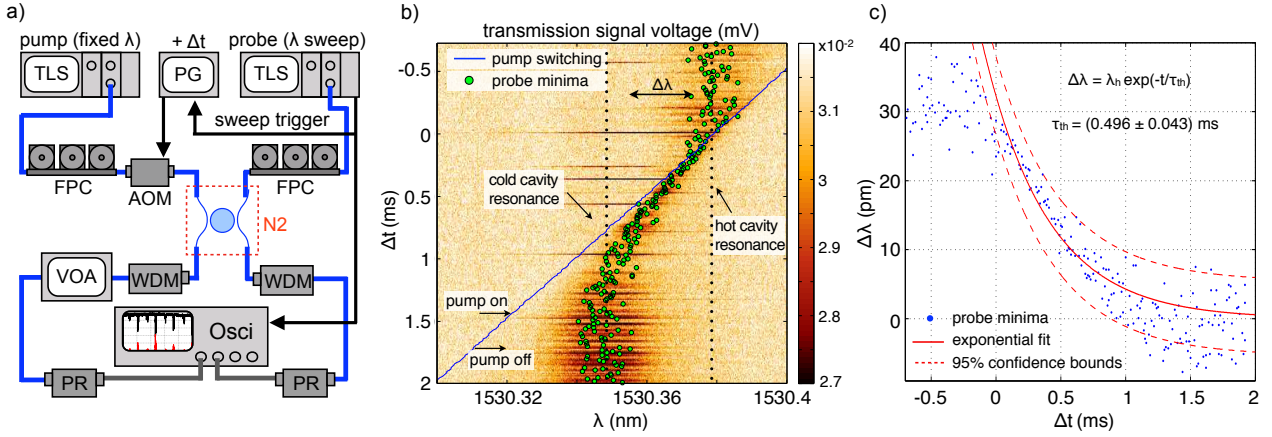


Fig. 5.4: Thermal relaxation time measurement by a pump and probe scheme. (a) The microdisk is pumped at a fixed resonance wavelength ( $\lambda_{\text{pump}} = 1543.03$  nm,  $P_{\text{pump}} = 2$  mW) and probed with a sweeping laser signal coupled through a second taper ( $\lambda_{\text{probe}} = 1530.35$  nm,  $P_{\text{probe}} = 0.1$  mW,  $v_{\text{sweep}} = 40$  nm s $^{-1}$ ). The sweeping start triggers a pulse generator (PG) driving an acousto-optical modulator (AOM), which switches off the pump laser (fall time approx. 200 ns) with a tunable time delay ( $\Delta t = 10$   $\mu$ s per sweep); TLS - tunable laser source, FPC - fiber polarization controller, N2 - nitrogen purged sample stage, WDM - wavelength division multiplexer, VOA - variable optical attenuator, PR - photo receiver, Osci - oscilloscope. (b) Measured probe transmission signal for increasing switching delay. As the switching delay of the pump approaches the sweeping delay of the probe resonance, a significant shift of the probe resonance can be observed. The green circles mark the transmission signal minimum corresponding to the resonance wavelength. (c) Plotting the resonance wavelength as a function of the switching delay (zero shifted to the hot cavity resonance), an exponential fit allows to extract the thermal relaxation time  $\tau_{\text{th}} = (0.496 \pm 0.043)$  ms.

probe in the respective arms. Starting with the pump switching at a time when the sweeping probe laser wavelength is far below  $\lambda_{\text{pump}}$ , in each subsequent sweep the switching delay was increased by  $\Delta t = 10$   $\mu$ s in order to shift the pump switching time across the time the probe laser is at the resonance  $\lambda_{\text{probe}}$ . A typical measurement is shown in Fig. 5.4(b). As the pump switching time (blue diagonal line) approaches the cold cavity probe resonance it gets shifted to its hot cavity value due to the temperature increase in the resonator. Plotting the extracted probe transmission signal minima as a function of the switching delay  $\Delta t$  [Fig. 5.4(c)] an exponential decay from hot to cold cavity resonance with a decay time of  $\tau_{\text{th}} = (0.496 \pm 0.043)$  ms was measured. For the strongly under-etched samples [compare Fig. 3.2(a)] that were used in this experiment this value agrees well with the above made estimate for the slow conducting thermal relaxation time  $\tau_{\text{th},s} \approx 420$  ms of the whole resonator (see Sect. 5.1). Measurements also reveal the independence of the relaxation time on the polarization of both pump or probe excitation. The measured total resonance shift  $\Delta\lambda = 32$  pm corresponds to  $\overline{\delta T} = 5$  K inside the disk, where the measured value  $\beta_{\text{th}} = 4 \times 10^{-6}$  K $^{-1}$  was used (see Sect. 5.5).

## 5.4 Nonlinear mode dynamics in coupled microdisks<sup>6</sup>

Since it was found in Sect. 3.4 that the advantageous characteristics of single microdisks are preserved when they are coupled to each other, we expect to observe nonlinear effects as described in Sect. 5.2 in coupled microdisks as well. Nonlinear effects in such coupled

resonator systems are of interest due to the ability of tuning the spectral response of only partial modes all optically in order to realize, e.g., sophisticated tunable filters and delay lines [Yan04, Mel10, Tob08].

For the theoretical description of the mode dynamics of coupled fused silica microdisks, taking into account thermal nonlinearity, Eqs. (5.4) and (5.6) of the single disk case can be expanded straightforwardly using the relations in Sect. 2.3.3. The resulting system of coupled nonlinear differential equations can be simplified by making use of the different time scales for the optical and thermal response. Due to the fast mode relaxation the steady state approximation of the mode amplitudes can be used, describing all dynamics on the time scale of the much slower thermal effects as done in Sect. 5.2. Further simplification can be made by assuming equal temperature coefficients for all of the individual disks in the coupled structure. This limits the observable stable solutions of the system as compared to the study of two nonidentical coupled microtoroids presented in Ref. [Gru09]. Nevertheless, the effects of inter-disk coupling as well as variable excitation of individual disks of the structure can be investigated for the used coupled disk samples. The final system of equations is written as

$$\bar{d}_{+m}^{(p)} = -\frac{i\Gamma_{\text{mc}}\bar{d}_{-m}^{(p)} + i\sum_{q=1, p \neq q}^N \Gamma_{qp}\bar{d}_{-m}^{(q)} + i\sqrt{2\Gamma_{\text{ext}}^{(p)}}\bar{a}_{\text{in}}}{i(\Delta\omega_m^{(p)} + \omega_0\beta_{\text{th}}\bar{\delta T}^{(p)}) - (\Gamma_0 + \Gamma_{\text{ext}}^{(p)})}, \quad (5.14)$$

$$\bar{d}_{-m}^{(p)} = -\frac{i\Gamma_{\text{mc}}\bar{d}_{+m}^{(p)} + i\sum_{q=1, p \neq q}^N \Gamma_{qp}\bar{d}_{+m}^{(q)}}{i(\Delta\omega_m^{(p)} + \omega_0\beta_{\text{th}}\bar{\delta T}^{(p)}) - (\Gamma_0 + \Gamma_{\text{ext}}^{(p)})}, \quad (5.15)$$

$$\frac{d}{dt}\bar{\delta T}^{(p)} = -\gamma_{\text{th},s}\bar{\delta T}^{(p)} + B_{\text{th}}(|\bar{d}_{+m}^{(p)}|^2 + |\bar{d}_{-m}^{(p)}|^2), \quad (5.16)$$

with the coefficients described in Sects. 5.1 and 5.2. Equation (5.16) is integrated numerically according to the sweeping speed dependence [Eq. (5.12)] of the frequency detuning  $\Delta\omega$  in Eqs. (5.14) and (5.15). The resulting values  $\bar{\delta T}^{(p)}(\Delta\omega)$  are then used to calculate the steady state amplitudes of  $\bar{d}_{\pm m}^{(p)}$  from which the transmissivity and the reflectivity can be calculated according to Eqs. (2.66) and (2.76). The values of the parameters used in the calculations can be found in appendix C. The coupling and loss rates ( $\Gamma$ -parameters) as well as a possible resonance detuning of the individual disks are determined independently by linear measurements as described in Sect. 3.4. The pump power applied to the system is the crucial parameter for nonlinear measurements and hence the taper transmission losses (see Sect. 3.2) have been taken into account for accurate calculations. The thermal relaxation rate  $\gamma_{\text{th}}$  was taken from the measurements in Sect. 5.3. Due to a variable radius of the silicon pedestal and hence a different thermal contact to the substrate, the relaxation rate may vary for different samples. In the following Eqs. (5.14), (5.15) and (5.16) were used to predict the spectral characteristics of two and three coupled disks for variable pump powers.

<sup>6</sup>The main results of this section are published in [CS3].

### 5.4.1 Two coupled disks

In Fig. 5.5 the measurements and simulations of the transmissivity and reflectivity for pump powers  $P_{\text{pump}} = 0.1 \text{ mW}$  to  $4.0 \text{ mW}$  are shown for the TE mode at  $\lambda_0 = 1555.3 \text{ nm}$  of the two coupled disks already investigated in the linear pump power regime in Fig. 3.9. The linear characterization reveals a resonance mismatch of the two disks, which results in a different excitation strength of the antisymmetric mode at short wavelengths [Figs. 5.5(a,c)] and the symmetric mode at long wavelengths [Figs. 5.5(b,d)]. In Fig. 5.5(a) the measured spectra for low  $P_{\text{pump}} = 0.1 \text{ mW}$  (solid line, white squares) and high  $P_{\text{pump}} = 4 \text{ mW}$  (solid line, gray dots) are shown together with the corresponding simulated transmissivity (red lines) and reflectivity (green lines). In the low power case the resonance was excited close to critical coupling. For the high pump power the coupling shifts to the undercoupled regime, which is due to an optically induced taper movement as discussed in Sect. 5.2. Using a slightly reduced  $\Gamma_{\text{ext}}$  in the simulations, this effect can be accounted for [blue dashed line in Fig. 5.5(a)]. Agreement between measurement and simulation was found and is underlined by the reproduced resonance bandwidths for low and high pump power as well as the small splitting induced by the coupling of cw and ccw modes. This feature is clearly observable in the transmission signal, whereas the reflection signal does not show that rich details. The right y-axis in Fig. 5.5(a) measures the calculated temperature variation  $\delta\bar{T}$  from the theoretical model, which is shown for disk 1 (the directly excited disk) as solid line with dark gray shading and for disk 2 as dashed line with light gray shading. The higher temperature in disk 1 indicates a higher intensity inside disk 1 than inside disk 2. A corresponding plot for the symmetric mode is shown in Fig. 5.5(b). Agreement between simulation and measurement is found in terms of resonance bandwidth and excitation strength, whereas the low power measurement is distorted and the splitting due to coupling of cw and ccw modes is not observed. The calculated higher temperature in disk 2 indicates a higher intensity for the excitation of the symmetric mode. Measurements with the excitation of disk 2 instead of disk 1 show an exchange of the excitation strengths between symmetric and antisymmetric mode, whereas the ratio of temperatures in the two disks at both resonances remains unchanged.<sup>7</sup> This indicates that the intensity distribution for each of the resonances depends only on the radius mismatch of the disks in agreement with the results in Sect. 2.2.2 and [CS5].

In Figs. 5.5(c,d) the measurements of transmissivity and reflectivity are compared to simulations for the whole pump power tuning range showing very good agreement in terms of resonance bandwidth, excitation strength and reflected intensity.<sup>8</sup> The irregular transitions of the transmissivity and reflectivity levels at the right edge of the resonances in the measured data are caused by fluctuations of the system (mainly attributed to changes in the taper excitation) as discussed in Sect. 5.2.

<sup>7</sup>The absolute value of temperatures correlates with the excitation strength.

<sup>8</sup>The transmission signals were normalized experimentally by fixing the working point of the detector using a VOA. The much weaker reflection signal was measured as is and normalized separately for each  $P_{\text{pump}}$ .

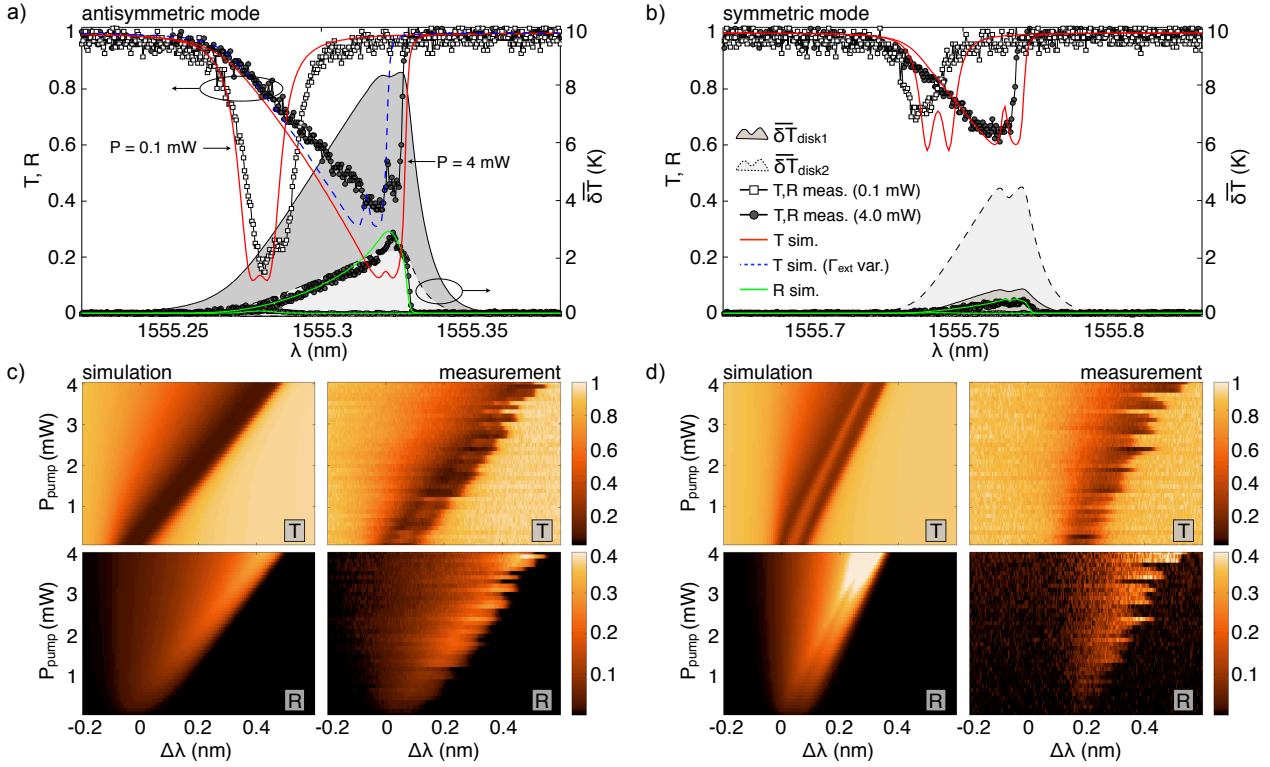


Fig. 5.5: Bistability measurements and simulations for two coupled disks with one disk (disk 1) excited by a tapered optical fiber. Comparison of measurements for  $P_{\text{pump}} = 0.1$  mW (solid line, white squares) and high  $P_{\text{pump}} = 4$  mW (solid line, gray dots) to simulations of transmissivity (red lines) and reflectivity (green lines) shows good agreement for (a) the antisymmetric mode and (b) the symmetric mode. Variations of the external coupling  $\Gamma_{\text{ext}}$  [blue dashed line in (a)] are caused by fluctuations of the taper position. The difference of the excitation strengths is caused by a resonance mismatch between the two disks and leads to differences of the temperature changes [right y-axis in (a) and (b)] expected in both disks. Simulations and measurement for the complete pump power tuning range are shown in (c) and (d) for transmissivity (T) and reflectivity (R). The sweeping speed is  $v_{\text{sweep}} = 40$  nm s $^{-1}$ .

### 5.4.2 Three coupled disks in linear arrangement

The observable effects of temperature induced resonance tuning and optical bistability for three coupled microdisks in a line arrangement are of even higher complexity due to the additional degree of freedom of the eigenmode dependent intensity distribution (see Sects. 2.2.2 and 4.5). Even in the case of identical coupled resonators the central mode of the three eigenmodes of the system shows no intensity in the center disk, whereas the intensities of the short and long wavelength modes are equally distributed in all three disks. Hence, significant differences in the power dependent spectral distortion can be expected for the excitation of different disks in the coupled disk system. Experimentally this was measured for three coupled disks of  $R_{\text{res}} = 20$   $\mu\text{m}$  and  $d_{\text{gap}} = 300$  nm, shown in Fig. 5.6. A linear characterization of the system according to Sect. 3.4 reveals a small resonance mismatch between the disks, resulting in different excitation strengths of the observable resonances. The individual disk resonances were found at  $\lambda_1 = 1543.31$  nm for disk 1,  $\lambda_2 = 1543.70$  nm for disk 2 and  $\lambda_3 = 1543.47$  nm for disk 3, which correspond to radius differences of the disks of about  $\Delta R_{\text{res}} \approx 6$  nm. Taking

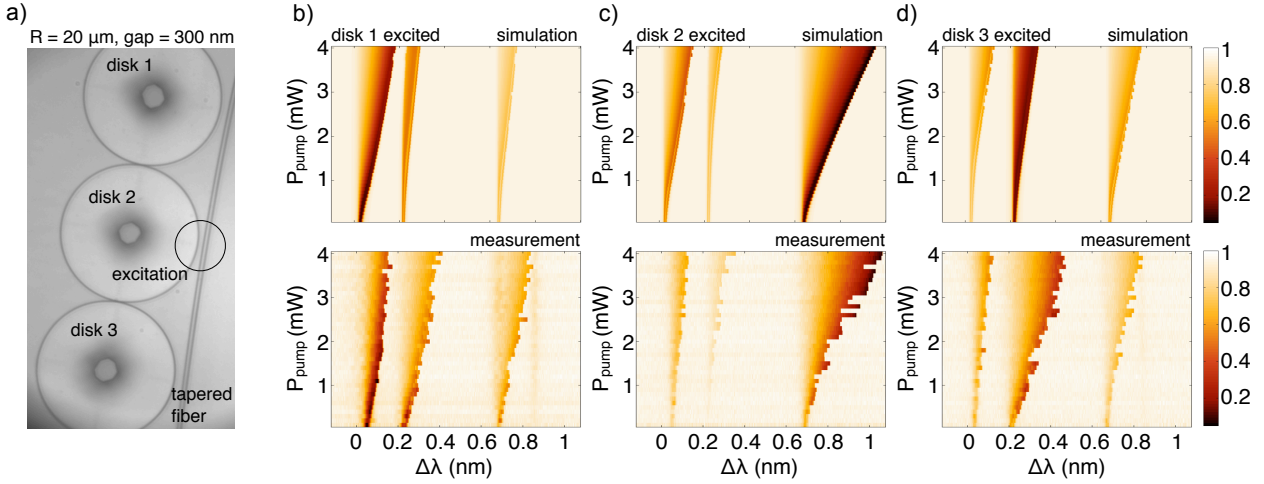


Fig. 5.6: Bistability simulations and measurements for three coupled disks shown on (a) excited at a TM mode family around  $\lambda = 1543$  nm. Changing the excited disk from (b) disk 1 over (c) disk 2 to (d) disk 3 the measured transmissivity shows different detuning for the three observable resonances when increasing the pump power. This is related to the different intensity distribution of the eigenstates of the coupled disk system and due to slight resonance mismatch between the disks. The sweeping speed is  $v_{\text{sweep}} = 40 \text{ nm s}^{-1}$ .

this into account the power dependent transmissivity can be calculated and compared to measurements as shown in Fig. 5.6 for changing the excitation from disk 1 [Fig. 5.6(b)] to disk 2 [Fig. 5.6(c)] and disk 3 [Fig. 5.6(d)]. The predicted characteristics are well reproduced in the measured data, especially for the excitation of disk 2. In that case the strong detuning of the long wavelength resonance can be explained by the strong intensity maximum in the center disk caused by the particular resonance mismatch of the disks. Pumping the center disk at the long wavelength therefore leads to a strong excitation and hence a strong heating and resonance shift. For the excitation of disk 3 the measured excitation strength and detuning of the short and long wavelength resonance are in agreement with the simulation, whereas the measurement for the central resonance shows stronger detuning. This is also the case for the central and long wavelength resonance when disk 1 is excited. A possible explanation of these observations can be heat transfer between the disks as well as different absorption and temperature relaxation rates of the individual disks, which were not taken into account in the simulation.

Nevertheless, the found characteristics can be used to selectively tune the resonances of a mode family all optically. This is demonstrated by a pump and probe experiment (according to Sect. 5.3) and the results are shown in Fig. 5.7. In the particular measurement both pump and probe were coupled to disk 3 with separate tapered fibers. For the pump a TE mode family around  $\lambda = 1550.8$  nm was chosen and the pump power was varied from  $P_{\text{pump}} = 0.1$  mW to 4 mW. For the low power probe a TE mode family around  $\lambda = 1524.8$  nm was used. Before the signals reach the detectors both wavelength ranges are separated by appropriate WDM, because in both fibers pump and probe signals are present due to the sample as a coupling element. In Fig. 5.7(a), (b) and (c) the pump wavelength was fixed at the short

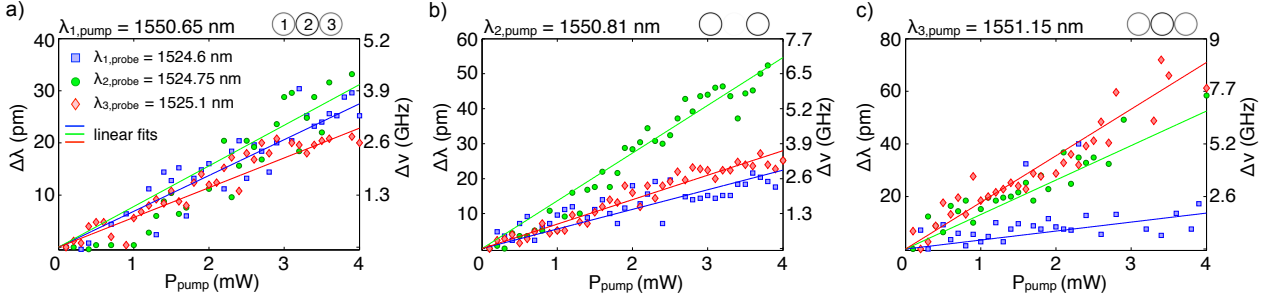


Fig. 5.7: Demonstration of a selective resonance tuning of three coupled disks using a pump and probe technique. For the pump a TE mode family around  $\lambda = 1550.8$  nm was chosen and the pump power was varied between  $P_{\text{pump}} = 0.1$  mW and  $P_{\text{pump}} = 4$  mW. For the low power probe a TE mode family was used with the resonances (from short to long wavelength)  $\lambda_{1,\text{probe}} = 1524.6$  nm (blue squares),  $\lambda_{2,\text{probe}} = 1524.75$  nm (green circles) and  $\lambda_{3,\text{probe}} = 1525.1$  nm (red diamonds). A selective tuning of the probe resonances can be observed when changing the pump wavelength: (a)  $\lambda_{1,\text{pump}} = 1550.65$  nm, almost equal tuning of all probe resonances; (b)  $\lambda_{2,\text{pump}} = 1550.81$  nm, strong tuning of  $\lambda_{2,\text{probe}}$ ; (c)  $\lambda_{3,\text{pump}} = 1551.15$  nm, strong tuning of  $\lambda_{2,\text{probe}}$  and  $\lambda_{3,\text{probe}}$ . At the top right of each graph the expected intensity distribution of the pump mode (ideal case of identical resonators) is shown. Both, pump and probe were coupled to disk 3 with separate tapered fibers.

wavelength resonance, central resonance and long wavelength resonance of the pump mode family, respectively. For each case the pump power was increased and the resonance detuning of the probe resonances at  $\lambda_{1,\text{probe}} = 1524.60$  nm,  $\lambda_{2,\text{probe}} = 1524.75$  nm and  $\lambda_{3,\text{probe}} = 1525.10$  nm were measured. When pumping at  $\lambda_{1,\text{pump}}$  all probe resonances are almost equally detuned. With the pump at  $\lambda_{2,\text{pump}}$  the central probe resonance  $\lambda_{2,\text{probe}}$  is much more strongly detuned than  $\lambda_{1,\text{probe}}$  and  $\lambda_{3,\text{probe}}$ . When the pump is fixed at  $\lambda_{3,\text{pump}}$  the central and long wavelength probe resonances  $\lambda_{2,\text{probe}}$  and  $\lambda_{3,\text{probe}}$  are strongly detuned, whereas the short wavelength probe  $\lambda_{1,\text{probe}}$  is weakly detuned. The observations are in agreement with the measurements in Fig. 5.6(d). The measured maximal detuning for the applied pump powers reaches  $\Delta\lambda = 70$  pm (corresponding to  $\Delta\nu = 8.3$  GHz) from the initial low power resonance. The spectral separation between the single resonances can be tuned from a few MHz to several GHz. This effect could be of interest for a potential application of the three coupled disks as a narrow bandwidth tunable wavelength division multiplexer (WDM). This device would allow the separation of three wavelengths with variable spectral spacing and depending on the pump wavelength three different tuning scenarios are possible:  $\lambda_1, \lambda_2, \lambda_3$  equally tuned;  $\lambda_3$  tuned differently from  $\lambda_1$  and  $\lambda_2$ ; and  $\lambda_1$  tuned differently from  $\lambda_2$  and  $\lambda_3$ .

## 5.5 Compensation of thermal nonlinearity<sup>9</sup>

The low threshold thermal nonlinear effects generally are of interest due to the dynamics they introduce to (coupled) microresonators. Besides the fundamental study to understand nonlinear interaction observable in such systems it might be of interest for possible applications, e.g., all optical switching [Alm04b]. Nevertheless, for some applications, like narrow band optical

<sup>9</sup>The main results of this section are published in [CS4].

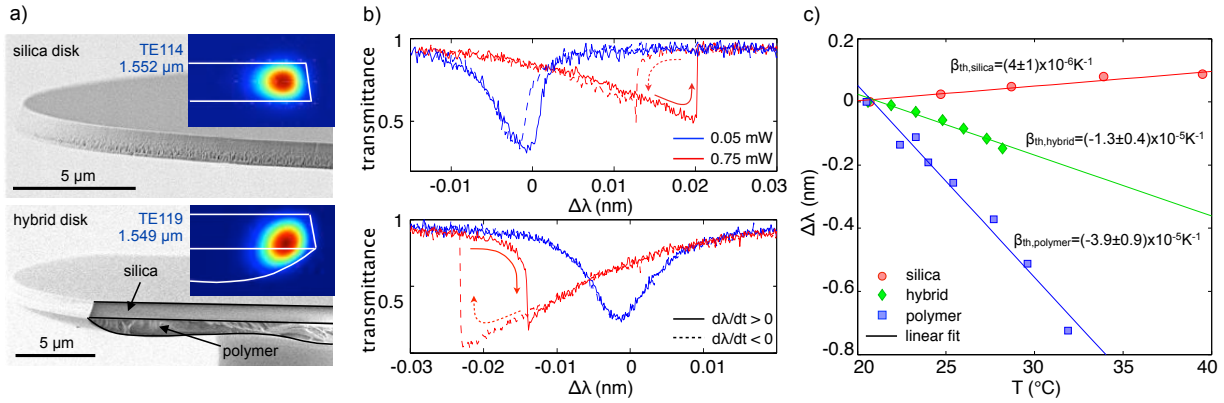


Fig. 5.8: (a) Comparison of the SEM profiles of a pure silica microdisk (top) and a hybrid microdisk containing a polymer layer (bottom), which can be deposited by additional etching steps during the fabrication. The insets show the distributions of respective first order WGMs under investigation. The partial overlap with the polymer layer results in an effective thermal coefficient (refraction and expansion) which is negative. This is indicated in (b) by the opposite nonlinear bistability sweeping curves of the two different disks. (c) Measuring the temperature induced resonance shift by heating the sample globally with a thermo-electric heater, the thermal coefficients of silica, hybrid and polymer microdisks can be measured. For the latter the silica layer on top of the polymer was removed by an additional etching step. The absolute value of the negative coefficient found for the polymer is one order of magnitude larger than for the silica.

filters [Tob08] or the stabilization of lasers [Vas03, Lia10] the dependence of the resonance wavelength on the optical pump power can be a disturbing effect. In order to avoid unwanted resonance shifts special resonator designs [Sol07a] were developed, which result in a better thermal contact to the substrate and hence a much faster relaxation. Another approach is the combination of materials with opposite thermal refractivity that partially guide the WGM, which for well designed layer thicknesses experiences an effective thermal refractivity close to zero. This approach was implemented in Ref. [He08] by deposition of polymer layers onto the microresonator using a wetting technique [Hes90] after the fabrication process.

Here we follow the approach of combining different materials in such a way that we generate the additional functional layer during the basic fabrication process. Making use of a time multiplexed deep etching process [Ayo99], which usually is used to fabricate vertically deep etched structures in silicon by alternating  $\text{SF}_6$  etching and passivation with  $\text{CHF}_3$  [Leg95] or  $\text{C}_4\text{F}_8$  [Hen12], thin fluorocarbon polymer films (Teflon) can be deposited on the surfaces of the microresonator. The polymer layer thickness is well controllable by variation of etching times and influences all samples on a wafer in the same way. In Fig. 5.8(a) a hybrid silica-polymer disk with a very thick polymer layer is shown. The polymer layer covers only the bottom surface of the disk since the top surface was protected by the chromium mask (see Fig. 3.1) during the multiplexed etching process. Removing the chromium mask before the deep etching process leads to deposition on top of the resonator, too, which allows to use thinner, more homogeneous single polymer layers with the same effect on the WGM.

The effect of the thermal properties of the polymer layer on the response of the hybrid microdisk is exemplified in Fig. 5.8(b). The high power sweeping curves show an opposite



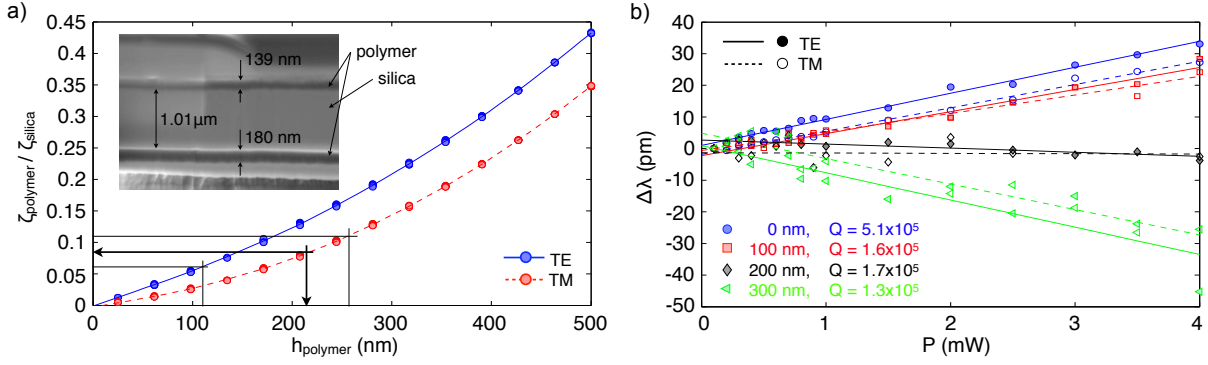


Fig. 5.9: (a) FEM calculation of the ratio of optical power fractions  $\zeta$  of the WGM in the silica and polymer layer for an increasing polymer layer thickness  $h_{\text{polymer}}$ . For the same thickness and polarization all modes (first and second radial order) show approximately the same ratio  $\zeta_{\text{polymer}}/\zeta_{\text{silica}}$ . A compensation is expected for  $h_{\text{polymer}} \approx 200$  nm (arrows) according to the measured temperature coefficients  $\beta_{\text{th}}$  of the two materials. The inset shows the profile of a tested sample with top and bottom polymer layer with a total thickness  $h_{\text{polymer}} \approx 300$  nm. (b) Pump power dependent resonance shift measurements for samples with different  $h_{\text{polymer}}$  show compensation for the 200 nm sample in agreement with the calculations. The polymer layer decreases the Q-factor only slightly as compared to the pure silica sample.

shift of the resonance compared to the pure silica disk, caused by an overcompensation of the positive thermal refractivity of silica. Although, the thickness of the polymer layer is too large for compensation, it can be used to measure the combined thermal refractivity and expansion coefficient of the polymer layer itself, since it forms a polymer microdisk after removing the silica layer by an additional etching step. To this end, the different samples (silica, hybrid and polymer disk) were placed on a thermoelectric heater and the global resonance shifts of a set of resonances around  $\lambda = 1550$  nm at low pump power (to avoid optically induced resonance shifts) were measured depending on the temperature of the sample. From the relation  $\Delta\lambda_{\text{th}} = \lambda_{T_0}\beta_{\text{th}}\delta T$  with  $\delta T = T - T_0$  the thermal refractivity and expansion coefficients  $\beta_{\text{th}} = 1/n(dn/dT) + \alpha_{\text{th}}$  of the different materials<sup>10</sup> and combinations can be obtained. The linear fit of the measured data in Fig. 5.8(c) gives the values  $\beta_{\text{th,silica}} = (4.0 \pm 0.1) \times 10^{-6} \text{ K}^{-1}$ ,  $\beta_{\text{th,hybrid}} = (-1.3 \pm 0.4) \times 10^{-5} \text{ K}^{-1}$  and  $\beta_{\text{th,polymer}} = (-3.9 \pm 0.9) \times 10^{-5} \text{ K}^{-1}$ . The measured value for the fused silica disk is close to a reported value of  $6 \times 10^{-6} \text{ K}^{-1}$  in Ref. [Car04].

The resonance shift of the hybrid microdisk depends on the temperature coefficients  $\beta_{\text{th}}$  and the particular fraction of optical power  $\zeta$  of the WGM in the corresponding layers and can be expressed as  $\Delta\lambda_{\text{th}} = \lambda_{T_0}(\beta_{\text{th},1}\zeta_1 + \beta_{\text{th},2}\zeta_2)\delta T$ . Extracting the profile of the hybrid disk from the SEM image in Fig. 5.8(a), FEM calculations of the mode distributions give a ratio of  $\zeta_{\text{polymer}}/\zeta_{\text{silica}} \approx 0.45$ . Together with the above measured thermal coefficients this results in an effective temperature coefficient of  $\beta_{\text{th,hybrid}}^{\text{eff}} = -1.44 \times 10^{-5} \text{ K}^{-1}$ , in agreement with the measured value for the hybrid disk  $\beta_{\text{th,hybrid}} = (-1.3 \pm 0.4) \times 10^{-5} \text{ K}^{-1}$ . A compensation ( $\Delta\lambda_{\text{th}} = 0$ ) can be obtained for a ratio of  $\zeta_{\text{polymer}}/\zeta_{\text{silica}} = 0.085 \pm 0.025$ . Assuming a single polymer layer, this ratio of power fractions in the two materials corresponds to a thickness of

<sup>10</sup>The refractive index of the polymer around  $\lambda = 1550$  nm was obtained by comparison of tactile and laser interferometric thickness measurements of a flat polymer layer on a silicon wafer to  $n_{\text{polymer}} = 1.47$ .

$h_{\text{polymer}} \approx 200$  nm as can be seen from FEM calculations shown in Fig. 5.9(a). The calculations are done for all first and second radial order modes in the wavelength range of  $1.4 \mu\text{m}$  to  $1.7 \mu\text{m}$ . An increase of  $h_{\text{polymer}}$  causes a red shift of all resonances according to the increased total thickness of the disk [compare Fig. 2.3(a)] but for fixed polarization and  $h_{\text{polymer}}$  all modes show approximately the same compensation ratio  $\zeta_{\text{polymer}}/\zeta_{\text{silica}} \approx 0.085$ , which allows for a broadband compensation. For TE polarization the desired ratio is reached at smaller  $h_{\text{polymer}}$  as compared to TM polarization. To test the compensation experimentally, four different samples with increasing  $h_{\text{polymer}}$  from 0 nm to 300 nm were fabricated. The polymer was deposited on already existing samples, which leads to a top and bottom layer of polymer [as shown in the inset of Fig. 5.9(a) for the 300 nm sample]. Taking the total thickness of both polymer layers, the expected compensation around 200 nm is obtained as can be seen from power dependent resonance shift measurements in Fig. 5.9(b). Since the polymer layer is relatively thin and has a smooth surface, the Q-factor is reduced only by a factor of 3 to  $Q \approx 1.7 \times 10^5$  as compared to the pure silica sample.

## Chapter summary

The nonlinear effects of single and coupled fused silica microdisks are to first order determined by temperature induced refractive index variations caused by the intrinsic optical absorption. This effect results in optical power dependent detuning of the microdisk resonances and optical bistability can be observed. It was shown that the nonlinear effects can be reliably measured by recording the pump power dependent distortion of the resonance shape when sweeping the pump laser wavelength through the resonance. In a static excitation regime strong mechanical oscillations of the bend tapered fiber can be induced, which inhibit reliable measurements, e.g., of a bistability hysteresis expected for proper pump power tuning. The thermal nonlinear effects can be taken into account in the CMT and the nonlinear resonance spectra for two and three coupled disk were calculated in agreement with measured data. A critical parameter for the nonlinear calculations is the thermal relaxation time, which was measured by a pump and probe technique and agrees with a theoretical approximation of the heat transfer from a thermalized disk to the substrate.

The found nonlinear characteristics of three coupled disks in a line arrangement allow for an all optically induced selective resonance tuning of the eigenmodes of the structures. This effect is caused by the eigenmode dependent inhomogeneous light intensity distribution in the resonators leading to a different heating of the individual coupled disks.

Finally, the compensation of the temperature induced resonance shift was demonstrated, allowing the stabilization of the resonance wavelength for a broad range of applied pump powers to the system. The compensation was realized by deposition of a properly sized polymer layer during the fabrication process of the disks showing a negative thermal refractivity.

## 6 Summary and perspective

In this work we have investigated ensembles of fused silica coupled optical disk microresonators in order to gain insight into the dynamics of the optical modes supported by such structures. One of the main questions deals with the impact of the optical coupling of WGM microresonators on the advantageous properties of individual microresonators. The particular characteristics which are of interest are the high quality factor and the small mode volume. They are related to the low threshold nonlinear effects observable in microresonators as well as the high sensitivity of the narrow band resonances on perturbations of the system, useful for sensing applications.

The choice of microdisks as a particular realization of coupled optical microresonators was accounted for by the fact that the optical coupling of microresonators relies mainly on the spectral overlap of their individual resonances. As with increasing Q-factor the resonance bandwidth decreases, it is a challenging task to achieve spectrally coinciding resonances of the individual microresonators, which demands a highly accurate and reproducible fabrication. Furthermore, the spatial overlap of the fields in the individual resonators is critical for efficient coupling and should on the one hand be variable for optimization and on the other hand stable for reliable experiments. To meet these requirements, in this thesis an electron beam lithography was used with subsequent etching steps to process the involved materials. The choice of etchants was optimized to allow for the fabrication of large scale arrays of coupled microdisks. With respect to the demands on a finite distance between the coupled microresonators and the reproducibility, the fabrication does not involve any reflow process, e.g., of the resist or the final coupled microresonators. The advantage of the particular realization of microdisks is twofold: First, the fabrication technique and the geometric peculiarities limit the Q-factor to the order of  $10^5$  to  $10^6$ , which can be translated to an acceptable size mismatch of the individual microdisks on the order of a few nanometers. This is captured by the accuracy and reproducibility of the used fabrication technique. Second, the on-chip microdisks are a highly flexible sample platform in terms of the variety of coupling arrangements, which can be characterized by a standardized experimental setup.

From a theoretical point of view the efficient mathematical description of optical microresonators depends strongly on their particular realization. Analytical solutions in 3D are possible only for spherical or spheroidal microresonators, whereas toroids and disks have to be treated approximately. As for the different resonator shapes and particular characteristics under in-

investigation various theoretical models are used in literature, one aim of this thesis was to summarize and extend existing approaches for a comprehensive analysis. In the particular case of circular microdisks the formulation of an analytical 2D scattering problem as well as a numerical finite element method were used. From these models resonance frequencies, Q-factors and mode volumes of single microdisks were calculated from their basic material and geometry parameters. The 2D scattering approach was extended to calculate the spectrum and mode distribution of coupled microdisks in a fast and reliable manner. Furthermore, a thorough description of the temporal mode dynamics in coupled microresonators based on a coupled mode theory (CMT) was presented. Several effects like intra-disk modal coupling, inter-disk coupling and the excitation by an external field as well as thermal nonlinearity can be treated perturbatively. This approach is quite universal and not restricted to coupled microdisks.

To verify the predictions of the theoretical models and to characterize the fabricated samples an automated experimental setup was developed and built. The excitation of the microdisks was realized by the use of tapered optical fibers. The setup allows to couple two tapered fibers at the same time to different microdisks of a coupled resonator sample in order to carry out pump and probe experiments. Additionally, a scanning near field optical microscope (SNOM) was installed for the implementation of near field mode mappings.

As a main part of this thesis, the mode mapping technique was realized, which uses a scattering SNOM tip to perturb the system of tapered fiber and excited microdisks. Depending on the position of the SNOM tip above the sample, the perturbation has a significant effect on the resonance spectrum of the microdisks, which alters the measured transmission and reflection signals at the tapered fiber. A combination of the CMT and the 2D calculations of the mode distribution in coupled disks allows for a detailed investigation of the system response taking into account the position dependent SNOM perturbation. A comparison between theory and experiment can be used to extract the intensity distribution of modes of coupled microdisks from the measured signals. This method, for the first time, allows experimental insight into the manifold distributions and symmetries of near fields of eigenmodes in coupled microresonators.

In the last part of this thesis the optically induced thermal nonlinearity in coupled microdisks was investigated experimentally and theoretically. An optical bistability was observed for pump powers in the low milliwatt regime which strongly depends on the inter-disk coupling and the resonance mismatch of the individual disks. Additionally, the thermal relaxation time of the microdisks was measured to a few hundreds of microseconds. For the particular experimental conditions this reveals the thermalization of the whole disk heated by the intensity located in the mode volume. The limiting time scale in this case is the relaxation of the whole disk due to conductive heat transfer into the substrate. Using the obtained knowledge of specific intensity distributions of different eigenmodes of the coupled microdisks in conjunction with the nonlinear effects, a selective all optical tuning of the resonances in such

systems was achieved.

As for potential applications the power dependent resonance shift is undesired, a broadband compensation of the thermal nonlinearity was demonstrated by an additional functional layer with an opposite thermal refractivity. As compared to existing approaches using a post-fabrication deposition of polymers on single resonators here a different method was developed. Additional etching steps allow for the precise deposition of polymer during the fabrication process leading to homogenous layers on all microdisks throughout the whole sample.

To seize on the initially asked question concerning the preservation of characteristic properties of optical microresonators when they are coupled to each other, a positive answer can be given from the obtained results in this thesis. Perspectively, further routes of investigations on coupled microresonators can be identified based on this work. Considering technical aspects, the quality of the samples might be further increased by reviewing the fabrication process or by removing fabrication induced errors in the sample geometry, e.g., using focused ion beam assisted etching. Furthermore, the mode mapping technique can be extended by an interferometric detection scheme for direct phase measurements of the fields in microdisks [Bla10]. So far the implemented method measures only intensities and the phase of the fields in adjacent disks is inferred from interference phenomena in the gap between the disks. Another interesting approach would be the use of a thermo-couple SNOM tip [Fish94] that is able to map the temperature distribution above the sample by direct heating or measure the intensity distribution due to absorptive heating of the tip. First experiments following this approach reveal a very high sensitivity, allowing to measure the intensity distribution of higher radial order low-Q modes in coupled microdisks.

Focused on fundamental physical characteristics the nonlinear effects could be investigated in a wider range of system parameters. In the presented analysis strongly coupled, almost identical disks were used, resulting in spectrally well separated resonances not influencing each other also in the high pump power regime. The situation is expected to change for the case of very weakly coupled disks with spectrally closely spaced resonances if either the Q-factors of adjacent disks of the coupled system or their excitation strength is different. Upon pump power increase particular modes may become unstable and the corresponding resonances may disappear in the spectrum as discussed for two nonidentical coupled microtoroids in [Gru09]. In addition, not only the size of the coupled microresonators but also their shape could be chosen on purpose, which would extend the coupled microresonator research to the field of chaotic microcavities [Nöc97, Son11].

From an application's point of view, the combination of the obtained results from the mode mapping experiments with the observed nonlinear effects widens the scope of possible applications of coupled microresonators. One may think of optically tunable frequency filters based on the selective optical resonance tuning or the generation of optically tunable signals in the GHz range using the difference frequency of the resonances. Another example would

be the use of coupled microresonators as sensors allowing for position detection with respect to the microdisk in the coupled arrangement. This would be based on the selective resonance detuning depending on the location of the perturbation of the coupled resonator structure. Such possible applications of microresonators stand and fall with the stability of the external coupling, which was a critical task also in this more fundamental study. Using tapered fibers would make it necessary to passively [War08, Lou10] or actively [O'S11] stabilize the coupling. Another way is to switch to more rigid concepts, e.g., prism coupling but with the drawback of less coupling efficiency or including the coupling waveguide on-chip.

This consequently motivates the concluding remark. In general, the applied methods and obtained results are applicable to microresonators based on other material systems. On the one hand they would be closer to real world applications like for silicon on insulator systems [Alm04a, Sol07a]. On the other hand additional physical effects can be introduced and investigated like free carrier dispersion in silicon microresonators [Joh06], properties of semiconductors like gallium arsenide [Din10a] or strong second order nonlinear polarization in lithium niobate microresonators [Für10]. Introducing the coupled resonator concept into these fields will open up further and even more interesting studies.

# A Bibliography

- [Abr72] M. Abramowitz and I. A. Stegun: *Handbook of Mathematical Functions with Formulas, Graphs, and Mathematical Tables* (Dover Publications, New York, 1972)
- [Agh06] I. Agha, J. Sharping, M. Foster, and A. Gaeta: “Optimal sizes of silica microspheres for linear and nonlinear optical interactions,” *Appl. Phys. B: Lasers Opt.* **83** (2), 303 (2006)
- [Alm04a] V. Almeida, C. Barrios, R. Panepucci, and M. Lipson: “All-optical control of light on a silicon chip,” *Nature* **431** (7012), 1081 (2004)
- [Alm04b] V. Almeida and M. Lipson: “Optical bistability on a silicon chip,” *Opt. Lett.* **29** (20), 2387 (2004)
- [Arm03] D. Armani, T. J. Kippenberg, S. M. Spillane, and K. J. Vahala: “Ultra-high-Q toroid microcavity on a chip,” *Nature* **421** (6926), 925 (2003)
- [Arm05] A. Armani, D. Armani, B. Min, K. J. Vahala, and S. M. Spillane: “Ultra-high-Q microcavity operation in H<sub>2</sub>O and D<sub>2</sub>O,” *Appl. Phys. Lett.* **87**, 151118 (2005)
- [Arm07] A. Armani, R. Kulkarni, and S. Fraser: “Label-free, single-molecule detection with optical microcavities,” *Science* (2007)
- [Arn03] S. Arnold, M. Khoshshima, I. Teraoka, S. Holler, and F. Vollmer: “Shift of whispering-gallery modes in microspheres by protein adsorption,” *Opt. Lett.* **28** (4), 272 (2003)
- [Ast04] V. N. Astratov, J. Franchak, and S. Ashili: “Optical coupling and transport phenomena in chains of spherical dielectric microresonators with size disorder,” *Appl. Phys. Lett.* **85**, 5508 (2004)
- [Ast07] V. Astratov and S. Ashili: “Percolation of light through whispering gallery modes in 3d lattices of coupled microspheres,” *Opt. Express* **15** (25), 17351 (2007)
- [Ayo99] A. Ayon, R. Braff, C. Lin, H. Sawin, and M. Schmidt: “Characterization of a time multiplexed inductively coupled plasma etcher,” *J. Electrochem. Soc.* **146** (1), 339 (1999)
- [Bal99] M. Balistreri and D. Klunder: “Visualizing the whispering gallery modes in a cylindrical optical microcavity,” *Opt. Lett.* **24** (24), 1829 (1999)
- [Bay98] M. Bayer, T. Gutbrod, J. Reithmaier, A. Forchel, T. Reinecke, P. Knipp, A. Dremin, and V. Kulakovskii: “Optical modes in photonic molecules,” *Phys. Rev. Lett.* **81** (12), 2582 (1998)

- [Bec11] T. Beckmann, H. Linnenbank, H. Steigerwald, B. Sturman, D. Haertle, K. Buse, and I. Breunig: “Highly tunable low-threshold optical parametric oscillation in radially poled whispering gallery resonators,” *Phys. Rev. Lett.* **106** (14), 143903 (2011)
- [Ber94] J. Berenger: “A perfectly matched layer for the absorption of electromagnetic waves,” *J. Comput. Phys.* **114** (2), 185 (1994)
- [Bir92] T. A. Birks and Y. Li: “The shape of fiber tapers,” *J. Lightwave Technol.* **10** (4), 432 (1992)
- [Bla10] S. Blaize, F. Gesuele, I. Stefanon, A. Bruyant, G. L  rondel, P. Royer, B. Martin, A. Morand, P. Benech, and J. Fedeli: “Real-space observation of spectral degeneracy breaking in a waveguide-coupled disk microresonator,” *Opt. Lett.* **35** (19), 3168 (2010)
- [Boh83] C. F. Bohren and D. R. Huffman: *Absorption and Scattering of Light by Small Particles* (Wiley, New York, 1983)
- [Bor04] S. Boriskina, P. Sewell, T. Benson, and A. Nosich: “Accurate simulation of two-dimensional optical microcavities with uniquely solvable boundary integral equations and trigonometric Galerkin discretization,” *J. Opt. Soc. Am. A* **21** (3), 393 (2004)
- [Bor05] M. Borselli, T. Johnson, and O. Painter: “Beyond the Rayleigh scattering limit in high-Q silicon microdisks: Theory and experiment,” *Opt. Express* **13** (5), 1515 (2005)
- [Bor06a] S. Boriskina: “Spectrally engineered photonic molecules as optical sensors with enhanced sensitivity: A proposal and numerical analysis,” *J. Opt. Soc. Am. B* **23** (8), 1565 (2006)
- [Bor06b] S. Boriskina: “Theoretical prediction of a dramatic Q-factor enhancement and degeneracy removal of whispering gallery modes in symmetrical photonic molecules,” *Opt. Lett.* **31** (3), 338 (2006)
- [Bor06c] S. Boriskina, V. Pishko, and A. Boriskin: “Optical spectra and output coupling engineering in hybrid WG-mode micro-and meso-scale cavity structures,” *2006 International Conference on Transparent Optical Networks* **1**, 84 (2006)
- [Bor06d] M. Borselli: *High-Q microresonators as lasing elements for silicon photonics*, Ph.D. thesis, California Institute of Technology (2006)
- [Bor06e] S. V. Boriskina, T. M. Benson, P. Sewell, and A. I. Nosich: “Q factor and emission pattern control of the WG modes in notched microdisk resonators,” *IEEE J. Sel. Top. Quantum Electron.* **12** (1), 52 (2006)
- [Bor07] S. Boriskina: “Spectral engineering of bends and branches in microdisk coupled-resonator optical waveguides,” *Opt. Express* **15** (25), 17371 (2007)



- [Boy01] R. Boyd and J. Heebner: “Sensitive disk resonator photonic biosensor,” *Appl. Opt.* **40**, 5742 (2001)
- [Boy03] R. W. Boyd: *Nonlinear Optics* (Academic Press, London, 2003)
- [Bra89] V. Braginsky, M. Gorodetsky, and V. Ilchenko: “Quality-factor and nonlinear properties of optical whispering-gallery modes,” *Phys. Lett. A* **137** (7-8), 393 (1989)
- [Cam91] A. Campillo, J. Eversole, and H. Lin: “Cavity quantum electrodynamic enhancement of stimulated emission in microdroplets,” *Phys. Rev. Lett.* **67** (4), 437 (1991)
- [Car04] T. Carmon, L. Yang, and K. J. Vahala: “Dynamical thermal behavior and thermal self-stability of microcavities,” *Opt. Express* **12** (20), 4742 (2004)
- [Car08] T. Carmon, H. G. L. Schwefel, L. Yang, M. Oxborrow, A. D. Stone, and K. J. Vahala: “Static envelope patterns in composite resonances generated by level crossing in optical toroidal microcavities,” *Phys. Rev. Lett.* **100** (10), 1 (2008)
- [Che94] W. Chew and W. Weedon: “A 3D perfectly matched medium from modified Maxwell’s equations with stretched coordinates,” *Microwave Opt. Technol. Lett.* **7** (13), 599 (1994)
- [Chr07] I. Chremmos and N. Uzunoglu: “Properties of regular polygons of coupled microring resonators,” *Appl. Opt.* **46** (31), 7730 (2007)
- [Col93] L. Collot, V. Lefèvre-Seguin, M. Brune, J. M. Raimond, and S. Haroche: “Very high-Q whispering-gallery mode resonances observed on fused silica microspheres,” *Europhys. Lett.* **23** (5), 327 (1993)
- [Cul76] A. Cullen: “Total internal reflection of a beam-wave at a curved interface,” *Ann. Telecommun.* **31** (11), 359 (1976)
- [Dav82] J. Davies, F. Fernandez, and G. Philippou: “Finite element analysis of all modes in cavities with circular symmetry,” *IEEE Trans. Microwave Theory Tech.* **30** (11), 1975 (1982)
- [Del07] P. Del’Haye, A. Schliesser, O. Arcizet, T. Wilken, R. Holzwarth, and T. Kippenberg: “Optical frequency comb generation from a monolithic microresonator,” *Nature* **450** (7173), 1214 (2007)
- [Det08] C. P. Dettmann, G. V. Morozov, M. Sieber, and H. Waalkens: “Directional emission from an optical microdisk resonator with a point scatterer,” *Europhys. Lett.* **82** (3), 34002 (2008)
- [Dey06] L. I. Deych and O. Roslyak: “Photonic band mixing in linear chains of optically coupled microspheres,” *Phys. Rev. E* **73** (3), 036606 (2006)
- [Din10a] L. Ding, C. Baker, P. Senellart, A. Lemaitre, S. Ducci, G. Leo, and I. Favero: “High frequency GaAs nano-optomechanical disk resonator,” *Phys. Rev. Lett.* **105** (26), 263903 (2010)

- [Din10b] L. Ding, C. Belacel, S. Ducci, G. Leo, and I. Favero: “Ultralow loss single-mode silica tapers manufactured by a microheater,” *Appl. Opt.* **49** (13), 2441 (2010)
- [Dom11] J. L. Dominguez-Juarez, G. Kozyreff, and J. Martorell: “Whispering gallery microresonators for second harmonic light generation from a low number of small molecules,” *Nat. Commun.* **2**, 254 (2011)
- [Dri07] A. Driessen, D. Geuzebroek, E. Klein, R. Dekker, R. Stoffer, and C. Bornholdt: “Propagation of short lightpulses in microring resonators: Ballistic transport versus interference in the frequency domain,” *Opt. Commun.* **270** (2), 217 (2007)
- [Dub08] R. Dubertrand, E. Bogomolny, N. Djellali, M. Lebental, and C. Schmit: “Circular dielectric cavity and its deformations,” *Phys. Rev. A* **77** (1), 013804 (2008)
- [Dun01] H. Dung, L. Knöll, and D. Welsch: “Decay of an excited atom near an absorbing microsphere,” *Phys. Rev. A* **64** (1), 013804 (2001)
- [Eic07] M. Eichenfield, C. Michael, R. Perahia, and O. Painter: “Actuation of micro-optomechanical systems via cavity-enhanced optical dipole forces,” *Nat. Photonics* **1** (7), 416 (2007)
- [Fom05] A. Fomin, M. Gorodetsky, I. S. Grudinin, and V. Ilchenko: “Nonstationary nonlinear effects in optical microspheres,” *J. Opt. Soc. Am. B* **22** (2), 459 (2005)
- [Ful91] K. Fuller: “Optical resonances and two-sphere systems,” *Appl. Opt.* **30** (33), 4716 (1991)
- [Für10] J. U. Fürst, D. V. Strelakov, D. Elser, M. Lassen, U. L. Andersen, C. Marquardt, and G. Leuchs: “Naturally phase-matched second-harmonic generation in a whispering-gallery-mode resonator,” *Phys. Rev. Lett.* **104** (15), 153901 (2010)
- [Gaa06] O. Gaathon, J. Culic-Viskota, M. Mihnev, I. Teraoka, and S. Arnold: “Enhancing sensitivity of a whispering gallery mode biosensor by subwavelength confinement,” *Appl. Phys. Lett.* **89**, 223901 (2006)
- [Gar61] C. Garrett, W. Kaiser, and W. Bond: “Stimulated emission into optical whispering modes of spheres,” *Phys. Rev.* **124**, 1807 (1961)
- [Gér96] J. Gérard, D. Barrier, J. Marzin, R. Kuszelewicz, L. Manin, E. Costard, V. Thierry-Mieg, and T. Rivera: “Quantum boxes as active probes for photonic microstructures: The pillar microcavity case,” *Appl. Phys. Lett.* **69** (4), 449 (1996)
- [Ger04] H. Gersen, D. Klunder, J. Korterik, A. Driessen, and N. van Hulst: “Propagation of a femtosecond pulse in a microresonator visualized in time,” *Opt. Lett.* **29** (11), 1291 (2004)
- [Gib85] H. Gibbs: *Optical bistability: Controlling light with light*, Quantum electronics—principles and applications (Academic Press, 1985)
- [Gor94] M. Gorodetsky and V. Ilchenko: “High-Q optical whispering-gallery microresonators: Precession approach for spherical mode analysis and emission patterns with prism couplers,” *Opt. Commun.* **113** (1-3) (1994)

- [Gor96] M. Gorodetsky, A. Savchenkov, and V. Ilchenko: “Ultimate Q of optical microsphere resonators,” *Opt. Lett.* **21** (7), 453 (1996)
- [Gor99] M. Gorodetsky and V. Ilchenko: “Optical microsphere resonators: Optimal coupling to high-Q whispering-gallery modes,” *J. Opt. Soc. Am. B* **16** (1), 147 (1999)
- [Gor00] M. Gorodetsky, A. Pryamikov, and V. Ilchenko: “Rayleigh scattering in high-Q microspheres,” *J. Opt. Soc. Am. B* (2000)
- [Gor04] M. Gorodetsky and I. S. Grudinin: “Fundamental thermal fluctuations in microspheres,” *J. Opt. Soc. Am. B* **21** (4), 697 (2004)
- [Göt01] S. Götzinger, S. Demmerer, O. Benson, and V. Sandoghdar: “Mapping and manipulating whispering gallery modes of a microsphere resonator with a near-field probe.” *J. Microsc.* **202** (1), 117 (2001)
- [Gre99] A. Greenwood and J. Jin: “A novel efficient algorithm for scattering from a complex BOR using mixed finite elements and cylindrical PML,” *IEEE Trans. Antennas Propag.* **47** (4), 620 (1999)
- [Gri08] C. Grillet, S. Bian, E. Magi, and B. Eggleton: “Fiber taper coupling to chalcogenide microsphere modes,” *Appl. Phys. Lett.* **92**, 171109 (2008)
- [Gru06] I. Grudinin, A. Matsko, A. Savchenkov, D. Strekalov, V. Ilchenko, and L. Maleki: “Ultra high-Q crystalline microcavities,” *Opt. Commun.* **265** (1), 33 (2006)
- [Gru09] I. Grudinin and K. J. Vahala: “Thermal instability of a compound resonator,” *Opt. Express* **17** (16), 14088 (2009)
- [Ham10] M. Hammer: “HCMT models of optical microring-resonator circuits,” *J. Opt. Soc. Am. B* (2010)
- [Har05] Y. Hara, T. Mukaiyama, K. Takeda, and M. Kuwata-Gonokami: “Heavy photon states in photonic chains of resonantly coupled cavities with supermonodispersive microspheres,” *Phys. Rev. Lett.* **94** (20), 203905 (2005)
- [Hau84] H. A. Haus: *Waves and Fields in Optoelectronics* (Englewood Cliffs, New Jersey 07632, 1984)
- [He08] L. He, Y. Xiao, C. Dong, J. Zhu, V. Gaddam, and L. Yang: “Compensation of thermal refraction effect in high-Q toroidal microresonator by polydimethylsiloxane coating,” *Appl. Phys. Lett.* **93** (20), 1102 (2008)
- [He09] L. He, Y. Xiao, J. Zhu, S. Ozdemir, and L. Yang: “Oscillatory thermal dynamics in high-Q PDMS-coated silica toroidal microresonators,” *Opt. Express* **17**, 9571 (2009)
- [Hec00] B. Hecht, B. Sick, U. Wild, V. Deckert, R. Zenobi, O. Martin, and D. Pohl: “Scanning near-field optical microscopy with aperture probes: Fundamentals and applications,” *J. Chem. Phys.* **112**, 7761 (2000)
- [Hee04] J. Heebner, P. Chak, S. Pereira, J. Sipe, and R. Boyd: “Distributed and localized

- feedback in microresonator sequences for linear and nonlinear optics,” *J. Opt. Soc. Am. B* **21** (10), 1818 (2004)
- [Hej93] H. Hejase: “On the use of Davidenko’s method in complex root search,” *IEEE Trans. Microw. Theory Tech.* **41** (1), 141 (1993)
- [Hen12] M. D. Henry and A. Scherer: *Microelectronics to Nanoelectronics: Materials, Devices & Manufacturability* (CRC Press, Boca Raton, FL 33487, 2012)
- [Hes90] F. Heslot, A. M. Cazabat, P. Levinson, and N. Fraysse: “Experiments on wetting on the scale of nanometers: Influence on the surface energy,” *Phys. Rev. Lett.* **65** (5), 599 (1990)
- [Hir05] K. R. Hiremath: *Coupled mode theory based modeling and analysis of circular optical microresonators*, Ph.D. thesis, University of Twente (2005)
- [Hop81] R. Hoppe: “A penalty method for the approximate solution of stationary Maxwell equations,” *Numer. Math.* **36** (4), 389 (1981)
- [Hop06] W. Hopman, K. V. D. Werf, A. Hollink, W. Bogaerts, V. Subramaniam, and R. D. Ridder: “Nano-mechanical tuning and imaging of a photonic crystal micro-cavity resonance,” *Opt. Express* **14** (19), 8745 (2006)
- [HZ07] M. Hossein-Zadeh and K. J. Vahala: “Free ultra-high-Q microtoroid: A tool for designing photonic devices,” *Opt. Express* **15** (1), 166 (2007)
- [Ilc92] V. Ilchenko and M. Gorodetsky: “Thermal nonlinear effects in optical whispering gallery microresonators,” *Laser Phys.* **2** (6), 1004 (1992)
- [Ilc03] V. Ilchenko, A. Matsko, A. Savchenkov, and L. Maleki: “Low-threshold parametric nonlinear optics with quasi-phase-matched whispering-gallery modes,” *J. Opt. Soc. Am. B* **20** (6), 1304 (2003)
- [Ilc04] V. Ilchenko, A. Savchenkov, A. B. Matsko, and L. Maleki: “Nonlinear optics and crystalline whispering gallery mode cavities,” *Phys. Rev. Lett.* **92** (4), 043903 (2004)
- [Ilc06] V. Ilchenko and A. B. Matsko: “Optical resonators with whispering-gallery modes—part II: Applications,” *IEEE J. Sel. Top. Quantum Electron.* **12** (1), 15 (2006)
- [Ish06] S. Ishii, A. Nakagawa, and T. Baba: “Modal characteristics and bistability in twin microdisk photonic molecule lasers,” *IEEE J. Sel. Top. Quantum Electron.* **12** (1), 71 (2006)
- [Jac99] J. D. Jackson: *Classical Electrodynamics* (Wiley, New York, 1999), 3rd edn.
- [Jia09] X. Jiang, Q. Lin, J. Rosenberg, K. J. Vahala, and O. Painter: “High-Q double-disk microcavities for cavity optomechanics,” *Opt. Express* (2009)
- [Jin02] J. Jin: *The Finite Element Method in Electromagnetics* (Wiley, New York, 2002), 2nd edn.

- [Joa95] J. D. Joannopoulos, R. D. Meade, and J. N. Winn: *Photonic Crystals: Molding the Flow of Light* (Princeton University Press, New Jersey, 1995)
- [Joh02] S. Johnson, M. Ibanescu, M. Skorobogatiy, O. Weisberg, J. Joannopoulos, and Y. Fink: “Perturbation theory for Maxwell’s equations with shifting material boundaries,” *Phys. Rev. E* **65**, 066611 (2002)
- [Joh06] T. Johnson, M. Borselli, and O. Painter: “Self-induced optical modulation of the transmission through a high-Q silicon microdisk resonator,” *Opt. Express* **14** (2), 817 (2006)
- [Joh09] T. Johnson: *Silicon Microdisk Resonators for Nonlinear Optics and Dynamics*, Ph.D. thesis, California Institute of Technology (2009)
- [Kim06] H. Kimble: “Strong interactions of single atoms and photons in cavity QED,” *Phys. Scr.* **T76**, 127 (1998)
- [Kip02] T. J. Kippenberg, S. M. Spillane, and K. J. Vahala: “Modal coupling in traveling-wave resonators,” *Opt. Lett.* **27** (19), 1669 (2002)
- [Kip03] T. J. Kippenberg, S. M. Spillane, D. Armani, and K. J. Vahala: “Fabrication and coupling to planar high-Q silica disk microcavities,” *Appl. Phys. Lett.* **83** (4), 797 (2003)
- [Kip04a] T. J. Kippenberg: *Nonlinear Optics in Ultra-high-Q Whispering-Gallery Optical Microcavities*, Ph.D. thesis, California Institute of Technology (2004)
- [Kip04b] T. J. Kippenberg, S. M. Spillane, and K. J. Vahala: “Kerr-nonlinearity optical parametric oscillation in an ultrahigh-Q toroid microcavity,” *Phys. Rev. Lett.* **93** (8), 83904 (2004)
- [Kip07] T. Kippenberg and K. Vahala: “Cavity opto-mechanics,” *Opt. Express* **15** (25), 17172 (2007)
- [Kip08] T. J. Kippenberg and K. J. Vahala: “Cavity optomechanics: Back-action at the mesoscale,” *Science* **321** (5893), 1172 (2008)
- [Kli99] V. Klimov, M. Ducloy, and V. Letokhov: “Strong interaction between a two-level atom and the whispering-gallery modes of a dielectric microsphere: Quantum-mechanical consideration,” *Phys. Rev. A* **59** (4), 2996 (1999)
- [Kni97] J. Knight, G. Cheung, F. Jacques, and T. A. Birks: “Phase-matched excitation of whispering-gallery-mode resonances by a fiber taper,” *Opt. Lett.* **22** (15), 1129 (1997)
- [Koe05] A. Koenderink, M. Kafesaki, B. Buchler, and V. Sandoghdar: “Controlling the resonance of a photonic crystal microcavity by a near-field probe,” *Phys. Rev. Lett.* **95** (15), 153904 (2005)
- [Kon77] A. Konrad: “High-order triangular finite elements for electromagnetic waves in anisotropic media,” *IEEE Trans. Microw. Theory Tech.* **25** (5), 353 (1977)

- [Kos84] M. Koshiba, K. Hayata, and M. Suzuki: “Vectorial finite-element method without spurious solutions for dielectric waveguide problems,” *Electron. Lett.* **20** (10), 409 (1984)
- [Kuz83] M. Kuznetsov and H. A. Haus: “Radiation loss in dielectric waveguide structures by the volume current method,” *IEEE J. Quantum Electron.* **19** (10), 1505 (1983)
- [Lal07] L. Lalouat, B. Cluzel, P. Velha, E. Picard, D. Peyrade, J. Hugonin, P. Lalanne, E. Hadji, and F. de Fornel: “Near-field interactions between a subwavelength tip and a small-volume photonic-crystal nanocavity,” *Phys. Rev. B* **76** (4), 041102 (2007)
- [Leg95] R. Legtenberg, H. Jansen, M. B. de, and M. Elwenspoek: “Anisotropic reactive ion etching of silicon using SF<sub>6</sub>/O<sub>2</sub>/CHF<sub>3</sub> gas mixtures,” *J. Electrochem. Soc.* **142** (6), 2020 (1995)
- [Lei68] R. Leis: “Zur Theorie elektromagnetischer Schwingungen in anisotropen inhomogenen Medien,” *Math. Zeitschr.* **106** (3), 213 (1968)
- [Lev93] A. F. J. Levi, R. E. Slusher, S. L. McCall, J. L. Glass, S. J. Pearton, and R. A. Logan: “Directional light coupling from microdisk lasers,” *Appl. Phys. Lett.* **62** (6), 561 (1993)
- [Li10] B.-B. Li, Q.-Y. Wang, Y.-F. Xiao, X.-F. Jiang, Y. Li, L. Xiao, and Q. Gong: “On chip, high-sensitivity thermal sensor based on high-Q polydimethylsiloxane-coated microresonator,” *Appl. Phys. Lett.* **96** (25), 251109 (2010)
- [Lia10] W. Liang, V. Ilchenko, and A. Savchenkov: “Whispering-gallery-mode-resonator-based ultranarrow linewidth external-cavity semiconductor laser,” *Opt. Lett.* (2010)
- [Lin86] H. Lin, A. Huston, B. Justus, and A. Campillo: “Some characteristics of a droplet whispering-gallery-mode laser,” *Opt. Lett.* **11** (10), 614 (1986)
- [Lin94] H. Lin and A. Campillo: “CW nonlinear optics in droplet microcavities displaying enhanced gain,” *Phys. Rev. Lett.* **73** (18), 2440 (1994)
- [Lin08] Q. Lin, T. Johnson, C. Michael, and O. Painter: “Adiabatic self-tuning in a silicon microdisk optical resonator,” *Opt. Express* **16** (19), 14801 (2008)
- [Lit99] B. Little, J. Laine, H. A. Haus, and L. Fellow: “Analytic theory of coupling from tapered fibers and half-blocks into microsphere resonators,” *J. Light. Technol.* **17** (4), 704 (1999)
- [Lou05] Y. Louyer, D. Meschede, and A. Rauschenbeutel: “Tunable whispering-gallery-mode resonators for cavity quantum electrodynamics,” *Phys. Rev. A* **72** (3), 031801 (2005)
- [Lou10] N. Lou, R. Jha, J. Domínguez-Juárez, and V. Finazzi: “Embedded optical micro/nano-fibers for stable devices,” *Opt. Lett.* **35** (4), 571 (2010)

- [Mal65] I. H. Malitson: “Interspecimen comparison of the refractive index of fused silica,” *J. Opt. Soc. Am.* **55** (10), 1205 (1965)
- [Mat75] M. Matsuhara and A. Watanabe: “Coupling of curved transmission lines, and application to optical directional couplers,” *J. Opt. Soc. Am.* **65** (2), 163 (1975)
- [Mat06] A. B. Matsko and V. Ilchenko: “Optical resonators with whispering-gallery modes—part I: Basics,” *IEEE J. Sel. Top. Quantum Electron.* **12** (1), 3 (2006)
- [Maz07a] A. Mazzei, S. Götzinger, L. de S. Menezes, G. Zumofen, O. Benson, and V. Sandoghdar: “Controlled coupling of counterpropagating whispering-gallery modes by a single Rayleigh scatterer: A classical problem in a quantum optical light,” *Phys. Rev. Lett.* **99** (17), 173603 (2007)
- [Maz07b] A. Mazzei, S. Götzinger, L. de S. Menezes, G. Zumofen, O. Benson, and V. Sandoghdar: “Controlled coupling of counterpropagating whispering-gallery modes by a single Rayleigh scatterer: A classical problem in a quantum optical light - supplementary information,” *Phys. Rev. Lett.* **99** (17), 1–5 (2007)
- [McC92] S. McCall, A. Levi, R. Slusher, S. Pearton, and R. Logan: “Whispering-Gallery mode microdisk lasers,” *Appl. Phys. Lett.* **60** (3), 289 (1992)
- [Mel10] A. Melloni, A. Canciamilla, C. Ferrari, F. Morichetti, L. O’Faolain, T. Krauss, R. D. L. Rue, A. Samarelli, and M. Sorel: “Tunable delay lines in silicon photonics: Coupled resonators and photonic crystals, a comparison,” *IEEE Photonics J.* **2** (2), 181 (2010)
- [Mic07] C. Michael, K. Srinivasan, T. Johnson, O. Painter, K. Lee, K. Hennessy, H. Kim, and E. Hu: “Wavelength- and material-dependent absorption in GaAs and AlGaAs microcavities,” *Appl. Phys. Lett.* **90**, 051108 (2007)
- [Min09] B. Min, E. Ostby, V. Sorger, E. Ulin-Avila, L. Yang, X. Zhang, and K. J. Vahala: “High-Q surface-plasmon-polariton whispering-gallery microcavity,” *Nature* **457** (7228), 455 (2009)
- [Mis02] M. I. Mishchenko, L. D. Travis, and A. A. Lacis: *Scattering, Absorption, and Emission of Light by Small Particles* (Cambridge University Press, Cambridge, 2002)
- [Miy00] H. Miyazaki and Y. Jimba: “Ab initio tight-binding description of morphology-dependent resonance in a bisphere,” *Phys. Rev. B* **62** (12), 7976 (2000)
- [Möl06] B. Möller, U. Woggon, and M. Artemyev: “Photons in coupled microsphere resonators,” *J. Opt. A: Pure Appl. Opt.* **8**, S113 (2006)
- [Möl07] B. Möller, U. Woggon, and M. Artemyev: “Bloch modes and disorder phenomena in coupled resonator chains,” *Phys. Rev. B* **75** (24), 245327 (2007)
- [Mor07] F. Morichetti, A. Melloni, A. Breda, A. Canciamilla, C. Ferrari, and M. Martinelli: “A reconfigurable architecture for continuously variable optical slow-wave delay lines,” *Opt. Express* **15** (25), 17273 (2007)

- [Mor11] F. Morichetti, A. Canciamilla, C. Ferrari, A. Samarelli, M. Sorel, and A. Melloni: “Travelling-wave resonant four-wave mixing breaks the limits of cavity-enhanced all-optical wavelength conversion,” *Nat. Commun.* **2**, 296 (2011)
- [Muk99] T. Mukaiyama, K. Takeda, H. Miyazaki, Y. Jimba, and M. Kuwata-Gonokami: “Tight-binding photonic molecule modes of resonant bispheres,” *Phys. Rev. Lett.* **82** (23), 4623 (1999)
- [Mur09] G. S. Murugan, J. Wilkinson, and M. Zervas: “Selective excitation of whispering gallery modes in a novel bottle microresonator,” *Opt. Express* **17** (14), 11916 (2009)
- [Nak05] A. Nakagawa, S. Ishii, and T. Baba: “Photonic molecule laser composed of GaInAsP microdisks,” *Appl. Phys. Lett.* **86**, 041112 (2005)
- [Nöc97] J. U. Nöckel and A. D. Stone: “Ray and wave chaos in asymmetric resonant optical cavities,” *Nature* **385**, 45 (1997)
- [Nos07] A. Nosich, E. Smotrova, S. Boriskina, T. Benson, and P. Sewell: “Trends in microdisk laser research and linear optical modelling,” *Opt. Quantum Electron.* **39** (15), 1253 (2007)
- [Oka06] K. Okamoto: *Fundamentals of Optical Waveguides* (Academic Press, San Diego, 2006), 2nd edn.
- [O’S11] D. O’Shea, C. Junge, M. Pöllinger, A. Vogler, and A. Rauschenbeutel: “All-optical switching and strong coupling using tunable whispering-gallery-mode microresonators,” *Appl. Phys. B: Lasers Opt.* **105** (1), 129 (2011)
- [Ost09] E. Ostby and K. Vahala: “Yb-doped glass microcavity laser operation in water,” *Opt. Lett.* **34** (8), 1153 (2009)
- [Oxb07] M. Oxborrow: “Traceable 2D finite-element simulation of the whispering-gallery modes of axisymmetric electromagnetic resonators,” *IEEE Trans. Microw. Theory Tech.* **55** (6), 1209 (2007)
- [Pal91] E. D. Palik: *Handbook of Optical Constants of Solids* (Academic Press, New York, 1991)
- [Per03] T. Pertsch: *Discrete localization in linear and nonlinear optical waveguide arrays*, Doctoral thesis, Friedrich-Schiller-Universität Jena (2003)
- [Pis07] S. Pishko, P. Sewell, T. Benson, and S. Boriskina: “Efficient analysis and design of low-loss whispering-gallery-mode coupled resonator optical waveguide bends,” *J. Light. Technol.* **25** (9), 2487 (2007)
- [Pöl09] M. Pöllinger, D. O’Shea, F. Warken, and A. Rauschenbeutel: “Ultrahigh-Q tunable whispering-gallery-mode microresonator,” *Phys. Rev. Lett.* **103** (5), 53901 (2009)
- [Poo06] J. Poon, L. Zhu, G. DeRose, and A. Yariv: “Transmission and group delay of microring coupled-resonator optical waveguides,” *Opt. Lett.* **31** (4), 456 (2006)



- [Pop06] M. Popovic, T. Barwicz, M. Watts, P. Rakich, L. Socci, E. Ippen, F. Kärtner, and H. Smith: “Multistage high-order microring-resonator add-drop filters,” *Opt. Lett.* **31** (17), 2571 (2006)
- [Pre92] W. H. Press, S. A. Teukolsky, W. T. Vetterling, and B. P. Flannery: *Numerical Recipes in C++: The Art of Scientific Computing* (Cambridge University Press, Cambridge, 1992), 2nd edn.
- [Qia86] S. Qian, J. Snow, H. Tzeng, and R. Chang: “Lasing droplets: Highlighting the liquid-air interface by laser emission.” *Science* **231** (4737), 486 (1986)
- [Raf97] D. Rafizadeh, J. Zhang, S. Hagness, A. Taflove, K. Stair, S. Ho, and R. Tiberio: “Waveguide-coupled AlGaAs/GaAs microcavity ring and disk resonators with high finesse and 21.6 nm free spectral range,” *Opt. Lett.* **22** (16), 1244 (1997)
- [Rak04] Y. Rakovich, J. Donegan, M. Gerlach, A. Bradley, T. Connolly, J. Boland, N. Gaponik, and A. Rogach: “Fine structure of coupled optical modes in photonic molecules,” *Phys. Rev. A* **70** (5), 051801 (2004)
- [Ray10] L. Rayleigh: “The problem of the whispering gallery,” *Philos. Mag.* **20**, 1001 (1910)
- [Ray14] L. Rayleigh: “Further applications of Bessel’s functions of high order to the whispering gallery and allied problems,” *Philos. Mag.* **27**, 100 (1914)
- [Riv11] R. Riviere, S. Deleglise, S. Weis, E. Gavartin, O. Arcizet, A. Schliesser, and T. J. Kippenberg: “Optomechanical sideband cooling of a micromechanical oscillator close to the quantum ground state,” *Phys. Rev. A* **83** (6), 063835 (2011)
- [Rob06] J. Robinson, S. Preble, and M. Lipson: “Imaging highly confined modes in sub-micron scale silicon waveguides using transmission-based near-field scanning optical microscopy,” *Opt. Express* **14** (22), 10588 (2006)
- [Rok05] H. Rokhsari and K. J. Vahala: “Observation of Kerr nonlinearity in microcavities at room temperature,” *Opt. Lett.* **30** (4), 427 (2005)
- [Ros09] J. Rosenberg, Q. Lin, and O. Painter: “Static and dynamic wavelength routing via the gradient optical force,” *Nat. Photonics* **3** (8), 478 (2009)
- [Row93] D. Rowland and J. Love: “Evanescent wave coupling of whispering gallery modes of a dielectric cylinder,” *IEE Proc.: Optoelectronics* **140** (3), 177 (1993)
- [Sac95] Z. Sacks, D. Kingsland, R. Lee, and J. Lee: “A perfectly matched anisotropic absorber for use as an absorbing boundary condition,” *IEEE Trans. Antennas Propag.* **43** (12), 1460 (1995)
- [Sak01] K. Sakoda: *Optical Properties of Photonic Crystals*, Springer series in optical science (Springer-Verlag, Berlin Heidelberg NewYork, 2001), 1st edn.
- [Sal91] B. E. A. Saleh and M. C. Teich: *Fundamentals of Photonics* (John Wiley , New York, 1991)

- [San96] V. Sandoghdar, F. Treussart, J. Hare, V. Lefevre-Seguin, J. Raimond, and S. Haroche: “Very low threshold whispering-gallery-mode microsphere laser,” *Phys. Rev. A* **54** (3), 1777 (1996)
- [Sav04] A. Savchenkov, A. Matsko, D. Strekalov, M. Mohageg, V. Ilchenko, and L. Maleki: “Low threshold optical oscillations in a whispering gallery mode  $\text{CaF}_2$  resonator,” *Phys. Rev. Lett.* **93** (24), 243905 (2004)
- [Sav07] A. Savchenkov, A. B. Matsko, V. Ilchenko, N. Yu, and L. Maleki: “Whispering-gallery-mode resonators as frequency references II. Stabilization,” *J. Opt. Soc. Am. B* **24** (12), 2988 (2007)
- [Sch09a] A. Schließer: *Cavity Optomechanics and Optical Frequency Comb Generation with Silica Whispering-Gallery-Mode Microresonators*, Doctoral thesis, Ludwig-Maximilians-Universität München (2009)
- [Sch09b] A. Schliesser, O. Arcizet, R. Rivière, G. Anetsberger, and T. Kippenberg: “Resolved-sideband cooling and position measurement of a micromechanical oscillator close to the Heisenberg uncertainty limit,” *Nat. Phys.* **5** (7), 509 (2009)
- [Sha09] J. Shainline, S. Elston, Z. Liu, G. Fernandes, R. Zia, and J. Xu: “Subwavelength silicon microcavities,” *Opt. Express* **17** (25), 23323 (2009)
- [Sny75] A. Snyder and J. Love: “Reflection at a curved dielectric interface - electromagnetic tunneling,” *IEEE Trans. Microw. Theory Tech.* **23** (1), 134 (1975)
- [Sny83] A. W. Snyder and J. D. Love: *Optical Waveguide Theory* (Chapman & Hall, 1983)
- [Sol07a] M. Soltani, Q. Li, S. Yegnanarayanan, and A. Adibi: “Improvement of thermal properties of ultra-high Q silicon microdisk resonators,” *Opt. Express* **15** (25), 17305 (2007)
- [Sol07b] M. Soltani, S. Yegnanarayanan, and A. Adibi: “Ultra-high Q planar silicon microdisk resonators for chip-scale silicon photonics,” *Opt. Express* **15** (8), 4694 (2007)
- [Sol10] M. Soltani, Q. Li, S. Yegnanarayanan, and A. Adibi: “Toward ultimate miniaturization of high-Q silicon traveling-wave microresonators,” *Opt. Express* **18** (19), 19541 (2010)
- [Son10] Q. Song, L. Ge, A. D. Stone, H. Cao, and J. Wiersig: “Directional Laser Emission from a Wavelength-Scale Chaotic Microcavity,” *Phys. Rev. Lett.* **105** (10), 103902 (2010)
- [Son11] Q. H. Song, L. Ge, J. Wiersig, J. B. Shim, J. Unterhinninghofen, A. Eberspächer, W. Fang, G. S. Solomon, and H. Cao: “Wavelength-scale deformed microdisk lasers,” *Phys. Rev. A* **84** (6), 063843 (2011)
- [Spi03] S. M. Spillane, T. J. Kippenberg, O. Painter, and K. J. Vahala: “Ideality in a fiber-taper-coupled microresonator system for application to cavity quantum electrodynamics,” *Phys. Rev. Lett.* **91** (4), 43902 (2003)

- [Spi04] S. M. Spillane: *Fiber-coupled Ultra-high-Q Microresonators for Nonlinear and Quantum Optics*, Ph.D. thesis, California Institute of Technology (2004)
- [Spi05] S. M. Spillane, T. J. Kippenberg, K. J. Vahala, K. Goh, E. Wilcut, and H. J. Kimble: “Ultra-high-Q toroidal microresonators for cavity quantum electrodynamics,” *Phys. Rev. A* **71** (1), 013817 (2005)
- [Sri06] K. Srinivasan, M. Borselli, O. Painter, A. Stintz, and S. Krishna: “Cavity Q, mode volume, and lasing threshold in small diameter AlGaAs microdisks with embedded quantum dots,” *Opt. Express* **14** (3), 1094 (2006)
- [Ste98] N. Stefanou and A. Modinos: “Impurity bands in photonic insulators,” *Phys. Rev. B* **57** (19), 12127 (1998)
- [Sum04] M. Sumetsky: “Whispering-gallery-bottle microcavities: The three-dimensional etalon,” *Opt. Lett.* **29** (1), 8 (2004)
- [Tal85] S. Talisa: “Application of Davidenko’s method to the solution of dispersion relations in lossy waveguiding systems,” *IEEE Trans. Microw. Theory Tech.* **33** (10), 967 (1985)
- [Tob08] L. Y. M. Tobing, P. Dumon, R. Baets, and M. Chin: “Boxlike filter response based on complementary photonic bandgaps in two-dimensional microresonator arrays,” *Opt. Lett.* **33** (21), 2512 (2008)
- [Tre98] F. Treussart, V. Ilchenko, J. Roch, J. Hare, V. Lefevre-Seguin, J. Raimond, and S. Haroche: “Evidence for intrinsic Kerr bistability of high-Q microsphere resonators in superfluid helium,” *Eur. Phys. J. D* **1** (3), 235 (1998)
- [Tze84] H. Tzeng, K. Wall, M. Long, and R. Chang: “Laser emission from individual droplets at wavelengths corresponding to morphology-dependent resonances,” *Opt. Lett.* **9** (11), 499 (1984)
- [Vah03] K. J. Vahala: “Optical microcavities,” *Nature* **424** (6950), 839 (2003)
- [Vas03] V. Vassiliev, S. Il’ina, and V. Velichansky: “Diode laser coupled to a high-Q microcavity via a GRIN lens,” *Appl. Phys. B: Lasers Opt.* **76** (5), 521 (2003)
- [Ver98a] D. Vernooy, A. Furusawa, N. Georgiades, V. Ilchenko, and H. Kimble: “Cavity QED with high-Q whispering gallery modes,” *Phys. Rev. A* **57** (4), 2293 (1998)
- [Ver98b] D. Vernooy, V. Ilchenko, H. Mabuchi, E. Streed, and H. Kimble: “High-Q measurements of fused-silica microspheres in the near infrared,” *Opt. Lett.* **23** (4), 247 (1998)
- [Vol02] F. Vollmer, D. Braun, A. Libchaber, M. Khoshshima, I. Teraoka, and S. Arnold: “Protein detection by optical shift of a resonant microcavity,” *Appl. Phys. Lett.* **80** (21), 4057 (2002)
- [Vos07] K. D. Vos, I. Bartolozzi, E. Schacht, P. Bienstman, and R. Baets: “Silicon-on-insulator microring resonator for sensitive and label-free biosensing,” *Opt. Express* **15** (12), 7610 (2007)

- [Wan10] S. Wang, K. Broderick, H. Smith, and Y. Yi: “Strong coupling between on chip notched ring resonator and nanoparticle,” *Appl. Phys. Lett.* **97** (5), 051102 (2010)
- [War06] J. Ward, D. OShea, B. Shortt, M. Morrissey, K. Deasy, and S. N. Chormaic: “Heat-and-pull rig for fiber taper fabrication,” *Rev. Sci. Instrum.* **77** (8), 083105 (2006)
- [War08] J. Ward, P. Féron, and S. Chormaic: “A taper-fused microspherical laser source,” *IEEE Photonics Technol. Lett.* **20** (5/8), 392 (2008)
- [Web03] M. J. Weber: *Handbook of optical materials* (CRC Press LLC, 2003)
- [Wei95] D. Weiss, V. Sandoghdar, J. Hare, V. Lefevre-Seguin, J. Raimond, and S. Haroche: “Splitting of high-Q Mie modes induced by light backscattering in silica microspheres,” *Opt. Lett.* **20** (18), 1835 (1995)
- [Wie06] J. Wiersig and M. Hentschel: “Unidirectional light emission from high-modes in optical microcavities,” *Phys. Rev. A* **73** (3), 031802 (2006)
- [Wie97] D. Wiersma, P. Bartolini, A. Lagendijk, and R. Righini: “Anderson localization of light,” *Nature* **390**, 671 (1997)
- [Yan03] L. Yang, D. Armani, and K. J. Vahala: “Fiber-coupled erbium microlasers on a chip,” *Appl. Phys. Lett.* **83**, 825 (2003)
- [Yan04] M. Yanik and S. Fan: “Stopping light all optically,” *Phys. Rev. Lett.* **92** (8), 83901 (2004)
- [Yan07] Y.-D. Yang and Y.-Z. Huang: “Symmetry analysis and numerical simulation of mode characteristics for equilateral-polygonal optical microresonators,” *Phys. Rev. A* **76** (2), 023822 (2007)
- [Yar97] A. Yariv: *Optical electronics in modern communications* (Oxford Univ. Press, 1997)
- [Yar99] A. Yariv, Y. Xu, R. Lee, and A. Scherer: “Coupled-resonator optical waveguide: A proposal and analysis,” *Opt. Lett.* **24** (11), 711 (1999)
- [Zha89] J. Zhang and R. Chang: “Generation and suppression of stimulated Brillouin scattering in single liquid droplets,” *J. Opt. Soc. Am. B* **6** (2), 151 (1989)
- [Zhu11] J. Zhu, Ş. K. Özdemir, L. He, and L. Yang: “Controlled manipulation of mode splitting in an optical microcavity by two Rayleigh scatterers,” *Opt. Express* **18** (23), 23535 (2010)
- [Zhu09] J. Zhu, S. K. Ozdemir, Y.-F. Xiao, L. Li, L. He, D.-R. Chen, and L. Yang: “On-chip single nanoparticle detection and sizing by mode splitting in an ultrahigh-Q microresonator,” *Nat. Photonics* **4**, 46 (2009)

## B Useful mathematics and calculations

This appendix summarizes some basic mathematical relations that are used for calculations or for the implementation of numerical models in the main part of this thesis. Almost all the relations can be found in the given references, but to the opinion of the author, it might be helpful to have it in a summarized form. Especially for the FEM explicit terms are given which can be used for implementation in other PDE solvers than COMSOL. Additionally, some technical analysis of optimal parameters for FEM simulations is given.

### B.1 Vector algebra and integral theorems

Some useful vector identities using  $a$  and  $b$  as scalars and  $\mathbf{a}$ ,  $\mathbf{b}$ , and  $\mathbf{c}$  as vectors as well as  $\nabla \cdot \mathbf{a}$  and  $\nabla \times \mathbf{a}$  denoting the divergence and curl of the vector  $\mathbf{a}$  (see also Ref. [Jin02])

$$\nabla \times (\nabla \times \mathbf{a}) = \nabla (\nabla \cdot \mathbf{a}) - \nabla^2 \mathbf{a}, \quad (\text{B.1})$$

$$\nabla \cdot (\nabla \times \mathbf{a}) = 0, \quad (\text{B.2})$$

$$\nabla \times (\nabla a) = 0, \quad (\text{B.3})$$

$$\nabla \times (\mathbf{a} \times \mathbf{b}) = \mathbf{a} \nabla \cdot \mathbf{b} - \mathbf{b} \nabla \cdot \mathbf{a} - (\mathbf{a} \cdot \nabla) \mathbf{b} + (\mathbf{b} \cdot \nabla) \mathbf{a}, \quad (\text{B.4})$$

$$\nabla \cdot (\mathbf{a} \times \mathbf{b}) = \mathbf{b} \cdot \nabla \times \mathbf{a} - \mathbf{a} \cdot \nabla \times \mathbf{b}, \quad (\text{B.5})$$

$$\nabla (\mathbf{a} \cdot \mathbf{b}) = \mathbf{a} \times \nabla \times \mathbf{b} + \mathbf{b} \times \nabla \times \mathbf{a} + (\mathbf{a} \cdot \nabla) \mathbf{b} + (\mathbf{b} \cdot \nabla) \mathbf{a}, \quad (\text{B.6})$$

$$\nabla \times (a\mathbf{b}) = a\nabla \times \mathbf{b} - \mathbf{b} \times \nabla a, \quad (\text{B.7})$$

$$\nabla \cdot (a\mathbf{b}) = a\nabla \cdot \mathbf{b} + \mathbf{b} \cdot \nabla a, \quad (\text{B.8})$$

$$\mathbf{a} \times (\mathbf{b} \times \mathbf{c}) = (\mathbf{a} \cdot \mathbf{c}) \mathbf{b} - (\mathbf{a} \cdot \mathbf{b}) \mathbf{c}, \quad (\text{B.9})$$

$$\mathbf{a} \cdot (\mathbf{b} \times \mathbf{c}) = \mathbf{b} \cdot (\mathbf{c} \times \mathbf{a}) = \mathbf{c} \cdot (\mathbf{a} \times \mathbf{b}). \quad (\text{B.10})$$

Divergence theorem<sup>1</sup>

$$\int_V (\nabla \cdot \mathbf{F}) dV = \oint_{\partial V} (\mathbf{F} \cdot \hat{\mathbf{n}}) d(\partial V), \quad (\text{B.11})$$

with  $\mathbf{F}$  being a continuously differentiable vector field on a subset of  $\mathbb{R}^3$  with a piecewise smooth boundary  $\partial V$  and the outward pointing unit surface normal  $\hat{\mathbf{n}}$ .

---

<sup>1</sup>Also known as Gauss' theorem.

### Green's theorems

According to Ref. [Jin02] with a formal substitution of the vector field  $\mathbf{F}$  in Eq. (B.11) by the expression  $a\nabla(\epsilon b)$  with the continuous scalar functions  $a$  and  $b$  and the parameter  $\epsilon$ , the first scalar Green's theorem can be written as

$$\begin{aligned} \int_V [\nabla \cdot (a\nabla(\epsilon b))] dV &= \int_V [a\nabla \cdot (\epsilon\nabla b) + \epsilon(\nabla a)(\nabla b)] dV \\ &= \oint_{\partial V} [(a\epsilon\nabla b) \cdot \hat{\mathbf{n}}] d(\partial V). \end{aligned} \quad (\text{B.12})$$

With a substitution of the vector field  $\mathbf{F}$  in Eq. (B.11) by the expression  $\mathbf{a} \times (\epsilon\nabla \times \mathbf{b})$  with the vector functions  $\mathbf{a}$  and  $\mathbf{b}$ , the first vectorial Green's theorem can be written as:

$$\begin{aligned} \int_V [\nabla \cdot (\mathbf{a} \times (\epsilon\nabla \times \mathbf{b}))] dV &= \int_V [\epsilon(\nabla \times \mathbf{a}) \cdot (\nabla \times \mathbf{b}) - \mathbf{a} \cdot (\nabla \times \epsilon\nabla \times \mathbf{b})] dV \\ &= \oint_{\partial V} [\epsilon(\mathbf{a} \times \nabla \times \mathbf{b}) \cdot \hat{\mathbf{n}}] d(\partial V). \end{aligned} \quad (\text{B.13})$$

## B.2 Functional formulation for the FEM

### B.2.1 The standard vector wave equation

Starting from the vector wave equation for the magnetic field [Eq. (2.27)]

$$\nabla \times (\hat{\epsilon}^{-1} \nabla \times \mathbf{H}(\mathbf{r}, \omega)) - k_0^2 \mathbf{H}(\mathbf{r}, \omega) = 0, \quad (\text{B.14})$$

the variational functional form can be obtained by taking the inner product [as defined in Eq. (2.30)]

$$\langle \mathbf{a}, \mathbf{b} \rangle = \int_V (\mathbf{b}^* \cdot \mathbf{a}) dV, \quad (\text{B.15})$$

of both sides with the test magnetic field  $\tilde{\mathbf{H}}$

$$\begin{aligned} F(\mathbf{H}) &= \langle \nabla \times (\hat{\epsilon}^{-1} \nabla \times \mathbf{H}), \tilde{\mathbf{H}} \rangle - \langle k_0^2 \mathbf{H}, \tilde{\mathbf{H}} \rangle \\ &= \int_V \tilde{\mathbf{H}}^* \cdot [\nabla \times (\hat{\epsilon}^{-1} \nabla \times \mathbf{H})] dV - \int_V \tilde{\mathbf{H}}^* k_0^2 \mathbf{H} dV. \end{aligned} \quad (\text{B.16})$$

Applying Eq. (B.13) to the first integral leads to

$$F(\mathbf{H}) = \int_V [(\nabla \times \tilde{\mathbf{H}}^*) \cdot (\hat{\epsilon}^{-1} \nabla \times \mathbf{H}) - k_0^2 \tilde{\mathbf{H}}^* \mathbf{H}] dV, \quad (\text{B.17})$$

with the natural boundary condition for an ideal conducting wall

$$\oint_{\partial V} [\hat{\epsilon}^{-1} (\tilde{\mathbf{H}}^* \times \nabla \times \mathbf{H}) \cdot \hat{\mathbf{n}}] d(\partial V) = 0. \quad (\text{B.18})$$

The boundary condition can be reformulated using  $\hat{\epsilon}^{-1}\nabla \times \mathbf{H} = -i\omega\epsilon_0\mathbf{E}$  to

$$i\omega\epsilon_0 \oint_{\partial V} [(\mathbf{E} \times \tilde{\mathbf{H}}^*) \cdot \hat{\mathbf{n}}] d(\partial V) = i\omega\epsilon_0 \oint_{\partial V} (\mathbf{S} \cdot \hat{\mathbf{n}}) d(\partial V) = 0, \quad (\text{B.19})$$

with the Poynting vector  $\mathbf{S}$  tangential to the boundary (indicating no power flow across the surface). Alternatively, one can use the cyclic permutation identity

$$(\tilde{\mathbf{H}}^* \times \hat{\epsilon}^{-1}\nabla \times \mathbf{H}) \cdot \hat{\mathbf{n}} = (\hat{\epsilon}^{-1}\nabla \times \mathbf{H} \times \hat{\mathbf{n}}) \cdot \tilde{\mathbf{H}}^* = (\hat{\mathbf{n}} \times \tilde{\mathbf{H}}^*) \cdot (\hat{\epsilon}^{-1}\nabla \times \mathbf{H}), \quad (\text{B.20})$$

to obtain the often used notation

$$\hat{\mathbf{n}} \times \mathbf{E} = 0 \quad \text{or} \quad \hat{\mathbf{n}} \times \hat{\epsilon}^{-1}\nabla \times \mathbf{H} = 0. \quad (\text{B.21})$$

As discussed in the main text (Sect. 2.1.2) the solutions are not divergence free, resulting in non-physical spurious solutions. Koshiba et al. [Kos84] suggested to enforce  $\nabla \cdot \mathbf{H} = 0$  explicitly by adding a penalty term [Lei68, Hop81] to the functional [Eq. (B.16)]

$$\begin{aligned} \tilde{F}(\mathbf{H}) &= F(\mathbf{H}) + \int_V (\nabla \cdot \tilde{\mathbf{H}}^*) (\nabla \cdot \mathbf{H}) dV \\ &= F(\mathbf{H}) - \int_V [\tilde{\mathbf{H}}^* \cdot \nabla (\nabla \cdot \mathbf{H})] dV + \oint_{\partial V} [\tilde{\mathbf{H}}^* \mathbf{n} (\nabla \cdot \mathbf{H})] d(\partial V). \end{aligned} \quad (\text{B.22})$$

The stationarity of the functional requires the first variation  $\partial\tilde{F}$  (with respect to the test function) to be zero

$$\begin{aligned} \partial\tilde{F}(\mathbf{H}) &= \int_V \partial\tilde{\mathbf{H}}^* \cdot [\nabla \times (\hat{\epsilon}^{-1}\nabla \times \mathbf{H}) - \nabla (\nabla \cdot \mathbf{H}) - k_0^2\mathbf{H}] dV \\ &\quad - \oint_{\partial V} \partial\tilde{\mathbf{H}}^* \cdot [\hat{\mathbf{n}} \times (\hat{\epsilon}^{-1}\nabla \times \mathbf{H}) - \mathbf{n} (\nabla \cdot \mathbf{H})] d(\partial V) = 0. \end{aligned} \quad (\text{B.23})$$

This is fulfilled when

$$\nabla \times (\hat{\epsilon}^{-1}\nabla \times \mathbf{H}) - \nabla (\nabla \cdot \mathbf{H}) - k_0^2\mathbf{H} = 0, \quad (\text{B.24})$$

$$\hat{\mathbf{n}} \times (\hat{\epsilon}^{-1}\nabla \times \mathbf{H}) = 0, \quad (\text{B.25})$$

$$\mathbf{n} (\nabla \cdot \mathbf{H}) = 0, \quad (\text{B.26})$$

where Eq. (B.24) is the modified vector wave equation corresponding to Eq. (2.29) in Sect. 2.1.2 with an  $\alpha$  added to adjust the strength of the penalty term. Equation (B.25) [identical with (B.21)] and (B.26) are the boundary conditions ensuring that the electric field is normal and the magnetic field is tangential to the boundary. To follow the logic in Sect. 2.1.2 one can perform all steps (B.15) to (B.21) for the modified vector wave equation (2.29) instead of Eq. (B.15) to obtain the functional (2.31).

## B.2.2 Weak terms for axisymmetric resonators

According to Ref. [Oxb07] the weak terms of the functional [Eq. (2.31), Sect. 2.1.2]

$$F(\mathbf{H}) = \int_V \left[ (\nabla \times \tilde{\mathbf{H}}^*) \cdot (\hat{\epsilon}^{-1} \nabla \times \mathbf{H}) + \alpha (\nabla \cdot \tilde{\mathbf{H}}^*) (\nabla \cdot \mathbf{H}) - k_0^2 \tilde{\mathbf{H}}^* \mathbf{H} \right] dV, \quad (\text{B.27})$$

can be calculated in the axisymmetric case for a field expression [Eq. (2.32)]

$$\mathbf{H}(\mathbf{r}) = (H_r(r, z), iH_\phi(r, z), H_z(r, z)) e^{im\phi}, \quad (\text{B.28})$$

the cylindrical coordinate volume element  $dV = r dr d\phi dz$  and the permittivity and permeability tensor  $\hat{\epsilon} = \text{diag}(\epsilon_r, \epsilon_\phi, \epsilon_z)$  and  $\hat{\mu} = \text{diag}(\mu_r, \mu_\phi, \mu_z)$ . Here the permeability is taken into account in order to implement the PMLs. To this reason the modified versions  $\hat{\tilde{\epsilon}}$  and  $\hat{\tilde{\mu}}$  from Eq. (2.33) have to be used. For the first term one obtains

$$\begin{aligned} r(\nabla \times \tilde{\mathbf{H}}^*) \cdot (\hat{\tilde{\epsilon}}^{-1} \nabla \times \mathbf{H}) &= \begin{bmatrix} \frac{1}{r} \tilde{H}_{z,\phi} + i \tilde{H}_{\phi,z} \\ \tilde{H}_{r,z} - \tilde{H}_{z,r} \\ \frac{1}{r} (-r i \tilde{H}_\phi)_r - \frac{1}{r} \tilde{H}_{r,\phi} \end{bmatrix}^T \cdot \begin{bmatrix} \tilde{\epsilon}_r^{-1} (\frac{1}{r} H_{z,\phi} - i H_{\phi,z}) \\ \tilde{\epsilon}_\phi^{-1} (H_{r,z} - H_{z,r}) \\ \tilde{\epsilon}_z^{-1} (\frac{1}{r} (r i H_\phi)_r - \frac{1}{r} H_{r,\phi}) \end{bmatrix} \\ &= r \left[ \tilde{\epsilon}_r^{-1} \left( -\frac{im}{r} \tilde{H}_z + i \tilde{H}_{\phi,z} \right) \left( \frac{im}{r} H_z - i H_{\phi,z} \right) \right. \\ &\quad \left. + \tilde{\epsilon}_\phi^{-1} (\tilde{H}_{r,z} - \tilde{H}_{z,r}) (H_{r,z} - H_{z,r}) \right. \\ &\quad \left. + \tilde{\epsilon}_z^{-1} \left( -\frac{i}{r} \tilde{H}_\phi - i \tilde{H}_{\phi,r} + \frac{im}{r} \tilde{H}_r \right) \left( \frac{i}{r} H_\phi + i H_{\phi,r} - \frac{im}{r} H_r \right) \right] \\ &= \tilde{\epsilon}_r^{-1} \left( -\frac{m^2}{r} \tilde{H}_z H_z - m \tilde{H}_z H_{\phi,z} - m \tilde{H}_{\phi,z} H_z + r \tilde{H}_{\phi,z} H_{\phi,z} \right) \\ &\quad + \tilde{\epsilon}_\phi^{-1} r \left( \tilde{H}_{r,z} H_{r,z} - \tilde{H}_{r,z} H_{z,r} - \tilde{H}_{z,r} H_{r,z} + \tilde{H}_{z,r} H_{z,r} \right) \\ &\quad + \tilde{\epsilon}_z^{-1} \left( \frac{1}{r} \tilde{H}_\phi H_\phi + \tilde{H}_\phi H_{\phi,r} - \frac{m}{r} \tilde{H}_\phi H_r + \tilde{H}_{\phi,r} H_\phi + r \tilde{H}_{\phi,r} H_{\phi,r} \right. \\ &\quad \left. - m \tilde{H}_{\phi,r} H_r - \frac{m}{r} \tilde{H}_r H_\phi - m \tilde{H}_r H_{\phi,r} + \frac{m^2}{r} \tilde{H}_r H_r \right) \\ &= \frac{1}{r} \left[ \tilde{\epsilon}_r^{-1} m^2 \tilde{H}_z H_z + \tilde{\epsilon}_z^{-1} (\tilde{H}_\phi H_\phi - m (\tilde{H}_\phi H_r + \tilde{H}_r H_\phi)) \right. \\ &\quad \left. + m^2 \tilde{H}_r H_r \right] \\ &\quad + \left[ \tilde{\epsilon}_z^{-1} (\tilde{H}_{\phi,r} (H_\phi - m H_r) + H_{\phi,r} (\tilde{H}_\phi - m \tilde{H}_r)) \right. \\ &\quad \left. - \tilde{\epsilon}_r^{-1} m (\tilde{H}_z H_{\phi,z} + \tilde{H}_{\phi,z} H_z) \right] \\ &\quad + r \left[ \tilde{\epsilon}_r^{-1} \tilde{H}_{\phi,z} H_{\phi,z} + \tilde{\epsilon}_\phi^{-1} ((\tilde{H}_{z,r} - \tilde{H}_{r,z}) (H_{z,r} - H_{r,z})) \right. \\ &\quad \left. + \tilde{\epsilon}_z^{-1} \tilde{H}_{\phi,r} H_{\phi,r} \right], \end{aligned} \quad (\text{B.29})$$



with  $H_{\phi,r}$  denoting the partial derivative of the azimuthal component of the magnetic field with respect to the radius (same notation is used for other coordinate combination, respectively). The second, penalty term can be calculated to

$$\begin{aligned}
\alpha r[\nabla \cdot (\hat{\mu}\tilde{\mathbf{H}}^*)][\nabla \cdot (\hat{\mu}\mathbf{H})] &= \alpha r \left[ \tilde{\mu}_r \tilde{H}_{r,r} + \frac{1}{r} \tilde{\mu}_r \tilde{H}_r - \frac{m}{r} \tilde{\mu}_\phi \tilde{H}_\phi + \tilde{\mu}_z \tilde{H}_{z,z} \right] \left[ \tilde{\mu}_r H_{r,r} + \frac{1}{r} \tilde{\mu}_r H_r \right. \\
&\quad \left. - \frac{m}{r} \tilde{\mu}_\phi H_\phi + \tilde{\mu}_z H_{z,z} \right] \\
&= \alpha \left[ \tilde{\mu}_r^2 \left( r \tilde{H}_{r,r} H_{r,r} + \tilde{H}_{r,r} H_r + \tilde{H}_r H_{r,r} + \frac{1}{r} \tilde{H}_r H_r \right) \right. \\
&\quad + \tilde{\mu}_\phi^2 \frac{m^2}{r} \tilde{H}_\phi H_\phi + \tilde{\mu}_z^2 \tilde{H}_{z,z} H_{z,z} \\
&\quad + \tilde{\mu}_r \tilde{\mu}_\phi m \left( r \tilde{H}_{r,r} H_\phi - \tilde{H}_\phi H_{r,r} + \frac{1}{r} (\tilde{H}_r H_\phi - \tilde{H}_\phi H_r) \right) \\
&\quad + \tilde{\mu}_r \tilde{\mu}_z \left( r (\tilde{H}_{r,r} H_{z,z} + \tilde{H}_{z,z} H_{r,r}) + \tilde{H}_r H_{z,z} + \tilde{H}_{z,z} H_r \right) \\
&\quad \left. - \tilde{\mu}_\phi \tilde{\mu}_z m \left( \tilde{H}_\phi H_{z,z} + \tilde{H}_{z,z} H_\phi \right) \right] \\
&= \alpha \left[ \frac{1}{r} \left( \tilde{\mu}_r^2 \tilde{H}_r H_r - \tilde{\mu}_r \tilde{\mu}_\phi m (\tilde{H}_r H_\phi - \tilde{H}_\phi H_r) + m^2 \tilde{\mu}_\phi^2 \tilde{H}_\phi H_\phi \right) \right. \\
&\quad + \left( \tilde{\mu}_r^2 (\tilde{H}_{r,r} H_r + \tilde{H}_r H_{r,r}) - \tilde{\mu}_r \tilde{\mu}_\phi m (\tilde{H}_{r,r} H_\phi - \tilde{H}_\phi H_{r,r}) \right. \\
&\quad \left. + \tilde{\mu}_r \tilde{\mu}_z (\tilde{H}_r H_{z,z} + \tilde{H}_{z,z} H_r) - \tilde{\mu}_\phi \tilde{\mu}_z m (\tilde{H}_\phi H_{z,z} + \tilde{H}_{z,z} H_\phi) \right) \\
&\quad \left. + r \left( \tilde{\mu}_r^2 \tilde{H}_{r,r} H_{r,r} + \tilde{\mu}_r \tilde{\mu}_z (\tilde{H}_{r,r} H_{z,z} + \tilde{H}_{z,z} H_{r,r}) + \tilde{\mu}_z^2 \tilde{H}_{z,z} H_{z,z} \right) \right]. \tag{B.30}
\end{aligned}$$

The third, temporal weak term can be written as

$$\begin{aligned}
-k_0^2 r \hat{\epsilon} \tilde{\mathbf{H}}^* \mathbf{H} &= -k_0^2 r \left( \tilde{\mu}_r \tilde{H}_r H_r + \tilde{\mu}_\phi \tilde{H}_\phi H_\phi + \tilde{\mu}_z \tilde{H}_z H_z \right) \\
&= -\left( \frac{2\pi}{c} \right)^2 r \left( \tilde{\mu}_r \tilde{H}_r H_{r,tt} + \tilde{\mu}_\phi \tilde{H}_\phi H_{\phi,tt} + \tilde{\mu}_z \tilde{H}_z H_{z,tt} \right), \tag{B.31}
\end{aligned}$$

where the subscript  $tt$  denotes the second partial derivative of the harmonic field with respect to time. The factors in the last relation are chosen to identify the general eigenvalue ( $\lambda$  in  $e^{-\lambda t}$ ) used in COMSOL with the optical frequency  $\nu$ .

Likewise the boundary conditions [Eq. (2.28), Sect. 2.1.2] are modified and with the surface normal components  $\mathbf{n} = (n_r, 0, n_z)$  can be calculated to

$$\mathbf{n} \times (\hat{\epsilon}^{-1} \nabla \times \mathbf{H}) = \begin{bmatrix} -n_z \tilde{\epsilon}_\phi^{-1} (H_{r,z} - H_{z,r}) \\ n_z \tilde{\epsilon}_r^{-1} \left( \frac{im}{r} H_z - i H_{\phi,z} \right) - n_r \tilde{\epsilon}_z^{-1} \left( \frac{im}{r} H_\phi + i H_{\phi,r} - \frac{im}{r} H_r \right) \\ n_r \tilde{\epsilon}_\phi^{-1} (H_{r,z} - H_{z,r}) \end{bmatrix} = 0, \tag{B.32}$$

and

$$\mathbf{n} \times (\hat{\mu}\mathbf{H}) = 0, \tag{B.33}$$

resulting in the three conditions

$$\begin{aligned}
 H_{r,z} - H_{z,r} &= 0 \\
 \frac{1}{r} [n_z \tilde{\epsilon}_z (mH_z - rH_{\phi,z}) - n_r \tilde{\epsilon}_r (H_\phi + rH_{\phi,r} - mH_r)] &= 0 \\
 n_r \tilde{\mu}_r H_r + n_z \tilde{\mu}_z H_z &= 0.
 \end{aligned} \tag{B.34}$$

One can easily notice that none of the resulting terms of the Eqs. (B.29) to (B.34) depends on  $\phi$ , which indicates the reduction of the problem to 2D. Furthermore it should be mentioned that all the above expressions are generally formulated for axisymmetric, anisotropic and magnetic materials and can (or should) be further simplified for use in a FEM software whenever possible, e.g., for isotropic and nonmagnetic materials.

### B.2.3 Convergence tests

To optimize the numerical solution by the FEM the thickness of the PML layer  $h_{\text{PML}}$ , the PML growth factor  $\delta_{\text{PML}}$ , the penalty term strength  $\alpha$ , the mesh resolution as well as the extension of the air domain between disk and PML (determined by  $h_{\text{air}}$  and  $R_{\text{air}}$ ) needs to be adjusted. A few calculations are performed to cover all the parameters and to point out their influences. The results are plotted in Fig. B.1, looking at the resonance wavelength and the Q-factor as the crucial values, depending on  $h_{\text{PML}}$ . Varying  $\delta_{\text{PML}}$  from 0 (no PML) to 7.5 for the largest air region ( $h_{\text{air}} = 20 \mu\text{m}$ ,  $R_{\text{air}} = 35 \mu\text{m}$ ) shows no influence on the resonance wavelength [all lines coincide at the thick blue line with light blue dots in Fig. B.1(a)], whereas the Q-factor decreases from  $10^{22}$  to realistic values around  $10^{11}$ . Reducing the thickness of the air layer ( $h_{\text{air}} = 12 \mu\text{m}$ ,  $R_{\text{air}} = 26 \mu\text{m}$ ) shifts the resonance slightly to longer wavelengths but shows less dependence on  $h_{\text{PML}}$ . The Q-factor converges at  $h_{\text{PML}} = 5 \mu\text{m}$ . Decreasing the thickness of the air layer further ( $h_{\text{air}} = 6 \mu\text{m}$ ,  $R_{\text{air}} = 25 \mu\text{m}$ ) leads to stronger influence of the PML layer ( $\delta_{\text{PML}}$ ) on the resonance wavelength as well as on the convergence of the Q-factor.

To test the influence of the penalty term strength  $\alpha$  was varied from 0 (no penalty term) to 7.5 for the medium sized air layer and  $\delta_{\text{PML}} = 5$ . All simulations result in a resonance wavelength difference of only a few pm (white to red filled squares in Fig. B.1). The Q-factor of all but the simulation with  $\alpha = 0$  leads to the same Q-factor in coincidence with the converged value. For all other simulations  $\alpha = 5$  was used.

A comparison of a fine and a coarse mesh was performed for the thinnest and thickest air layer and  $\delta_{\text{PML}} = 2.5$  (green lines and symbols in Fig. B.1). Whereas the Q-factor for the thick air layer converges also for the coarse mesh at  $h_{\text{PML}} = 5 \mu\text{m}$ , the resonance wavelength deviates a few tens of pm with a large variation for different  $h_{\text{PML}}$ . For the thin air layer even the Q-factor does not converge. For the resonance wavelength accuracy of a few pm and a converged Q-factor the optimal parameters can be summarized to  $h_{\text{air}} = 12 \mu\text{m}$ ,  $R_{\text{air}} = 26 \mu\text{m}$ ,  $\delta_{\text{PML}} = 5$ ,  $h_{\text{PML}} = 5 \mu\text{m}$ ,  $\alpha = 5$  and a not too coarse mesh ( $\geq 10^5$  elements).

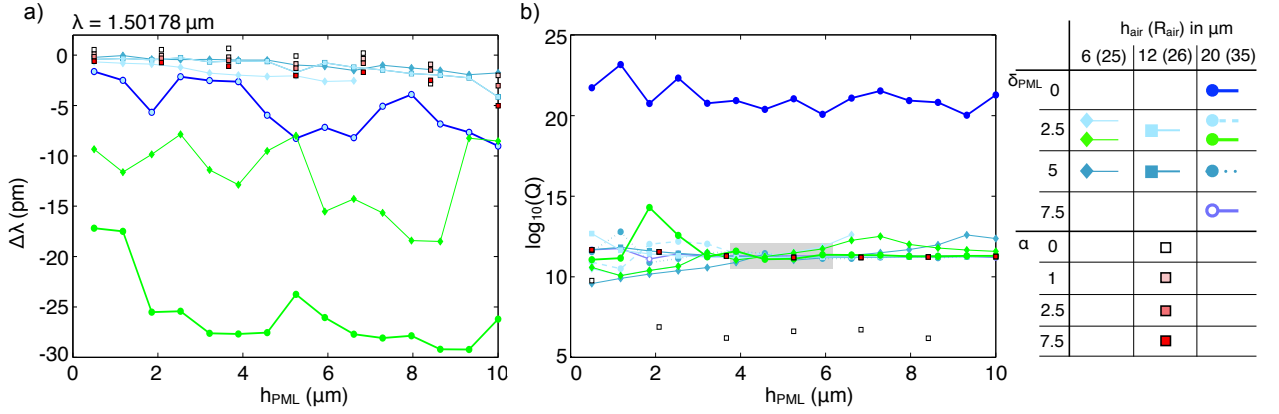


Fig. B.1: Parameter scans to determine the optimal values for precise calculation of (a) the resonance wavelength and (b) the Q-factor. A large enough air layer ( $h_{\text{air}} = 12 \mu\text{m}$ ,  $R_{\text{air}} = 26 \mu\text{m}$ ) gives reasonable results for  $\delta_{\text{PML}} \geq 2.5$ ,  $h_{\text{PML}} = 5 \mu\text{m}$  and  $\alpha \geq 1$ . A small distance between disk and PML layer (thin air layer) as well as a too coarse mesh (green lines and symbols) leads to strong variations of the resonance wavelength and bad convergence of the Q-factor. A too thick air layer gives good results but wastes computational resources. The convergence of the Q-factor is marked by the shading in (b), whereas the correct resonance wavelength is reached around  $\Delta\lambda = 0 \text{ pm}$ .

### B.3 Characteristic equation of a slab waveguide

The 2D effective index approximation used for calculating the resonances of single and coupled microdisks is based on the vertical confinement of the mode similar to that of a slab waveguide. Therefore the characteristic equation of a slab waveguide is of particular interest for the calculation of the effective 2D refractive disk index and its derivation is summarized here (see also [Oka06]). Choosing a slab mode propagating in  $y$ -direction the electromagnetic fields are invariant in  $x$ -direction [see Fig. B.2(a)] and the guided modes can be separated into two independent classes: TE and TM polarized modes. Therefore, the nonzero components of the general electromagnetic fields  $\tilde{\mathbf{F}}(\mathbf{r}) = \mathbf{F}(x, z)e^{i(\omega t - \beta y)}$  are  $F_{\text{TE}} = (E_y, H_x, H_z)$  and  $F_{\text{TM}} = (E_x, E_z, H_y)$  for TE and TM polarization, respectively. Using the field components in plane of the slab and transversal to the propagation direction the wave equation can be given as

$$\frac{\partial}{\partial z} \left( \tilde{n} \frac{\partial F_x}{\partial z} \right) + \tilde{n} (k_0 n^2 - \beta^2) F_x = 0, \quad (\text{B.35})$$

with the parameter  $\tilde{n} = 1$  for TE and  $\tilde{n} = 1/n^2$  for TM polarization, respectively. Since we are interested in guides modes of the slab, the ansatz of an oscillating field in the slab layer and exponentially decaying fields in the substrate and cladding can be used

$$F_x = \begin{cases} A \cos(k_f \frac{d_f}{2} - \Phi) e^{-k_c(z - \frac{d_f}{2})} & z > \frac{d_f}{2} \\ A \cos(k_f z - \Phi) & -\frac{d_f}{2} \leq z \leq \frac{d_f}{2} \\ A \cos(k_f \frac{d_f}{2} + \Phi) e^{k_s(z + \frac{d_f}{2})} & z < -\frac{d_f}{2}, \end{cases} \quad (\text{B.36})$$

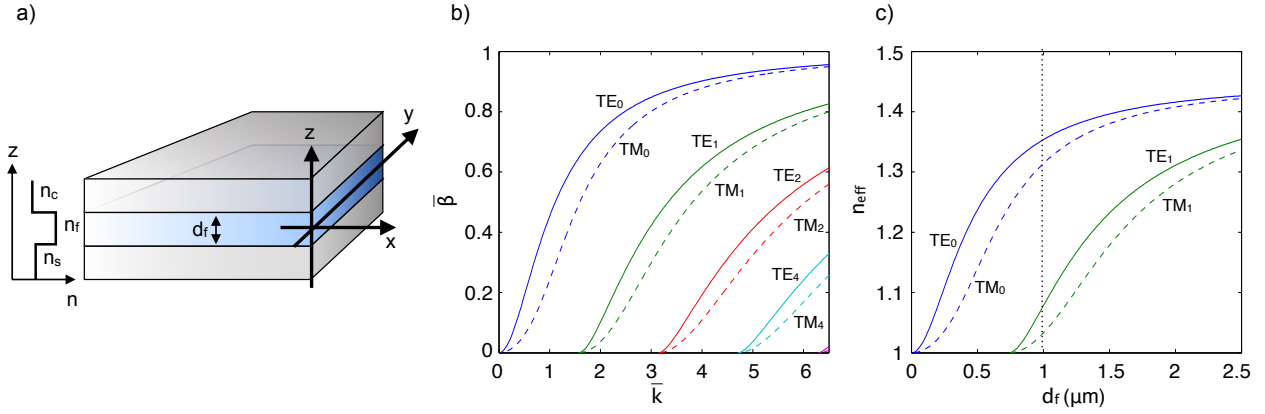


Fig. B.2: (a) Slab waveguide geometry with thickness  $d_f$ , refractive index of slab  $n_f$ , substrate  $n_s$  and cladding  $n_c$ , respectively. The mode propagation is in  $y$ -direction and the fields are invariant in  $x$ -direction. (b) Solution of Eq. (B.40) in terms of normalized parameter  $\bar{\beta}(\bar{k})$  for  $n_c = n_s = 1$ ,  $n_f = 1.45$ , and  $d_f = 1 \mu\text{m}$ . (c) Effective mode index for the first two orders modes of TE and TM polarization at  $\lambda = 1550 \text{ nm}$  for varying thickness  $d_f$ .

where  $d_f$  is the thickness of the slab layer,  $\Phi$  is the optical phase and the wavenumbers along the  $z$ -axis for the different regions (f - film or slab, c - cladding, s - substrate) are given as

$$k_f = \sqrt{k_0^2 n_f^2 - \beta^2}, \quad (\text{B.37})$$

$$k_c = \sqrt{\beta^2 - k_0^2 n_c^2}, \quad (\text{B.38})$$

$$k_s = \sqrt{\beta^2 - k_0^2 n_s^2}. \quad (\text{B.39})$$

Using Eq. (B.36) together with the boundary conditions, e.g., continuous tangential fields ( $F_x, F_y$ ) across the boundaries between the layers, yields the characteristic equation

$$2\bar{k}\sqrt{1 - \bar{\beta}} = l_z\pi + \arctan\left(\bar{n}_s\sqrt{\frac{\bar{\beta}}{1 - \bar{\beta}}}\right) + \arctan\left(\bar{n}_c\sqrt{\frac{\bar{\beta} + \gamma}{1 - \bar{\beta}}}\right), \quad (\text{B.40})$$

where we used the normalized wavenumber

$$\bar{k} = \frac{d_f}{2}\sqrt{k_f^2 + k_s^2} = k_0\frac{d_f}{2}\sqrt{n_f^2 - n_s^2}, \quad (\text{B.41})$$

and the normalized propagation constant

$$\bar{\beta} = \frac{n_{\text{eff}}^2 - n_s^2}{n_f^2 - n_s^2}, \quad (\text{B.42})$$

with the effective refractive index of the slab mode  $n_{\text{eff}} = \beta/k$ , as well as the refractive index symmetry parameter

$$\bar{\gamma} = \frac{n_s^2 - n_c^2}{n_f^2 - n_s^2}. \quad (\text{B.43})$$

The parameters  $\bar{n}_s$  and  $\bar{n}_c$  account for the differences of TE and TM polarization

$$\bar{n}_{s,c} = \begin{cases} 1 & \text{for TE} \\ n_f^2/n_{s,c}^2 & \text{for TM.} \end{cases} \quad (\text{B.44})$$

The mode order in  $z$ -direction, e.g., the number of zero crossings of the field in the slab layer in this direction is denoted by  $l_z$ .

A general solution can be found by solving Eq. (B.40) numerically looking for  $\bar{\beta}(\bar{k})$ , which is given in Fig. B.2(b) for different polarization and mode orders  $l_z$ . TE modes of the same order are confined much better than TM modes. In the case of microdisks we are interested in the lowest order slab modes only. In Fig. B.2(c) the effective index of both, the TE and TM fundamental slab modes are shown for a fixed wavelength of  $\lambda = 1550$  nm as a function of the thickness of the disk or slab ( $h$  or  $d_f$ , respectively). One can see that for the thickness of about 1  $\mu\text{m}$ , used for the microdisks in this thesis, the second order slab modes play only a minor role.

## C Symbols, constants and parameters

$a_m(\omega)$	Mode amplitude in eigenfunction expansion of incident field $F_{\text{inc}}$
$a_m^{(p)}(\omega)$	$a_m(\omega)$ distinguishing between different disks $p$ ; Similar notation for $b_m(\omega)$ , $d_m(\omega)$ , $F_{\text{inc,sc,int}}$
$\bar{a}_{\text{in}}(t)$	Slowly varying incident taper mode amplitude in time domain (CMT); similar notation for reflected/transmitted taper mode amplitude $\bar{a}_{\text{refl}}(t)/\bar{a}_{\text{trans}}(t)$
$b$	FHWM width of the WGM profile ( $b \approx 1 \mu\text{m}$ )
$b_m(\omega)$	Mode amplitude in eigenfunction expansion of scattered field $F_{\text{sc}}$
$b_j$	Mode amplitude of a reservoir mode (SNOM scattering)
$c$	Speed of light in vacuum ( $c = 2.9979 \times 10^8 \text{ m s}^{-1}$ )
$d_0$	Initial fiber diameter
$d_{\text{ext}}$	Minimum distance between tapered fiber and excited disk
$d_{\text{gap}}$	Minimum distance between adjacent disks (gap size)
$d_m(\omega)$	Mode amplitude in frequency domain (CMT)
$\bar{d}_m(t)$	Slowly varying mode amplitude in time domain (CMT); appears also as $\bar{d}_{\pm m}(t)$ accounting for counter-propagating modes ( $+m, -m \rightarrow \text{cw, ccw}$ ); appears also as $\bar{d}_{s,a}(\omega)$ for steady state amplitudes of symmetric and antisymmetric combinations of $\bar{d}_{\pm m}$
$d_m(t)$	Mode amplitude in eigenfunction expansion of internal field $F_{\text{int}}$
$d_{\text{sep}}$	Minimum distance between intensity maxima of tapered fiber and resonator mode
$d_{\text{tf}}$	Diameter of tapered optical fiber
$f(\mathbf{r}_{\text{tip}})$	normalized WGM field strength at the position of the SNOM tip
$g$	Coupling coefficient of intra disk modal coupling induced by a SNOM tip
$g'$	Coupling coefficient of WGM to reservoir modes induced by a SNOM tip
$h$	Height of microdisks (typically $h = 1 \mu\text{m}$ )
$h_{\text{air}}$	Thickness of air layer (used in FEM)
$h_{\text{polymer}}$	Thickness of polymer layer
$h_{\text{PML}}$	Thickness of PML layer (used in FEM)
$i$	Imaginary unit ( $i^2 = -1$ )
$k_0$	Vacuum wave number
$k$	Modulus of the wave vector
$k_{\text{eff}}$	Modulus of the effective wave vector

$k_{\text{th}}$	Thermal conductivity ( $k_{\text{th}} = 1.4 \text{ W m}^{-1} \text{ K}^{-1}$ , [Boy03])
$l$	Mode order of tapered fiber mode
$l_{\text{pull}}$	Pull length during tapered fiber fabrication
$m$	Azimuthal mode number of resonator mode; if different mode orders need to be distinguished $n$ is used additionally
$n_0$	Refractive index of surrounding medium of resonator
$n(\mathbf{r}, \omega)$	Refractive index (also appears as $n(z)$ or $n(r, z)$ with omitted $\omega$ -dependence)
$n_{\text{cl,air}}$	Refractive index of the fiber cladding/ surrounding air
$n_{\text{eff},z}(\omega)$	Effective refractive index of a slab mode or microdisk mode
$n_{\text{eff}}$	Effective refractive index of a tapered fiber mode or microdisk mode
$n_g$	Group index
$n_h$	Effective index in 2D of microdisk with height $h$ ( $n_h \equiv n_{\text{eff},z}$ )
$n_{\text{res}}$	Bulk refractive index of resonator material ( $n_{\text{res}} = 1.44$ to $1.45$ )
$\bar{n}$	Relative refractive index in 2D ( $\bar{n} = n_0/n_h$ )
$\hat{\mathbf{n}}$	Outward pointing surface normal of $\partial V$ ; also used as field unit vectors with subscripts (mode, j) (SNOM scattering)
$r$	Radial component of the space vector $\mathbf{r}$ in cylindrical coordinates
$\bar{r}$	Modified radial coordinate (introducing PML in the FEM)
$\mathbf{r}$	Spatial coordinates [cartesian $(x, y, z)$ or cylindrical $(r, \phi, z)$ ]
$\mathbf{r}_0$	Spatial coordinates of the center of the Gaussian distribution approximating tapered fiber excitation (coupled disk analysis)
$\mathbf{r}_p$	Spatial coordinates of the center of the $p$ th disk (coupled disk analysis)
$\mathbf{r}_{\text{tip}}$	Spatial coordinates of the SNOM tip
$\hat{\mathbf{r}}$	Unit radius vector
$s_r$	Stretching parameter in radial direction (introducing PML in the FEM)
$s_z$	Stretching parameter in axial direction (introducing PML in the FEM)
$t$	Time
$\hat{\mathbf{u}}_{\text{surf}}(\hat{\mathbf{r}})$	Spatially averaged electric field energy density at the disk edge
$v_g$	Group velocity of a light pulse
$v_{\text{sweep}}$	Wavelength sweeping speed of the pump TLS ( $v_{\text{sweep}} = 40 \text{ nm s}^{-1}$ )
$w$	Width of Gaussian distribution approximating tapered fiber excitation (coupled disk analysis)
$x$	Normalized frequency ( $x = \omega R_{\text{res}}/c$ ; generally complex-valued $x = x_1 + ix_2$ ); also used as cartesian component of $\mathbf{r}$
$x_{\text{gl}}^{(p)}$	Global $x$ coordinate of the boundary of the $p$ th disk (coupled disk analysis)
$y_{\text{gl}}^{(p)}$	Global $y$ coordinate of the boundary of the $p$ th disk (coupled disk analysis)
$z$	$z$ /axial component of space vector $\mathbf{r}$ in cartesian/cylindrical coordinates
$\alpha$	Strength of the divergence condition in the penalty term (FEM); also used as polarizability

$\alpha_{\text{abs}}$	Linear material absorption coefficient ( $\alpha_{\text{abs}} = 6 \times 10^{-2} \text{ m}^{-1}$ , [Fom05])
$\alpha_m(x)$	Modal scattering coefficient [ $\alpha(x) = b_m(x)/a_m(x)$ ]; $x$ is normalized frequency
$\alpha_{\text{th}}$	Temperature dependent expansion coefficient
$\beta_m(x)$	Ratio of modal expansion coefficient of internal and scattered field [ $\beta(x) = d_m(x)/b_m(x)$ ]; $x$ is normalized frequency
$\beta_{\text{res}}^{\text{eff}}$	Effective propagation constant of resonator
$\beta_{\text{tf, res}}$	Propagation constant of tapered fiber/resonator mode
$\beta_{\text{th}}$	Thermal coefficient (sum of thermal refractivity and expansion; $\beta_{\text{th}} = 4 \times 10^{-6} \text{ K}^{-1}$ measured)
$\beta_{\text{th, n}}$	Thermal refractivity
$\gamma_0$	Intrinsic energy loss rate
$\gamma_{\text{ext}}$	External energy loss rate
$\gamma_{\pm m, \mp m}$	Intra disk modal coupling rate
$\gamma_{qp}$	Inter disk modal coupling rate
$\gamma_{\text{rs}}$	Damping rate due to SNOM induced coupling to reservoir modes (scattering)
$\gamma_{\text{th}}$	Temperature relaxation rate (additional subscripts f - fast, s - slow, conv. - convective)
$\delta\epsilon(\mathbf{r}, \omega_m)$	Variation of dielectric function (relative permittivity) accounting for inter disk modal coupling (CMT)
$\delta\lambda_{\text{FSR}}$	Free spectral range in wavelength domain
$\delta\omega_{\text{FSR}}$	Free spectral range in frequency domain
$\delta T(\mathbf{r}, t)$	Spatial and temporal temperature variation
$\delta(\text{arg})$	Dirac delta function of argument $\text{arg}$
$\delta_{\text{PML}}$	Growth factor of PML attenuation
$\delta\bar{T}(t)$	Mode distribution averaged temperature change
$\epsilon_0$	Vacuum electric permittivity constant ( $\epsilon_0 = 8.8542 \times 10^{-12} \text{ A s V}^{-1} \text{ m}^{-1}$ )
$\epsilon_{\text{med}}$	Relative permittivity of the surrounding medium of the SNOM tip
$\epsilon_{r, \phi, z}$	Radial/azimuthal/axial component of the relative permittivity
$\epsilon_{\text{tip}}$	Relative permittivity of the SNOM tip material
$\epsilon(\mathbf{r}, \omega)$	Dielectric function (relative permittivity) in frequency domain
$\hat{\epsilon}(\mathbf{r}, \omega)$	Relative permittivity tensor
$\hat{\epsilon}^{-1}(\mathbf{r}, \omega)$	Inverse relative permittivity tensor
$\hat{\tilde{\epsilon}}(\mathbf{r}, \omega)$	Modified relative permittivity tensor (introducing PML in the FEM)
$\zeta_i$	Fraction of optical energy of the WGM in $i$ th layer of the structure ( $i = \text{polymer, silica}$ )
$\kappa$	Coupling coefficient of microdisk and tapered fiber ( $\kappa = \sqrt{\gamma_{\text{ext}}}$ ; CMT); appears also as $\kappa_{i,j}$
$\lambda$	Free space optical wavelength (typically around $\lambda = 1550 \text{ nm}$ )
$\mu_0$	Vacuum magnetic permeability constant ( $\mu_0 = 4\pi \times 10^{-7} \text{ V s A}^{-1} \text{ m}^{-1}$ )



$\hat{\mu}(\mathbf{r}, \omega)$	Relative permeability tensor
$\hat{\tilde{\mu}}(\mathbf{r}, \omega)$	Modified relative permeability tensor (introducing PML in the FEM)
$\nu$	Optical frequency
$\rho$	material density ( $\rho = 2.2 \times 10^3 \text{ kg m}^{-3}$ , [Gru09])
$\sigma_R$	Standard deviation of surface roughness (radial direction)
$\tau_0$	Intrinsic WGM mode energy decay time
$\tau_{\text{rt}}$	Round trip time of a photon in a WGM
$\tau_{\text{sweep}}$	Sweeping time through WGM resonance of TLS
$\tau_{\text{th}}$	Temperature relaxation time (additional subscripts f - fast, s - slow, conv. - convective); measured slow relaxation: $\tau_{\text{th}} = (0.496 \pm 0.043) \text{ ms}$
$\phi$	Azimuthal angle (of the space vector $\mathbf{r}$ in cylindrical coordinates)
$\phi_p$	Azimuthal angle measured in $p$ th disk (coupled disk analysis)
$\omega$	Angular optical frequency ( $\omega = 2\pi\nu$ )
$\omega_0$	Angular optical frequency of external excitation
$\omega_m$	Angular optical frequency of eigenmode $m$
$A$	Amplitude of Gaussian distribution (coupled disk analysis)
$A_{\text{mode}}$	Cross sectional area of a WGM
$\mathbf{A}_{\text{rad}}$	Vector potential of radiation problem
$B_{\text{th}}$	Specific mode absorption coefficient (thermal nonlinearity)
$\mathbf{B}(\mathbf{r}, \omega)$	Magnetic induction in frequency domain
$C_p$	Specific heat capacity at constant pressure ( $C_p = 6.7 \times 10^2 \text{ m}^2 \text{ s}^{-2} \text{ K}^1$ , [Gru09])
$D$	Distance between centers of two adjacent disks; also used as diameter of disks
$\mathbf{D}(\mathbf{r}, \omega)$	Dielectric displacement in frequency domain
$E_{r,\phi,z}$	Radial/azimuthal/axial component of electric field strength
$\mathbf{E}(\mathbf{r}, \omega)$	Electric field strength in frequency domain
$\mathbf{E}_m(\mathbf{r}, \omega_m)$	Electric field strength of unperturbed eigenmode at frequency $\omega_m$
$\mathbf{E}_{\text{tf,res}}$	Electric field strength in tapered fiber (tf) and resonator (res) modes
$\hat{\mathbf{E}}_{i,j}^\perp$	Normalized electric field strength of the unperturbed taper and resonator modes perpendicular to propagation direction in the tapered fiber ( $i, j \rightarrow \text{res, tf}$ )
$F(\mathbf{H})$	Functional of vector field $\mathbf{H}$
$F_{\text{inc}}^i(r, \phi, \omega)$	Incident field onto a microresonator, single polarization [ $F_{\text{inc}} = F_{z,\parallel}$ ]
$F_{\text{inc}}^{\text{glob}}$	Global incident field onto coupled microdisks
$F_{\text{int}}^i(r, \phi, \omega)$	Internal field of a microresonator, single polarization [ $F_{\text{int}} = F_{z,\parallel}$ ]
$F_{\text{sc}}(r, \phi, \omega)$	Scattered field of a microresonator, single polarization [ $F_{\text{sc}} = F_{z,\parallel}$ ]
$F_z$	Field coefficient for linear/axial polarization [ $F_z = F_z(r, \phi, z)$ ]
$F_{z,\parallel}$	In disk plane components of linear polarized field coefficient [ $F_{z,\parallel} = X(r, \phi) = X_r(r)X_\phi(\phi)$ ]

$F_{z,\perp}$	Transverse to disk plane component of linear polarized field coefficient [ $F_{z,\perp} = Y(z)$ ]
$\mathcal{F}$	Finesse
$G(\hat{r})$	Polarization dependent geometrical radiation factor
$G_m(x)$	Denominator of $\alpha_m(x)$ in characteristic equation of scattering problem of 2D microdisk; $x$ is normalized frequency
$\mathbf{F}(\mathbf{r}, t)$	General vector field; $\mathbf{F} = (\mathbf{E}, \mathbf{D}, \mathbf{B}, \mathbf{H})$
$\mathbf{F}(\mathbf{r}, \omega)$	Fourier transform of general vector field with respect to $t$
$H_m^{(1)}(arg)$	Hankel function of the first kind (argument $arg$ , order $m$ )
$H_{r,\phi,z}$	Radial/azimuthal/axial component of magnetic field strength (only a single subscript appears)
$H_{r,\phi}$	Partial derivative of the radial component of magnetic field strength with respect to the azimuthal angle (all combinations of $(r, \phi, z)$ possible; FEM)
$\mathbf{H}(\mathbf{r}, \omega)$	Magnetic field strength in frequency domain
$\bar{\mathbf{H}}(\mathbf{r}, \omega)$	Test function magnetic field (FEM)
$I$	Modulus square of the electric field (maximum $I_{\max}$ ); Intensity
$I_{\text{circ}}$	Circulating Intensity in a WGM
$\Im(arg)$	Imaginary part of complex argument $arg$
$J_m(arg)$	Bessel function of the first kind (argument $arg$ , order $m$ ); appears also with order $l$ for the calculation of tapered fiber modes
$\mathbf{J}$	Polarization currents Vector potential of radiation problem
$K_l(arg)$	Modified Bessel function of the second kind (argument $arg$ , order $l$ )
$L_0$	Length of the heating zone (tapered fiber fabrication process)
$L_c$	Correlation length of the surface roughness of a microdisk
$N$	Number of coupled disk in an ensemble
$P_{\text{circ}}$	Optical power circulating in a microdisk
$P_{\text{loss}}$	Lost optical power
$P_{\text{pump}}$	Optical pump power ( $P_{\text{pump}} = 0.1 \text{ mW}$ to $4 \text{ mW}$ in experiments)
$P_{\text{rad}}$	Total radiated optical power
$P_{\text{tresh}}$	Threshold optical pump power for nonlinear effects
$\mathbf{P}(\mathbf{r}, \omega)$	Dielectric polarization
$Q$	Quality factor (for investigated samples up to $Q = 5 \times 10^5$ measured); appears with different subscripts to distinguish different loss mechanisms
$R_{\text{air}}$	Radius of air layer around microdisk (used in FEM)
$R_{\text{pil}}$	Radius of the substrate pillar supporting the microdisk
$R_{\text{tip}}$	Radius of SNOM tip
$R_p$	Radius of $p$ th microdisk (coupled disk analysis)
$R_{q,p}$	Radial coordinate of the center of the $p$ th disk in the coordinate system of the $q$ th disk (coupled disk analysis)

$R_{\text{res}}$	Radius of microdisks (typically $R_{\text{res}} = 15 \mu\text{m}$ or $R_{\text{res}} = 20 \mu\text{m}$ )
$\Re(\text{arg})$	Real part of complex argument $\text{arg}$
$\mathcal{R}(\Delta\omega_m)$	Reflectivity of tapered fiber as function of detuning from resonance
$\langle \mathbf{S} \rangle$	Averaged Poynting vector
$\mathcal{T}(\Delta\omega_m)$	Transmissivity of tapered fiber as function of detuning from resonance
$U$	Electromagnetic energy; also used as $U$ -parameter in characteristic equation of step index fiber
$U_{\text{all}}$	Electromagnetic energy in resonator and environment
$U_{\text{res}}$	Electromagnetic energy stored in the resonator
$V$	Volume (of calculation domain); also used as $V$ -parameter in characteristic equation of step index fiber
$V_{\text{d}}$	Volume of a microdisk
$V_j$	Quantization volume of a reservoir mode (SNOM scattering)
$V_{\text{mode}}$	Mode volume of WGM (typically $V_{\text{mode}} = 0.5 \times 10^{-16} \text{m}^3$ to $1.1 \times 10^{-16} \text{m}^3$ ; for nonlinear simulations $V_{\text{mode}} = 0.67 \times 10^{-16} \text{m}^3$ )
$V_{\text{s}}$	Effective volume of a scatterer at the surface of a disk
$W$	$W$ -parameter in characteristic equation of step index fiber
$\Gamma_0$	Intrinsic loss coefficient ( $\Gamma_0 = \gamma_0/2$ ; CMT); for nonlinear simulations $\Gamma_0 = 1.6 \text{GHz}$
$\Gamma_{\text{ext}}$	External loss coefficient ( $\Gamma_{\text{ext}} = \gamma_{\text{ext}}/2$ ; CMT)
$\Gamma_{\text{ext,crit}}$	Critical external loss/coupling coefficient ( $\mathcal{T} = 0$ at $\Delta\omega = 0$ )
$\Gamma_{\text{mc}}$	Intra disk modal coupling coefficient ( $\Gamma_{\text{mc}} = \gamma_{\pm m, \mp m}/2$ ; CMT); for nonlinear simulations $\Gamma_{\text{mc}} = 2.88 \text{GHz}$
$\Gamma_{qp}$	Inter disk modal coupling coefficient ( $\Gamma_{qp} = \gamma_{qp}/2$ ; CMT); appears also as $\Gamma_{12}$ , for nonlinear simulations $\Gamma_{12} = 144 \text{GHz}$
$\Gamma_{\text{rs}}$	Loss coefficient due to SNOM induced coupling to reservoir modes (scattering)
$\Delta n_{\text{res}}$	Variation of resonator material refractive index $n_{\text{res}}$
$\Delta h$	Variation of disk thickness $h$
$\Delta\beta$	Propagation constant (phase) mismatch
$\Delta\epsilon(\omega_m)$	Perturbation of complex relative permittivity at $\omega_m$ [ $\Delta\epsilon(\mathbf{r}, \omega_m) = \Delta\epsilon'(\mathbf{r}, \omega_m) + i\Delta\epsilon''(\omega_m)$ ] (CMT)
$\Delta\hat{\epsilon}^{(p)}(\mathbf{r}, \omega_m)$	Perturbation of the relative permittivity (dielectric function) introduced by the $p$ th disk (CMT)
$\Delta\lambda$	Variation of optical wavelength $\lambda$ ; also appears as resonance splitting due to inter disk coupling
$\Delta\lambda_{12}$	Resonance mismatch of coupled disks (typically $\Delta\lambda_{12} = 0.2 \text{nm}$ )
$\Delta\lambda_b$	Bandwidth covered by the splitting of resonances of coupled disks
$\Delta\lambda_{\text{mc}}$	Resonance splitting due to intra disk modal coupling
$\Delta\lambda_{\text{th}}$	Temperature induced resonance wavelength shift

---

$\Delta\nu_b$	Frequency bandwidth according to $\Delta\lambda_b$
$\Delta\nu_{\text{th}}$	Temperature induced resonance frequency shift
$\Delta\omega_m$	Detuning of the excitation from the resonance frequency ( $\Delta\omega_m = \omega_0 - \omega_m$ )
$\Delta\Omega^{(p)}$	Abbreviation for $i\Delta\omega_m^{(p)} - (\Gamma_0 + \Gamma_{\text{ext}}^{(p)})$ (CMT)
$\Delta\mathbf{P}(\mathbf{r}, \omega)$	Perturbation polarization term in frequency domain (CMT)
$\Delta\bar{\mathbf{P}}(\mathbf{r}, t)$	Slowly varying perturbation polarization term in time domain (CMT)
$\Delta\bar{\mathbf{P}}_{\text{loss}}(\mathbf{r}, t)$	Slowly varying perturbation polarization term accounting for intrinsic resonator losses (CMT)
$\Delta\bar{\mathbf{P}}_{\text{ext}}(\mathbf{r}, t)$	Slowly varying perturbation polarization term accounting for external coupling (CMT)
$\Delta\bar{\mathbf{P}}_{\text{mc}}(\mathbf{r}, t)$	Slowly varying perturbation polarization term accounting for intrinsic modal coupling (CMT)
$\Delta\bar{\mathbf{P}}_m^{(p)}(\mathbf{r}, t)$	Slowly varying perturbation polarization term accounting for inter disk coupling (CMT)
$\Delta\bar{\mathbf{P}}_{\text{th}}(\mathbf{r}, t)$	Slowly varying perturbation polarization term accounting for temperature induced nonlinearity (CMT)
$\Delta R_i$	Variation of disk radius ( $i = \text{res}$ or $i = 1, 2, \dots$ )
$\Theta_{q,p}$	Azimuthal coordinate of the center of the $p$ th disk in the coordinate system of the $q$ th disk (coupled disk analysis)
$\Omega$	Fourier thermal frequency
$\Omega^{(p)}$	Boundary of $p$ th disk
$\partial V$	Surface enclosing the volume $V$
$\nabla a$	Gradient of $a$
$\nabla \cdot \mathbf{a}$	Divergence of vector $\mathbf{a}$
$\nabla \times \mathbf{a}$	Curl of vector $\mathbf{a}$

## D List of Abbreviations

1D	One dimensional	PC	Personal computer
2D	Two dimensional	PDE	Partial differential equation
3D	Three dimensional	PML	Perfectly matched layer
AOM	Acousto-optical modulator	PR	Photo receiver
CCD	Charged coupled device	Q-factor	Quality factor
CCW	Counter clockwise	Sect.	Section
Chap.	Chapter	SEM	Scanning electron microscope
CHF <sub>3</sub>	fluoroform	SF <sub>6</sub>	Sulfur hexafluoride
CMT	Coupled mode theory	SNOM	Scanning near field optical microscopy
(C)QED	(Cavity) quantum electrodynamics	TE	Transverse electric
CROW	Coupled resonator optical waveguide	TEC	Temperature controller
CW	clockwise	TLS	Tunable laser source
EBL	Electron beam lithography	TM	Transverse magnetic
EIM	Effective index method effective index approximation	VIS	Visible
Eq.	Equation	VOA	Variable optical attenuator
FDTD	Finite difference time domain	VR	Vibration reduction
FEM	Finite element method	WDM	Wavelength division multiplexing
FEP	Fluorinated ethylene propylene resist	WGM(s)	Whispering gallery mode(s)
FFT	Fast Fourier transform		
Fig.	Figure		
FPC	Fiber polarization controller		
FSR	Free spectral range		
FSU	Friedrich-Schiller-Universität		
FWHM	Full width at half maximum		
IAP	Institute of Applied Physics		
ICP	Inductively coupled plasma etch		
IFTO	Institute of Condensed Matter Theory and Solid State Optics		
InGaAs	Indium gallium arsenide		
IR	Infrared		
KOH	Potassium hydroxide		
N <sub>2</sub>	Nitrogen		
ODE	Ordinary differential equation		

# E Zusammenfassung

Die vorliegende Dissertation beschäftigt sich mit gekoppelten optischen Flüstergalerie-Resonatoren und deren kollektiven resonanten Anregungen, den sogenannten Flüstergalerie-Moden. Flüstergalerie-Resonatoren sind rotationssymmetrische Strukturen, in denen das Licht durch fortwährende Totalreflexion geführt und nach einem Umlauf durch Interferenz für die entsprechenden Wellenlängen resonant verstärkt wird. Durch geeignete Herstellungsprozesse und Querschnitte können aufgrund sehr glatter Oberflächen und den damit verbundenen geringen Streuverlusten sehr hohe optische Güten erzielt werden. Die typischen Abmessungen dieser Strukturen liegen im Mikrometerbereich, wodurch das Licht in einem sehr kleinen Volumen lokalisiert werden kann. Diesem Umstand ist die alternative Bezeichnung Mikroresonatoren geschuldet. Hohe optische Güten und kleine Modenvolumina sind von besonderem Interesse aufgrund der damit verbundenen niedrigen Pumpleistungsschwellen für die Beobachtung nicht-linearer optischer Effekte sowie der hohen Empfindlichkeit der schmalbandigen Resonanzen gegenüber Störungen am System, was für Sensoranwendungen von Bedeutung ist. Die gegenseitige Kopplung von Flüstergalerie-Resonatoren verbindet dabei die genannten vorteilhaften Eigenschaften einzelner Mikroresonatoren mit Charakteristiken diskret-optischer Systeme und eröffnet neue Untersuchungsfelder.

Die Kopplung benachbarter Resonatoren erfordert eine räumliche und spektrale Überlappung der Resonatormoden. Die räumliche Überlappung wird durch einen geringen Abstand zwischen den einzelnen Mikroresonatoren erreicht, wodurch ein Energieaustausch über die evaneszenten Felder möglich ist. Die Realisierung der spektralen Überlappung ist weitaus schwieriger und erfordert eine sehr genaue und reproduzierbare Herstellung einzelner Mikroresonatoren, insbesondere da mit steigender Resonatorgüte die Resonanzbandbreite kleiner wird. Um diesen Anforderungen gerecht zu werden, wurden im Rahmen dieser Arbeit freistehende gekoppelte Scheibenresonatoren aus amorphem Quarzglas mittels Elektronenstrahlolithographie hergestellt. Dieses Herstellungsverfahren limitiert die erreichbaren Güten auf  $10^5$  bis  $10^6$ . Die dadurch auftretenden, minimalen Resonanzbandbreiten erlauben einen spektralen Überlapp der Resonanzen benachbarter Mikroresonatoren, auch wenn deren Radien sich um wenige Nanometer unterscheiden. Diese Anforderungen werden durch die Reproduzierbarkeit des Herstellungsverfahrens erfüllt. Desweiteren erlaubt die Elektronenstrahlolithographie die Herstellung beliebiger zweidimensional gekoppelter Strukturen auf einem einheitlichen Chip-basierten Probenträger, wodurch eine systematische Untersuchung erleichtert wird.

Ein Hauptziel der Arbeit war die umfassende experimentelle Charakterisierung gekoppelter

Mikroresonatoren, um zu zeigen, dass durch die Kopplung mehrerer Scheibenresonatoren die herausragenden Eigenschaften, wie etwa die hohe optische Güte, nur geringfügig beeinflusst werden. Der Nachweis der optischen Kopplung der Moden in den vorliegenden Strukturen wurde anhand der charakteristischen spektralen Resonanzaufspaltung erbracht, die von der Anzahl als auch der Anordnung der einzelnen Mikroresonatoren abhängt. Zur Untermauerung der spektralen Resonanzaufspaltung als Indiz einer optischen Kopplung wurde eine Methode entwickelt, mit welcher erstmals die Intensitätsverteilung der kollektiven Anregungen in gekoppelten Scheibenresonatoren mit einer räumlichen Auflösung im Nanometerbereich gemessen werden konnte. Die Methode beruht dabei auf der ortsabhängigen Störung der Resonatormode, und damit des Resonanzspektrums, durch eine streuende Spitze eines Rasternahfeldmikroskops (SNOM). Neben der für die einzelnen beobachtbaren Resonanzen charakteristischen Intensitätsverteilung wurde damit auch die Symmetrie der kollektiven Anregung bestimmt.

Begleitend zur experimentellen Charakterisierung bestand ein wesentlicher Teil der Arbeit in der umfassenden theoretischen Modellierung der gekoppelten Mikroresonatoren. Dafür wurden bestehende analytische und numerische Konzepte adaptiert, zusammengefasst und erweitert, um das experimentelle System, wann immer möglich, in einem hohem Detailgrad zu beschreiben. Basierend auf der quantitativen Übereinstimmung zwischen theoretischen und experimentellen Ergebnissen konnten charakteristische Systemparameter bestimmt werden.

Aufbauend auf der Realisierung gekoppelter Mikroresonatoren erfolgte die Untersuchung des Einflusses thermischer nichtlinearer Effekte auf die Resonatormoden. Diese dynamische Licht-Materie-Wechselwirkung wird durch Absorption des Lichts in den Mikroresonatoren hervorgerufen und tritt aufgrund der starken Intensitätsüberhöhung schon bei geringen optischen Anregungsleistungen im Mikrowattbereich auf. Im Rahmen der vorliegenden Arbeit konnten in diesem Zusammenhang anregungsleistungsabhängige Resonanzverschiebungen und optische Bistabilität in gekoppelten Mikroresonatoren gezeigt werden. Die theoretische Modellierung und Vorhersage dieser Effekte erfolgte mit Hilfe einer gekoppelten Modentheorie, unter Einbeziehung der dynamischen Temperaturänderung in den Mikroresonatoren. Als entscheidender Parameter ist dabei die thermische Relaxationszeit anzusehen, welche experimentell bestimmt wurde. Des Weiteren konnte in gekoppelten Mikroresonatoren eine differentielle opto-optische Resonanzverstimmung beobachtet werden, welche eine Konsequenz der charakteristischen Intensitätsverteilung der einzelnen Moden ist.

Die detaillierte Kenntnis der thermo-optischen Eigenschaften der untersuchten Mikroresonatoren erlaubte die Realisierung einer Methode zur Kompensation der thermisch induzierten Resonanzverstimmungen. Durch Modifikationen im Herstellungsprozess ist es möglich, Polymer-schichten bestimmter Dicke auf den Quarzglas-Scheibenresonatoren aufzubringen, die eine zu Quarzglas entgegengesetzte thermische Refraktivität aufweisen. Durch das schichtdickenabhängige Verhältnis der Anteile der geführten Mode in den jeweiligen Schichten kann so eine effektive thermische Refraktivität nahe Null erreicht werden. Es wurde eine nahezu polarisationsunabhängige Kompensation bis zu optischen Leistungen von mehreren Milliwatt realisiert.

# F Publications

## Peer-reviewed Journals

- [CS1] N. K. Sakhnenko, A. Chipouline, C. Schmidt, A. G. Nerukh, and T. Pertsch: “Modeling of transient dynamics in two-dimensional circular microresonators using the pulsed complex source point beam concept,” *J. Opt. Soc. Am. A* **29**, 2197-2203 (2012)
- [CS2] C. Schmidt, M. Liebsch, A. Klein, N. Janunts, A. Chipouline, T. Käsebier, C. Etrich, F. Lederer, E.-B. Kley, A. Tünnermann, T. Pertsch: “Near-field mapping of optical eigenstates in coupled disk microresonators,” *Phys. Rev. A* **85**, 033827 (2012)
- [CS3] C. Schmidt, A. Chipouline, T. Käsebier, E.-B. Kley, A. Tünnermann, and T. Pertsch: “Temperature induced nonlinearity in coupled microresonators,” *Appl. Phys. B - Lasers and Optics* **104**, 503-512 (2011)
- [CS4] C. Schmidt, A. Chipouline, T. Käsebier, E.-B. Kley, A. Tünnermann, and T. Pertsch: “Thermal nonlinear effects in hybrid silica/polymer microdisks,” *Opt. Lett.* **35**, 3351-3353 (2010)
- [CS5] C. Schmidt, A. Chipouline, T. Käsebier, E.-B. Kley, V. Shuvayev, L. Deych, A. Tünnermann, and T. Pertsch: “Observation of optical coupling in microdisk resonators,” *Phys. Rev. A* **80**, 43841 (2009)
- [CS6] L. Deych, C. Schmidt, A. Chipouline, A. Tünnermann, and T. Pertsch: “Propagation of the fundamental whispering gallery modes in a linear chain of microspheres,” *Appl. Phys. B - Lasers and Optics* **93**, 21-30 (2008)
- [CS7] L. Deych, C. Schmidt, A. Chipouline, A. Tünnermann, and T. Pertsch: “Optical coupling of fundamental whispering-gallery modes in bispheres,” *Phys. Rev. A* **77**, 51801 (2008)
- [CS8] C. Schmidt, A. Chipouline, O. Egorov, F. Lederer, A. Tünnermann, L. Deych, and T. Pertsch: “Nonlinear thermal effects in optical microspheres at different wavelength sweeping speeds,” *Opt. Express* **16**, 6285-6301 (2008)



## Conference Contributions

1. C. Schmidt, M. Liebsch, A. Klein, N. Janunts, A. Chipouline, T. Käsebier, E.-B. Kley, A. Tünnermann, and T. Pertsch: “Characteristics of optical modes in coupled disk microresonators,” Doctoral Student’s Conference for the Discussion of Optical Concepts (DoKDoK), 7th to 11th October 2012, Oppurg, Germany - *Talk, Conference Paper*
2. C. Schmidt, M. Liebsch, A. Klein, N. Janunts, A. Chipouline, T. Käsebier, E.-B. Kley, and T. Pertsch: “Mode dynamics in coupled disk microresonators,” 492nd WE-Heraeus Seminar “Micro and macro-cavities in classical and non-classical light,” 30th October to 3rd November 2011, Bad Honnef, Germany - *Invited Talk, Abstract*
3. C. Schmidt, M. Liebsch, A. Chipouline, N. Janunts, T. Käsebier, E.-B. Kley, L. Deych, A. Tünnermann, and T. Pertsch: “Coupled disk microresonators,” 13th International Conference on Transparent Optical Networks (ICTON), 26th to 30th June 2011, Stockholm, Sweden - *Invited Talk, Conference Paper*
4. C. Schmidt, A. Chipouline, T. Käsebier, E.-B. Kley, A. Tünnermann, and T. Pertsch: “Thermal nonlinearity in coupled disk microresonators,” CLEO Europe and EQEC Conference, 22th to 26th May 2011, Munich, Germany - *Talk, Conference Paper*
5. C. Schmidt, M. Liebsch, A. Chipouline, N. Janunts, T. Käsebier, E.-B. Kley, A. Tünnermann, and T. Pertsch: “Mapping of whispering-gallery-modes in coupled disk microresonators,” CLEO Europe and EQEC Conference, 22th to 26th May 2011, Munich, Germany - *Talk, Conference Paper*
6. C. Schmidt, A. Chipouline, T. Käsebier, E.-B. Kley, L. Deych, A. Tünnermann, and T. Pertsch: “Linear and nonlinear optics in disk microresonators,” Doctoral Student’s Conference for the Discussion of Optical Concepts (DoKDoK), 21th to 25th March 2011, Naumburg, Germany - *Talk, Conference Paper*
7. C. Schmidt, A. Chipouline, T. Käsebier, E.-B. Kley, L. Deych, A. Tünnermann, and T. Pertsch: “Spectral characteristics of coupled silica disk micro resonators,” International Workshop on Photonic Nanomaterials (PhoNA), 24th to 25th March 2010, Jena, Germany - *Poster, Abstract*
8. C. Schmidt, A. Chipouline, T. Käsebier, E.-B. Kley, A. Tünnermann, L. Deych, and T. Pertsch: “Thermal and free electron nonlinearities in silica and hybrid silica/silicon disc micro resonators,” Frontiers in Optics, 11th to 15th Oktober 2009, San Jose, USA - *Talk, Conference Paper*
9. C. Schmidt, A. Chipouline, T. Käsebier, L. Deych, E.-B. Kley, A. Tünnermann, and T. Pertsch: “Spectral characteristics of coupled silica disc micro resonators,” Frontiers in Optics, 11th to 15th Oktober 2009, San Jose, USA - *Talk, Conference Paper*

10. C. Schmidt, A. Chipouline, T. Käsebier, E.-B. Kley, L. Deych, A. Tünnermann, and T. Pertsch: “Experimental and theoretical investigation of microresonators at Jena University,” 11th International Conference on Transparent Optical Networks (ICTON), 28th June to 2th July 2009, Ponta Delgada, Portugal - *Invited Talk, Conference Paper*
11. C. Schmidt, A. Chipouline, T. Käsebier, L. Deych, E.-B. Kley, A. Tünnermann, and T. Pertsch: “Spectral properties of coupled silica disc micro resonators,” CLEO Europe and EQEC Conference, 14th to 19th June 2009, Munich, Germany - *Poster, Conference Paper*
12. C. Schmidt, A. Chipouline, T. Käsebier, L. Deych, E.-B. Kley, A. Tünnermann, and T. Pertsch: “Nonlinear optical response of silica and hybrid silica/silicon disc micro resonators,” CLEO Europe and EQEC Conference, 14th to 19th June 2009, Munich, Germany - *Talk, Conference Paper*
13. C. Schmidt, A. Chipouline, T. Käsebier, L. Deych, E.-B. Kley, A. Tünnermann, and T. Pertsch: “Spectral characteristics of coupled silica disc micro resonators,” IEEE/LEOS Winter Topicals Meeting Series on Nanophotonics, 12th to 14th January 2009, Innsbruck, Austria - *Talk, Conference Paper*
14. C. Schmidt, A. Chipouline, T. Käsebier, G. K. Chowdhury, E.-B. Kley, A. Tünnermann, L. Deych, and T. Pertsch: “Nonlinear effects in silica and hybrid silica/silicon disc micro resonators,” IEEE/LEOS Winter Topicals Meeting Series on Nonlinear Dynamics in Photonic Systems, 12th to 14th January 2009, Innsbruck, Austria - *Talk, Conference Paper*
15. C. Schmidt, A. Chipouline, T. Käsebier, E.-B. Kley, O. Egorov, F. Lederer, A. Tünnermann, and T. Pertsch: “Spectral characteristics of single and coupled microresonators,” 407th WE-Heraeus Seminar “Discrete Optics and Beyond,” 19th to 21th May 2008, Bad Honnef, Germany - *Poster, Abstract*
16. L. Deych, C. Schmidt, A. Chipouline, A. Tünnermann, and T. Pertsch: “Coupling of the fundamental whispering gallery mode in bi-spheres,” 9th International Conference on Transparent Optical Networks (ICTON), 1st to 5th July 2007, Rome, Italy - *Talk, Conference Paper*
17. C. Schmidt, A. Chipouline, O. Egorov, F. Lederer, A. Tünnermann, L. Deych, and T. Pertsch: “Nonlinear effects due to thermo-optical instability in microsphere resonators,” 9th International Conference on Transparent Optical Networks (ICTON), 1st to 5th July 2007, Rome, Italy - *Talk, Conference Paper*
18. C. Schmidt, A. Chipouline, O. Egorov, F. Lederer, A. Tünnermann, L. Deych, and T. Pertsch: “Broadening and shift of resonances in microsphere resonators due to

- thermo-optical nonlinearity,” CLEO Europe and IQEC Conference, 17th to 22th June 2007, Munich, Germany - *Talk, Conference Paper*
19. C. Schmidt, A. Chipouline, O. Egorov, F. Lederer, A. Tünnermann, L. Deych, and T. Pertsch: “Nonlinear effects due to thermo-optical instability in microsphere resonators,” CLEO/QELS, 5th to 12th May 2007, Baltimore, USA - *Poster, Conference Paper*

# G Acknowledgements

This work would never exist without the support of several people and organizations. Most of all, I would like to thank Prof. Dr. Andreas Tünnermann and Prof. Dr. Thomas Pertsch for kindly housing me as a PhD student at the Institute of Applied Physics at the Friedrich-Schiller-Universität Jena.

Especially, I would like to thank Prof. Dr. Thomas Pertsch for the time he spent to supervise me during the last years. It was a great pleasure for me to join your group from the very beginning and to always benefit from the pleasant working environment. Thank you for introducing me to the real world of scientific research, teaching me scientific soft skills and thank you for the opportunity to participate in international conferences and workshops.

Very special thanks are devoted to Dr. Arkadi Chipouline who introduced me (and the Nanooptics group) to the world of optical whispering gallery microresonators and helped to enrich my knowledge on experimental methods as well as theoretical approaches solving various problems concerned with this thesis.

Furthermore, I would like to thank Dr. Ernst-Bernhard Kley, Thomas Käsebier and all people from the Microstructure Technology group at the IAP who were involved in the fabrication of the microdisk samples.

I also appreciate the collaboration with Prof. Lev Deych from the Physics Department at the Queens College, New York, who introduced me to theoretical concepts for the description of coupled microresonators.

Likewise, I would like to thank Dr. Christoph Etrich from the Institute of Condensed Matter Theory and Solid State Optics (IFTO) at the Friedrich-Schiller-Universität Jena supporting this work with computationally demanding FDTD simulations.

Often forgotten in this context, I would like to thank Bodo Martin for keeping the computers and the basic lab functions running as well as Dr. Lutz Leine (IFTO) for taking care of the compute cluster used for some calculations in this thesis.

Special thanks are devoted to all colleagues and (former) members of the Nanooptics group for their support and for creating an open-minded and fruitful atmosphere also off the office and lab hours. In particular, I would like to thank Mattes Liebsch for his persistence and patience in the lab under my supervision. I also thank Dr. Frank Setzpfandt and Reinhard Geiss for their help and support in the lab and in keeping all things somehow organized. Likewise, I would like to thank Falk Eilenberger for sharing his knowledge, in particular about efficient Labview programming. Many thanks also to Dr. Norik Janunts and Angela Klein for supporting me with the SNOM, as well as to Reinhard Geiss and Michael Steinert for SEM inspection and post-fabrication manipulation of the microdisk samples. Furthermore, special thanks are devoted to Dr. Jörg Petschulat. It was a great pleasure to work with you, I enjoyed our business and conference trips very much.

Finally, many thanks to all the volunteers for their accurate proofreading of the manuscript of this thesis.

Last but not least, I thank all my family and friends that supported me during the last years and always helped to keep my life balanced.

Jena, 19.12.2012

# H Short Curriculum Vitae

## Personal data

Name Carsten Schmidt  
Date of birth September 8th 1981  
Place of birth Erfurt, Germany



## Academic career

12/2012 Submittance of doctoral thesis entitled  
“Mode dynamics in coupled disk optical microresonators”  
03/2007 - current Scientific employee and PhD student at the Institute of Applied  
Physics at the Friedrich-Schiller-Universität Jena, Germany

## Lecture activity

winter term 2007 Seminar leader “Computational Physics”  
summer term 2008 Supervisor “Physikalisches Grundpraktikum”  
winter term 2008 Seminar leader “Computational Physics”  
summer term 2009 Seminar leader “Computational Physics”  
winter term 2009 Seminar leader “Computational Physics”  
summer term 2010 Seminar leader “Computational Physics”, Supervisor “Oberseminar”

## Education

01/2007 Diploma degree in Physics from the Friedrich-Schiller-Universität  
Jena, Germany  
12/2006 Diploma thesis entitled “Nichtlineare thermo-optische  
Effekte in sphärischen Mikroresonatoren”  
09/2004 - 08/2005 Student assistant at the Fraunhofer Institute for Applied Optics  
and Precision Engineering, Jena  
10/2001 - 01/2007 Study of Physics at the Friedrich-Schiller-Universität Jena, Germany  
09/2000 - 7/2001 Civil service at town administration, Werdau, Germany  
09/1992 - 07/2000 Georgengymnasium Zwickau, Germany; Abitur 07/2000

Jena, 19.12.2012

# Ehrenwörtliche Erklärung

Hiermit erkläre ich ehrenwörtlich, dass ich die vorliegende Arbeit selbständig, ohne unzulässige Hilfe Dritter und ohne Benutzung anderer als der angegebenen Hilfsmittel und Literatur angefertigt habe. Die aus anderen Quellen direkt oder indirekt übernommenen Daten und Konzepte sind unter Angabe der Quelle gekennzeichnet.

Weitere Personen waren an der inhaltlich-materiellen Erstellung der vorliegenden Arbeit nicht beteiligt. Insbesondere habe ich hierfür nicht die entgeltliche Hilfe von Vermittlungs bzw. Beratungsdiensten (Promotionsberater oder andere Personen) in Anspruch genommen. Niemand hat von mir unmittelbar oder mittelbar geldwerte Leistungen für Arbeiten erhalten, die im Zusammenhang mit dem Inhalt der vorgelegten Dissertation stehen.

Die Arbeit wurde bisher weder im In- noch im Ausland in gleicher oder ähnlicher Form einer anderen Prüfungsbehörde vorgelegt.

Die geltende Promotionsordnung der Physikalisch-Astronomischen Fakultät ist mir bekannt.

Ich versichere ehrenwörtlich, dass ich nach bestem Wissen die reine Wahrheit gesagt und nichts verschwiegen habe.

Jena, 19.12.2012

Carsten Schmidt